tecnun
Universidad
de Navarra

Pº Manuel Lardizabal, 13.
20018 Donostia-San Sebastián, Spain
Tel.943 219 877
Fax 943 311 442
www.tecnun.es

Towards high performance bulk thermoelectric materials with enhanced mechanical properties by Severe Plastic Deformation (SPD)

Jon Ander Santamaría Regueiro

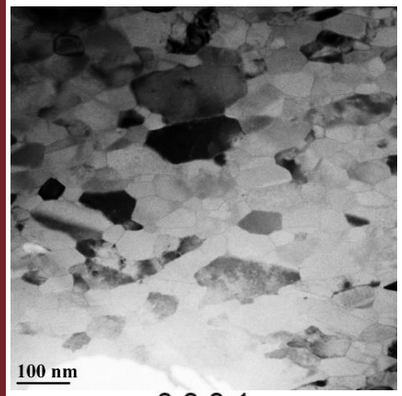

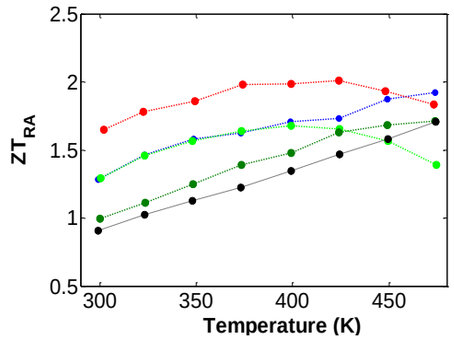

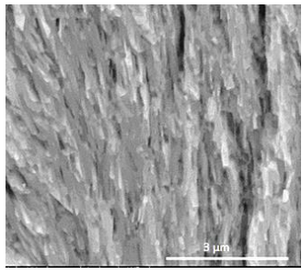

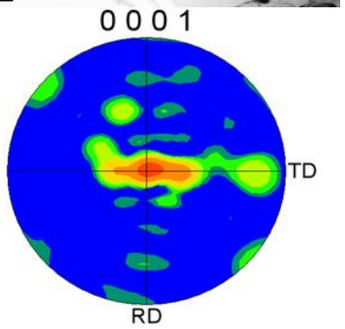

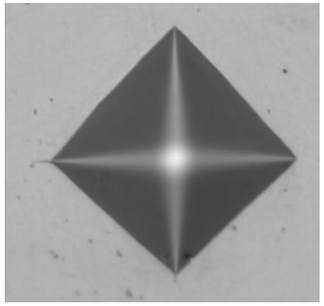

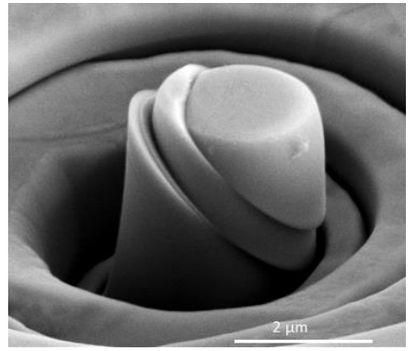

Towards high performance bulk thermoelectric materials with enhanced mechanical properties by Severe Plastic Deformation (SPD)

Dissertation
Submitted for the Degree of Doctor of Philosophy by
Jon Ander Santamaría Regueiro
Under the supervision of
Dr. Jon Alkorta Barragán and
Prof. Javier Gil Sevillano

Donostia-San Sebastián, December 2015

tecnun
Universidad
de Navarra

UNIVERSIDAD DE NAVARRA

ESCUELA SUPERIOR DE INGENIEROS

Towards high performance bulk thermoelectric materials with enhanced mechanical properties by Severe Plastic Deformation (SPD)

DISSERTATION

Submitted for the Degree of Doctor of Philosophy by

Jon Ander Santamaría Regueiro

Under the supervision of

Dr. Jon Alkorta Barragán

and

Prof. Javier Gil Sevillano

Donostia-San Sebastián, December 2015

A mis padres

ACKNOWLEDGEMENTS
AGRADECIMIENTOS
ESKERRAK

First of all, I would like thank CEIT and TECNUN (University of Navarra) for giving me the chance of being a Ph.D candidate. Also, I would like to acknowledge the financial support of the Spanish Ministry of Economy and Competitiveness through FPI grant for four years and finally to the Basque government for its financial assistance to buying the Linseis LSR3- 800 apparatus.

I would like to express my most sincere gratitude to Javier Gil Sevillano and Jon Alkorta Barragán for their supervision and support during this doctoral thesis. Thank you both, for all your help and support, for your valuable guidance and encouragement. It has been a pleasure to work with you. Gracias Jon por compartir tus conocimientos de microscopia electrónica conmigo. Por introducirme en la técnica de la nanoindentation, y por darme las primeras nociones en FEM. Sin tu apoyo no sería posible culminar esta tesis doctoral cuyos comienzos fueron tan difíciles y en ocasiones frustrantes. Las siglas HPT (ese pequeño monstruo que creaste y del que tanto nos hemos quejado Tamayo, Tobi y yo. Debes estar muy orgulloso de tu monstruito ya que ha sido ya herramienta fundamental de 3 tesis y espero que sea de muchas más.) y FIB quedaran siempre grabadas en mi memoria gracias a ti.

I also thank Univ. Prof. Dr. Reinhard Pippan and Dr. Anton Hohenwarter for hosting me during my stay at the Erich Schmid Institute of Materials Science (ESI). Tampoco me olvido de mi amigo de Leoben que habla un poquito de español, Peter Kutleša (Mr. HPT) fue un placer trabajar contigo. Special thanks to Dr. Verena Maier-Kiener for performing the SRS nanoindentation tests.

Desearía agradecer a todo el departamento de materiales del CEIT por compartir conmigo su tiempo y conocimiento. No me olvido del gran trabajo que hacéis tod@s los técnic@s. Gracias Reyes por guiarme con los ensayos de micro-compresión. Gracias Nerea por introducirme en la técnica LFA. La caracterización térmica no sería posible sin tu ayuda.

Quiero agradecer a todos los amigos y compañeros con los que he disfrutado trabajando en el CEIT. Los que todavía quedan y los que ya dejaron el CEIT, algunos aún están por lugares cercanos, otros se fueron a tierras lejanas, pero a todos ellos os llevo en el corazón. Sinceramente conseguís que el trabajo del día a día sea muy agradable.

Por supuesto agradezco a mi despacho y al extenso grupo del café. A la gente asidua a los pintxo-potes, aquellos que empezamos en Amara y nos trasladamos a Gros. Que grandes recuerdos me vienen a la cabeza… gracias a Mikel y Lutxo por el constante esfuerzo de hacerme grande y fuerte jajaj, por vuestros ánimos y apoyo. Por esas cenas en el txino que a alguno le resultaban algo indigestas…

Gracias a Emma y DJ por vuestro cariño y apoyo. Me habéis ayudado muchísimo en la escritura. Voy ahorrando para la cena en el alto de Miracruz DJ…

Gracias a la recién Dr. Llanos por estar siempre dispuesta a ayudarte.

Eskerrik asko kuadrillakuei, azkenaldixan ez naiz asko egon zuekin eta… baña orain botaku juerga handi batzuk bai. Eskerrik asko zuen pazientzia eta animuengatik.

Por último, querría agradecer de todo corazón a mi familia, por vuestro cariño incondicional, por apoyarme y animarme en este largo camino. Aita y ama vosotros sois sin duda los que más merecéis mis agradecimientos.

ABSTRACT

Nowadays, one of the most promising strategies to produce highly efficient thermoelectric (TE) materials is to reduce the lattice thermal conductivity by introducing phonon scattering centres (such as submicron sized grain boundaries, second-phase nano-particles, and point defects) at different length scales. For highly anisotropic crystals such as Bi_2Te_3-based thermoelectrics, the combination of nanosized grain structures (to improve phonon scattering) together with strong crystallographic texture (to exploit the anisotropic properties of the crystal) is not readily accessible by the standard high energy ball-milling and powder consolidation techniques. This work presents a novel technique that permits to obtain, simultaneously, highly textured submicron grained structures in $Sb_{2-x}Bi_xTe_3$ thermoelectric material.

The severe plastic deformation (SPD) induced by high pressure torsion (HPT) of $Sb_{2-x}Bi_xTe_3$ leads to fully dense disk-shaped samples with stable homogeneous grain sizes of ~100 nm and a strong crystallographic texture with the basal plane preferentially oriented perpendicular to the torsion axis. Such combination has a synergistic effect on the enhancement of the thermoelectric performance. For instance, after HPT processing, $Sb_{1.6}Bi_{0.4}Te_3$ compound displays a good TE performance in a wide range of temperatures and shows a maximum zT_{RA} (i.e. *PF* measured in-plane and κ out of plane) of ~2 at 375 K, (zT_{RR}~1.5 estimated in-plane). Moreover, HPT improves significantly the hardness of the processed samples, although thetheir strong crystal texture is detrimental for their flexural strength.

HPT has also been successfully applied to pure PbTe. The results confirm HPT processing as a promising alternative to spark plasma sintering to process mechanically improved PbTe-based thermoelectric compounds with all-scale hierarchical architectures.

RESUMEN

Actualmente una de las estrategias más eficaces para procesar materiales termoeléctricos eficientes se basa en introducir defectos cristalinos a diferentes escalas. Es bien sabido que los fonones se dispersan efectivamente mediante defectos tales como las juntas de grano, partículas de segundas fases o defectos puntuales, lo que conlleva una reducción significativa de la conductividad térmica.

En el caso de lo los materiales altamente anisótropos, como las aleaciones basadas en Bi_2Te_3, además de generar estructuras nanométricas es de vital importancia controlar la textura cristalográfica del compuesto ya que las propiedades termoeléctricas son óptimas únicamente en su plano basal. Hasta la fecha no se han obtenido materiales nanocristalinos preferentemente orientados mediante las técnicas de pulvimetalurgia convencionales. Este trabajo presenta una técnica novedosa que permite procesar materiales termoeléctricos de grano ultrafino y altamente texturizados basados en Bi_2Te_3.

La deformación plástica severa (SPD) inducida mediante la torsión bajo alta presión (HPT) permite producir muestras en forma de disco totalmente densas, fuertemente texturizadas (con el plano basal preferentemente orientado perpendicular al eje de torsión) y nanoestructuradas (con un tamaño de grano homogéneo del orden de 100 nm). Debido a la fuerte textura cristalográfica y grano ultrafino obtenidos mediante HPT, tras HPT se mejoran notablemente las propiedades termoeléctricas de los compuestos basados en Bi_2Te_3. En el caso del compuesto $Sb_{1.6}Bi_{0.4}Te_3$, por ejemplo, se logró una figura de mérito ZT_{RA} (obtenida tras medir el factor de potencia (*PF*) en el plano y la conductividad térmica (κ)a lo largo del eje axial) de ~2 a 425 K. Además el compuesto muestra un buen rendimiento termoeléctrico en un amplio rango de temperatura.

El procesamiento mediante HPT incrementa la dureza y la resistencia a compresión de las muestras, sin embargo la fuerte textura cristalográfica afecta negativamente a la resistencia a flexión.

Por último, también se han procesado satisfactoriamente muestras de PbTe puras mediante HPT. Los resultados confirman que el procesamiento mediante HPT es una alternativa viable a la sinterización activada por plasma (SPS), la cual permite fabricar compuestos basados en PbTe que contienen defectos o segundas fases desde la escala atómica hasta la meso-escala.

LABURPENA

Gaur egun, termodinamikoki eraginkorrak diren material termoelektrikoak prozesatzeko estrategia ohikoenetako bat fonoien bidez garraiaturiko eroankortasun termikoa gutxitzean datza. Helburu hori lortzeko, akats kristalografiko ugari (mikra azpiko ale mugak, nanopartikulak, edota defektu puntualak) sortu behar dira.

Material termoelektriko anisotropoen kasuan, Bi_2Te_3-a esaterako, nanoegiturak sortzeaz gain, aleak orientazio zehatz batean orientatzeak ere berebiziko grarrantzia du. Gaur egun arte, hauts-metalurgian oinarrituriko metodo tradizionalen bitartez ez da lortu bortizki orientaturiko material nanoegituratuak fabrikatzea. Arazo hori ikusita, lan honetan teknika berri bat proposatzen da, zeinak Bi_2Te_3-an oinarrituriko material termoelektriko nanoegituratuak eta bortizki orientatuak prozesatzea ahalbidetzen duen.

Presio altupeko tortsioaren (HPT) bitaztez eragindako deformazio plastikoaren ondorioz guztiz trinkoak diren disko formako laginak prozesatu dira. Deformazio plastiko honen poderioz, materialaren kristal-aleek orientazio kristalografiko jakin bat hartzen dute (aleen planu basala tortsio ardatzarekiko perpendikularra izanik) eta 100 nm inguruko ale tamaina izatera irits daitezke. Honi esker, HPT prozesaketak propietate termoelektrikoen hobekuntza dakar. Adibidez, $Sb_{1.6}Bi_{0.4}Te_3$-aren zT_{RA} (potenzia faktorea diskoaren (PF) planoan neurturik eta eroankortasun termikoa (κ) diskoaren artatzen neurturik lortzen den zT-a) ~2 da 425 K inguruan.

HPT prozesaketak, materialaren gogortasuna hobetzen du, baina orientazio kristalografiko bortitzak flexio erresintentziaren murriztea dakar.

Modu berean, HPT-ren bitartez PbTe-a ere prozesatu da. Lortutako emaitzek HPT teknika plasma bidez aktibuturiko sinterizazioaren alternatiba eraginkor bat dela frogatzen dute.

Contents

OVERVIEW

The development of sustainable energy sources is one of the major challenges that must face our society in this century. According to the International Energy Agency (IEA) (data of the year 2014), only 10% of the primary energy consumption comes from renewable energy sources whereas 81% comes from burning fossil fuels. It is well known that fossil fuels are not unlimited and that its extraction, transportation and final consumption cause a significant health and environmental problems.

The current global population expansion and the improvement of the living standards in many countries will entail a notorious increase in the global primary energy demand. To confront the energy and environmental crisis in which our society is immersed it is required to develop, and use in an efficient way, a sustainable supply of energy resources. Nowadays, more than 60% of the primary energy is lost as heat during the combustion of fossil fuels. Thermoelectric (TE) devices have the unique capability to convert directly heat waste into electricity; so, the use of TE modules could lead to save an enormous amount of energy.

TE modules can be also used as solid state (Peltier) cooling modules; TE cooling provides environmentally friendly refrigeration (since it does not use or generate gases of any kind) in very compact modules, which make them very attractive for the microprocessor industry. Heat dissipation problem is one of the biggest issues in the quest for increasing the processing power of the microprocessors.

Despite their potential advantages, TE devices still have a poor thermodynamic efficiency and also poor mechanical properties. Thus, for everyday use of the TE devices in a wide range of applications it is necessary to improve both, their thermoelectric performance and their mechanical properties.

Thus, the main objective of this thesis is to develop mechanically enhanced high-performance bulk thermoelectric materials by means of severe plastic deformation.

Two families of TE materials have been studied in the present thesis: Bi_2Te_3-based alloys, a well-known thermoelectric material which its optimum thermoelectric performance is close to room temperature and pure PbTe, with an optimum performance near 800 K (an excellent candidate for the automotive sector).
The thesis is divided into two parts organized in nine chapters; each part corresponds to each family of thermoelectrics. Chapter 1 lists the specific objectives of the thesis. In the second chapter a general background of the thermoelectric state of the art is presented. Moreover, the current most promising approaches to design high-performance TE materials are described. Nanostructuring TE materials is one of the most promising strategies to improve *zT*; consequently a variety of methods that enables the production of ultrafine-grained materials are described. Finally, a literature review of Bi_2Te_3-based TE materials is presented.
Chapter 3 describes the materials and techniques used in this work. In chapter 4, 5 and 6, a full characterization of Bi_2Te_3-based alloys is carried out (chemical, microstructural, crystallographic, thermoelectric, and mechanical characterization), besides discussing the results.

Chapter 7 corresponds to PbTe-based thermoelectric materials. In this case, a preliminary work has been done to show that HPT is an excellent candidate to fabricate PbTe-based alloys with all-scale hierarchical architectures.

In chapter 8 the conclusions reached during this research work are highlighted.

Finally, in chapter 9 some guidelines about the future work are presented derived from the experience acquired during this work.

Chapter 1: Objectives

The main objective of this thesis is to develop a new route for high-performance bulk thermoelectric (TE) materials through high pressure torsion (HPT). Among all the severe plastic deformation (SPD) techniques, HPT is the most promising one to produce TE materials due to the following reasons:

1) The strong imposed shear strains involved in HPT induce a severe grain refinement (typically below 200-300 nm) that could lead to improved thermoelectric properties through a reduction of the lattice thermal conductivity.

2) The huge quasi-hydrostatic pressures (1-5 GPa) involved in HPT, permits the processing and/or consolidation of brittle materials and powders, like TE materials, without fracture at relative low temperatures.

3) HPT is performed at low homologous temperatures which allow for the fully dense and submicron grained (SMG) consolidation of powders. In contrast, spark plasma sintering (SPS) and other similar processes require typically higher processing temperatures that induce certain grain growth.

4) In contrast to the randomly oriented nanograin structures obtained through other top-bottom approaches such as ball milling + SPS, HPT imposes monotonous shear strains that typically induce strong crystallographic textures. This permits the exploitation of the high anisotropic properties of non-cubic TE materials such as Bi_2Te_3.

5) HPT is versatile and up-scalable. Imposed shear strains, applied temperature and pressures can be adequately tailored in order to optimize the thermoelectric and mechanical properties.

6) Improved mechanical properties are expected from HPT processing of TE materials: crystalline materials become stronger and tougher.

Among all the TE families, during this work I have mainly focused on *p*-type Bi_2Te_3 alloys. Bi_2Te_3 alloys are currently one of the most widely used TE materials which exhibit the best thermoelectric performance close to room temperature. Therefore, the submicron grained structures obtained after HPT are expected to be preserved during the TE device operation.

The specific objectives of this work are:

- Evaluate the viability of HPT to process and consolidate brittle thermoelectric materials without cracks.
- Attain submicron grained structures through HPT in TE materials with strong crystallographic texture.
- Optimize the processing parameters to improve the thermoelectric properties of Bi_2Te_3 through the reduction of lattice thermal conductivity by phonon scattering.
- Optimize the carrier concentration of Bi_2Te_3 alloys by point defect engineering and by optimizing the chemical composition.
- Improve the mechanical properties of Bi_2Te_3 alloys via grain refinement.
- Have a better knowledge of the effects of SPD on the mechanical and thermoelectric properties of Bi_2Te_3 based alloys.

Chapter 2: Introduction

Energy resources are essential in order to produce wealth and improve the living standards for individuals and societies. However, a significant number of environmental and health problems are caused or related to the production, transformation and final consumption of energy. For instance, eleven major areas of environmental issues in which energy production plays an important role have been identified by international agencies, which include crucial problems such as global warming, ozone depletion water pollution, maritime pollution, land use and siting impact, radiation and radioactivity, solid waste disposal, hazardous air pollutants, ambient air quality, and acid deposition [1]. Those environmental problems affect directly the human health as has been reported elsewhere[2-3-4]. Therefore, the development of environmentally friendly energy sources is essential to confront the environmental crisis in which our society is immersed. This issue could be one of the major challenges that our world has to face during the XXI century.

The growing energy demand is another energy-related challenge that must face our society. In 2050, the world population is expected to double and the economic development is likely to continue, this fact will entail a considerable improvement in the living standards of many countries increasing notoriously the energy demand. The predictions show that by 2050, the global demand for energy services will be increased by up to 10 times and the primary energy demand by 1.5–3 times.[5,6] Consequently, to successfully confront such difficult challenges it is necessary to develop a sustainable supply of energy resources, i.e. an energy source that in the long term is readily and sustainably available at reasonable cost and can be utilized for all required tasks without causing negative societal impacts.[7]

But this only is not enough, it is equally important to use energy resources in an effective and efficient way.

Thermoelectric (TE) devices have the ability to convert heat directly into electricity; it is well-known that more than 60 % of primary energy is lost as heat during the combustion process causing a harmful impact on our environment. Nowadays, the world's energy consumption is estimated to 22 billion $kWh \cdot yr^{-1}$. To meet such huge energy demand near 6.6 billion metric tons carbon equivalent of greenhouse gas emission are released in the atmosphere[8]. Approximately, 80% is due to the carbon emissions that are produced during the combustion of energy fuels.
Because of this unique capability to directly convert heat waste into electricity, the adequate use of TE modules could lead to the saving of an enormous amount of energy [9,10] leading us to use energy resources in a more effective and efficient way.

TE modules can be also used as a solid state cooling module (Peltier cooling modules). This phenomenon was discovered in 1834 by Peltier[11–13], but it did not reach commercial success until semiconductors were developed during the 20th Century. The TE cooling enables environmentally friendly refrigeration. Conventional refrigeration systems cannot be fabricated without using chlorofluorocarbons (they have destructive effects on the ozone layer[14]) or other chemicals that may be harmful to the environment; in contrast, TE devices do not use or generate gases of any kind. In addition, these modules are able to operate without any moving parts so they are virtually maintenance free, avoiding noise and vibrations. Other important advantages of the TE devices are their high reliability (their typical life is greater than 200,000 hours), their small size and weight compared with traditional mechanical system, and their precise temperature control.[15]

Due to the advantages described above, in recent years TE materials have attracted a growing interest; particularly from sectors such as aerospace, microelectronics and automotive. [16–19]

Because of their high reliability and operation simplicity, the space power generation is one of the niche markets of the TE devices. Almost all the space probes sent further than Mars have used some type of radioisotope heat-powered thermoelectric generator (RTGs). The RTGs are able to convert the heat produced from the nuclear decay of radioactive isotopes (the most common one is the plutonium-238) into electricity using TE modules. [18] A scheme of the key components and the basis for operation are shown in figure 2.1.

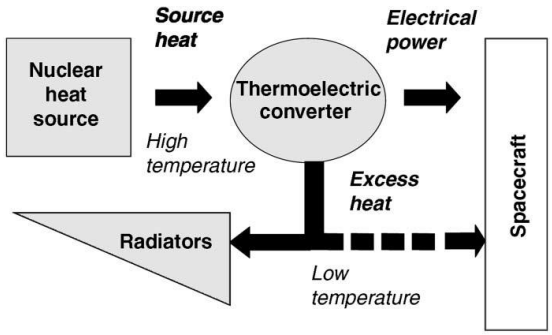

Figure 2.1: Scheme of the components and the basis for operation of a space-based radioisotope thermoelectric generator (RTGs) [18].

The microelectronics sector has also shown a great interest in TE devices. Nowadays, apart the problem of scaling the microprocessors, there is a problem to dissipate the heat produced during operation. This problem is more severe in portable electronic devices, which to satisfy the necessities of the customers require high processing power and they usually are densely packed. Thus, the heat generated in microprocessors is nearly touching 100 W/cm^2 [20]. According to many studies per every temperature increase of 2 K the reliability of the silicon chip decreases by 10%, being temperature increase the reason for more than 50% of the electronic failures [21]. Since TE devices are compact and light, they can play an important role in microelectronic refrigeration.

TEG can also be used for harvesting heat energy from the human body; by this way with the resulting electric current it will be possible to power some electronic gadgets. For instance, Seiko has produced the first wristwatch (Seiko Thermic) that is powered by body heat[22]. Recently, many efforts have been made to develop flexible thermoelectric generator for generating electrical energy from the human body heat [23,24].

The third niche market of the TE materials is the automotive sector. On the one hand the automotive industry can benefit by using TE materials as thermoelectric generators (TEG), also called Seebeck generators, in order to improve the fuel efficiency. As it has been said above, it is reported that more than 60 % of primary energy is wasted as heat in the combustion process. According to the International Energy Agency (IEA) (data of year 2014) the transportation sector demands 27% of energy use worldwide. The 95 % of that transportation energy comes from the combustion of petroleum or natural gas; 92 % and 3 % respectively[25]. So, an important amount of energy can be saved by developing TEG and transforming the waste heat from the exhaust pipe into electrical power. This power could be used for charging car's battery or to run the car's electrical utilities. Figure 2.2 a) shows a scheme of the primary energy consumption by source and sector for the 2014 year. Also, a diagram of the energy losses that take place in gasoline-fueled internal-combustion engine vehicles is displayed in figure 2.2 b).

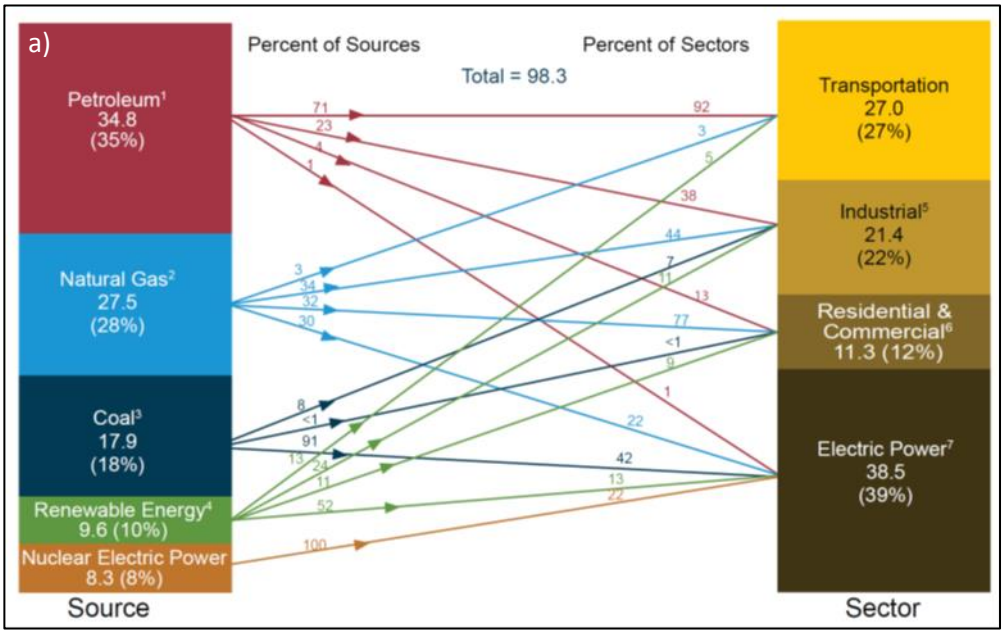

b)

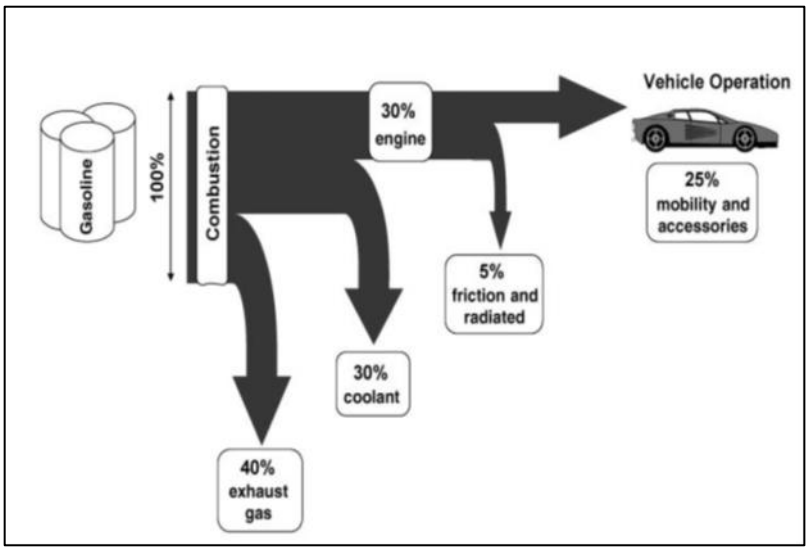

Figure 2.2: a) scheme for the 2014 year of the primary energy consumption by source and sector. [25] b) a diagram of the energy losses that take place in gasoline-fueled internal-combustion engine vehicles [18].

On the other hand, seats based on Peltier effect that allow an accurate temperature control, providing all-season comfort to the owners are available today[26].

Thus, based on the advantages of the TE devices and on the several applications discussed above, it is clear that there is a large and increasing market for TE materials. However, their usually low thermodynamic efficiency (which is still below 5 % in most cases) and their high cost compared to traditional mechanical generators or cooling devices have limited their expansion in the new markets. Fortunately, because of the fast progress that has taken place in the recent years in the creation of nanostructured materials, this fact could change soon. Taking advantage of the effects that occur at the nanoscale[9,27–29] it is possible to enhance the thermoelectric properties of such materials improving drastically the dimensionless thermoelectric figure of merit, which usually is denoted as ZT and will be further discussed in the next section 2.2.

Another critical issue that has limited the use of TE materials in many commercial applications, particularly to be used as TEG in the automotive industry, is that the most common TE materials such as skutterudites, PbTe based alloys or Bi_2Te_3 alloys are usually very brittle materials[30–34]. The mechanical properties of TE materials are critical for long term reliability. During their operation life, TEG are subjected to a thermal gradient, consequently thermo-mechanical stresses are generated which can cause the formation of micro or macro-cracks. Thus, if the mechanical properties are not good enough a brittle fracture or the premature death of the device may occur.

Therefore, for everyday use of the TE devices in a broad range of applications it is essential to improve their performance. To achieve this goal is vital to enhance the thermoelectric efficiency but, of equal importance is the need of improving the mechanical properties. All of this should be done at reasonable cost and using easily scalable processes.

Therefore, there is no doubt that the development of TE devices for a wide range of applications is a challenging issue.

2.1.Thermoelectric Effect

TE power generation is based on the **Seebeck (*S*) effect**. The effect was discovered by Thomas Johann Seebeck in 1821. He showed that an electromotive force could be produced when a temperature gradient is imposed in the junction between two dissimilar electrical conductors.
Let us assume a circuit formed by two different materials respectively *A* and *B*, in which the temperature at their junctions differs from an amount ΔT (figure 2.3). According to the Seebeck effect, the voltage that appears in either conductor when the circuit is opened is given by the following expression:

$$\Delta V = S_{AB}\Delta T \qquad (1.1)$$

Where S_{AB} is named as the relative Seebeck coefficient between the two conductors, ΔV is the voltage difference and ΔT is the temperature difference between the hot and cold sides of the junction. S_{AB} is defined as positive if the voltage difference tends to drive an electric current through conductor *A* from the hot junction to the cold junction[11–13]. Thus, *n*-type semiconductors have a negative Seebeck value while *p*-type ones have a positive value, i.e. electrons and holes tend to diffuse in opposite direction along the junction.

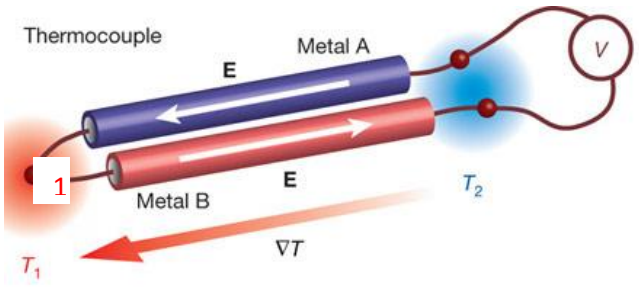

Figure 2.3: A thermocouple formed by two dissimilar conductors *A* and *B*.

Thirteen years after that the German physicist Seebeck made his discovery, Jean **Peltier**, a French watchmaker, observed the second of the thermoelectric effects. He perceived that if a current flows in a circuit consisting of two dissimilar electrical conductors, then one of the junctions is heated while the other is cooled. The absorbed or produced heat rate (q) at the junction between electrical conductors A and B in given by:

$$q = \Pi_{AB} I \qquad (1.2)$$

Where I is the electric current that flows thought the circuit, and Π_A and Π_B are the absolute Peltier coefficients of each conductor ($\Pi_{AB} = \Pi_A - \Pi_B$). Similarly to the Seebeck coefficient, the Peltier coefficient is regarded as positive if junction 1 becomes heated and junction 2 is cooled when the electric current through conductor A passes from junction 1 to 2 [11–13].

Seebeck and Peltier did not realize that the effects observed were connected. However, some years after that these two phenomena were described, in 1855, William **Thomson,** better known as Lord Kelvin, was able to demonstrate the interdependence between the two effects establishing a relationship between the two coefficients that describes the Seebeck and Peltier effects. This interdependence if given by the following expressions, which are called the Kelvin relationships:

$$\begin{aligned} \Pi_{AB} &= S_{AB} T; \\ \tau_{AB} / T &= dS_{AB} / dT \end{aligned} \qquad (1.3)$$

Where $\tau_{AB} = \tau_A - \tau_B$ is the difference between the Thomson coefficient of conductors A and B. The first of these equations is particularly important because enable us to determine the Peltier coefficient from the Seebeck coefficient. The later one is easier to measure since the Peltier effect is always accompanied by the Joule heating effect.

His theory also predicted that a third thermoelectric effect should exist, now known as the Thomson effect. According to the Thomson effect, heat is absorbed or produced when an electric current flows through a conductor with a temperature gradient. As equation 1.4 shows, the heat which is absorbed or produced (q) due to the flow of the electric current is proportional to both the electric current (I) and the temperature gradient (ΔT). The proportionality constant, known as the Thomson coefficient (τ) is linked to the Seebeck coefficient by the Kelvin relationships (equation 1.3) [11,12]

$$q = \tau I \Delta T \qquad (1.4)$$

Since the Seebeck and Peltier effects only take place at junctions between different conductors, one might believe that they are interfacial phenomena but, they are really dependent on the properties of the materials involved. Nowadays it is well-known that the electric current is consequence of a flow of mobile charge carriers (electrons and holes). When the junction is heated, because of mobile charge carriers at the hot side of the junction have more thermal energy than carriers on the cold side; they tend to diffuse from the hot side to the cold side. Therefore, there are more mobile charge carriers on the cold side than on the hot side, causing an inhomogeneous charge distribution and giving rise to an electric field which opposes the diffusion of the carriers. If the thermocouple is in open circuit, equilibrium will be reached when the diffusion of the carriers due to the thermal gradient is balanced by the electric field. Thus, in equilibrium, as a result of a thermal gradient an electrochemical potential is generated, which is known as the Seebeck voltage.

In the same way, when a current passes from one material to another, the energy transported by the electrons is altered, and this energy difference causes the heating or cooling of one end of the junction. This effect is known as the Peltier effect[11,35].

2.2. Thermoelectric figure of merit

The problem of energy conversion using thermocouples was first analyzed in 1911 by Altenkirch[11]. Thanks to his work, the concept of the thermoelectric figure of merit, which defines the efficiency of TE materials, was introduced some years after. The dimensionless thermoelectric figure of merit (zT), defined as: $zT = (S^2\sigma/\kappa)T$ (see section 2.3 for its derivation) is a function of the transport properties of a given TE material, where S, σ, κ, and T are the Seebeck coefficient, the electrical conductivity, the thermal conductivity, and the absolute temperature at which the properties are measured, respectively [11–13]. So, to be an efficient TE material zT should be as high as possible, i.e. a good TE material must be a good electrical conductor, a thermal insulator and should have a high Seebeck coefficient. Unfortunately, all three (S, σ, κ) are functions of the carrier concentration, so optimizing all the parameters together turns out to be a difficult challenge (figure 2.4). Metals have a high electrical conductivity but also a very high thermal conductivity because electrons also contribute to the heat transport as described by the Wiedemann-Franz law[36]. On the other hand, glasses have very low thermal conductivity but also are electrical insulators. A material with a combination of low electrical resistivity, as an ordered metal, and low thermal conductivity, as a glass, would therefore have extremely good TE properties. A material like this was termed as ‘‘phonon glass, electron crystal’’[12]

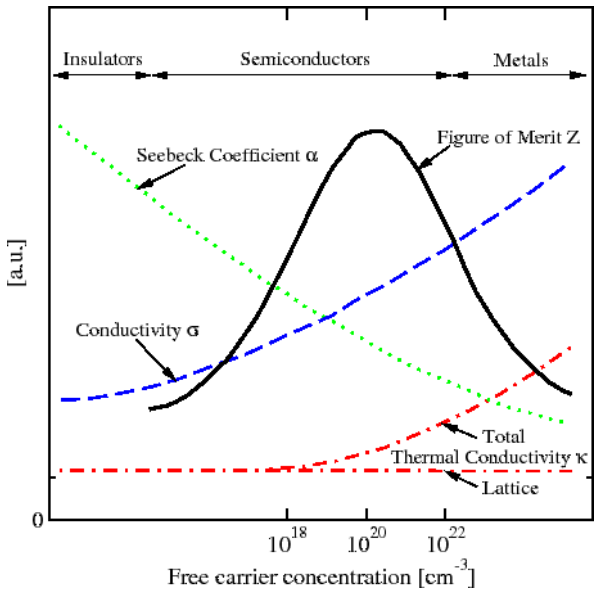

Figure 2.4: Seebeck coefficient, electrical conductivity, thermal conductivity, and figure of merit with respect to free carrier concentration. [40]

As shown in figure 2.4, the figure of merit reaches its maximum value around a carrier concentration of 10^{20} cm^{-3}; which corresponds to heavily doped or near degenerate semiconductors. The free carrier concentration depends on both the temperature and the specific transport properties of the semiconductor. Thus, the optimum thermoelectric performance of each TE material is limited to a certain range of temperatures; for instance, bismuth telluride (Bi_2Te_3) based alloys are satisfactory up to ~ 250º C [37,38], while lead telluride (PbTe) alloys [9] or skutterudites [29] are suitable in the temperature range of 500-700º C. For high-temperature applications, semiconductors with high melting point such as silicon-germanium alloys are the most promising ones [39]. In figure 2.5 an overview of zT versus operation temperature for different state of the art TE materials is plotted.

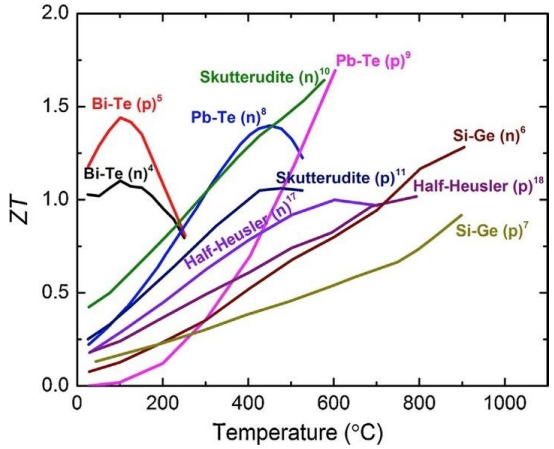

Figure 2.5: An overview of ZT versus operation temperature for state of the art thermoelectric materials [117].

2.3 Thermoelectric Devices as Refrigerators, Heat Pumps and Power Generators

TE devices allow for direct thermal-to-electrical energy conversion as well as conversely performing as solid-state electronic refrigeration materials. For this proposes, usually thermoelectric modules (figure 2.6) are fabricated because the output Seebeck voltage of a single thermocouple is very small (on the order of millivolts) for technical applications. To increase the voltage drops across the TE device many thermocouples are connected electrically in series but thermally in parallel. The most common thermocouples consist of two different semiconductor materials defined as *n*-type and *p*-type elements. In the first one, the dominant free carriers are electrons while in the second one the dominant free carriers are positive (holes). Thus, the absolute Seebeck coefficient of *p*-type elements is positive while for *n*-type elements it is negative. This way, the relative Seebeck coefficient of the junction is maximized.

Let's determine the performance of thermoelectric refrigerators and heat pumps assuming a single thermocouple model as shown in figure 2.6 b). To establish the performance, we will assume that there is no thermal resistance between the thermocouple and the heat source or sink. Also, in the model it is supposed that all the heat transfer between the heat source and heat sink takes place within the thermocouple. The two *n*- and *p*-type elements will have constant cross-sectional areas and finally, they will satisfy a relationship between their form factors (ratio of cross-section to the length) which leads to maximizing the performance.

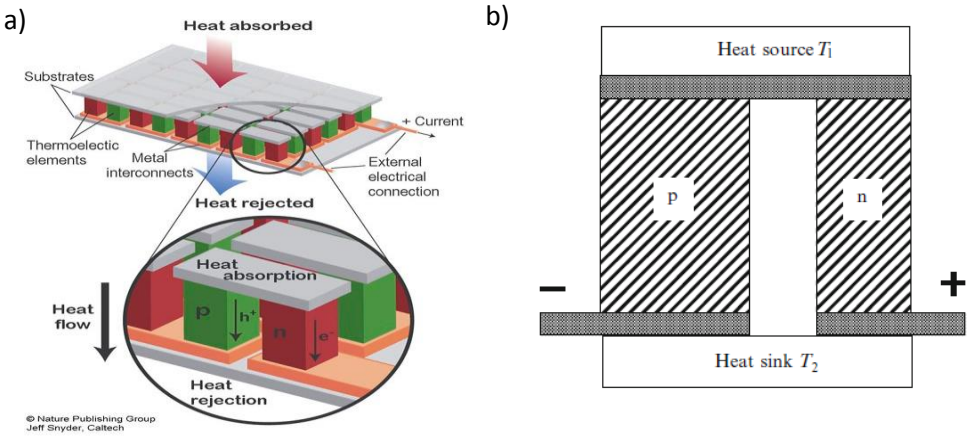

Figure 2.6 Illustration of a TE module for being used as a) TEG b) refrigeration device.

The coefficient of performance (COP) is used to quantify the performance of refrigeration, which is defined as the ratio of the heat extracted from the source to the electrical power supplier to the device.

The expression for the cooling power can be estimated as:

$$q = (S_p - S_n)IT_1 - (T_2 - T_1)(\mathrm{K}_P + K_n) - I^2(R_p + R_n)/2 \qquad (1.5)$$

Where T_1 and T_2 are the absolute temperatures of the heat source and the heat sink respectively, $\mathrm{K}_{p,n}$ are the thermal conductances of the *n* and *p*-type elements (i.e. $\mathrm{K}_{p,n} = \kappa_{p,n} A_{p,n} / L_{p,n}$ where $A_{p,n}$ is the cross-sectional area of each thermoelectric element, $L_{p,n}$ is its length and $\kappa_{p,n}$ its thermal conductivity.) and $R_{p,n}$ are the electrical resistances of each thermoelement ($R_{p,n} = \rho_{p,n} L_{p,n} / A_{p,n}$ where $\rho_{p,n}$ is the electrical resistivity of the *p* and *n* elements respectively).
The first term, which is positive, corresponds to the Peltier cooling effect while the second and third one, which are negative, because they oppose the cooling effect, are related to the Fourier heat transport from the hot junction to the cold junction and the Joule heating within the thermoelements.

The power supplied to the device is:

$$w = (S_p - S_n)I(T_2 - T_1) + I^2(R_p + R_n) \qquad (1.6)$$

So, the energy supplied to the device is spent on overcoming the thermoelectric voltage and on resistive losses.
Thus, the COP is given by:

$$COP = \frac{q}{w} = \frac{(S_p - S_n)IT_1 - (T_2 - T_1)(\mathrm{K}_p + \mathrm{K}_n) - I^2(R_p + R_n)/2}{(S_p - S_n)I(T_2 - T_1) + I^2(R_p + R_n)} \qquad (1.7)$$

Therefore, the COP depends on the current. As it can be seen, the Peltier cooling effect increases linearly when the current is increased. However, the

Joule heating effect, which depends on I^2 decreases the COP. Thus, there is a specific current at which the cooling power reaches its maximum value ($(\partial COP/\partial I)=0$) which is the following one:

$$I_{opt}=\frac{(S_p-S_n)(T_2-T_1)}{(R_p-R_n)((1+ZT_m)^{1/2}-1)} \qquad (1.8)$$

Where Z is equal to $(S_p-S_n)^2/((\mathrm{K}_p+\mathrm{K}_n)(R_p+R_n))$ and T_m is the average temperature between the hot and cold ends ($T_m=(T_1+T_2)/2$). Thus, replacing I_{opt} The optimum COP is:

$$(COP)_{opt}=\frac{T_1((1+ZT_m)^{1/2}-(T_2/T_1))}{(T_2-T_1)((1+ZT_m)^{1/2}+1)} \qquad (1.9)$$

Equation 1.9 shows that the optimum COP depends only on *Z*, which is known as the figure of merit of the thermocouple, and on the absolute temperatures of the heat source and heat sink. *Z* has dimensions of [K^{-1}], so it is usual to multiply *Z* by *T* in order to get the dimensionless thermoelectric figure of merit (*ZT*). As shows figure 2.7 the COP increases when increasing *Z*, researching the ideal Carnot efficiency (i.e. $COP_{Carnot}=T_1/(T_2-T_1)$) when $Z\to\infty$.

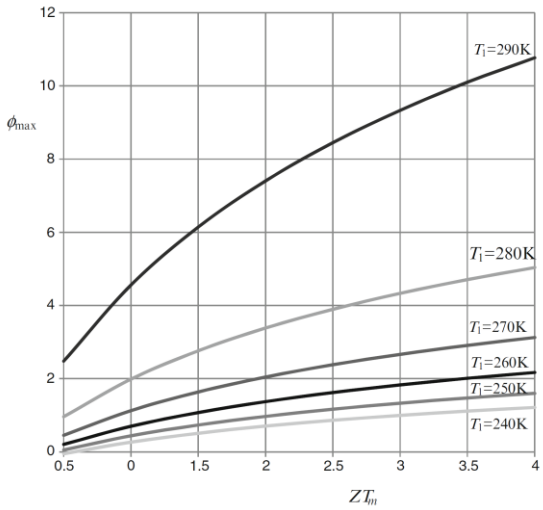

Figure 2.7: Plot of optimum COP against ZT_m when the heat sink is at 300 K. The COP is high for small temperature depressions but, it decreases significantly for higher temperature depressions. [11]

The geometry of the thermoelectric elements can be optimized to improve *ZT and* consequently COP. To maximize *ZT*, the factor $\left((\mathrm{K}_p + K_n)(R_p + R_n)\right)$ should be minimized. Both $K_{p,n}$ and $R_{p,n}$ depends on the geometry and the transport properties ($\kappa_{p,n}$ or $\rho_{p,n}$) of each thermoelement. It can be proven that *Z* is minimized when the form factors of the thermoelements satisfy the following relation:

$$\frac{L_n A_p}{L_p A_n} = \sqrt{\frac{\rho_p \kappa_n}{\rho_n \kappa_p}} \qquad (1.10)$$

when (1.10) is satisfied the dimensionless thermoelectric figure of merit, which only depends on the transport properties of the *n* ad *p*-type branches, is given by:

$$ZT = \frac{(S_p - S_n)^2}{(\sqrt{\kappa_p \rho_p} + \sqrt{\kappa_n \rho_n})^2} \qquad (1.11)$$

It is not common to evaluate ZT of a thermocouple, therefore it is convenient to define the dimensionless thermoelectric figure of merit (zT) for a single element, which is defined as $(S^2\sigma/\kappa)T$ as mentioned in the former chapter; note that in most cases ZT in close the mean value of each thermoelement ($ZT = (zT_p + zT_n)/2$).

An important quantity of the refrigerators is the maximum temperature depression (ΔT_{max}) that can be achieved. ΔT_{max} is reached when the cooling power falls to zero, so from equation (1.9) we get that $\Delta T_{max} = \frac{1}{2} ZT_1^2$. Since, in bulk bismuth antimony telluride alloys (their maximum zT in near room temperature) ZT_m has remained around unity for more than 50 years, the maximum temperature depression that can be achieved using TE devices is close to 100° C (figure 2.8).

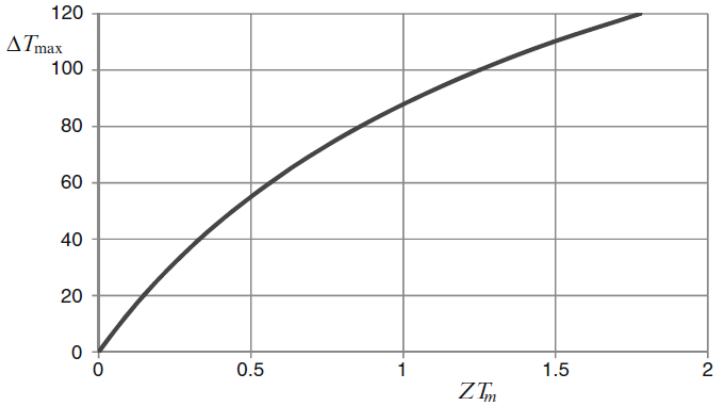

Figure 2.8: Plot of the maximum temperature depression that can be achieved versus ZT_m when the heat sink is at 300 K [11]

Now we will determine the efficiency coefficient *(η)* of the TE devices when are used as TEGs; in this case the same assumptions than in the previous case have been done.

To assess *η*, a simple thermocouple model has been assumed so; the TE device consists of two branches (one *p*-type and the other one n-type) which are joined by a contact element that performs as a heat source maintaining the temperature constant at T_1. The ends of the two elements are connected to a load resistance R_L and they are maintained at a fixed temperature T_2 (figure 2.9).

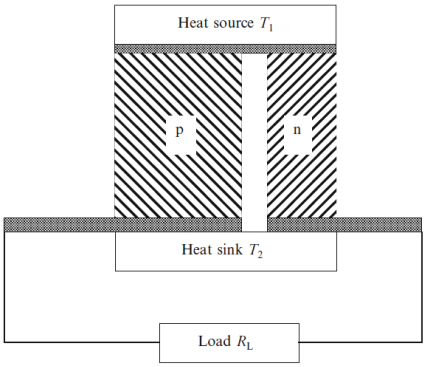

Figure 2.9: a simple scheme of a TE device performing as a TEG.[11]

The Seebeck voltage for this simple thermocouple will be equal to $(S_p - S_n)(T_1 - T_2)$, the equivalent resistance of the device can be approximate by the following expression: $R_{eq} = (\rho_p L_p / A_p + \rho_n L_n / A_n + R_L)$, therefore according to the ohm's law the current that flows into the branches is:

$$I = \frac{(S_p - S_n)(T_1 - T_2)}{R_{eq}} \qquad (1.12)$$

The electrical power delivered to the load resistance is:

$$w = I^2 R_L = \left(\frac{(S_p - S_n)(T_1 - T_2)}{R_{eq}} \right)^2 R_L \qquad (1.13)$$

One part of the heat absorbed by the source will flow along the branches to the sink due to the Fourier heat conduction. Another part will be used to balance the Peltier cooling which develops with the electrical current that flows within the branches associated with the Seebeck effect. Thus, the heat balance equation is:

$$q_1 = (S_p - S_n) I T_1 + (\mathrm{K}_p + \mathrm{K}_n)(T_1 - T_2) \qquad (1.14)$$

Therefore, the efficiency, which is defined as the ratio w/q_1 is equal to:

$$\eta = \frac{(S_p - S_n)^2 (T_1 - T_2)^2 R_L}{R_{eq}^2 ((S_p - S_n) I T_1 + (\mathrm{K}_p + \mathrm{K}_n)(T_1 - T_2)} \qquad (1.15)$$

From equation (1.13) we get that the maximum useful power is reached when the load resistance is equal to the thermocouple resistance (i.e. R_L=R_p+R_n). So, maximizing the efficiency and defining Z as was done in the former case we get:

$$\eta = \frac{(T_1 - T_2)(\sqrt{1 + ZT_m} - 1)}{T_1 \left(\sqrt{1 + ZT_m} + T_2 / T_1 \right)} \qquad (1.16)$$

Therefore for TEG the efficiency also depends directly on the thermoelectric figure of merit. For power generation, the efficiency of the device increases with Z (figure 2.10), reaching the Carnot efficiency $((T_1 - T_2)/T_1)$ when ZT_m approaches infinity.

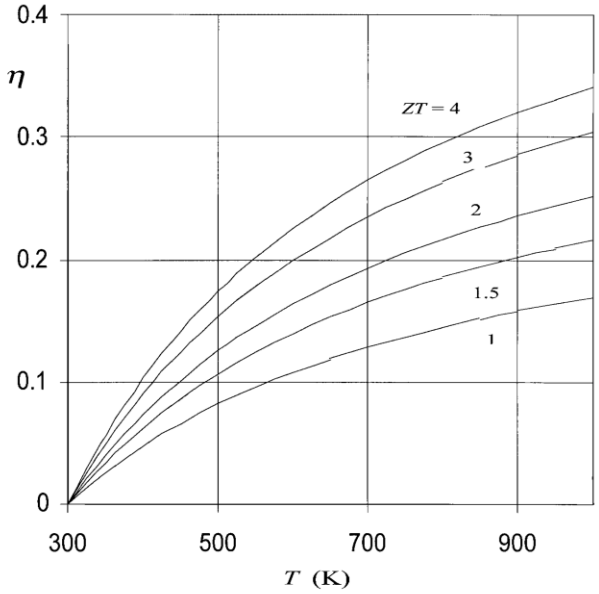

Figure 2.10: The efficiency for TEG versus source Temperature supposing that the heat sink is fixed at 300 K [13].

2.4 Strategies for improving the dimensionless figure of merit (*zT*)

In the previous section we have seen that improving *zT* leads to an increase in the efficiency of the thermoelectric heat refrigerators or pumps as well the efficiency of the thermoelectric power generators. Unfortunately, improving *zT* is a difficult challenge because, as previously mentioned, all three parameters (*S*, σ and κ) that must be optimized to get a satisfactory *zT* are interconnected since all of them depend on the carrier concentration. For improving *zT*, the power factor (*PF*), which is defined as $S^2\sigma$, and it is strongly dependent on the carrier concentration must be maximized while the thermal conductivity (κ) should be minimized. The latter is less sensitive to the carrier concentration because the heat transport is mainly dominated by the lattice contribution when free carrier concentration is close to 10^{-19}

cm^{-3} (the electronic contribution is usually less than 25 % under this conditions[40]).
Therefore, to improve *zT* one option is to enhance the power factor, the second one is to reduce the thermal conductivity and the last option is the combination of both two.

Alloying is a popular option to simultaneously enhance *PF* and reduce κ. As proposed by Ioffe in 1956[41], the formation of a solid solution between two semiconductors that have the same crystal structure leads to a lower thermal conductivity. The mean free path length of phonons varies strongly with their vibrational frequency. The high-frequency phonons are scattered mainly by the point defects, such as those created by solid solution alloy substitution. Because of the alloying, there are atomic shifts away from the ideal lattice sites which cause structural disorder. Also, the mass differences between the atoms of the solid solutions disrupt the phonon path causing a thermal conductivity reduction. Therefore, site substitution (alloying) with isoelectronic elements generates disturbances in the short-range order leading to a reduction of the thermal conductivity without reducing the mobility of the free charge carriers since the long-range order is preserved. The wavelength associated with the carrier is rather large, so it is suggested that they would not suffer any additional scattering.[11,42–44] In addition, the electronegativity difference between the isoelectronic atoms optimizes the electronic band structure enhancing the so-called power factor [45,46]

The generation of low-dimensional thermoelectric materials is another suitable strategy to improve *zT* by simultaneously reducing the thermal conductivity and enhancing the power factor. As proposed by Hicks and Dresselhaus in 1993[47] the transport properties of low-dimensional thermoelectric materials differs from that in bulk 3D materials. In the case of the latter, as mentioned above, the quantities *S*, σ and κ are interrelated because all of them are dependent on the free carrier concentration. However, when the system size approaches to nanometer length scales, the

density of electronic states (D.O.S) differs drastically from that of conventional 3D bulk crystalline semiconductors (figure 2.11) due to quantum-confinements effects, allowing varying quasi-independently *S*, σ and κ.

Thus, the low-dimensionality enhances *S* as a result of the quantum-confinement phenomena leading to control quasi-independently *S* and σ, and hence improving the power factor. In addition, as a result of the numerous interfaces, the thermal conductivity is significantly decreased without reducing strongly the mobility of the carriers since phonons are more effectively scattered than free carriers.[48]

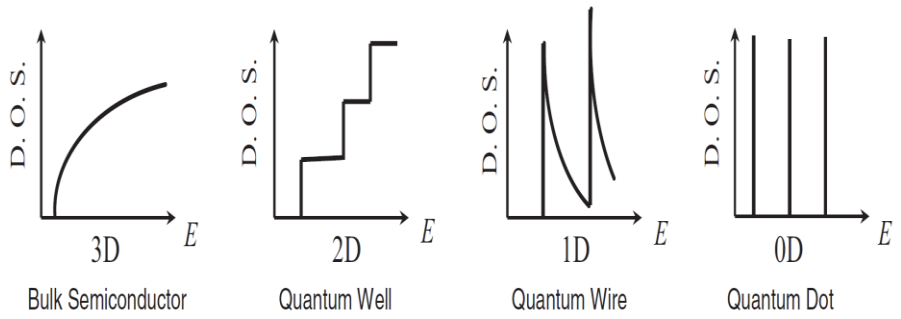

Figure 2.11: Electronic density of states versus dimensionality [48]

Based on the low-dimensional strategy, record *zT* values (up to ~ 2.4) have been reported for Bi_2Te_3/Sb_2Te_3 superlattice thin film prepared by molecular beam epitaxial method[27]. Despite achieving a record *zT* value, these nanostructures are generally obtained by thin films techniques (Molecular Beam Epitaxy, Knudsen cells, Pulsed laser, CVD...), which are too costly to be used for mass production of TE materials necessary for large scale applications.

The power factor can be enhanced by tuning the electronic and atomic structural features of TE materials. The band engineering consists in

optimizing the thermoelectric performance by adjusting the doping level and the composition of the existing TE materials [49]. The *PF* can be expressed as, $(S^2n)q\mu$, here the electrical conductivity is written as $\sigma = n\mu q$ where n is the charge carrier concentration, q its charge and μ its mobility. The product (S^2n) is a purely electronic property, dominated by the electronic band structure and by the scattering mechanisms[50]. One approach to increasing the product (S^2n) and, therefore, the *PF*, is to converge many 'degenerate valleys' within the electronic band structure. Converging the valence (or conduction) bands conducts to a high valley degeneracy that enhances the *PF* because leads simultaneously to a high Seebeck coefficient and a high electrical conductivity [43,51]. By this way, Pei et al.[51] reported a remarkable *zT* value of 1.8 near 850 K as a result of converging at least 12 valleys in Na doped $PbTe_{1-x}Se_x$ alloys. Another promising route to enhance (S^2n) is to generate distortions of the electronic density of states near the Fermi energy level via doping. Introducing dopants whose energy levels are in the electronic band of the host TE material can generate resonant levels leading to distort the density of states near the Fermi level. This way, the effective mass of the carriers is increased without changing its concentration, which results in an improvement of the S^2n product. However, this strategy, unlike the former one, has the risk of reducing the mobility of the free carriers[51]. Tl-doped PbTe is a good example of improving *zT*, it has a notable *zT* value close to 1.5 at 773 K[52], by creating resonant impurity levels. It has been also reported that the substitution of Ce atoms on Pb sites of PbTe can increase the Seebeck coefficient due to the formation of a resonance level in the density of states near the Fermi energy[53]. Similarly, doping Bi_2Te_3 also enhances its *PF* as a result of the distortion of the electronic density of states due to Sn resonant impurities[54].

For having an optimum PF value, bipolar effects should be reduced. Since TE materials are narrow band semiconductors, they can have in each electronic band two types of carriers, electrons and holes. Bipolar effects

become more prominent as the temperature is raised, because electron-hole pairs are produced by excitation across the energy gap.[11] Although, those effects are positive for enhancing the electrical conductivity, when the mixed conduction takes place the Seebeck coefficient is significantly suppressed because electrons and holes have opposite charges and, therefore, the *PF* can be reduced significantly. In addition, the bipolar effects can have a remarkable contribution to the total thermal conductivity at high temperatures. The onset of mixed conduction can be minimized by adding donor or acceptor impurities (i.e. increasing the carrier concentration) or by scattering preferentially minority carriers via grain boundaries[35,43]

As mentioned above, minimizing the total thermal conductivity is also a promising strategy to enhance the dimensionless thermoelectric figure of merit. The different approaches that lead to considerately reduce the thermal conductivity are discussed in the next section 2.5.

2.5 Approaches to minimize the lattice thermal conductivity.

In the recent years to reduce the thermal conductivity and hence, to enhance the thermoelectric figure of merit, two principal approaches are taken. The first one consists of creating new advanced families of bulk TE materials. These families have very complex crystal structures which can exhibit a low lattice thermal conductivity enabling high carrier mobility. $CoSb_3$ based skutterudites, which are also so-called phonon-glass/electron-crystal materials are promising TE materials that are based on this strategy [55–57].

Recently, a new and promising family of TE materials has gained the attention of the scientific community; in silver and copper chalcogenides a reversible first-order phase transition take place at moderate temperature (near 400 K). During the transition, abrupt changes and fluctuations of the

electronic structure, the crystallographic structure, chemical composition, and density take place causing a strong critical scattering of carriers and phonons which leads to a very low thermal conductivity[58,59] and in many cases high power factor[58–60] Thus, during the phase transformation, exceptional thermoelectric performance can be achieved. For Cu_2Se, an uncommon zT value of 2.3 at 400 K has been reported[59].

The other approach is to create nanostructured materials. By using the same "classical" (such Bi_2Te_3 alloy, PbTe, SiGe,...) TE materials but in a nanostructured form, it is possible to reduce the thermal conductivity because phonons are scattered at the boundaries of crystals when the phonon mean free path approaches the grain dimensions[61].

2.5.1 Reducing the thermal conductivity by synthesizing complex crystal structures

Filled skutterudites are among the most promising TE materials. Binary skutterudites are based on $CoAs_3$ mineral, a naturally occurring mineral that was first found in Norway. The general chemical formula for binary compounds is MX_3, where M is the transition-metal (M = Co, Rh, or Ir) and X is phosphorus, arsenic or antimony [55,62]. Its crystallographic structure contains generally 32 atoms per unit cubic cell (see figure 2.12). Skutterudites form covalent structures with low coordination numbers; consequently, there are many empty spaces in the structure, called voids of the structure. Therefore, so-called filled skutterudites compounds can be formed filling these voids by atoms of other elements such as ions of rare-earths, alkaline earths, or alkali metals [55].

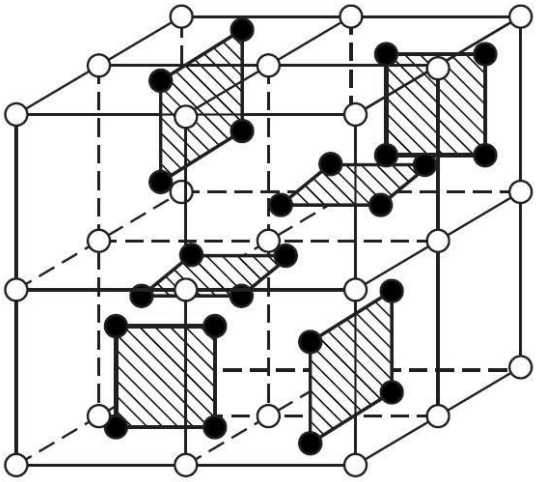

Figure 2.12: Scheme of the unit cell for unfilled skutterudite crystal structures [56].

Among the skutterudite family, $CoSb_3$ has attracted the greatest interest. As a result of its high degree of covalent bonding, the mobility of the free carriers is high compared to other family members [62]. $CoSb_3$ has usually a high power factor, nevertheless due to its strong bonding and simply ordered crystal structure the thermal conductivity is high (10 W m^{-1} K^{-1}) [62], therefore, for binary skutterudites the figure of merit is not so high (zT~0.5)[55]. However, placing atoms in the interstitial voids of this crystal system (i.e. producing filled skutterudites) reduces the thermal conductivity since new phonon-scattering centers are introduced [56]. Y. Z. Pei et al. synthesized successfully single-element-filled $CoSb_3$ skutterudites reaching a maximum value of zT close to unity at 800 K for $K_{0.38}Co_4Sb_{12}$ [63]. According to Shi et al., only the phonons with frequencies close to the vibrational frequency of the fillers atoms can be successfully scattered by resonant scattering. [64]. Yang et al. calculated the spring constants and resonance frequencies for various fillers in $CoSb_3$; they showed that the thermal conductivity is more effectively reduced by filling the voids of skutterudites with Ba and La (or Ce) rather than by filling Ba and Sr [65]. They suggested that this fact is a consequence of the large difference

between the vibrational frequencies of Ba and La fillers, which provide a broader range of resonant phonon scattering and thereby, reduce more effectively the thermal conductivity. Shi et al. suggested that filling Ba and Yb into the voids of skutterudites should be even more effective to reduce the thermal conductivity of $CoSb_3$ because the spring constants and resonant frequencies for Yb and Ba differ more than other possible filler pair combinations. By this approach they achieved a maximum *zT* value of 1.36 at 800 K for *n*-type $Ba_xYb_yCo_4Sb_{12}$ [64]. The thermal conductivity can be reduced even more by producing multiple-filled skutterudites, which leads to achieve very promising *zT* values, close to two (*zT*=1.7 at 850 K), as reported by Shi et al. for multiple co-fillers Ba, La, and Yb $CoSb_3$ skutterudites [55].

Another thermoelectric material which possesses inherently very low thermal conductivity value is single-crystalline tin selenide (SnSe). SnSe at room temperature has a layered orthorhombic Pnma space group crystal structure. When the temperature increases to 800 K an orthorhombic-to-orthorhombic phase transition takes place. The high-temperature phase has a Cmcm space group. Along *b* and *c* directions the bonding between Sn and Se atoms are strong while they are weakly bonded along the *a* direction. Therefore, single crystalline SnSe is easily cleaved along the (l00) planes [66]. As a result of its layered crystallographic structure, the thermoelectric properties are very anisotropic. Single crystalline SnSe compounds exhibits an extremely high *zT* value of 2.6 ± 0.3 at 923 K when its thermoelectric properties are measured along the *b* axis of the room-temperature orthorhombic unit cell. The thermoelectric performance is also high along the *c* axis ($zT=2.3 \pm 0.3$), however, *zT* is significantly reduced when it is measured along the a axis ($zT=0.8 \pm 0.2$) [66].
The *PF* of SnSe is moderate, but its exceptional high value of *zT* arises mainly from its extremely low thermal conductivity. According to Zhao et al. the ultralow thermal conductivity is a consequence of the strong anharmonicity of the chemical bonding [66].

The thermal conductivity for phonon conduction can be expressed as:

$$\kappa = \tfrac{1}{3} Cvl \qquad (1.17)$$

Where C is the heat capacity per unit volume, v is the average phonon velocity, and l is the mean free path of phonons between collisions[36]. The phonon mean free path l is mainly determined by geometrical scattering (i.e. scattering by crystal boundaries, lattice imperfections, chemical impurities, amorphous structures…) and by phonon-phonon scattering. If the forces between the atoms are purely harmonic, there is not any mechanism that enables the collisions between different phonons, and consequently, in such 'idealistic' case, the mean free path would be limited only by the collisions of phonons with crystal imperfections [36]. In other words, in a perfect crystal of an insulator (the thermal conduction is only driven by phonons), harmonic phonons would never be scattered, so such a crystal would have infinite thermal conductivity at all temperatures.

Peierls, who first introduced the idea of phonons to represent the lattice vibrations, showed that phonons could interact with one another via normal or N-processes or by umklapp or U-processes. In the first case, the momentum of the phonons is conserved whereas is the last one the momentum is not conserved[36]. Both, normal and umklapp processes are illustrated in figure 2.13.

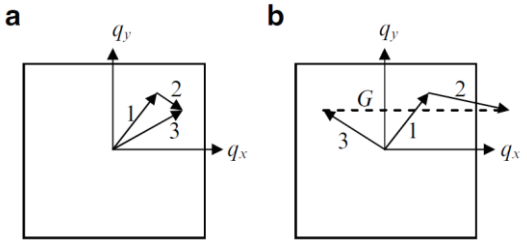

Figure 2.13: illustration of a) normal $q_1+q_2=q_3$ and b) umklapp $q_1+q_2=q_3$ +G phonon collision processes in a two-dimensional square lattice.

In figure 2.13 can be seen how two phonons called 1 and 2 interacts and consequently a third phonon is produced. In the case of *N*-process the third phonon is obtained by simply vector addition of phonons 1 and 2 while in *U*-process a reciprocal lattice vector G should be added to bring the third phonon within the crystal cell[36]. Both processes can be represented as:

$$q_1 + q_2 = q_3 \,(N\text{-process})$$
$$\text{and}$$
$$q_1 + q_2 = q_3 + G \;\; (U\text{-process}) \quad (1.18)$$

It can be shown that only the *U*-processes can affect the thermal conductivity. At elevated temperatures, ($T > \theta_D$, where θ_D is the Debye temperature) all phonons are excited, therefore the *U*-processes become more probable since there are many phonons with wave-vectors that are sufficiently large to produce a resultant vector which is outside the unit cell in the wave-vector space [36]. Thus, the intrinsic thermal conductivity of a solid in a temperature range in which heat is conducted only by acoustic phonons, and only assuming anharmonic umklapp phonon-phonon scattering processes, is given by [67]:

$$\kappa_L = A \frac{\breve{M} \theta_D^3 \delta}{\gamma^2 n^{2/3} T} \quad (1.19)$$

Where, n is the number of atoms in the primitive unit cell, δ is the volume per atom, $\breve{M}$ is the average mass of the atoms in the crystal, *A* is a physical constants and is the γ Grüneisen parameter that defines the relationship between phonon frequency and volume change, which is a direct measurement of the anharmonicity of the bonds [68]:

$$\gamma_s = \frac{V}{\omega_s(\vec{k})} \frac{\partial \omega_s(\vec{k})}{\partial V} \quad (1.20)$$

Thus, according to equation (1.19) $\kappa_L \propto \gamma^{-2}$, compounds with very anharmonic bonds usually have very low thermal conductivity and consequently they can be suitable thermoelectric materials, as in the case of single crystalline SnSe [66] or $AgBiSe_2$ alloys [69,70].
Despite the excellent TE properties of single crystalline SnSe, for many applications is not very adequate to use single crystals with layered structures since they tend to fail easily along their cleavage plane. Moreover, growing single crystals is expensive, and time and energy consuming[45]. For many applications, it would be more convenient to produce highly texturized SnSe polycrystalline compounds.

2.5.2. Reducing the thermal conductivity by lattice defects such grain boundaries, point defects and impurities

As mentioned in section 2.4, alloying is a well-known strategy to reduce the thermal conductivity since the alloying elements introduce structural disorders in the lattice cell that are effective to scatter high-frequency phonons. Refining the grain size leads to a further reduction of the thermal conductivity because the low-frequency phonons, although they are scarce, their free path length is large and they make a remarkable contribution to the lattice conductivity. Because of their long free path, low-frequency phonons are particularly sensitive to boundary scattering. Consequently, grain boundary scattering is a suitable approach to disperse long wavelength phonons and thereby, to reduce the lattice thermal conductivity[9,42]. In figure 2.14, the contribution to the lattice conductivity of phonons of angular frequency ω is plotted against ω. The thermal lattice conductivity of a large pure crystal is represented by the area under the upper curve. The double-hatched region represents the reduction in thermal conductivity due to boundary scattering while the single-hatched region is related to the loss of lattice conductivity due to point-defect scattering attributed to alloying [42].

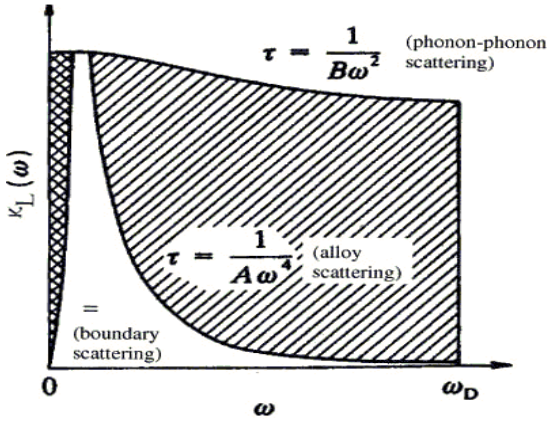

Figure 2.14: Schematic plot of the contributions to the lattice thermal conductivity of different angular frequency phonons. The double-hatched region represents the thermal conductivity reduction due to boundary scattering. The single-hatched region shows the contribution removed by alloy scattering in a solid solution.

Obviously, the mobility of the free carriers will also be affected by the grain boundaries. To enhance *zT*, the electrical conductivity should not be significantly affected by such crystallographic defects. TE materials are usually heavily doped; therefore in the majority of the cases the mean free path of carriers is very short in comparison with the phonon mean free path[71]. Consequently, phonons will be more effectively scattered than free carriers and a significant enhancement of *zT* is expected. In addition to the nanostructuring approach, it should be noted that by preferential scattering of low-energy electrons at grain boundaries is possible to improve the Seebeck coefficient. Thus, the reduction in the electrical conductivity can be compensated by *S* enhancement[71]. Moreover, by nanostructuring TE materials, the bipolar conduction can be reduced[28]. For many TE materials, especially at elevated temperatures, the bipolar thermal conductivity is a significant component of the total thermal conductivity, which leads to decrease *zT*. As aforementioned in section 2.4., preferential scattering of the minority carriers is a satisfactory strategy to reduce the bipolar effect[35]. Although it is not well understood why electrons are preferentially scattered with grain boundaries in *p*-type $Bi_xSb_{2-x}Te_3$, this mechanism is effective for minimizing the bipolar effects. Consequently, in nanostructured $Bi_xSb_{2-x}Te_3$

alloys a high figure of merit can be achieved over a wide range of temperatures[28]. In literature, there are many works that report a significant *zT* enhancement for *p*-type $Bi_xSb_{2-x}Te_3$ via interface scattering. The majority of them are based on combining high-energy ball milling and hot-pressing (or spark plasma sintering (SPS)) methods [28,72–74]. By melt- spinning plus SPS sintering a high *zT* value of 1.56 at 300 K was reported by Xie et al [38]. Severe plastic deformation (SPD) methods can be suitable for achieving satisfactory *zT* values too. A figure of merit of 3.85×10^{-3} K^{-1} was reported[75] for $(Bi,Sb)_2Te_3$ alloys processed by rotary-die equal channel angular pressing (ECAP) along their transverse direction.

2.6. Approaches to produce ultrafine-grained and nanostructured materials

Nowadays, there are available a variety of physical and chemical processes that enable the production of nanocrystalline bulk TE materials. These methods can be classified mainly into two categories, 'top-down' and 'bottom-up' approaches (figure 2.15). In the first approach, existing coarse-grained materials are processed in order to get ultrafine-grained (UFG) or nanostructured (NS) materials. Methods such as ball milling or melt spinning are the most frequently used [38,74,76,77]. However, by these methods it is not possible to accurately control the particle size and morphology and during processing oxidation or/ and contamination of the powders can be expected. Severe plastic deformation (SPD) processing is a well-known process which allows the production of UFG or NS materials irrespective of their initially coarse grain size[78]. During SPD the starting material is subjected to the very large strains under typically high hydrostatic pressures which lead to a substantial grain refinement without the introduction of any contaminant. Materials produced by SPD techniques usually have grain sizes in the range of 100–1000 nm[79].

On the other hand, in the 'bottom-up' approach, bulk nanostructured solids are fabricated by assembling individual atoms or nanoparticles. The

'bottom-up' strategy allows a better control of the particle size and morphology through fine-tuning of various parameters. PVD and CVD techniques like molecular beam epitaxy (MBE) [27] or metal organic chemical vapor deposition (MOCVD) [80] are able to get thin films with enhanced TE properties. However, these methods exhibit low growing rates and involve the use of high-vacuum pumps. Therefore, the production of TE materials by such methods is costly and, in addition, they are not versatile for large scale production. Currently, other cost-effective and more easily scalable methods that are also based on the 'bottom-up' approach have been developed. Hydrothermal or colloidal synthesis are suitable methods to produce nanosized powders at a reasonable cost, due to the chemical reactions that take place at low temperatures and they do not need the use of ultrapure compounds as raw materials. This fact makes attractive these approaches to produce nanostructured TE materials [81–83]. However, in order to fabricate TE devices, the nanosized powders must be consolidated into a bulk sample which is still a challenging issue. The consolidation process is usually carried out by hot pressing (HP) or spark plasma sintering (SPS) which enables powder consolidation by applying a uniaxial pressure at a moderate temperature. However such consolidation routes inevitably leads to grain growth. Introduction of porosity is another drawback: the relative densities of pellets consolidated from nanosized raw powders are usually close to 90-95% [82,84]. Although it seems that porosity decreases in the same proportion the electrical conductivity and the thermal conductivity[85], it does not affect notoriously *zT*. However, it is well-known that it degrades significantly the mechanical properties. On the other hand, since the production of the nanocrystals takes place in presence of organic molecules [81,83], it is possible to get an organic layer on the surface of the nanocrystals. Organic layers are electrical insulator and therefore they are extremely harmful for the electrical transport [86].

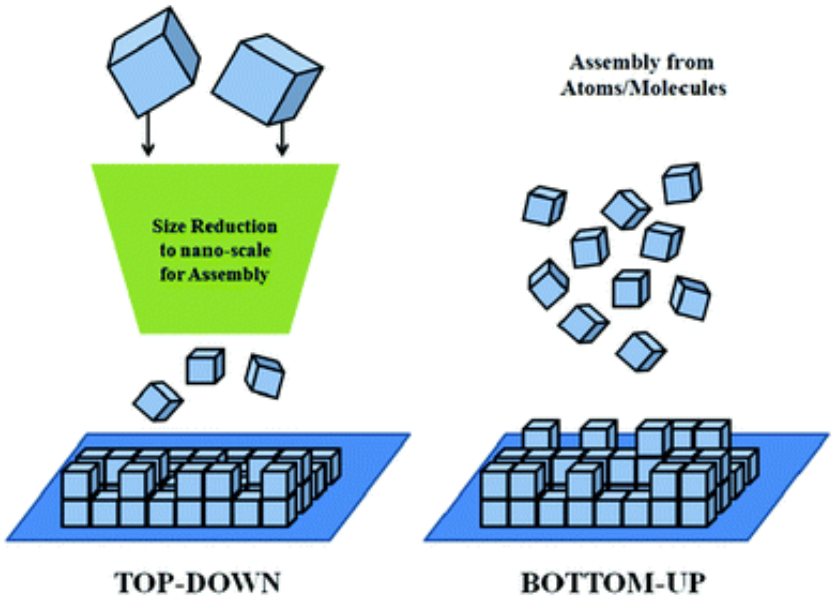

Figure 2.15: illustration of 'top-down' and 'bottom-up' approaches [118].

2.6.1. Severe Plastic Deformation (SPD), a 'top-down' approach for producing nanostructured thermoelectric materials.

As I mentioned above, severe plastic deformation (SPD), is an efficient method to produce ultrafine-grained or even nanocrystalline bulk materials. Traditional grain refinement techniques, such as extrusion, forging, or rolling, do not allow the application of such large plastic strains without premature fracture of samples [87]. Therefore, they do not permit the production of NC materials. The grain refinement obtained by SPD is accompanied by a significant reduction in the residual porosity and impurities compared to traditional techniques that allow the production of bulk NC materials from powders, such mechanical-milling plus cold/hot pressing [78]. Another remarkable advantage of SPD technique is its potential for being easily scalable.

According to R. Valiev et al. SPD methods are defined as: *'Any method of metal forming under an extensive hydrostatic pressure that may be used to impose a very high strain on a bulk solid without the introduction of any significant change in the overall dimensions of the sample and having the ability to produce exceptional grain refinement'*.[88]. In the last 25 years, many SPD methods that fulfill all these requirements have been developed, being high-pressure torsion (HPT), equal angular channel pressing (ECAP) and accumulative roll bonding (ARB), the most widely used ones.

2.6.1-1 Accumulative roll bonding (ARB)

During ARB process, two sheets are stacked together and roll-bonded. After that, the length of rolled material is sectioned into two halves. If necessary, the interfaces of the strips are surface-treated in advance to enhance their bond strength. The sectioned strips are again surface-treated, stacked and roll-bonded. The whole process is repeated over and over [89] (see figure 2.16). If the sheet thickness is reduced a 50 % per cycle, the total reduction after n cycles is $t = t_0 / 2^n$ where t_0 is the initial thickness of strips. Thus, assuming von Mises criterion, the equivalent plastic strain is given by:

$$\varepsilon = \frac{2}{\sqrt{3}} n \cdot \ln(1/2) \qquad (1.21)$$

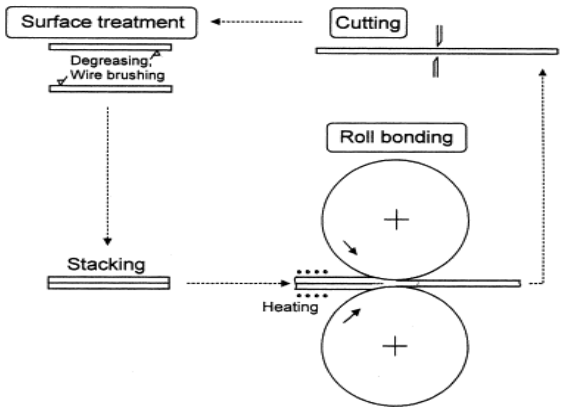

Figure 2.16: Illustrative sketch of the ARB process [89]

2.6.1-2 Equal angular channel pressing (ECAP)

In ECAP; as shown in figure 2.17, a sample is pressed several times through a die. The die consists of two channels with identical cross-sections connected by an intersection with a specific curvature (Ψ) that usually is 90°. When the sample passes through the die simple shear strain is imposed. The amount of applied strain depends on die geometry and is given by [90]:

$$\gamma = 2\cot\left(\frac{\Phi}{2}+\frac{\Psi}{2}\right)+\Psi\operatorname{cosec}\left(\frac{\Phi}{2}+\frac{\Psi}{2}\right) \qquad (1.21)$$

Since the cross-sectional area remains unchanged, the same sample may be pressed many times to attain exceptionally high strain. The von Mises equivalent strain, after N passes is generally expressed by [90]:

$$\varepsilon_N = \frac{N}{\sqrt{3}}\left[2\cot\left(\frac{\Phi}{2}+\frac{\Psi}{2}\right)+\Psi\cos ec\left(\frac{\Phi}{2}+\frac{\Psi}{2}\right)\right] \qquad (1.22)$$

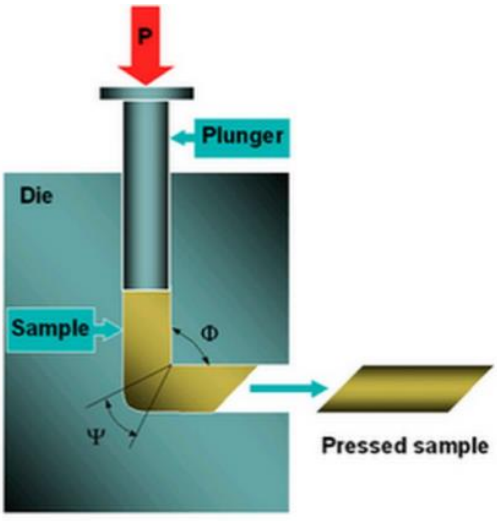

Figure 2.17: Illustration of the ECAP process [119]

J.T. Im et al.[91] and Z.M. Sun et al. [75] have processed satisfactorily *p*-type Bi_2Te_3 alloys by ECAP at elevated temperature (~500° C; ~0.86T_m). Their works show that ECAP is a suitable process to get fine-grained TE material[91]. As a result of the grain refinement, an improvement of the mechanical properties accompanied by a reduction in the thermal conductivity was reported. However, after ECAP the samples had not a strong preferred orientation[91]. Since Bi_2Te_3 alloys have a layered rhombohedral crystallographic structure their thermoelectric properties are very anisotropic[12], consequently, in order to achieve high zT values strongly oriented nanostructures should be processed.

2.6.1-3 High-pressure torsion (HPT)

In the case of HPT a disk-shaped sample is compressed between two anvils by applying a high hydrostatic pressure, which usually ranges between 2 and 6 GPa, while one of the anvils is rotated with respect to the other (figure 2.18). This way, the sample is deformed by simple shear. The equivalent strain, assuming von Mises criterion can be calculated by[78]:

$$\varepsilon = \frac{2\pi r N}{\sqrt{3}t} \qquad (1.23)$$

where *r* denotes the radius of the sample, *t* its thickness and *N* is the number of applied revolutions. To ensure a homogeneous microstructure in the majority of the specimen, the ratio of its thickness, *t*, to its diameter, *d*, should not exceed a given value, which is close to 1/10 or smaller [92,93] Assuming that geometry, the applied equivalent plastic strain per revolution is close to 20, which is much higher than in any other SPD technique per cycle (in the case of ARB and ECAP the applied strain per cycle is about 0.8 and 1.2 per cycle, respectively).

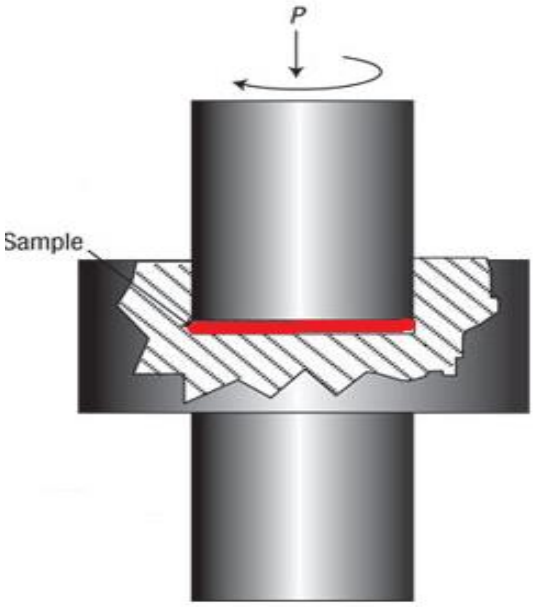

Figure 2.18 schematic illustration of HPT processing

During HPT processing, if a proper geometry is given to the cavity between the anvils, the sample is strained under high quasi-hydrostatic compression, which enables processing even brittle materials without fracture at relative low temperature. This fact is one of the biggest advantages of HPT over other SPD processes [92,94]. The resulting microstructures after HPT or after any other SPD process usually have a high density of crystal defects, such as dislocations and low and high angle grain boundaries [78]. As discussed in section 1.5, phonons are strongly scattered by these defects which results in a drastic reduction of the thermal conductivity. On the other hand, refining the grain size enhances the mechanical properties (strength and toughness, the well-known Hall-Petch effect). However, a high density of dislocations has a negative toughening effect for some materials[95]; therefore the toughening effect of HPT for TE materials should be accurately investigated.

HPT can be equally applied to consolidate powders into a bulk sample. HPT has been used to consolidate many different materials such as copper-based

amorphous alloys [96], metallic fine powders [97,98] or ceramics [99], achieving in all the cases densities close to 100 %. For instance, Valiev et al. were able to produce fully dense (close to 95% of the theoretical density) nanocrystalline nickel with a grain size of ~20 nm by SPD consolidation process of ball-milled Ni fine powder. Thus, HPT can be an alternative to the existing methods to consolidate nano-sized powders at relatively low-temperature. This way, residual porosity and grain growth may be avoided giving rise to a simultaneous improvement of the thermoelectric and mechanical properties.

2.7 Bismuth telluride based alloys as high-performance thermoelectric materials

Bi_2Te_3 has been studied extensively since 1954[100] being currently one of the most widely used TE materials. Bi_2Te_3 and its alloys are known as the most effective TE materials near room temperature [21]. As figure 2.19 shows, the Seebeck coefficient of pure Bi_2Te_3 depends strongly on the tellurium concentration. Bi_2Te_3 is an *n*-type semiconductor for a tellurium amount higher than 62.5 % (At. %) while *p*-type for lower concentrations. The *p*-type material exhibits a maximum Seebeck coefficient at a tellurium concentration of 60%[12].

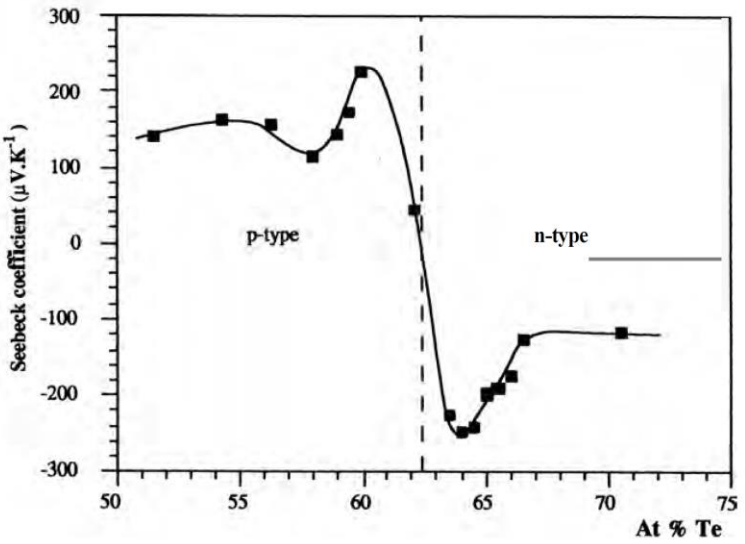

Figure 2.19: Seebeck coefficient against Tellurium concentration for both n- and p-type pure Bi_2Te_3 [12]

However, the carrier concentration is also sensitive to the lattice defects generated during mechanical alloying. Schultz et al.[101] showed that heavy plastic deformation produces non-basal slip in Bi_2Te_3, which introduces a large concentration of 'electrically active' point defects. They suggested that the non-basal slip produces at least 3 Te to 2 Bi vacancy-interstitial pairs. Tellurium and Bismuth vacancies produce one acceptor and one donor respectively; therefore, after plastic deformation there are more donors than acceptors (named as 'deformation-induced donor-like effect'), which results in changing the conduction behavior from *p*-to *n*-type [102]. Anti-site defects, i.e. Bi atoms that enter into Te vacancies, are also easily produced because of the small electronegativity difference between Bi and Te elements [103]. Navrátil et al. [104], based on these results, proposed an equation that describes the interaction between Te and Bi vacancies with anti-site defects by the following equation:

$$2V_{Bi}^{'''} + 3V_{Te}^{\circ\circ\circ} + Bi_{Te}^{\cdot} = V_{Bi}^{'} + Bi_{Bi}^{\times} + 4V_{Te}^{\circ} + 3e^{'} \qquad (1.24)$$

Where $^{\circ}$ and $^{'}$ denotes donor and acceptor production respectively. There are several works that have reported the *p*-type to *n*-type conduction change for pure Bi_2Te_3 after hot-pressing or SPS sintering [34,105,106].

Bismuth telluride itself, when grown from the melt, is non-stoichiometric being at ordinary temperatures *p*-type extrinsic semiconductor. When it is alloyed with Sb_2Te_3, the non-stoichiometry becomes even more pronounced and it is rather difficult to add sufficient donor impurities or crystallographic defects to convert into an *n*-type semiconductor. On the other hand, alloying Bi_2Te_3 with Bi_2Se_3 enables the production of *n*-type semiconductors with optimum carrier concentration[11].

One important parameter that affects the TE properties is the weighted mobility (U) defined as $U = \mu(m^*/m_e)^{3/2}$, where m^* and m_e are the effective mass of the valence band and the free electron mass respectively. For a unipolar TE material (i.e. only electrons or holes predominate) the total thermal conductivity can be expressed as the sum of the lattice thermal conductivity (κ_L) and the electronic thermal conductivity (κ_e). The last one, according to the Wiedemann–Franz law, is related to the electrical conductivity as $\kappa = L_0\sigma T$ where L_0 is the Lorenz number [36]. Similarly, the electrical conductivity can be defined as, $\sigma = ne\mu$. Therefore, *zT* can be rewritten as (for further details see reference [12], Appendix: Calculation of *ZT* for PGEC):

$$zT = \frac{\left(S/\sqrt{L_0}\right)^2}{1+\frac{1}{L_0 eT}\left(\frac{\kappa_L}{U}\right)\left[\frac{\left(m^*/m_0\right)^{3/2}}{n}\right]} \qquad (1.25)$$

In the $(Bi–Sb)_2Te_3$ system, the weighted mobility increases as the proportion of Sb_2Te_3 rises. As shown in figure 2.20, the minimum lattice conductivity is found when the concentration of Sb_2Te_3 is about 75%. When the Sb_2Te_3 is higher the lattice thermal conductivity increases, at the cost of Seebeck

coefficient since Sb_2Te_3 itself displays near-metallic properties and consequently its Seebeck coefficient is usually lower than 100 $\mu V \cdot K^{-1}$ [11].
Thus, optimum alloying of Bi_2Te_3 with Sb_2Te_3 generates disturbances in the short-range order, which contributes to reducing the thermal conductivity without affecting the mobility of the free charge carriers since the long-range order is preserved[11]. So, the simultaneous enhancement of the weighted mobility and reduction of the lattice thermal conductivity leads to improved *zT*. For traditionally grown ingots, the Sb_2Te_3 amount that optimizes the TE performance is close to 75% [107]. However, an excess of electrons or holes can be introduced into the lattice by the plastic deformation-induced lattice defects, which significantly change the carrier concentration. On the one hand, an excess of electrons can be introduced into the lattice as a result of the aforementioned deformation-induced donor-like effect. On the other hand, Poudel et al [28] suggested that anti-site defects are more likely to occur at interfaces causing an increment of the hole density in the grains (i.e. the grain boundaries plays the role of acceptors as proposed by Kim et al.[108]). Therefore, for polycrystalline samples subjected to powder processing, the alloy composition can differ from $Sb_{1.5}Bi_{0.5}Te_3$, that is the optimum one for unidirectionally grown ingots. For instance, Hu et al. [109] showed that the optimum composition is shifted to a higher Sb content for the polycrystalline samples produced by hot press and subsequent hot deformation process due to the deformation induced donor-like effect.

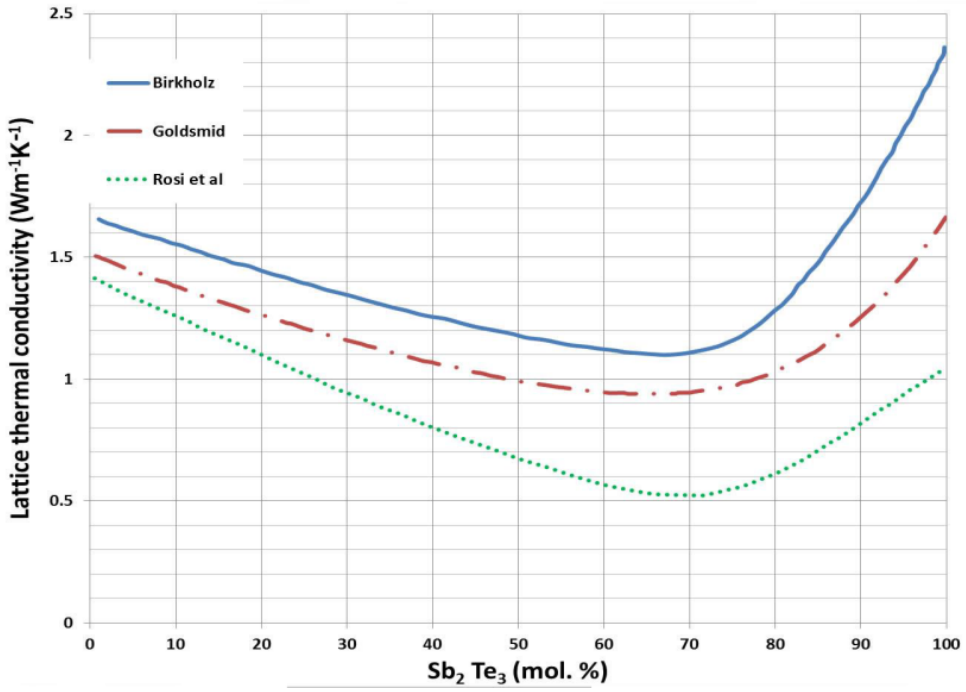

Figure 2.20: Lattice thermal conductivity versus the molar percentage of Sb_2Te_3 for Bi_2Te_3 based on data from Birkholz, Goldsmid and Rosi et al [120].

Bi_2Te_3 alloys have a rhombohedral structure with R3m space group; the crystal is composed of atomic layers in the order of Te(1)-Bi-Te(2)-Bi-Te(1) along the *c* axis. Bi-Te(2) and Bi-Te(1) bonds are ionic-covalent type, while bonding between Te(1)-Te(1) layers is due to van der Waals interaction (figure 2.21). As a result of the weak van der Waals bonding, Bi_2Te_3 is easily cleaved along the c-plane, and consequently it is an extremely brittle material. Due to the layered rhombohedral structure, the thermoelectric properties are very anisotropic too. The electrical and thermal conductivities along the cleavage plane are respectively about four and two times larger than those along the c-axis, therefore z*T* in the *c*-plane is approximately two times larger than along the c axis[12]. Due to the inherent anisotropy of the TE properties of Bi_2Te_3 alloys, producing highly texturized nano-grained materials is one of the most promising strategies to improve the TE

performance of Bi_2Te_3 alloys. Unfortunately, this fact is not easy to achieve via conventional powder processing techniques. Firstly because it is quite difficult to orient preferentially particles smaller than 5 μm [105,110] and secondly because during consolidation process at moderate temperature grain growth is expected.

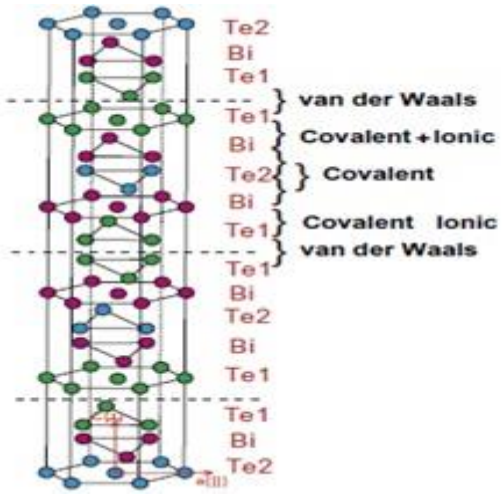

Figure 2.21: scheme of the crystal structure of Bi_2Te_3 alloys [121]

The search for an optimum process that warrants a nanosized grain structure with preferred crystal orientation is still in progress. For example, in 2008, Poudel et al.[28] reported a nanostructured $Bi_xSb_{2-x}Te_3$ bulk material, fabricated by mechanical milling of a commercial ingot into nanopowder and subsequent consolidation by hot pressing, with zT=1.4 at 373 K. The TE properties of these compounds were isotropic (grains were not properly oriented) and the zT enhancement was attributed to a significant decrease in the lattice thermal conductivity due to both, grain boundary scattering and the presence of tellurium nano-precipitates. Cao et al.[82] produced Bi_2Te_3/Sb_2Te_3 bulk nanocomposites with laminated nanostructures by combining a hydrothermal synthesis route and hot-pressing. By this way they obtained satisfactory zT value of 1.47 at 438 K. Xie et al.[38] fabricated

high performance *p*-type thermoelectric materials (zT ~1.56 at 300 K) by combining a melt spinning technique followed by a quick spark plasma sintering procedure. Kim et al.[110] showed that the zT of polycrystalline $Bi_{0.5}Sb_{1.5}Te_3$ can be enhanced by improving the crystal alignment. Using a high magnetic field, they were able to improve the alignment degree of fine powders and consequently enhance zT.

In the case of Bi_2Te_3 alloys since the bonding between Te(1)-Te(1) layers is due to the weak van der Waals interaction, a strong (000l) fiber texture is observed after HPT processing because of the easy glide on the (0001) plane[111].

Therefore, HPT is expected to be a suitable technique to produce nanograined and highly oriented Bi_2Te_3 alloys which would lead to improved thermoelectric properties.

2.8. Mechanical properties of TE materials

The mechanical properties of most promising TE materials such skutterudites, PbTe based compounds or Bi_2Te_3 based alloys are usually poor [30,32,33,112]. For design and in-use reliability of thermoelectric systems in many applications, such as heat recovery in vehicles, enhancement of the mechanical properties of TE materials is of paramount importance because during operation they are subjected to mechanical and thermal stresses which can cause brittle fractures or premature failure of the devices. Consequently, high strength, good toughness and large resistance to thermal shock are desirable qualities for TE materials. The thermal shock resistance parameter (R_T) can be expressed as:

$$R_T = \frac{\sigma_f (1-\nu)\kappa}{\alpha E} \qquad (1.26)$$

Where ν is Poisson's ratio, κ is thermal conductivity, α the thermal expansion coefficient, E the elastic modulus and σ_f the fracture strength. Adequate TE materials should have a low thermal conductivity, so increasing the fracture strength is a good point to enhance $R_{T.}$

Single-crystalline Bi_2Te_3 alloys, due to the weak van der Waals bonding between Te(1)-Te(1) layers are easily cleaved along the *c*-plane and consequently exhibit poor mechanical properties. In order to improve the mechanical properties bulk polycrystalline Bi_2Te_3 alloys are often prepared by powder/sintering methods like ball milling plus hot-pressing (HP) or spark-plasma sintering (SPS). The production of polycrystalline samples enhances the hardness and fracture stress [113]. The reported bending strength of polycrystalline materials are much higher than that of the materials prepared by unidirectional growing methods such zone-melting or Bridgman methods (see table 2.I).

Table 2.I: Bending Strength of Bi_2Te_3 based alloys

Fabrication method	**Grain size (µm)**	**Bending strength (MPa)**	**Reference**
zone-melting	-	10	[114]
Bridgman method	-	19.2	[115]
Melting/grinding hot-pressing	~38	50	[115]
Zone-melting/grinding SPS	~100	80	[114]
Ball-milling SPS –hot forging	-	120	[34]

The addition of SiC nanoparticles is an alternative strategy to improve the mechanical properties of Bi_2Te_3 alloys. Zhao et al[116] reported that adding a 0.2 vol % of SiC nanoparticles enhances the micro-hardness and fracture-toughness. Adding SiC nanoparticles reduces also the thermal conductivity since low-to-mid frequency phonons can be significantly scattered by nanoparticles[43]. However, the mechanical and thermoelectric properties are degraded quickly at higher SiC concentration. The first one is associated with the increase of the residual porosity of the bulk samples while the

second one is due to SiC has much higher electrical and thermal conductivity than Bi_2Te_3.

Since grain refining has a toughening effect in brittle polycrystals, nanostructuring Bi_2Te_3 is expected to have a mechanical benefit besides its benefit on the *zT* figure of merit. Similarly, it is expected to strengthen the plastic resistance of Bi_2Te_3 through the Hall-Petch effect too. Consequently, HPT processing is expected to be a suitable technique to produce high-performance Bi_2Te_3 based TE materials with enhanced mechanical properties.

2.9. References

1. Rosen, M. & Dincer, I. On exergy and environmental impact. Int. J. Energy Res. 21, 643–654 (1997).

2. Pope, C. A. & Dockery, D. W. Health Effects of Fine Particulate Air Pollution: Lines that Connect. J. Air Waste Manage. Assoc. 56, 709–742 (2006).

3. Samet, J. M., Dominici, F., Zeger, S. L., Schwartz, J. & Dockery, D. W. The National Morbidity, Mortality, and Air Pollution Study. Part I: Methods and methodologic issues. Res. Rep. Health. Eff. Inst. 5–14; discussion 75–84 (2000). doi:PubMed ID: 11354823

4. Ilyin, L. A. et al. Radiocontamination patterns and possible health consequences of the accident at the Chernobyl nuclear power station. J. Radiol. Prot. 10, 3 (1990).

5. Dincer, I. Renewable energy and sustainable development: a crucial review. Renew. Sustain. Energy Rev. 4, 157–175 (2000).

6. Nakićenović, N., Grübler, A. & McDonald, A. Global energy perspectives. (Cambridge University Press, 1998).

7. Dincer, I. Renewable energy and sustainable development: a crucial review. Renew. Sustain. Energy Rev. 4, 157–175 (2000).

8. Bos, Eduard; My T. Vu; Massiah, Ernest; Bulatao, R. A. World population projections 1994-95 edition : estimates and projections with related demographic statistics, Volume 1. (1994).

9. Biswas, K. et al. High-performance bulk thermoelectrics with all-scale hierarchical architectures. Nature 489, 414–8 (2012).

10. Riffat, S. . & Ma, X. Thermoelectrics: a review of present and potential applications. Appl. Therm. Eng. 23, 913–935 (2003).

11. H.Julian Goldsmith. Introduction to Thermoelectricity. (2010). doi:10.1007/978-3-642-00716-3

12. D.M. Rowe. CRC Handbook of Thermoelectrics. (1995).

13. Tritt, T. M. Recent Trends in Thermoelectric Materials Research I. (2001).

14. Ravishankara, A. R. et al. Do hydrofluorocarbons destroy stratospheric ozone? Science 263, 71–75 (1994).

15. Ferrotec. at <https://www.ferrotec.com/Technology/Thermoelectric/Thermalref04>

16. Majumdar, A. Thermoelectric devices: Helping chips to keep their cool. Nat Nano 4, 214–215 (2009).

17. Sharp, J., Bierschenk, J. & Lyon, H. B. Overview of solid-state thermoelectric refrigerators and possible applications to on-chip thermal management. Proc. IEEE 94, 1602–1611 (2006).

18. Yang, J. & Caillat, T. Thermoelectric Materials for Space and Automotive Power Generation. MRS Bull. 31, 224–229 (2006).

19. Yang, J. & Stabler, F. R. Automotive applications of thermoelectric materials. in J. Electron. Mater. 38, 1245–1251 (2009).

20. Kordás, K. et al. Chip cooling with integrated carbon nanotube microfin architectures. Appl. Phys. Lett. 90, (2007).

21. Alam, H. & Ramakrishna, S. A review on the enhancement of figure of merit from bulk to nano-thermoelectric materials. Nano Energy 2,190–212 (2013).

22. Canumalla, S. & Viswanadham, P. Portable Consumer Electronics: Packaging, Materials, and Reliability. (PennWell, 2010). at <https://books.google.at/books?id=OkvpbmzaPkUC>

23. Jo, S. E., Kim, M. K., Kim, M. S. & Kim, Y. J. Flexible thermoelectric generator for human body heat energy harvesting. Electron. Lett. 48, 1015 (2012).

24. Schwyter, E., Glatz, W., Durrer, L. & Hierold, C. Flexible micro thermoelectric generator based on electroplated B1 2+xTe3-x. in DTIP MEMS MOEMS - Symp. Des. Test, Integr. Packag. MEMS/MOEMS 46–48 (2008). doi:10.1109/DTIP.2008.4752949

25. EIA. No Title. (2011). at <http://www.eia.gov/totalenergy/data/annual/#consumption>

26. Gentherm. (2015). at <http://www.gentherm.com/en/page/climate-seats>

27. Venkatasubramanian, R., Siivola, E., Colpitts, T. & O'Quinn, B. Thin-film thermoelectric devices with high room-temperature figures of merit. Nature 413, 597–602 (2001).

28. Poudel, B. et al. High-thermoelectric performance of nanostructured bismuth antimony telluride bulk alloys. Science 320, 634–8 (2008).

29. Rogl, G. et al. High-pressure torsion, a new processing route for thermoelectrics of high ZTs by means of severe plastic deformation. Acta Mater. 60, 2146–2157 (2012).

30. Salvador, J. R. et al. Transport and mechanical properties of Yb-filled skutterudites. Philos. Mag. 89, 1517–1534 (2009).

31. Zhang, L. et al. Mechanical properties of filled antimonide skutterudites. Mater. Sci. Eng. B Solid-State Mater. Adv. Technol. 170, 26–31 (2010).

32. Gelbstein, Y., Gotesman, G., Lishzinker, Y., Dashevsky, Z. & Dariel, M. P. Mechanical properties of PbTe-based thermoelectric semiconductors. Scr. Mater. 58, 251–254 (2008).

33. Ni, J. E. et al. Room temperature Young's modulus, shear modulus, Poisson's ratio and hardness of PbTe–PbS thermoelectric materials. Mater. Sci. Eng. B 170, 58–66 (2010).

34. Zhao, L. D., Zhang, B.-P., Li, J.-F., Zhang, H. L. & Liu, W. S. Enhanced thermoelectric and mechanical properties in textured n-

type Bi2Te3 prepared by spark plasma sintering. Solid State Sci. 10, 651–658 (2008).

35. Minnich, A. J., Dresselhaus, M. S., Ren, Z. F. & Chen, G. Bulk nanostructured thermoelectric materials : current research and future prospects. Energy Environ. Sci. 2, 466–479 (2009).

36. Kittel, C. Introduction to Solid State Physics. (Wiley, 2004). at

37. Hu, L. P. et al. Improving thermoelectric properties of n-type bismuth–telluride-based alloys by deformation-induced lattice defects and texture enhancement. Acta Mater. 60, 4431–4437 (2012).

38. Xie, W., Tang, X., Yan, Y., Zhang, Q. & Tritt, T. M. Unique nanostructures and enhanced thermoelectric performance of melt-spun BiSbTe alloys. Appl. Phys. Lett. 94, 102111 (2009).

39. Bhandari, C. M. & Rowe, D. M. Silicon–germanium alloys as high-temperature thermoelectric materials. Contemp. Phys. 21, 219–242 (1980).

40. Dughaish, Z. H. Lead telluride as a thermoelectric material for thermoelectric power generation. Phys. B Condens. Matter 322, 205–223 (2002).

41. A.F. Ioffe, S.V. Airepetyants, A.V. Ioffe, N.V. Kolomoets, L.S. Stil'bans, D. A. N. No Title. SSSR 106, 981 (1956).

42. Tritt, T. M. Thermal Conductivity Theory, Properties, and Applications. (2004).

43. He, J., Kanatzidis, M. G. & Dravid, V. P. High performance bulk thermoelectrics via a panoscopic approach. Mater. Today 16, 166–176 (2013).

44. Snyder, G. J. & Toberer, E. S. Complex thermoelectric materials. Nat. Mater. 7, 105–114 (2008).

45. Xie, W. et al. High performance Bi2Te3 nanocomposites prepared by single-element-melt-spinning spark-plasma sintering. J. Mater. Sci. 48, 2745–2760 (2012).

46. Lee, J. H., Wu, J. & Grossman, J. C. Enhancing the thermoelectric power factor with highly mismatched isoelectronic doping. Phys. Rev. Lett. 104, (2010).

47. Hicks, L. D. & Dresselhaus, M. S. Thermoelectric figure of merit of a one-dimensional conductor. Phys. Rev. B 47, 16631–16634 (1993).

48. Dresselhaus, M. S. et al. New Directions for Low-Dimensional Thermoelectric Materials. Adv. Mater. 19, 1043–1053 (2007).

49. Pei, Y., Wang, H. & Snyder, G. J. Band engineering of thermoelectric materials. Adv. Mater. 24, 6125–6135 (2012).

50. Heremans, J. P., Wiendlocha, B. & Chamoire, A. M. Resonant levels in bulk thermoelectric semiconductors. Energy Environ. Sci. 5, 5510 (2012).

51. Pei, Y. et al. Convergence of electronic bands for high performance bulk thermoelectrics. Nature 473, 66–9 (2011).

52. Heremans, J. P. et al. Enhancement of thermoelectric efficiency in PbTe by distortion of the electronic density of states. Science 321, 554–557 (2008).

53. Ahn, K. et al. Exploring resonance levels and nanostructuring in the PbTe-CdTe system and enhancement of the thermoelectric figure of merit. J. Am. Chem. Soc. 132, 5227–5235 (2010).

54. Jaworski, C. M., Kulbachinskii, V. & Heremans, J. P. Resonant level formed by tin in Bi2 Te3 and the enhancement of room-temperature thermoelectric power. Phys. Rev. B - Condens. Matter Mater. Phys. 80, (2009).

55. Shi, X. et al. Multiple-filled skutterudites: High thermoelectric figure of merit through separately optimizing electrical and thermal transports. J. Am. Chem. Soc. 133, 7837–7846 (2011).

56. Nolas, G. S., Morelli, D. T. & Tritt, T. M. SKUTTERUDITES: A Phonon-Glass-Electron Crystal Approach to Advanced Thermoelectric Energy Conversion Applications. Annu. Rev. Mater. Sci. 29, 89–116 (1999).

57. Caillat, T., Fleurial, J.-P. & Borshchevsky, A. Skutterudites for thermoelectric applications. Fifteenth Int. Conf. Thermoelectr. Proc. ICT '96 (1996). doi:10.1109/ICT.1996.553265

58. Drymiotis, F., Day, T. W., Brown, D. R., Heinz, N. a. & Jeffrey Snyder, G. Enhanced thermoelectric performance in the very low thermal conductivity Ag2Se0.5Te0.5. Appl. Phys. Lett. 103, 5–9 (2013).

59. Liu, H. et al. Ultrahigh thermoelectric performance by electron and phonon critical scattering in Cu2Se1-xIx. Adv. Mater. 25, 6607–6612 (2013).

60. Xiao, C., Li, Z., Li, K., Huang, P. & Xie, Y. Decoupling interrelated parameters for designing high performance thermoelectric materials. Acc. Chem. Res. 47, 1287–95 (2014).

61. Goldmid, H. J. A. W. P. Boundary Scattering of phonons in solid solutions. Phys. Lett. 27 A, 523–524 (1968).

62. Li, J.-F., Liu, W.-S., Zhao, L.-D. & Zhou, M. High-performance nanostructured thermoelectric materials. NPG Asia Mater. 2, 152–158 (2010).

63. Pei, Y. Z. et al. Synthesis and thermoelectric properties of K[sub y]Co[sub 4]Sb[sub 12]. Appl. Phys. Lett. 89, 221107 (2006).

64. Shi, X. et al. Low thermal conductivity and high thermoelectric figure of merit in n-type BaxYbyCo4Sb12 double-filled skutterudites. Appl. Phys. Lett. 92, 182101 (2008).

65. Yang, J., Zhang, W., Bai, S. Q., Mei, Z. & Chen, L. D. Dual-frequency resonant phonon scattering in Bax Ry Co4 Sb12 (R=La, Ce, and Sr). Appl. Phys. Lett. 90, (2007).

66. Zhao, L.-D. et al. Ultralow thermal conductivity and high thermoelectric figure of merit in SnSe crystals. Nature 508, 373–7 (2014).

67. Morelli, D. T., Jovovic, V. & Heremans, J. P. Intrinsically minimal thermal conductivity in cubic I-V-VI2 semiconductors. Phys. Rev. Lett. 101, (2008).

68. Ashcroft, N. W. & Mermin, N. D. Solid State Physics. Solid State Phys. 2, (1976).

69. Guin, S. N., Srihari, V. & Biswas, K. Promising thermoelectric performance in n-type AgBiSe2: effect of aliovalent anion doping. J. Mater. Chem. A 3, 648–655 (2015).

70. Pan, L., Bérardan, D. & Dragoe, N. High thermoelectric properties of n-type AgBiSe2. J. Am. Chem. Soc. 135, 4914–4917 (2013).

71. Lan, Y., Minnich, A. J., Chen, G. & Ren, Z. Enhancement of Thermoelectric Figure-of-Merit by a Bulk Nanostructuring Approach. Adv. Funct. Mater. 20, 357–376 (2010).

72. Kitagawa, H., Kurata, a., Araki, H., Morito, S. & Tanabe, E. Effect of Deformation Temperature on Texture and Thermoelectric Properties of Bi0.5Sb1.5Te3 Prepared by Hot-Press Deformation. J. Electron. Mater. 39, 1692–1695 (2010).

73. Hyun, D.-B., Hwang, J.-S., Shim, J.-D. & Oh, T. Thermoelectric properties of (Bi0.25Sb0.75)2Te3 alloys fabricated by hot-pressing method. J. Mater. Sci. 36, 1285–1291 (2001).

74. Ma, Y. et al. Enhanced thermoelectric figure-of-merit in p-type nanostructured bismuth antimony tellurium alloys made from elemental chunks. Nano Lett. 8, 2580–2584 (2008).

75. Sb, D. Effect of rotary-die equal channel angular pressing on the thermoelectric properties of a (Bi , Sb) 2 Te 3 alloy. 895–903 (2005). doi:10.1557/JMR.2005.0120

76. Yang, J. Y., Aizawa, T., Yamamoto, A. & Ohta, T. Thermoelectric properties of n-type (Bi 2 Se 3). 312, 326–330 (2000).

77. Prasad Yadav, T., Manohar Yadav, R. & Pratap Singh, D. Mechanical Milling: a Top Down Approach for the Synthesis of Nanomaterials and Nanocomposites. Nanosci. Nanotechnol. 2, 22–48 (2012).

78. Valiev, R. Z., Islamgaliev, R. K. & Alexandrov, I. V. Bulk nanostructured materials from severe plastic deformation. Prog. Mater. Sci. 45, 103–189 (2000).

79. Pérez-Prado, M. T., Gimazov, a. a., Ruano, O. a., Kassner, M. E. & Zhilyaev, a. P. Bulk nanocrystalline ω-Zr by high-pressure torsion. Scr. Mater. 58, 219–222 (2008).

80. Boulouz, A. et al. Preparation and characterization of MOCVD bismuth telluride thin films. J. Cryst. Growth 194, 336–341 (1998).

81. Shi, W., Zhou, L., Song, S., Yang, J. & Zhang, H. Hydrothermal synthesis and thermoelectric transport properties of impurity-free antimony telluride hexagonal nanoplates. Adv. Mater. 20, 1892–1897 (2008).

82. Cao, Y. Q., Zhao, X. B., Zhu, T. J., Zhang, X. B. & Tu, J. P. Syntheses and thermoelectric properties of Bi2 Te3 Sb2 Te3 bulk nanocomposites with laminated nanostructure. Appl. Phys. Lett. 92, (2008).

83. Ibáñez, M. et al. Core-shell nanoparticles as building blocks for the bottom-up production of functional nanocomposites: PbTe-PbS thermoelectric properties. ACS Nano 7, 2573–2586 (2013).

84. Ibáñez, M. et al. Colloidal synthesis and thermoelectric properties of Cu2SnSe3 nanocrystals. J. Mater. Chem. A 1, 1421 (2013).

85. Yang, L., Wu, J. S. & Zhang, L. T. Synthesis of filled skutterudite compound La0.75Fe3CoSb12 by spark plasma sintering and effect of porosity on thermoelectric properties. J. Alloys Compd. 364, 83–88 (2004).

86. Cadavid, D. et al. Organic ligand displacement by metal salts to enhance nanoparticle functionality: thermoelectric properties of Ag2Te. J. Mater. Chem. A 1, 4864 (2013).

87. Pippan, R. et al. Saturation of Fragmentation During Severe Plastic Deformation. Annu. Rev. Mater. Res. 40, 319–343 (2010).

88. Valiev, R. et al. Producing bulk ultrafine-grained materials by severe plastic deformation. JOM 58, 33–39 (2006).

89. Saito, Y., Utsunomiya, H., Tsuji, N. & Sakai, T. Novel ultra-high straining process for bulk materials—development of the accumulative roll-bonding (ARB) process. Acta Mater. 47, 579–583 (1999).

90. Valiev, R. Z. & Langdon, T. G. Principles of equal-channel angular pressing as a processing tool for grain refinement. Prog. Mater. Sci. 51, 881–981 (2006).

91. Im, J.-T., Hartwig, K. T. & Sharp, J. Microstructural refinement of cast p-type Bi2Te3–Sb2Te3 by equal channel angular extrusion. Acta Mater. 52, 49–55 (2004).

92. Hohenwarter, A., Bachmaier, A., Gludovatz, B., Scheriau, S. & Pippan, R. Technical parameters affecting grain refinement by high pressure torsion. Int. J. Mater. Res. 100, 1653–1661 (2009).

93. Sakai, G., Nakamura, K., Horita, Z. & Langdon, T. G. Developing high-pressure torsion for use with bulk samples. Mater. Sci. Eng. A 406, 268–273 (2005).

94. Pippan, R., Scheriau, S., Hohenwarter, A. & Hafok, M. Advantages and Limitations of HPT: A Review. in Mater. Sci. Forum 584-586, 16–21 (2008).

95. Zhao, Y. H. et al. Tougher ultrafine grain Cu via high-angle grain boundaries and low dislocation density. Appl. Phys. Lett. 92, (2008).

96. Asgharzadeh, H. & Kim, H. S. Consolidation of Cu-based amorphous alloy powders by high-pressure torsion. J. Mater. Res. 3164–3174 (2015). doi:10.1007/s10853-015-8877-4

97. Valiev, R. Z., Mishral, R. S., Grozal, J. & Mukherjee, A. K. Processing of nanostructured nickel by severe plastic deformation consolidation of ball-milled powder. Scr. Mater. 34, 1443–1448 (1996).

98. Edalati, K., Horita, Z., Fujiwara, H. & Ameyama, K. Cold consolidation of ball-milled titanium powders using high-pressure torsion. Metall. Mater. Trans. A Phys. Metall. Mater. Sci. 41, 3308–3317 (2010).

99. Edalati, K. & Horita, Z. Application of high-pressure torsion for consolidation of ceramic powders. Scr. Mater. 63, 174–177 (2010).

100. R.W. Douglas H.J. Goldsmid. The use of semiconductors in thermoelectric refrigeration. Br. J. Appl. Phys. 5, 386 (1954).

101. Schultz, J. M., McHugh, J. P. & Tiller, W. a. Effects of Heavy Deformation and Annealing on the Electrical Properties of Bi2Te3. J. Appl. Phys. 33, 2443 (1962).

102. Ionescu, R., Jaklovszky, J., Nistor, N. & Chiculita, A. Grain size effects on thermoelectrical properties of sintered solid solutions based on Bi2Te3. Phys. status solidi 27, 27–34 (1975).

103. Horák, J., Čermák, K. & Koudelka, L. Energy formation of antisite defects in doped Sb2Te3 and Bi2Te3 crystals. J. Phys. Chem. Solids 47, 805–809 (1986).

104. Navrátil, J., Starý, Z. & Plecháček, T. Thermoelectric properties of p-type antimony bismuth telluride alloys prepared by cold pressing. Mater. Res. Bull. 31, 1559–1566 (1996).

105. Zhang, Z., Sharma, P. a., Lavernia, E. J. & Yang, N. Thermoelectric and transport properties of nanostructured Bi2Te3 by spark plasma sintering. J. Mater. Res. 26, 475–484 (2011).

106. Zhao, L. D., Zhang, B.-P., Liu, W. S., Zhang, H. L. & Li, J.-F. Effects of annealing on electrical properties of n-type Bi2Te3 fabricated by mechanical alloying and spark plasma sintering. J. Alloys Compd. 467, 91–97 (2009).

107. Jiang, J., Chen, L., Bai, S., Yao, Q. & Wang, Q. Thermoelectric properties of p-type (Bi2Te3)x(Sb2Te3)1−x crystals prepared via zone melting. J. Cryst. Growth 277, 258–263 (2005).

108. Kim, D.-H. & Mitani, T. Thermoelectric properties of fine-grained Bi2Te3 alloys. J. Alloys Compd. 399, 14–19 (2005).

109. Hu, L., Zhu, T., Liu, X. & Zhao, X. Point defect engineering of high-performance bismuth-telluride-based thermoelectric materials. Adv. Funct. Mater. 24, 5211–5218 (2014).

110. Kim, D. H., Kim, C., Je, K.-C., Ha, G. H. & Kim, H. Fabrication and thermoelectric properties of c-axis-aligned Bi0.5Sb1.5Te3 with a high magnetic field. Acta Mater. 59, 4957–4963 (2011).

111. Ashida, M. et al. Texture of bismuth telluride-based thermoelectric semiconductors processed by high-pressure torsion. J. Phys. Chem. Solids 70, 1089–1092 (2009).

112. Eilertsen, J., Subramanian, M. A. & Kruzic, J. J. Fracture toughness of Co4Sb12 and In0.1Co4Sb12 thermoelectric skutterudites evaluated by three methods. J. Alloys Compd. 552, 492–498 (2013).

113. Kim, H. & Hong, S. Microstructure and Thermoelectric Properties of N-type 95%Bi2Te3-5%Bi2Se3 Compound Prepared by High Energy Milling and Hot Extrusion. Curr. Nanosci. 10, 118–122 (2014).

114. Jiang, J., Chen, L., Bai, S., Yao, Q. & Wang, Q. Thermoelectric properties of textured p-type (Bi,Sb)2Te3 fabricated by spark plasma sintering. Scr. Mater. 52, 347–351 (2005).

115. Shin, H. S., Ha, H. P., Hyun, D. Bin, Shim, J. D. & Lee, D. H. Thermoelectric properties of 25%Bi2Te3-75%Sb2Te3 solid solution prepared by hot-pressing method. J. Phys. Chem. Solids 58, 671–678 (1997).

116. Zhao, L.-D. et al. Thermoelectric and mechanical properties of nano-SiC-dispersed Bi2Te3 fabricated by mechanical alloying and spark plasma sintering. J. Alloys Compd. 455, 259–264 (2008).

117. Chen, S. & Ren, Z. Recent progress of half-Heusler for moderate temperature thermoelectric applications. Mater. Today 16, 387–395 (2013).

118. Birol, H., Renato Rambo, C., Guiotoku, M. & Hotza, D. Preparation of ceramic nanoparticles via cellulose-assisted glycine nitrate process: a review. RSC Adv. 3, 2873 (2013).

119. Sklenicka, V., Dvorak, J., Svoboda, M., Kral, P. & Kvapilova, M. Equal-Channel Angular Pressing and Creep in Ultrafine- Grained Aluminium and Its Alloys. InTech Open Access J. 3–46 (2013). doi:1372CEA0E1BB853588B8A84E3AE0450E

120. Keshavarz, M. K., Vasilevskiy, D., Masut, R. A. & Turenne, S. p-Type Bismuth Telluride-Based Composite Thermoelectric Materials Produced by Mechanical Alloying and Hot Extrusion. J. Electron. Mater. 42, 1429–1435 (2013).

121. Tong, Y., Yi, F., Liu, L., Zhai, P. & Zhang, Q. Molecular dynamics study on thermo-mechanical properties of bismuth telluride bulk. Comput. Mater. Sci. 48, 343–348 (2010).

Chapter 3 Materials and Experimental Techniques

This chapter describes the methods that have been employed to produce ultrafine grained and highly oriented Bi_2Te_3 based thermoelectric materials by means of severe plastic deformation (section 3.1). Section 3.2 relates the techniques that were used to characterize the microstructure, phases and micro/macro-texture. Finally, sections 3.3 and 3.4 describe respectively the methods and systems that were used to determinate the thermoelectric and the mechanical properties of the produced materials.

3.1. Nanostructuring $Sb_{2-x}Bi_xTe_3$ by High-Pressure Torsion (HPT)

3.1.1. Raw materials and production of $Sb_{2-x}Bi_xTe_3$ alloys

High-purity Bi_2Te_3 (99.999 %, < 1 mm, American Elements) and Sb_2Te_3 (99.99%, < 149 μm, Hainhang industry Co., Ltd.) were used as raw material. In order to prepare $Sb_{2-x}Bi_xTe_3$ alloys, the starting powders (Bi_2Te_3 and Sb_2Te) were weighed, mixed in a three-dimensional shaker-mixer and cold pressed by a hydraulic press applying a uniaxial pressure of 200 MPa. After that, the pressed pieces were loaded into a carbon coated silica tube and sealed in vacuum (below 10^{-4} mbar). The pieces were melted at 980 K for approximately 24 h, and them the molten alloy was rapidly cooled into an ingot. The as-solidified ingot was hand-milled into powders using an agate mortar.

3.1.2. Consolidation techniques

3.1.2-1 Hot-pressing (HP)

The hot pressing (HP) method was used to consolidate the fine powders. HP enables to consolidate powder into bulk by applying a uniaxial pressure (usually ranges from 40 to 80 MPa) at a relative high temperature. The fine powders were placed into a graphite die; the graphite punches in contact with the sample were covered by a layer of boron nitride to avoid any reaction with the sample. A Sintris 10STV model was used (figure 3.1). The HP machine heats mainly by heating wires, but also by applying a low intensity DC current through the die. In this study, $Sb_{2-x}Bi_xTe_3$ powders were compacted by HP at 723 K under an axial compressive stress of 40 MPa in Ar atmosphere. Holding time under load was 3 min.

Figure 3.1: Hot- pressing machine (Sintris 10STV) employed for powder consolidation.

3.1.2-2 Direct powder consolidation by High-Pressure Torsion

HPT technique was used to get ultrafine-grained and fully dense $Sb_{2-x}Bi_xTe_3$ samples. The powder consolidation was performed in a home-made HPT machine located at the Erich Schmid Institute of Materials Science (ESI) (Leoben, Austria). The HPT tool has a load capacity of 400 kN. The tool is also equipped with an induction heating system and with liquid nitrogen based cooling system which enables processing the powders or bulk samples between -196° C and 700° C. In this study $Sb_{2-x}Bi_xTe_3$ powders were fabricated by HPT under the following parameters:

- Hydrostatic pressure: 2.5-5 GPa
- Temperature:200-350 ° C
- Equivalent strain (von Mises criterion): ~90
- Strain rate:~ 0.12 s^{-1}

3.1.2-3 Two-step approach HP+HPT

HPT was used as a "top-down" approach to produce ultrafine grained Bi_2Te_3 based alloys. HP disks were processed between 423 K and 523 K by HPT under a hydrostatic pressure close to 3 GPa. The disks were deformed by applying 5 revolutions (nominal strain rate ~0.1-0.3 s^{-1}). The applied maximum plastic shear strain was about 160 at the disk rim (Von Mises tensile equivalent true strain of about 90). In this work, three different home-made HPT tools were used (figure3.2). Their most significant technical parameters are summarized in table 3.I.

Table 3.I: Summary of the most significant technical parameters of the used HPT tools.

	Load Capacity (kN)	**Temperature range (° C)**	**Heating system**
HPT CEIT	520	RT-150	Resistive (Joule effect)
HPT "small" ESI	400	-196-700	Induction
HPT "large" ESI	4000	RT-350	Induction

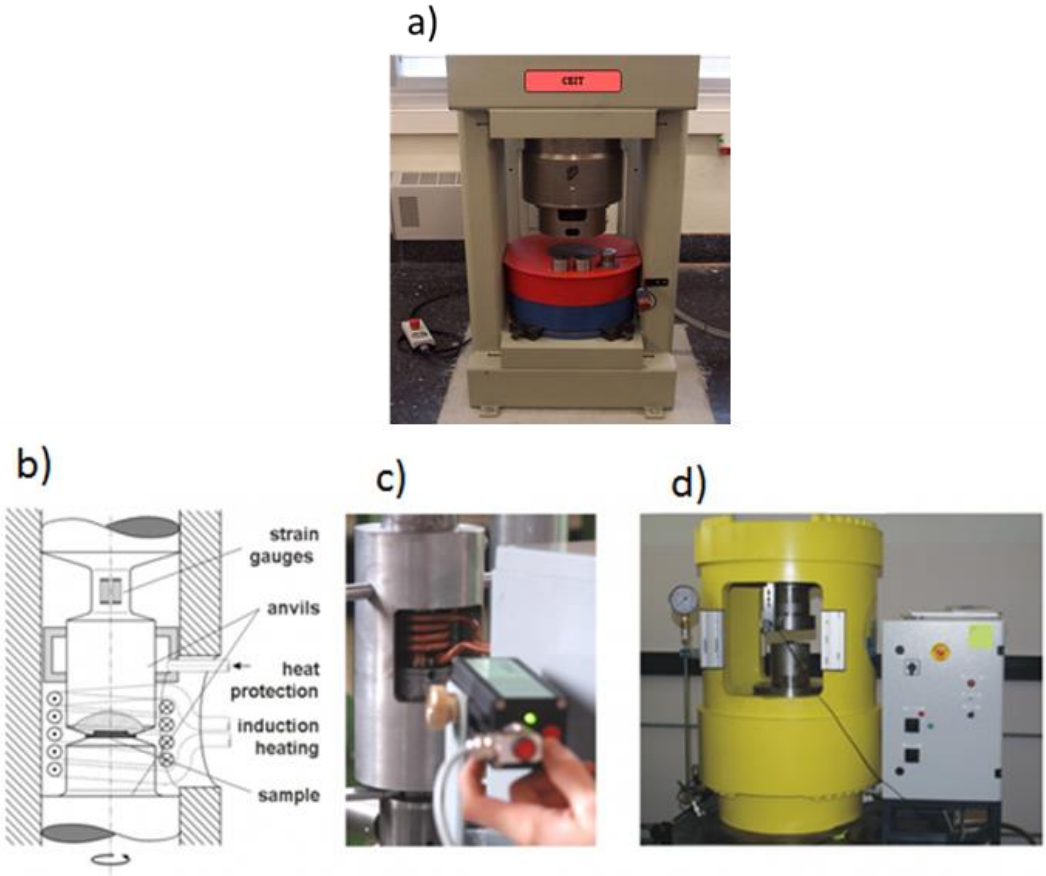

Figure 3.2: a) Image of the HPT tool located at CEIT. Load capacity 520 kN. b) Scheme of the "small" HPT tool with a load capacity of 400 kN. Heating with induction heating or cooling with liquid nitrogen enables processing between -196° C and 700° C. c) Image of the "small" HPT tool during an experiment. d) "Large" HPT tool (located at ESI) with a load capacity of 4 MN.

3.2. Characterization of microstructure, chemical composition, and crystallographic texture

This section summarizes the different techniques that were used to carry out the chemical and microstructural characterization.

3.2.1. Metallographic preparation

Samples were ground with 1200 and 4000 SiC paper. After that, they were polished using a 6, 3 and 1 µm liquid based diamond suspension. Finally, a prolonged (~ 2h) polishing with colloidal silica was performed.

3.2.2. X-Ray Diffraction (XRD)

To determine the phases of the Bi_2Te_3 bases alloys, a Philips 1PW 1825 diffractometer with copper $K_{\alpha 1}$ wavelength (1.540562 Å), equipped with ICDD software was utilized. The accelerating voltage and current were 40 kV and 40 mA, respectively.

The obtained diffractogram was also used to determinate the orientation factor (*OF*) (i.e. the degree of alignment of the crystallographic *c* planes with respect to the torsion axis), which was estimated by the Lotgering method[1]: $OF = (P - P_0)/(1 - P_0)$; $P = \sum I(00l) \Big/ \sum I(hkl)$; where P and P_0 are constant coefficients which were obtained by dividing the sum of the integrated areas of all (00l) planes and all (hkl) planes for the preferentially oriented (bulk samples) and randomly oriented samples (raw powder), respectively.

3.2.3 Scanning electron Microscopy (SEM)

The scanning electron microscope investigations were performed at high-resolution field emission gun scanning electron microscopes (FEG-SEM, see Table 3.II). The main difference between a conventional SEM and an FEG-SEM is to be found in its filament. In the first one, the electrons emission source is a thermionic filament while in the second one; the electrons are extracted by applying a strong electric field at the tip of the filament. The capacity to extract electrons is much higher by applying an electric field than by heating. That means that the brightness and stability in the electron beam are greater for field emission gun. The nominal resolution at 30 kV for SEM and FEG-SEM is of around 10 nm, and 1.2 nm respectively.

The microscopes used in this work are also equipped with Electron Backscatter Diffraction (EBSD- Oxford HKL Channel 5 equipped with a Nordlys II detector) and Energy Dispersive Spectroscopy (EDS – INCA Energy 350, Oxford Instruments). Both techniques will be described in the next sections.

The different scanning electron microscopes that were used in this thesis work are summarized in table 3.II.

Table 3.II: Description of SEM microscopes used in this thesis work.

SEM model	Filament type	EDS	EBSD	FIB* Gun	Location
Philips XL30cp	Thermionic	YES	YES	NO	CEIT
JEOL JSM-700 F	Schottky FEG	YES	YES	NO	CEIT
FEI Quanta 3D FEG	Schottky FEG	YES	NO	YES	CEIT
Zeiss Leo 1525	Schottky FEG	YES	YES	NO	ESI

* Focused ion beam (see section 3.2.7)

3.2.4. Energy Dispersive Spectroscopy (EDS)

Energy Dispersive X-Ray Analysis (EDS) is an x-ray technique used to identify and semi-quantify the elemental composition of materials. In an electron column, electrons acquire kinetic energy as a result of being accelerated through an electric field. This energy is dissipated in the sample which yields a variety of signals for analysis (figure 3.3 a). When, the electron beam interacts with the sample, electrons may be scattered inelastically by the coulomb field of an atomic nucleus losing some or all of their energy. Since, electrons are charged particles and they suffer a deceleration, they emit an electromagnetic radiation. In this particular case, the emitted radiation is in form of X ray-radiation, called bremsstrahlung. Since the incident electron can give up any amount of its energy, the energy distribution of the emitted x-rays is continuous. However, the incident electrons are also capable of ejecting an electron from an inner atomic shell. This phenomenon results in an ion in an excited state. To return to its normal ground state, an electron from an outer shell fills the hole, and the difference in energy between the higher-energy shell and the lower energy shell is released in the form of an X-ray. Each drop results in a loss of a specific amount of energy (characteristic for each element), which is equal to the energy difference between the vacant shell and the shell contributing the electron. The intensity and energy of the X-rays emitted from the specimen can be measured by an energy-dispersive spectrometer. The identification of the lines in the spectrum enables the qualitative analysis of the elements, while determination of the concentrations of the elements in the sample entails measuring the line intensities for each element.

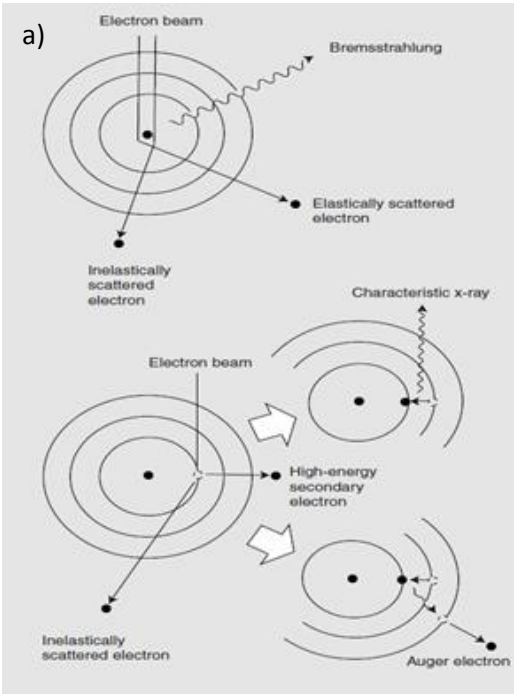

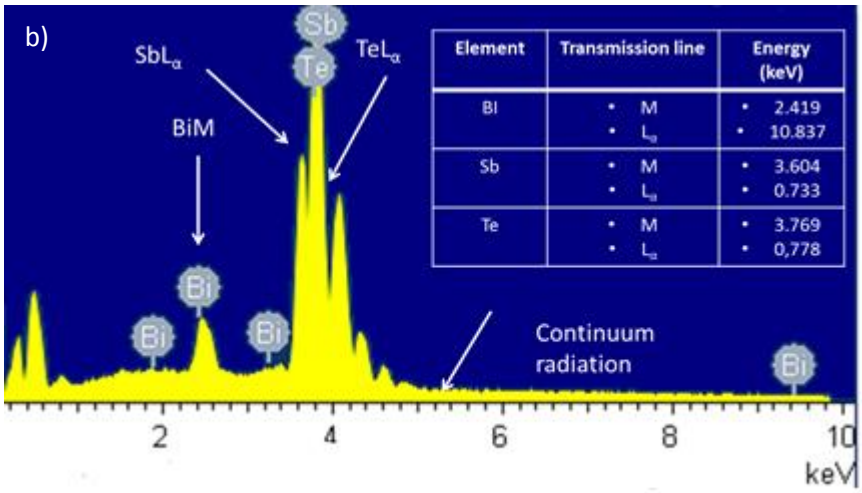

Figure 3.3: a) Schematic illustration of the principal results of the interaction of an electron beam with a specimen. b) An example of a typical EDS spectrum. Continuum radiation and the characteristic x-rays peaks of the elemental elements which are present in the sample can be also observed.

3.2.5 Determination of the Oxygen content by inert gas fusion technique

A LECO TC-400 Series Oxygen/Nitrogen fusion analyzer was used to determine the Oxygen content of the $Sb_{2-x}Bi_xTe_3$ powders. Prior to conducting the measurements, purges to remove the oxygen present in the circuit were performed with ultrapure helium. This gas was also used as the carrier gas. Further verification of the calibration curve was carried out with a pattern. The powders were weighed, placed on tin foil cups and inserted into a nickel basket to act as fluxing agent. The basket is then charged into the analyzer and this, in turn, in a graphite crucible which will react with the oxygen content of the sample at high temperatures (2000° C) forming CO and CO_2. CO is transformed to CO_2 by a catalyst and the amount of Oxygen is determined by an infrared detector for CO_2.

3.2.6 Electron BackScatter Diffraction (EBSD)

Electron Backscatter diffraction (EBSD) is a well-established scanning electron microscopy technique that allows determining simultaneously the crystallographic phase and orientation of crystalline samples. Figure 3.4 is an illustration that shows the main components of the EBSD system. Those components can be enumerated as follows:

- Scanning electron microscope (SEM)
- A phosphor screen which is fluoresced by electrons from the sample to form the diffraction pattern.
- CCD camera to record the diffraction patterns captured by the phosphor screen.
- Software for acquisition and analysis of the data.

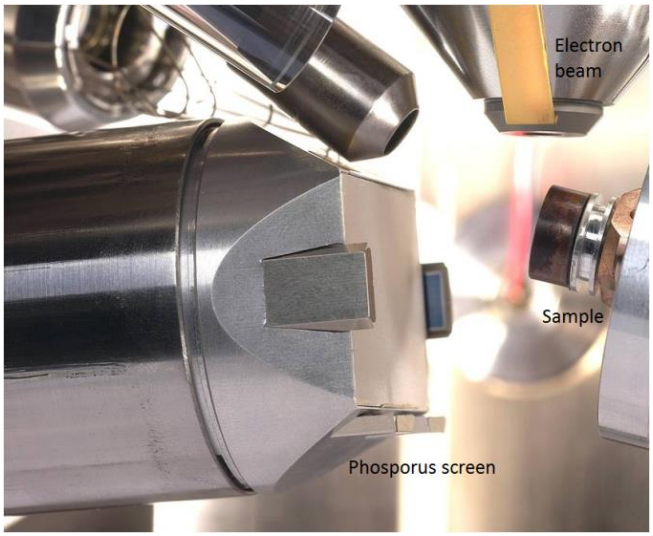

Figure 3.4: Image of the main components of a typical EBSD set up.

EBSD technique is based on indexing the so-called Kikuchi patterns to determine the crystallographic orientation and phase in all scanned points. When a high energetic electron beam interacts with a crystalline sample, the atoms in the material inelastically scatter a fraction of the electrons. Consequently, the incident electrons suffer a small loss of energy and they form a divergent source of electrons close to the surface of the sample. Some of these electrons diffract on the atomic planes at angles which satisfy the Bragg equation:

$$n\lambda = 2d\sin(\theta) \qquad (3.1)$$

Where n is an integer, λ is the wavelength of the electrons, d is the spacing of the diffracting plane, and θ is the angle of incidence of the electrons on the diffracting plane. These electrons are diffracted forming paired large angle cones that correspond to each diffracting plane. When the phosphor screen of the EBSD camera is positioned so as to intercept the diffraction cones, the regions with enhanced electron intensity between the cones

produce the characteristic Kikuchi bands of the electron backscatter diffraction pattern (see figure 3.5).

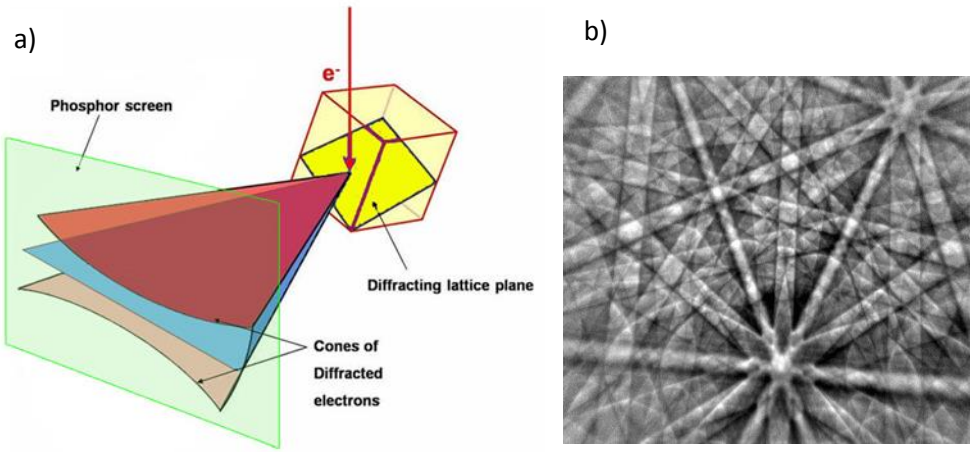

Figure 3.5: a) Formation of the electron backscattered diffraction pattern. Electrons from a divergent source incident on the crystallographic planes at the Bragg angle are diffracted into a pair of cones forming Kikuchi bands in the diffraction pattern[14] b) Example of a EBSD diffraction pattern.

Since each Kikuchi band corresponds to a determinate crystallographic plane, they can be indexed by the Miller indices. The intersections of the Kikuchi bands correspond to a zone axis (the common direction shared between two crystal planes when they intersect). In practice, the Kikuchi bands are detected through image analysis algorithms (usually applying Hough transform algorithms) and identified automatically to determine the crystal structure and calculate the orientation relationship between the crystal reference system and the microscope reference system.

Summarizing, as diffraction patterns are closely related to the crystal structure of the sample, when the crystal orientation changes, the resultant diffraction pattern also changes.

3.2.7 Focused Ion Beam (FIB)

The microscope used in this thesis work was a Dual Beam Quanta 3D FEG-SEM/FIB located at CEIT. The equipment is composed by an electron and a Gallium ion gun which are tilted one respect to the other 52 ° (see figure 3.6). The electron gun works as a conventional FEG-SEM, while ions are extracted from a liquid gallium metal ion source (melting-point Ga 302.93 K). The extracted Ga^+ ions are accelerated by a high electric field, subsequently they are aligned and finally, they are focused by a series of apertures and electrostatic lenses into the site of interest. In the present equipment, the accelerating voltage and the current beam are in the range of 2 kV to 30 kV and 1 pA to 65 nA, respectively. The system is also equipped with an OmniProbe 200 micromanipulator, which enables the preparation of thin lamellas for Transmission Electron Microscopy (TEM).

During this work, the Dual Beam was used for the following proposes:

- Microstructure characterization, i.e. it was used as a conventional FEG-SEM
- Preparation of thin lamellas, via FIB "lift-out" technique[2], for posterior TEM observation.
- Fabrication of micro-samples for performing micro-mechanical tests.

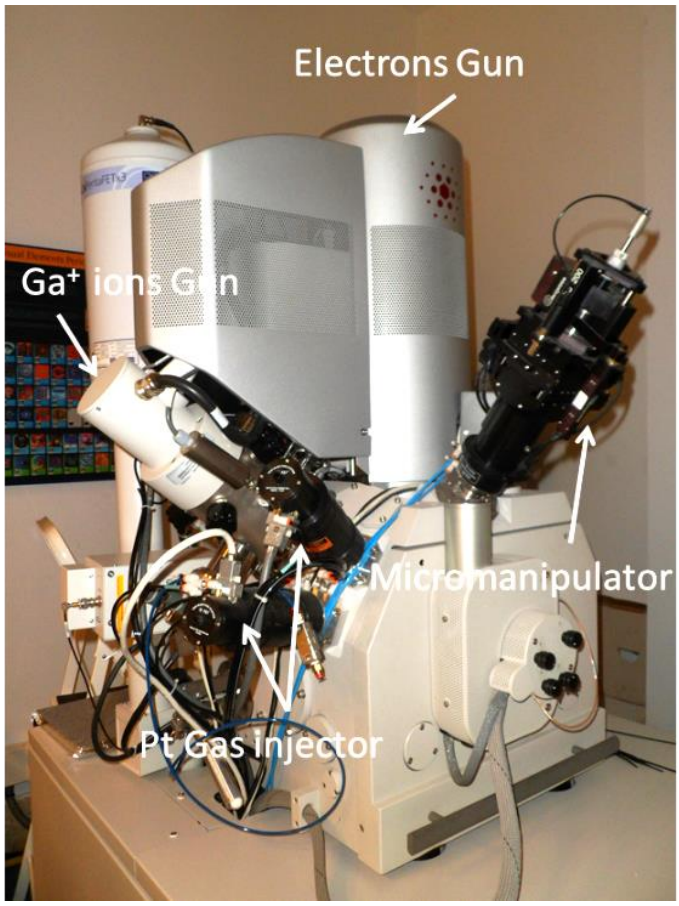

Figure 3.6: FIB equipment located at the materials department of CEIT. Model: Dual Beam Quanta 3D FEG-SEM/FIB from FEI.

3.2.8. Transmission Electron Microscopy (TEM)

Transmission Electron Microscopy (TEM) investigations were carried out in order to investigate the microstructures of severely plastically deformed (SPD) samples. For sample characterization, a JEOL JSM-2100 operated at 200 kV with a LaB_6 was used (figure3.7)

Figure 3.7: TEM equipment located at the materials department of CEIT. Model: JEOL JSM-2100

3.3. Thermoelectric characterization

As aforementioned, the efficiency of thermoelectric devices is determined by its dimensionless figure-of-merit (*ZT)* (see equation 1.11). However, it is not common to evaluate *ZT* of a thermocouple. It is more convenient to define the dimensionless thermoelectric figure of merit (*zT*) of a single element, defined as $zT = \frac{S^2\sigma}{\kappa}T$, where *S*, σ, κ and *T* are the Seebeck coefficient, the electrical conductivity, the thermal conductivity, and the absolute temperature at which the properties are measured, respectively.
To evaluate the efficiency of the fabricated TE materials all those magnitudes were determined by the methods described in this section. . The measurement uncertainty of *S*, σ, κ are respectively $\pm 3.5\,\%, \pm 5\,\%$, and ± 3.5 %. Therefore, the combined uncertainty for the experimental determination of *zT* is ~ $\pm$ 10-15 %.

3.3.1. Characterization of Seebeck coefficient and electrical resistivity.

Seebeck coefficient and electrical resistivity were simultaneously measured using the Linseis LSR-3 800 apparatus. Figure 3.8 shows the schematic diagram of the LSR-3 800 equipment. As it is shown, the system has a primary furnace that heats the sample. The equipment located at CEIT enables to determine *S* and ρ in the temperature range from RT to 800° C. Infrared quartz lamps are used to heat the sample, while temperature control was carried out by platinum/rhodium (Pt/Rh) thermocouples.
The sample is placed between two platinum electrodes and when the desired temperature is reached the secondary heater placed in the lower electrode block creates a set temperature gradient. Two contacting Pt/Rh thermocouples then measure the temperature gradient (ΔT) by determining the temperature of the sample at points 1 and 2. Using the same thermocouples, the generated Seebeck voltage (ΔV) is measured. Thus, the Seebeck coefficient relative to platinum electrodes is given by:

$$S_{SP} = \frac{\Delta V}{\Delta T} \qquad (3.2)$$

Since the absolute Seebeck coefficient of platinum (S_P) is well-known[3], the absolute Seebeck coefficient of the evaluated sample (S_S) can be easily subtracted as follows:

$$S_{SP} = S_S - S_P \rightarrow S_S = S_{SP} + S_P \qquad (3.3)$$

Thus, based on the static *dc* method, the absolute Seebeck coefficient was measured.

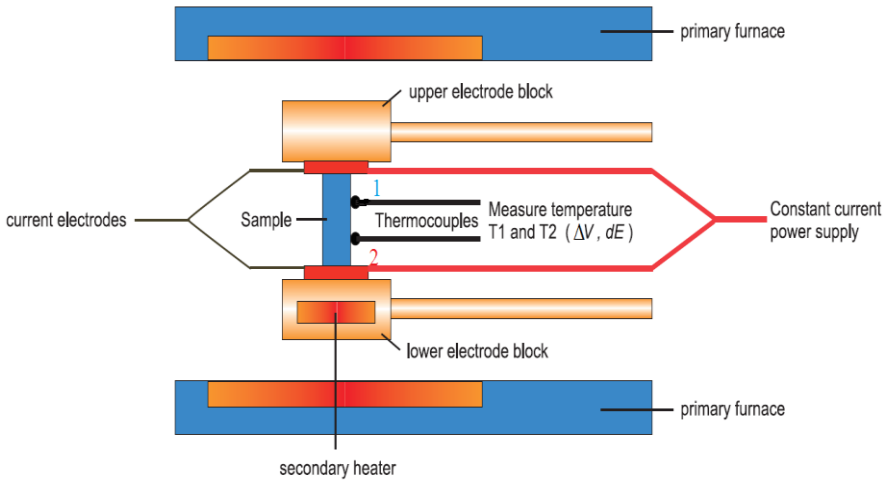

Figure 3.8: Schematic diagram of the LSR-3 800 equipment used to determinate simultaneously the absolute Seebeck coefficient and electrical conductivity.

The electrical resistivity was measured by means of the standard four-probe technique[4]. The method consists in applying a constant dc current (I) at both ends of the sample and measure the voltage drop (ΔV) between points *1* and *2*. If the contact is ohmic (this fact can be checked prior to testing by varying the intensity of the power supply and measuring the voltage drop.) the electrical resistance if given by:

$$R = \frac{\Delta V}{I} \qquad (3.4)$$

Thus, knowing the sample resistance and its shape and size, the electrical resistivity (ρ) can be assessed by the following expression:

$$R = \rho \frac{l}{A} \qquad (3.5)$$

Where *l* is the distance between the contact points *1* and *2*, and *A* is the cross-sectional area of the specimen.
In order to generate a suitable temperature gradient in the sample and avoid oxidation, the measurements were carried out under helium atmosphere.

3.3.2. Thermal conductivity

Steady-state thermal conductivity measurements become increasingly difficult as the temperature becomes higher because of the rapidly rising radiation factor (radiation factor $\propto T^4$). Consequently, the thermal diffusivity (*D*) is often determined instead of the thermal conductivity.
D is defined by the following relation:

$$D = \frac{\kappa}{C_p d} \qquad (3.6)$$

Where, κ is the thermal conductivity, *d* is sample density, and C_p is the heat capacity.

To determinate *D* of the samples, the laser flash method (LFA 457 Microflash, Netzsch) was used. A picture of the equipment and its most essential components are shown in figure 3.9. In the laser flash system, one of the faces of the sample is irradiated by a pulsed laser and the fluctuations

in temperature at the opposite face are registered by an infrared sensor. Then, the temperature rise at the back surface is compared with that which is reached in the steady state when the sample is continuously heated. The time, $t_{1/2}$, taken to reach one-half of the steady-state temperature rises can be used to determine D as shows equation 3.7 [5]:

$$D = \frac{1.37T^2}{\pi^2 t_{½}} \qquad (3.7)$$

Where, T is the thickness of the evaluated sample.

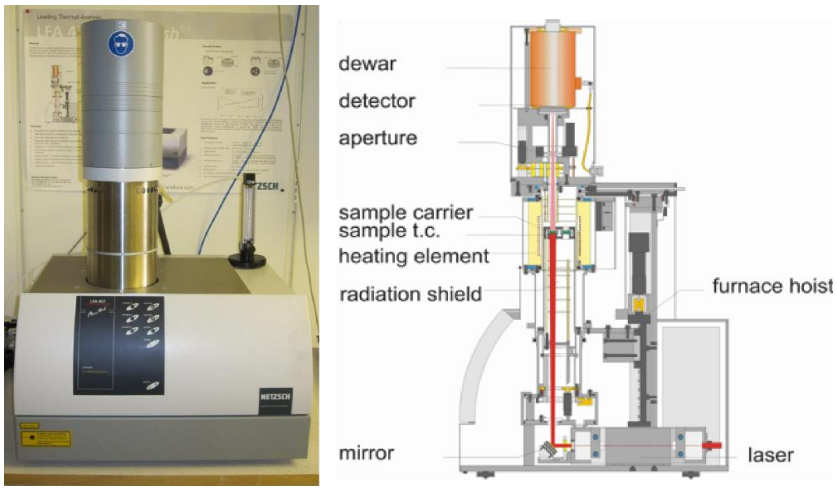

Figure 3.9: Netzsch LFA 457 Microflash apparatus together with an illustration of its essential components.

Thus, κ was obtained through equation 3.6. The density (d) was measured at room temperature by water immersion technique (Archimedes' method). For calculating the density in all the temperature range between room temperature and 473 K, the thermal expansion of Bi_2Te_3 was taken into account by using the equation proposed by Pavlova et al[6]. The specific heat (C_p) was estimated according to the literature[7], and it was in good accordance with indirectly derived values using a Pyroceram 9606 standard.

Measurements were performed under argon atmosphere. To improve the emissivity of the samples, they were coated with a graphite film before testing.

3.4. Mechanical characterization

3.4.1. Microhardness

Vickers microhardness HV measurements were performed with a LECO M-400-G2 microhardness tester at a maximum load of 0.2 kgf (1.96 N). The equipment has a diamond pyramidal tip (136° between opposite faces).
At least twenty repeated measurements were made for Hot Pressed samples. To account the strain-dependence of hardness of HPT samples (equation 1.23) Vickers hardness measurements were performed along the diameter of the disk.

3.4.2. The ball on three balls (B3B) test

The ball on three balls (B3B) test[8] was carried out to determine the strength of the fabricated samples. As figure 3.10 shows, in the B3B test a disk-shape specimen is supported on three balls that are placed equidistantly from the disk center. The center of the opposite face is loaded with a fourth ball normal to the disk plane and the fracture load is measured.

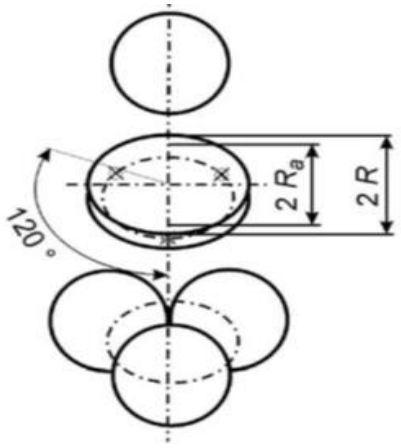

Figure 3.10: Scheme of the 3 ball on three balls test

To reduce the parameters that have influence on the test, all balls have the same size and the three supporting balls touch each other. Since the supporting balls are placed equidistantly, their contact points with the sample form an equilateral triangle. Its circumradius is known as the support radius of the disk (R_a). To define the strength, the maximum principal tensile stress (σ_{max}) in the disk is evaluated. σ_{max} is given by the following equation:

$$\sigma_{\max} = f \frac{F}{t^2} \qquad (3.8)$$

Here, f is a dimensionless factor, F is the applied force, and t is the thickness of the tested disk. According to A. Börger et al[8]. f can be approximated by:

$$f\left(\frac{t}{R}, \frac{R_a}{R}, \nu\right) = c_0 + \frac{\left(c_1 + c_2 \frac{t}{R} + c_3\left(\frac{t}{R}\right)^2 + c_4\left(\frac{t}{R}\right)^3\right)}{1 + c_5 \frac{t}{R}} \times \left(1 + c_6 \frac{R_a}{R}\right) \qquad (3.9)$$

Where R is the radius of the disk and c_0 to c_6 are coefficients that depend on the Poisson's ratio (ν) (see table 3.III).

Table 3.III: Values of the dimensionless c_i constant calculated by A. Börger et al.[8]

	ν=0.2	**ν=0.25**	**ν=0.3**	**ν=0.35**
$\mathbf{c_0}$	-12.354	-14.671	-17.346	-20.859
$\mathbf{c_1}$	15.549	17.988	20.774	24.403
$\mathbf{c_2}$	489.2	567.22	622.62	716.41
$\mathbf{c_3}$	-78.707	-80.945	-76.879	-76.16
$\mathbf{c_4}$	52.216	53.486	50.373	49.615
$\mathbf{c_5}$	36.554	36.01	33.736	32.553
$\mathbf{c_6}$	0.082	0.0709	0.0613	0.0523

The tests were performed at constant displacement rate (0.05 mm/min) at a commercial tensile/compression testing machine (Instron Mini 44)

3.4.3. Nanoindentation

Nanoindenation tests were performed using a Nano Indenter® II (Agilent, formerly Nano Instruments, Inc.,) with a Berkovich tip, a three-sided diamond pyramid. The tests were carried out under a constant deformation rate $(\dot{h}/h)$ of 0.1 s^{-1} until reaching a maximum load of 1 mN or 8 mN. In order to assess both, Young's modulus and nanohardness, by the technique proposed by Oliver and Pharr[9] at least 40 indentations were performed for each sample and load.

The experimental parameters needed to determine the nanohardness and Young's modulus are shown in figure 3.11.

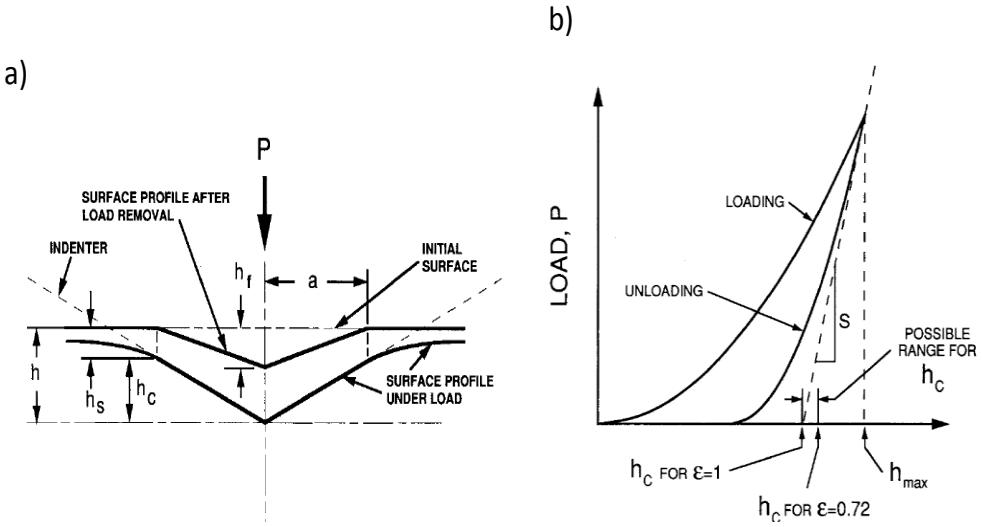

Figure 3.11: a) Schematic representation of a cross-section of an indentation showing various quantities used in the data analysis. b) An example of a typical load versus indenter displacement graph showing quantities used in the data analysis.

According to the method, the value of the initial unloading slope can be used to determine the reduced modulus of the sample (E_r) if the contact area of the peak load can be measured independently.

The unloading curves can be accurately described by the following power law relation:

$$P = \mathrm{B}(h - h_f)^m \qquad (3.10)$$

Where P is the load, (h-h_f) is the elastic displacement, and B and m are constant values. The unloading stiffness, S, is then established by differentiating equation (3.10) at the maximum depth of penetration:

$$S = \left(\frac{dP}{dh}\right)_{h=h_{\max}} = \mathrm{B}m(h_{\max} - h_f)^{m-1} \qquad (3.11)$$

The reduced elastic modulus of the tested material; $E_r = \frac{(1-\nu^2)}{E} + \frac{(1-\nu_i{}^2)}{E_i}$ (E and ν are the Young's modulus and Poisson's ratio for the specimen and E_i and ν_i are the same parameter for the indenter; for the employed tip 1050 GPa and 0.2 respectively) can be determined by:

$$E_r = \frac{\sqrt{\pi}}{2}\frac{S}{\sqrt{A}} \quad (3.12)$$

Where A is the projected contact area, which can be determined by the geometry of the indenter (which is carefully calibrated through indentation on fused silica samples) and the depth of contact, h_c (i.e. the geometry of the indenter can be described by an area function $f(h_c)$ that relates the indenter cross-sectional area to h_c).
The contact depth h_c can be calculated as follows:

$$h_c = h_{\max} - \varepsilon\frac{P_{\max}}{S} \quad (3.13)$$

In equation 3.13 $P_{\max}$ is the peak load and ϵ is a constant value which depends on the indenter geometry. For a Berkovich indenter ϵ is equal to 0.75[9].
The area function for a perfect Berkovich indenter is approximately given by $A(h_c) = 24.5h_c^2$. However, indenters used in practical nanoindentation tests are not ideally sharp. In this work, the area function was calibrated by the method proposed by Oliver and Pharr[9] using a fused silica pattern.

To perform accurate nanoindentation tests, it is also important to take into account the load frame compliance. The displacements measured in nanoindentation tests are the sum of the displacements in the specimen and the load frame. In the present thesis work the load-displacement data were

corrected taking into account the load frame compliance. To subtract the load frame compliance a fused silica pattern was employed[9].

In addition to the modulus, the data obtained using the described method can be also used to determine the nanohardness (*H*) of the tested material. *H* can be calculated from:

$$H = \frac{P_{max}}{A} \quad (3.14)$$

Where *A* is the projected area of contact at peak load, which is derived from the area function.

3.4.4. Micro-mechanical tests

Due to the high triaxiality involved during the indentation process there is not direct relationship with other material parameters such as yield stress. In fact, it has been repeatedly shown that there is not a one-to-one correspondence between instrumented sharp indentation and elastic-plastic properties[10–12] Consequently, during this thesis work, additional micro-compression tests[13] were performed to have a better knowledge of the mechanical properties of the fabricated TE materials.

A commercial TriboIndenter® nanoindentation system from Hysitron Inc. was used to carry out *ex-situ* micropillar compression experiments. Pillars of 2 µm in diameter and an aspect ratio close to 2.5 were compressed until a nominal compressive strain of 5% or until failure under a constant displacement rate of 10 nm/s (i.e., at a nominal equivalent strain rate of $2.2 \cdot 10^{-3}$ s^{-1}) using a flat diamond tip of 2.5 µm in diameter. Thanks to the contact scanning mode imaging technique of the nanoindentation system, the indenter tip was accurately centered on the pillar.

3.4.4-1 Sample fabrication

The micro-pillars were fabricated by a FEI Quanta 3D Dual Beam Microscope Focused Ion Beam (FIB)/Field Emission Gun Scanning Electron Microscopy (FEG-SEM) by a two-step process as described by Volkert and Lilleodden[13]: firstly, the surface of the bulk sample was oriented normal to the FIB gun and using concentric annular patterns a cavity of 20 µm in outer diameter was carved leaving a cylinder of inner diameter of 8 µm. The purpose of machining such a large cavity was to ensure no contact of the flat indenter tip with any other surfaces than the micro-pillar. In a second step, the beam current was progressively reduced as decreasing the pillar diameter. So when we finished with the milling process we got several pillars of approximately 2 µm in diameter and 4.5 µm in height. The aim of reducing the beam current was to minimize Ga^+ ion damage, material re-deposition and taper angle of the pillars; the final step was performed using an accelerating beam voltage and a beam current of 30 kV and 10 pA respectively.

3.5. References

1. Lotgering, F. K. Topotactical reactions with ferrimagnetic oxides having hexagonal crystal structures—I. J. Inorg. Nucl. Chem. 9, 113–123 (1959).

2. Giannuzzi, L. a. & Stevie, F. a. A review of focused ion beam milling techniques for TEM specimen preparation. Micron 30, 197–204 (1999).

3. Ozenbas, M. G. and M. P. and M. An instrument for the high temperature measurement of the Seebeck coefficient and electrical resistivity. Meas. Sci. Technol. 25, 55901 (2014).

4. Susa, R. E. and S. M. and Y. J. and R. L. and M. K. and Y. K. and M. Electric Resistivity Measurements of Sb 2 Te 3 and Ge 2 Sb 2 Te 5 Melts Using Four-Terminal Method. Jpn. J. Appl. Phys. 49, 65802 (2010).

5. H.Julian Goldsmith. Introduction to Thermoelectricity. (2010). doi:10.1007/978-3-642-00716-3

6. Pavlova, L. M., Shtern, Y. I. & Mironov, R. E. Thermal expansion of bismuth telluride. High Temp. 49, 369–379 (2011).

7. Landholt-Bornstein. O. Madelung, M. S. and H. W. Numerical Data and Functional Relationships in Science and Technology. (1983).

8. Börger, A., Supancic, P. & Danzer, R. The ball on three balls test for strength testing of brittle discs: Part II: Analysis of possible errors in the strength determination. J. Eur. Ceram. Soc. 24, 2917–2928 (2004).

9. Oliver, W. C. & Pharr, G. M. An improved technique for determining hardness and elastic modulus using load and displacement sensing indentation experiments. J. Mater. Res. 7, 1565–1583 (1992).

10. Tho, K. K., Swaddiwudhipong, S., Liu, Z. S., Zeng, K. & Hua, J. Uniqueness of reverse analysis from conical indentation tests. J. Mater. Res. 19, 2498–2502 (2011).

11. Alkorta, J., Martínez-Esnaola, J. M. & Sevillano, J. G. Absence of one-to-one correspondence between elastoplastic properties and sharp-indentation load–penetration data. J. Mater. Res. 20, 432–437 (2011).

12. Chen, X., Ogasawara, N., Zhao, M. & Chiba, N. On the uniqueness of measuring elastoplastic properties from indentation: The indistinguishable mystical materials. J. Mech. Phys. Solids 55, 1618–1660 (2007).

13. Volkert, C. a. & Lilleodden, E. T. Size effects in the deformation of sub-micron Au columns. Philos. Mag. 86, 5567–5579 (2006).

14. Oxford instruments.. at <http://www.ebsd.com/ebsd-explained/basics-of-ebsd/pattern-formation>

Chapter 4: Chemical, structural and crystallographic characterization

4.1. Introduction

In this chapter, the chemical composition, microstructure and crystallographic texture of the processed thermoelectric (TE) materials is characterized to study the viability of High Pressure Torsion (HPT) to fabricate Bi_2Te_3-based TE materials with a submicron grained (SMG) structure and a strong crystallographic texture.

The combination of the SMG structures together with a strong crystallographic texture is an effective way to maximize the thermoelectric performance of Bi_2Te_3-based materials. Thus, to enhance zT the microstructure, crystallographic texture and chemical composition must be finely tuned.

4.2. Characterization of the raw materials

The starting materials were high-purity powders of Bi_2Te_3 99.999 % (<1 500 μm, American elements) and Sb_2Te_3 99.99% (<500 μm, Haihang Industry Co., Ltd.). As it is shown in figure 4.1 particle size distribution is heterogeneous and their morphology is irregular. This fact facilitates the powder consolidation.

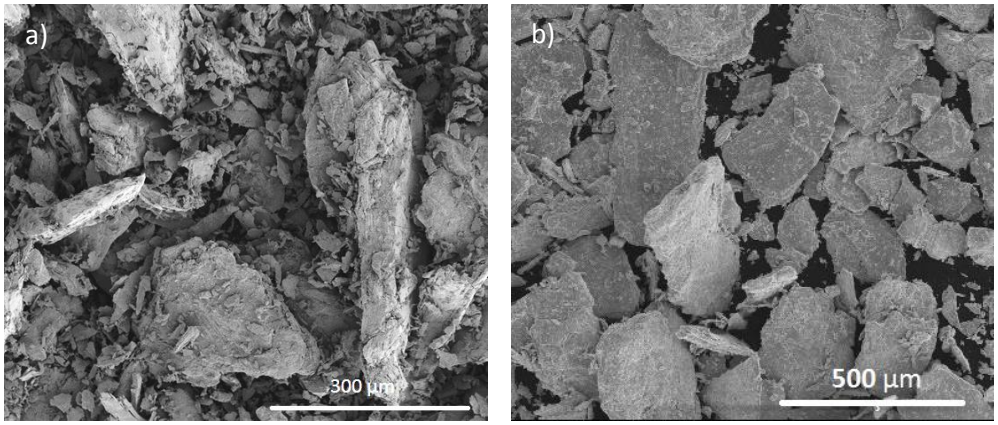

Figure 4.1: SEM micrographs of the raw materials. a) Bi_2Te_3 b) Sb_2Te_3

Bi_2Te_3 has a rhombohedral layered structure, the crystal is composed of atomic layers in the order of Te(1)–Bi–Te(2)–Bi–Te(1) along the *c* axis. Bi–Te(2) and Bi-Te(1) bonds are ionic-covalent type, while bonding between Te(1)–Te(1) layers is due to van der Waals interaction. As a result of the weak van der Waals bonding, Bi_2Te_3 is easily cleaved along the basal plane. Figure 4.4 shows clearly that the powder particles are preferentially fractured along the basal plane.

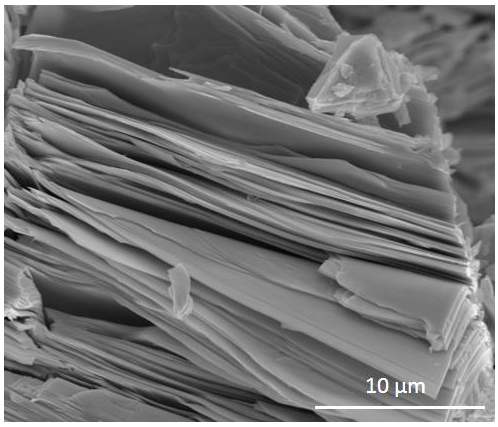

Figure 4.2: High magnification SEM micrographs of a Bi_2Te_3 particle

In order to semi-quantify the chemical composition, Energy Dispersive X-Ray Analysis (EDS), were carried out using an accelerating voltage of 15 kV. The results of the analysis (table 4.I) are very close to the standard composition. However, because the binary phase diagram is quite complex (see figure 4.3) and the Bi_2Te_3 intermetallic is formed in a very narrow composition range, Bi_2Te_3 powders show the presence of a small quantity of a secondary eutectic phase which is composed by pure tellurium element and lamellae of bismuth telluride. Figure 4.2 shows both phases, the white phase, the matrix, is Bi_2Te_3 (spectrum 1);the darker phase (spectrum 2) corresponds to the eutectic phase.

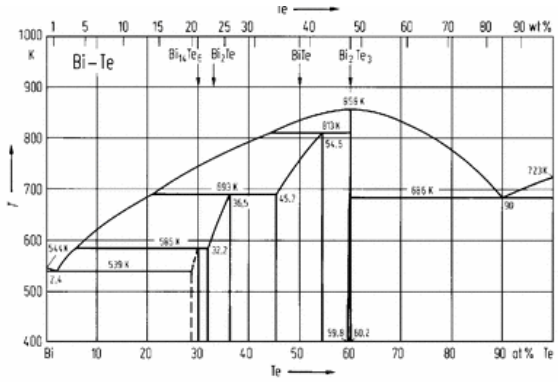

Figure 4.3: Bismuth-Telluride binary phase diagram[43].

Table 4.I: EDS component analysis results of the matrix and the dual phase in at. %

	Matrix	**Dual phase**
Bismuth	49.40 ± 0.5	10.30 ± 0.5
Tellurium	59.5 ± 0.5	89.70 ± 0.5

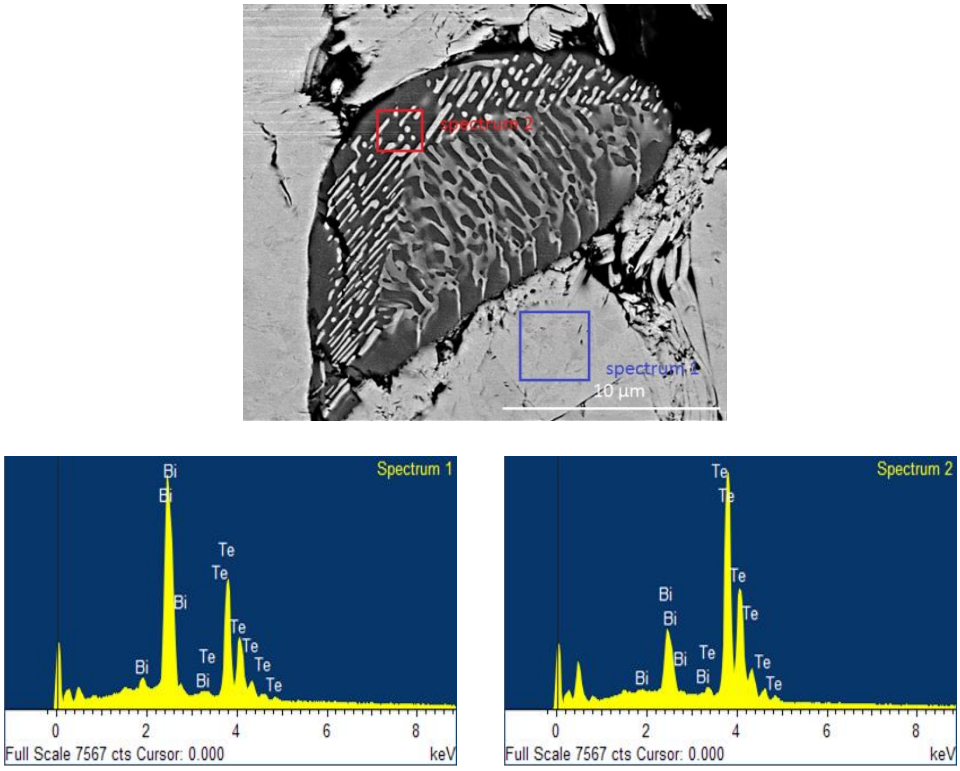

Figure 4.4: SEM micrographs showing both phases, the darker phase (spectrum 2) corresponds to the dual phase while the lighter one corresponds to the Bi_2Te_3 matrix

The presence of this eutecticl phase was not detected by X-Ray Diffraction (XRD) so its total volume fraction must be very low (below the detection threshold of XRD, typically 1%). Figure 4.5 shows the XRD pattern of the Bi_2Te_3 raw powders and all peaks corresponds to Bi_2Te_3 phase.

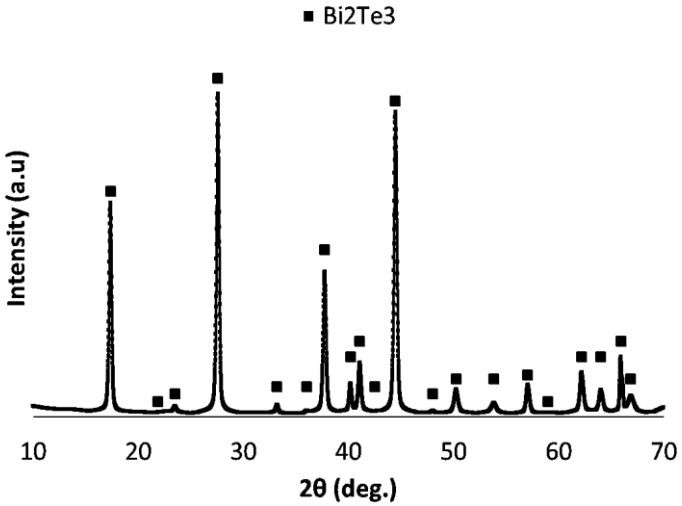

Figure 4.5: XDR pattern of raw Bi_2Te_3 powders. Square markers correspond to the indexed peaks according to 00-018-0863 reference pattern.

4.3. Characterization of $Sb_{2-x}Bi_xTe_3$ compound

After characterizing the morphology and the chemical composition of the raw materials (Bi_2Te_3 and Sb_2Te_3 powders), $Sb_{2-x}Bi_xTe_3$ solid solutions were prepared. For this propose, the starting powders were weighed, mixed in a three-dimensional shaker-mixer and cold pressed by a hydraulic press applying a uniaxial pressure of 200 MPa. After that, the pressed pieces were loaded into a carbon coated silica tube and sealed in vacuum (below 10^{-4} mbar). The pieces were melted at 980 K for approximately 24 h, and them the mellt was cooled into an ingot at different cooling rates:

1. Slow cooling rate (2 K/min)
2. Medium cooling rate (air cooling)
3. Fast cooling rate (quenching in water)

The goal was to obtain a homogeneous ingot with an accurate control of the stoichiometry. However, as I aforementioned controlling tellurium

segregation is not an easy issue at all. Furthermore, adjusting the global chemical composition is also challenging because tellurium sublimes easily due to its low vapor point (10^{-4} Torr at 550 K)[1].

Figure 4.6 shows that the obtained microstructures strongly depend on the cooling rate. In the case of slow cooling rates, the presence of the dual phase is notorious while in the case of rapidly solidified ingots the Te-rich phase is not abundant.

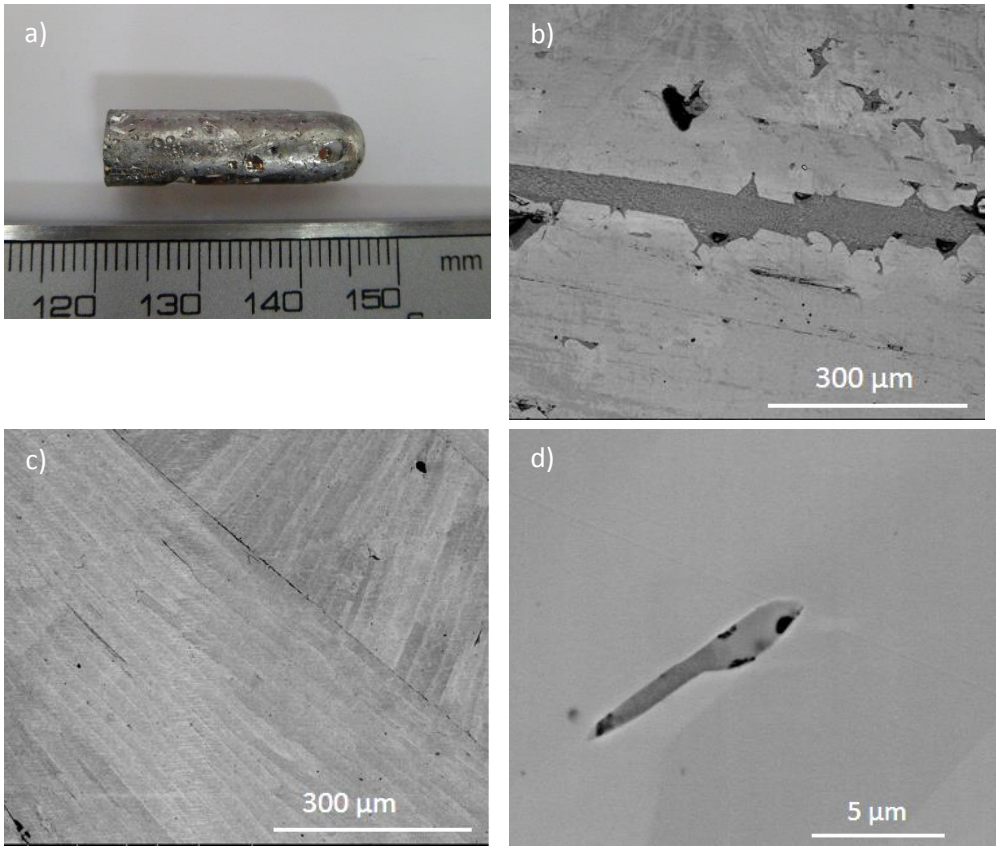

Figure 4.6: a) image of one of the solidified $Sb_{1.6}Bi_{0.4}Te_3$ ingot. b) Low magnification SEM image of the slowly solidified ingots. The presence of the dual phase is notorious in this case. c) Low magnification SEM image of quickly solidified ingots. d) High magnification SEM image of quickly solidified ingots.

In general,to improve the TE efficiency (i.e. dimensionless figure of merit, (*zT*), tellurium-rich phases should be avoided. Custódio and Hernandes[2] measured the Seebeck coefficient (*S)* profile of crystals which were grown by the Bridgman technique. The chemical composition of the obtained crystals was not homogeneous and consequently, *S* was not constant along the entire ingot. They concluded that in the presence of the Tellurium-rich phase the Seebeck coefficient decreases considerably owing to the increase of free carriers. However, very recently Y. Luo et al.[3] have studied the melting and solidification process of $Sb_{1.5}Bi_{0.5}Te_3$ solid solutions under a variable high magnetic field. Their ingots also show Te-rich phases, but in this particular case the morphology of the bismuth antimony telluride matrix and the dual phase (composed by the tellurium (Te) element and the eutectic bismuth antimony telluride) was significantly changed by the extrinsic magnetic field. According to the authors, the high magnetic field activates the nucleation of bismuth antimony telluride alloys and promotes the formation of eutectic bismuth antimony telluride (BST_{II}) nanorods. Te-BST_{II} nanorods interfaces act as an energy filter for conduction holes, scattering the low energy carriers at these interfaces and hence enhancing the Seebeck coefficient as proposed by Faleev et al[4]. Such interfaces are detrimental for carrier mobility; however carrier mobility can be improved by controlling the crystallographic texture. The high magnetic field promotes *c*-axis alignment of $Sb_{1.5}Bi_{0.5}Te_3$ in the direction perpendicular to the magnetic field. It is well known that since the layered crystallographic structure, the mobility in the basal plane is significantly higher than along the *c* axis[5]. Thus, the simultaneous formation of an optimum amount of (BST_{II}) nanorods and the texture enhancement improves the so-called power factor *(PF)* and in the same way reduces the lattice thermal conductivity because BST_{II} nanorods scatter a considerable proportion of the middle to long wavelength phonons. By this way, Luo et al.[3], concluded that when $Sb_{1.5}Bi_{0.5}Te_3$ alloys are solidified under a 2 T magnetic field, both the

electrical and thermal transport properties are optimized reaching an enhanced *zT* value of 1.71 at 323 K.

In our case, the solidification process was carried out without using a magnetic field, therefore; we decided to minimize the formation of the Te-rich phase and consequently the ingots selected for the preparation of our samples were rapidly solidified.
By this process, homogeneous ingots with an accurate control of the stoichiometry were processed. Figure 4.7 shows the micrographs of the EDS spectrums that were carried out at the bottom side and on the top side of the $Sb_{1.6}Bi_{0.4}Te_3$ ingot. The average chemical composition of the ingots is summarized in table 4.II

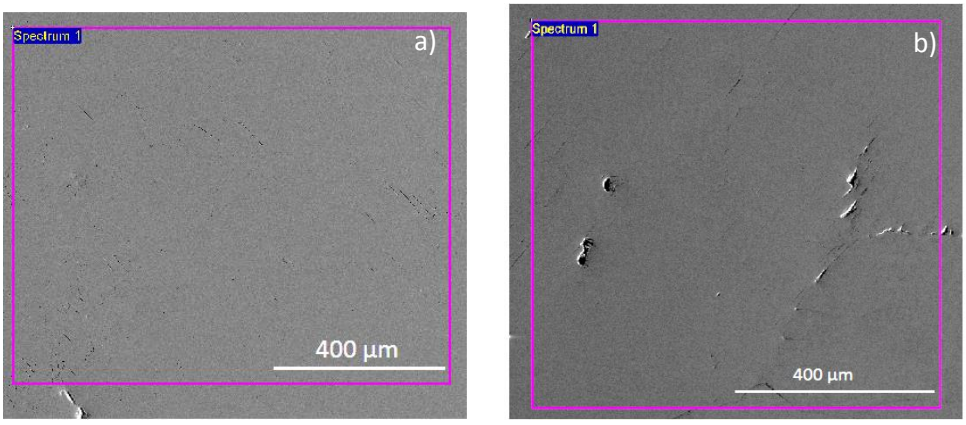

Figure 4.7: Micrographs of the EDS spectrums carried out on the bottom side a) and on the top side (b) of the $Sb_{1.6}Bi_{0.4}Te_3$ ingot.

Table 4.II: nominal composition and EDS results of the processed ingots

Nominal composition	**EDS average composition bottom side (at. %)**			**EDS average composition top side (at. %)**		
$Sb_{1.5}Bi_{0.5}Te_3$	Sb	Bi	Te	Sb	Bi	Te
	31.0 ± 0.4	10.0 ± 0.4	59.0 ± 0.4	31.8 ± 0.4	9.6 ± 0.4	58.7 ± 0.4
$Sb_{1.6}Bi_{0.4}Te_3$	Sb	Bi	Te	Sb	Bi	Te
	32.2 ± 0.2	8.6 ± 0.1	59.2 ± 0.3	32.0 ± 0.1	8.8 ± 0.1	59.1 ± 0.2
$Sb_{1.8}Bi_{0.2}Te_3$	Sb	Bi	Te	Sb	Bi	Te
	36.1 ± 0.2	4.3 ± 0.1	59.8 ± 0.3	36.2 ± 0.2	4.1 ± 0.1	59.6 ± 0.4

The as-solidified ingots were hand-milled (HM) into powders using an agate mortar or by a high-energy ball milling (HEBM) process (1425 rpm, 20 min) under argon atmosphere. During this process oxidation of the powders occurs. The oxygen content of the raw powders and of the crushed and milled ingots was established using the inert gas fusion technique. The results are summarized in table 4.III. The oxygen content in both cases is higher than the measured one in the raw powders; however, after high-energy milling process the oxygen content is an order of magnitude higher. This is due to the increase in the free surface of nanostructured powder after ball milling.

Table 4.III: Oxygen content of the powders measured by inert gas fusion technique

Sample	Oxygen content (% wt.)
Bi_2Te_3 (raw powder)	0.076 ± 0.002
Sb_2Te_3 (raw powder	0.090 ± 0.002
$Sb_{1.6}Bi_{0.4}Te_3$ (HEBM)	1.03 ± 0.02
$Sb_{1.6}Bi_{0.4}Te_3$ (HM)	0.145 ± 0.004
$Sb_{1.5}Bi_{0.5}Te_3$ (HM)	0.125 ± 0.009
$Sb_{1.8}Bi_{0.2}Te_3$ (HM)	0.128 ± 0.001

The initial particle size is not a crucial parameter to produce submicron grained (SMG) structures by SPD. The saturated grain size of single-phase materials (the smallest grain size that can be achieved by HPT) is independent of the initial microstructure[6]; thus, in order to avoid powder contamination, the ingots were crushed to powder by hand.

Figure 4.8 shows the XDR diffraction pattern and the SEM micrographs of $Sb_{1.6}Bi_{0.4}Te_3$ powders produced by the optimum fabrication process (i.e. rapid solidification of the ingots + hand-milling) which enables to produce homogeneous powders (with negligible fraction of Te-rich phases) with minimum amounts of contaminants. Neither secondary phases nor

contaminants are detected in the diffraction patterns. The morphology of the powders is irregular and they have a very wide particle size distribution.

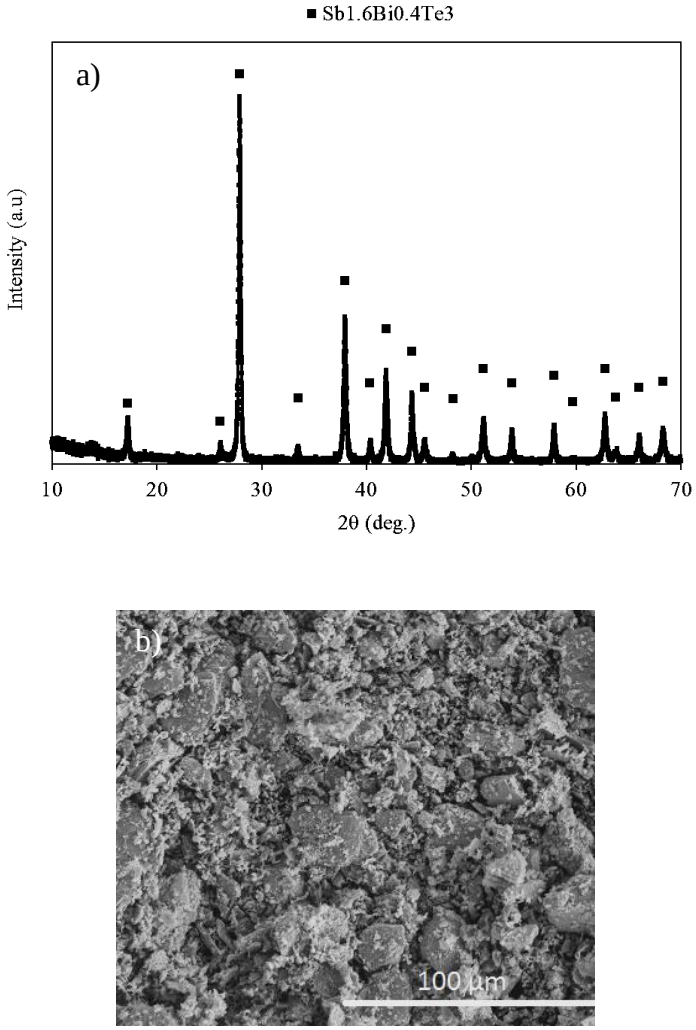

Figure 4.8: a) the XDR diffraction patterns of $Sb_{1.6}Bi_{0.4}Te_3$ powders produced by rapid solidification of ingots and subsequent hand-milling. Neither secondary phases nor contaminants are detected in the diffraction patters. b) SEM image of $Sb_{1.6}Bi_{0.4}Te_3$ powders showing their morphology and particle distribution.

4.4. Microstructural characterization of the processed bulk samples

In the present section, the microstructural evolution during the different three processing steps (solidification, hot-pressing, HPT) is investigated.

4.4. 1. Solidified ingots

Figure 4.9 shows the microstructure of the water quenched $Sb_{1.6}Bi_{0.4}Te_3$ ingots. Although the melt was solidified rapidly, long grains can be seen on the sections perpendicular to the cylindrical axis. This can be attributed to the low thermal diffusivity of such alloys which is usually lower than 2 mm^2/s [5,7] Similar microstructures were reported by O. Yamashita et al.[8] for $Sb_{1.5}Bi_{0.5}Te_3$ ingots that were cooled from 953 K to room temperature at a cooling rate of 2375 K/min. Micro-cracks are also appreciated at the grain interfaces; we believe that they can be generated during the solidification process because the thermal expansion coefficient of Bi_2Te_3 is 1.7 times bigger on the basal plane than along the *c* axis[9]. Consequently, the thermal expansion mismatches between the adjacent grains can generate mechanical stresses and hence micro-cracks.

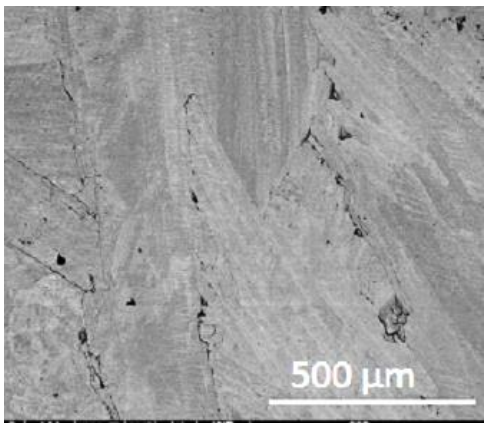

Figure 4.9: SEM micrograph of rapid solidified $Sb_{1.6}Bi_{0.4}Te_3$ ingots.

Such laminated microstructures that contain many micro-cracks are not adequate to be deformed by HPT, therefore prior to SPD processing, the as solidified ingots were crushed as described above and subsequently hot-pressed (for further details see section 3.1.2-1).

4.4. 2. Hot-pressed specimens

The hot-pressed samples (HP) show a polycrystalline structure with a coarse grain size. The distribution of sizes is quite heterogeneous (figure 4.10) because the particle size distribution of the starting materials varies in a wide range. Besides, residual porosity can be appreciated in the micrographs, especially at the grain boundaries of the fine grains. The relative density of HP samples was about 97 % (determined by Archimedes' water immersion technique).

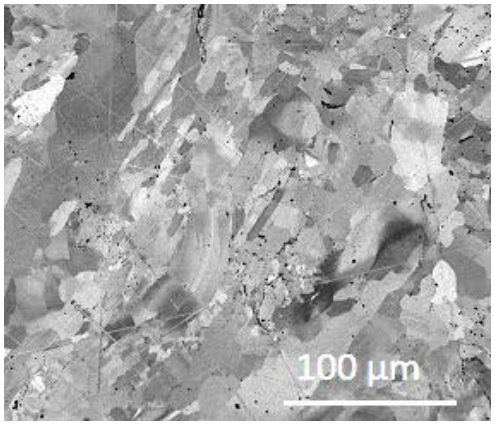

Figure 4.10: SEM images of $Sb_{1.6}Bi_{0.4}Te_3$ HP samples

4.4. 3. High-Pressure Torsioned specimens

After HPT processing, the grains appear equiaxed on the shear plane, and the size distribution is narrow (figure 4.11). Since the samples were subjected to severe plastic strains (up to an equivalent true strain of about 90), the mean grain size has been extraordinarily reduced from tens of micrometers (HP samples) to the submicrometer level (100 nm). In the tangential cross-section (this direction coincides with the macroscopic shear direction during the HPT deformation), the grains appear elongated (its shape factor is approximately 3) along a preferred orientation. One may expect that at such large strains, this preferred direction should correspond to the shear direction, however, in HPT deformed $Sb_{1.6}Bi_{0.4}Te_3$ compounds this is not the case. As figure 4.11 b) shows, a well-defined angle between the preferred direction of the elongated grains and the shear direction is observed. Such misorientation has been repeatedly reported for different materials after large deformation by HPT. According to Pippan el al., [6,10] this angle depends on the HPT processing temperature and alloying; moreover at higher processing temperatures the alignment of the elongated grains with the shear direction loses its significance. Anyway, it should be noted that this TEM micrograph corresponds to a very localized area; a careful study with several larger areas should be considered to confirm this behavior.

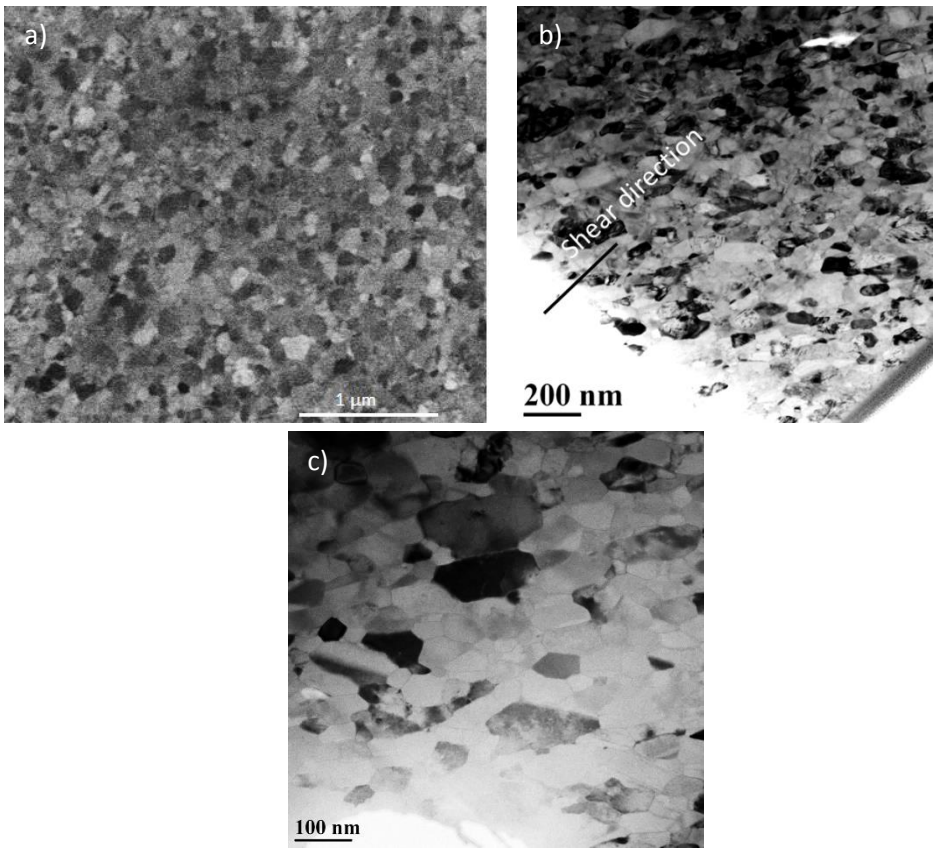

Figure 4.11.: a) FEG-SEM image of a $Sb_{1.6}Bi_{0.4}Te_3$ solid solution after being HPT-ed. The micrograph is taken in axial direction at the disk rim after 5 revolutions ε~90 (HPT processing temperature 150° C). b) TEM low magnification image of HPT-ed $Sb_{1.6}Bi_{0.4}Te_3$ (tangential cross-section). A well-defined angle between the preferred direction of the elongated grains and the shear direction is observed. c) TEM high-magnification image (tangential cross-section). The saturated grain size is close to 100 nm for $Sb_{1.6}Bi_{0.4}Te_3$ solid solutions.

As it is shown, during SPD processing extreme grain refinement takes place; however, the dominant mechanisms of the grain refinement are far from being well understood. In particular, there is not generally accepted scenario of the microstructural evolution at high strain levels, and the underlying processes are still an open question for researchers today. Even if the microstructural evolution depends heavily on crystal structure, homologous temperature, stacking fault energy and many other material properties, it is generally accepted that at low homologous temperatures, a

dislocation cell structure is formed in the first stages of plastic deformation, which gradually transforms into high angle grain boundary structures[11]. The experimental results support this point. For instance, in the case of polycrystalline copper or nickel alloys the EBSD mappings show that the elevated density of dislocations generated as a result of the SPD process is not randomly stored in the microstructure, but that rather they concentrate mainly at the grain boundaries.

Typically, after low equivalent strain up to about 0.5 plastic deformation piles up heterogeneously at grain boundaries and at cell dislocation boundaries within the original grains. At higher equivalent strains the misorientation angle of the newly created dislocation cell boundaries increases, varying significantly from grain to grain.[6,12]. As the imposed shear strain increases, the size of the subgrains decreases while the misorientation angle of the newly created cell/subgrain boundaries evolves towards high angle grain boundaries and the original grain structure vanishes. However, at a certain strain levels (which depends mainly on the material's properties and the processing temperature) the refinement process saturates and the cell block and dislocation cell structures which are characteristics at small and medium strain levels transforms to a uniform granular structure that, on average, remains dynamically stable.[6,13,14]

When the grain size in not further reduced (i.e. in the saturation regime) the generation of defects, such dislocations, vacancies and new boundaries has to be in equilibrium with the annihilation of these defects. Nevertheless, the external applied continuous shearing (in the case of HPT processing) would suppose a continuous elongation of the grain structure that is not actually observed[6]. (see figures 4.11 a) and 4.11 c), for instance) This means that if a steady-state microstructutal regime is reached, the increasing length of grains requires a subdivision of the grains. This may be governed by the process known as "geometric dynamic recrystallization". Grain boundaries tend to develop irregularities of 'serrations' during the dynamic recovery.

The wavelength of these serrations is generally similar to the subgrain size. If the material is subjected to large strains, its original grains become elongated whereas the subgrain size is nearly the same because it is almost independent of the imposed strain. Consequently, the fraction of high angle grain boundaries (HAGB) increases with increasing the strain and for a critical value the size of the boundary serrations will be comparable with the thickness of the grains. At that point, the interpenetration of the scalloped boundaries may occur and a microstructure composed by equiaxed grains with a grain size comparable with the subgrain size is developed[15] (see figure 4.12).

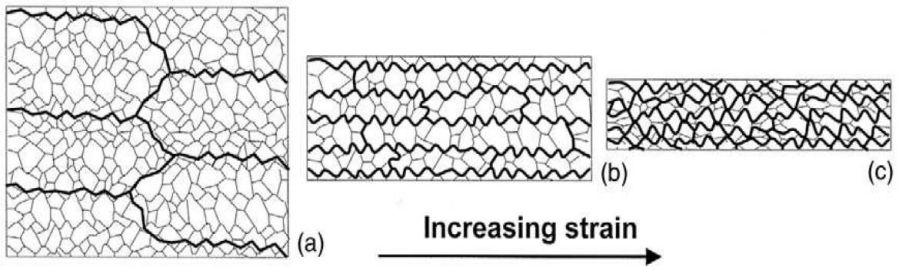

Figure 4.12: Schematic diagram showing the geometric dynamic recrystallization. As the strain increases the serrated high angle grain boundaries (HAGB) are closer, while the subgrain size is nearly independent of the imposed strain. Eventually, interpenetration of the HAGBs occur, resulting in a microstructure of equiaxed grains with a size comparable with the subgrain size.[15]

When the interpenetration of HAGB occurs, the grain size saturates and even at very large strains, no further refinement occur (i.e. the HAGB spacing does not become smaller than the subgrain size). This is a consequence of the dynamic grain growth. When the grain spacing is larger than the subgrain size, the migration of the HAGB is inhibited by the pinning of the substructure. In contrast, when the HAGB spacing is smaller than the subgrain size, such pinning effect is suppressed; the lamellar structure collapses as a result of the surface tensions at the node points and the grains tend to spheroidise and growth due to the lateral migration of the junctions (see figure 4.13) . As the grain size becomes similar to the

subgrain size, the substructure acts again as an inhibitor of the HAGBs migration and in this way a constant grain size is reached by dynamic equilibrium[15].

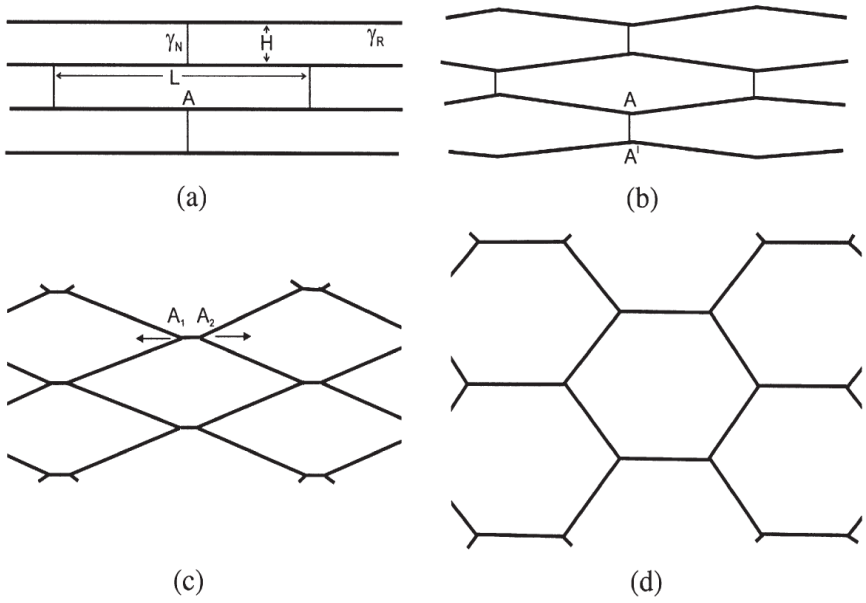

Figure 4.13: Illustration of the collapse of the lamellar microstructure followed by the spheroidisation process and the grain growth. a) Initial structure, b) collapse of the lamellar boundaries, c) beginning of the spheroidisation, d) further spheroidisation process and grain growth.

Electron backscatter diffraction (EBSD) analyses performed at the radial direction of HPT-ed $Sb_{1.6}Bi_{0.4}Te_3$ compounds may support that the grain boundary migration and grain fragmentation can be governed by a process similar to geometrical dynamic recrystallization. As shown figure 4.14, the resulting microstructure is composed by ultrafine grains (note that the grain size is overestimated because the grains have been dilated to remove the noise. Grain boundaries do not have a defined crystallographic orientation so they cannot be indexed) with a high density of HAGBs. The morphology is quite similar to that sketched in figure 4.12 c.

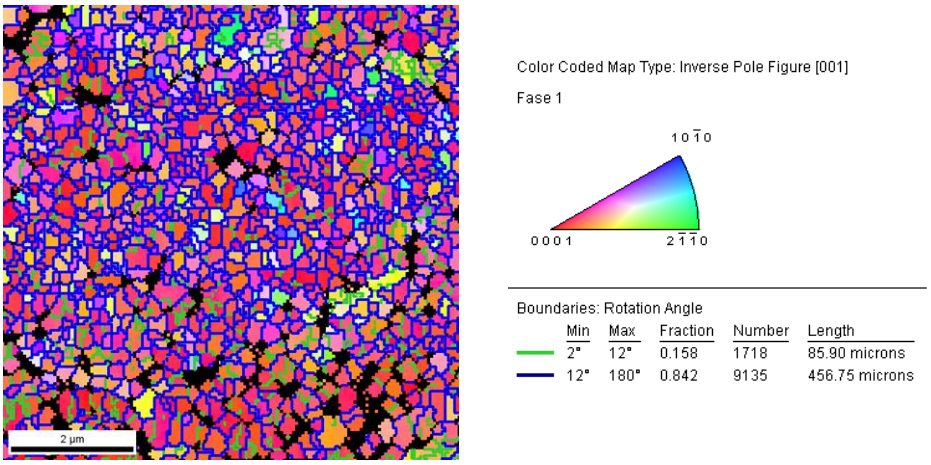

Figure 4.14: Distribution of high-and low-angle boundaries in HPT deformed $Sb_{1.6}Bi_{0.4}Te_3$ sample. The EBSD mapping was performed at the rim of the disk (ε~90) in the radial direction. High- and low angle boundaries are marked in blueand green respectively. The orientation map is also shown.

Similarly, Pippan et al.[6] pointed that since the saturated grain size depends strongly on the deformation temperature, the steady-stage microstructure is governed by dynamic restoration processes, which are continuously changing from the high-temperature regime to the low-temperature regime. At the medium-temperature regime, the grain boundary movement is governed by processes similar to dynamic recrystallization. The boundary movement reduces the dislocation density and is controlled mainly by dislocation density and diffusion. Conversely, in the low-temperature regime, the boundary movement is governed by stress induced boundary migration.

Deformation temperature plays a significant role in determining the saturated grain size. The lower is the HPT processing temperature the smaller is the grain size. Unfortunately, as a result of the weak van der Waals bonding between Te-Te layers, Bi_2Te_3 based alloys are extremely brittle and we were not able to deform our alloy without cracking at temperatures lower than 150° C (423 K). However, alloying and the

impurities level are also important parameters which determine the minimum grain size that can be achieved by SPD processes[6]. Figure 4.15 shows the microstructures of pure Bi_2Te_3 (figure 4.15 a) and b)) and alloyed $Sb_{1.6}Bi_{0.4}Te_3$ (figure 4.15 c) and d)). Both samples were processed at 423 K. Since the melting point of both alloys is quite similar, 586° C and 614° C [16] respectively, both materials were deformed nearly at the same homologous temperature ($0.49T_m$ and $0.48T_m$ for Bi_2Te_3 and $Sb_{1.6}Bi_{0.4}Te_3$ respectively), consequently one might expect that the saturated grain size should be the same. However, this is not the case and the saturated grain size is quite different in both cases. It seems that the alloying significantly reduces the final saturated grain size from approximately 300 nm to 100 nm. This alloying effect has also been observed in many metals[17–20] and it has been frequently associated with the change in the stacking-fault energy (γ_{SFE})[19–21]. The stacking-fault energy, which is related to the atomic bonding in the material, determines the extent to which unit dislocations dissociate into partial dislocations. Such dissociation, which is promoted by a low value of (γ_{SFE}), hinders the climb and cross slip of dislocations, which are the basic mechanisms responsible for recovery[15]. Consequently, in materials with a high value of stacking-fault energy ($\gamma_{SFE} > 90$ mJ/m^2), the dynamic recovery is an effective mechanism because the mobility of the dislocations is very high. However, continuous dynamic recrystallization may take place when despite the strong recovery processes a critical amount of stored energy remains (straining up to large deformations) or when the mobility of the HAGBs is inhibited. The energy stored by plastic deformation is dissipated by dislocations accumulating at existing HAGBs as well as in the subgrains which transform into HAGBs by the successive increase of misorientation. During the continuous dynamic recrystallization process, a new grain structure consisting of equiaxed grain sizes approximately of the subgrain size is formed homogeneously[15,22]. In contrast, in materials with a low value of stacking-fault energy ($\gamma_{SFE} < 20$ mJ/m^2), the dislocations are strongly dissociated; therefore the recovery process is not efficient and the classical

dynamic recrystallization is easily activated. Figure 4.16 shows schematically the differences between recovery and recrystallization processes.

Thus, is not surprising that at the first stages of the deformation, the hardening behavior or even the saturation strain differ significantly according to the value of the stacking-fault energy of the processes alloy, because as said, γ_{SFE} is a significant parameter for the dislocation cell formation. However, is not clear if the γ_{SFE} controls the final saturation grain size. For instance, X. H. An et al. pointed that for Cu and Cu–Al alloys processed by HPT (the samples were strained up to von Mises equivalent true strain of about 105 at the disk rim), the final average grain size decreased with decreasing γ_{SFE}[19]. Conversely, Pippan el al.[6] did not see important differences in the final saturation grain size of three pure metals with significant differences in their stacking-fault energy. These pure metals Ni, Cu and Ag (their γ_{SFE} are 125 mJ/m^2, 40 mJ/m^2 and 16 mJ/m^2 respectively) were deformed by HPT at the same homologous temperature. Measuring the torque during the deformation process and determining the saturated grain size by EBSD, they showed that although the hardening behavior of the pure metals is very different, the saturation grain size was very similar. So, based on this experimental evidence, they pointed that the stacking-fault energy influences strongly the structure formation but does not determine the saturated grain size. According to the authors, the grain boundary migration-controlling effects are more important and hence, they claimed that the observed alloying effect is related to the change in the grain boundary mobility.

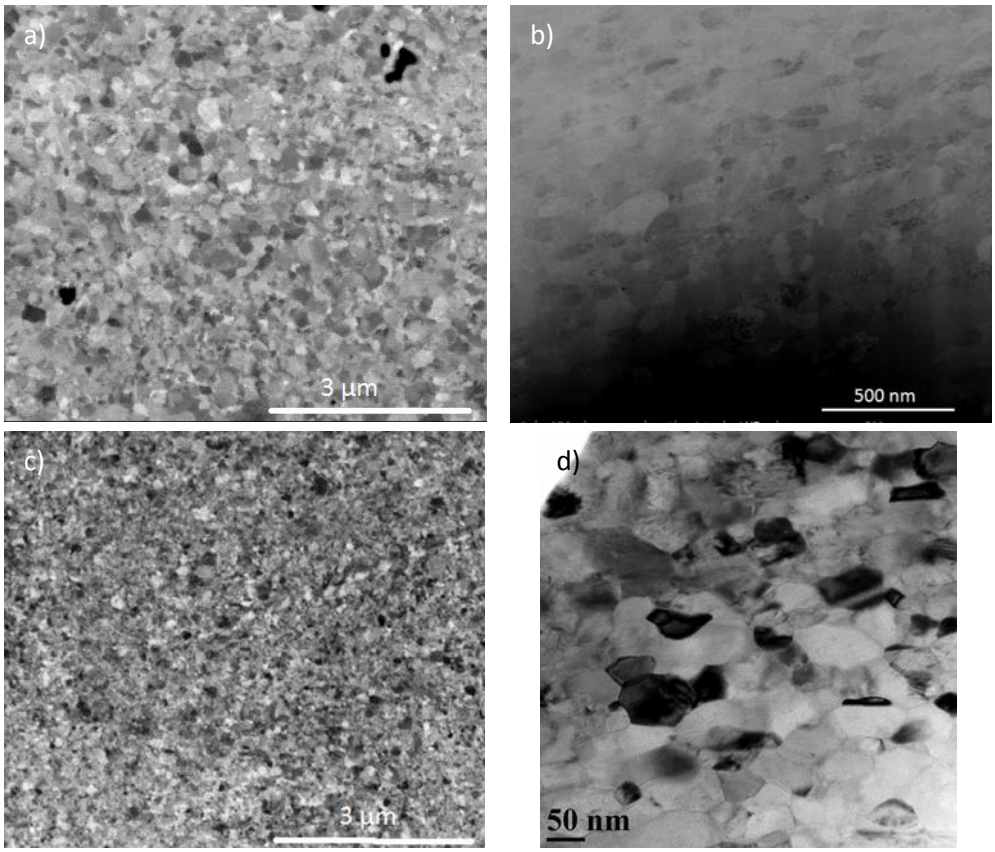

Figure 4.15: Effect of alloying and the impurities level in the final saturated grain size. a) and b) images corresponds to pure Bi_2Te_3, FEG-SEM and STEM images, respectively. The average saturated grain size is close to 300 nm in this case. c) and d) images corresponds to $Sb_{1.6}Bi_{0.4}Te_3$ alloy, FEG-SEM and STEM images, respectively. In this case the saturated grain size is significantly smaller, close to 100 nm.

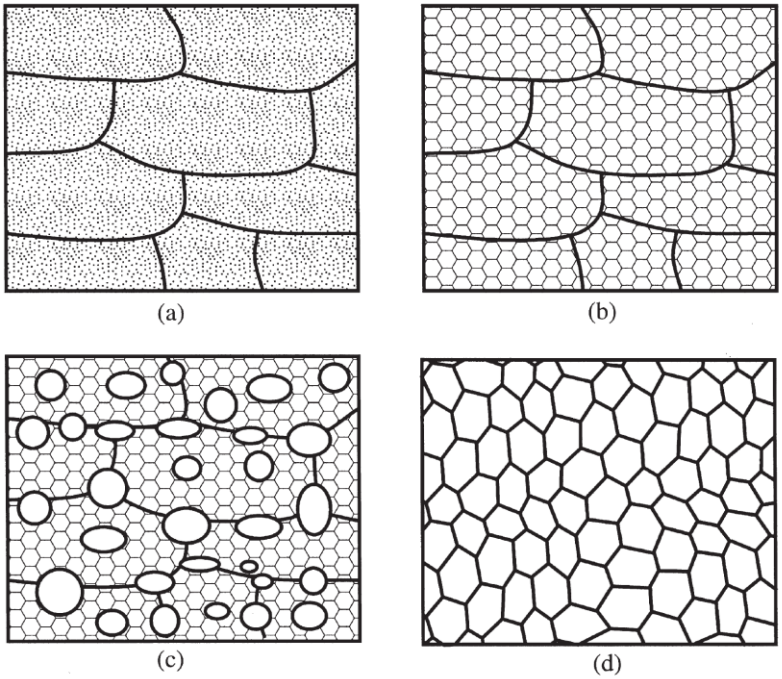

Figure 4.16: Schematic diagram of recovery and recrystallization processes[6]. a) Disordered defect structure. b) Rearrangement of low-angle grain boundaries (LAGBs) by recovery. c) Partial formation of new grains by recrystallization. d) Fully recrystallized microstructure.

Reaching a finer microstructure due to the alloying effect makes HPT processing even a more interesting route to produce thermoelectric materials. As I mentioned previously, creating solid solutions with isoelectronic atoms is a well-established approach to reducing the thermal conductivity without affecting significantly the electrical conductivity. The generated point defects due to the alloying act as scattering centers dispersing the long to middle-frequency phonons. Besides, the alloying effect also enhances indirectly the phonon grain-boundary scattering. Since the saturated grain size is even smaller due to the alloying effect, the low-frequency phonons are scattered more effectively at grain boundaries giving rise to a further reduction of the thermal conductivity.

The higher impurities level of the $Sb_{1.6}Bi_{0.4}Te_3$ alloys also explains the obtained finer-grained microstructure after HPT processing. As it is shown in table 4.III, the oxygen content of the $Sb_{1.6}Bi_{0.4}Te_3$ alloy is about two times higher than the measured one on pure Bi_2Te_3. Fine second phase particles act as growth inhibitors by Zener pinning (i.e. they pin dislocations and grain boundaries). Accordingly, they prevent recovery and recrystallization during the deformation, therefore a finer microstructure should be obtained[15,23]. We believe that the oxide layers fracture into small particles during the deformation process and as the strain increases they distribute along the grain boundaries and triple junctions of the grains as proposed A. Bachmaier et al[24].

Nano-dispersing small amounts of second phase particles is becoming a well-established approach to control the grain growth and reduce the thermal conductivity of the TE compounds through phonon scattering with nanoparticles[25–29]. Besides reducing the thermal conductivity, the second-phase particles, if they are added in a proper amount, strengthen the matrix effectively [24–26,30]. For instance, D.W. Liu et al. reported[25] that nano-dispersing SiC particles in *p*-type $Bi_{0.5}Sb_{1.5}Te_3$ polycrystalline alloys leads to a simultaneous improvement of its thermoelectric and mechanical properties. According to these authors, the maximum dimensionless figure of merit (zT_{max}) at 323 K improves from 0.88 for SiC-free $Bi_{0.5}Sb_{1.5}Te_3$ to 0.97 for 0.1 vol. % SiC-dispersed $Bi_{0.5}Sb_{1.5}Te_3$, while Vickers hardness, fracture toughness and bending strength increases from 0.81 GPa, 0.82 $MPa \cdot m^{1/2}$, 65.8 MPa to 0.87 GPa, 0.91 $MPa \cdot m^{1/2}$, 73.8 MPa respectively, when a 0.1 % SiC in volume percentage is added.

The second phase particles also enhance the thermal stability of the reached submicron grained (SMG) structures. Generally, the microstructures of pure materials processed by SPD methods are thermally unstable because of the huge stored energy in the material in form of crystalline defects such dislocations and "non-equilibrium" grain boundaries[31]. Due to the high density of dislocations, the boundary motion driving force is usually high

for SMG materials (i.e. recovery and recrystallization phenomena are easily activated); however, this boundary motion is inhibited by the drag force caused by the pinning of the boundary at the incoherent interfaces, thus, if the driving force is insufficient to overcome the drag force, which depends on particle size and the boundary surface energy, then grain growth is suppressed and the microstructure will be stable at that temperature[15]. This approach has been repetitively used to improve the thermal stability of pure or alloyed metals processed by SPD methods. For example, adding small amounts of strontium and/or zirconium is effective to prevent grain growth due to the presence of stable $Al_3(Zr_xSc_{1-x})$ precipitates[32] (see figure 4.17). The oxide layers which are present at the raw powders have a similar effect. As discussed above when high strains are imposed, the oxide layers are fractured and dispersed along grain boundaries deterring recovery and recrystallization during the deformation and hence, preventing the grain growth. In such a way, thanks to the dispersed alumina particles, HPT-ed aluminum samples exhibit good grain size stability up to annealing temperatures of $0.60T_m$ (290° C)[30].

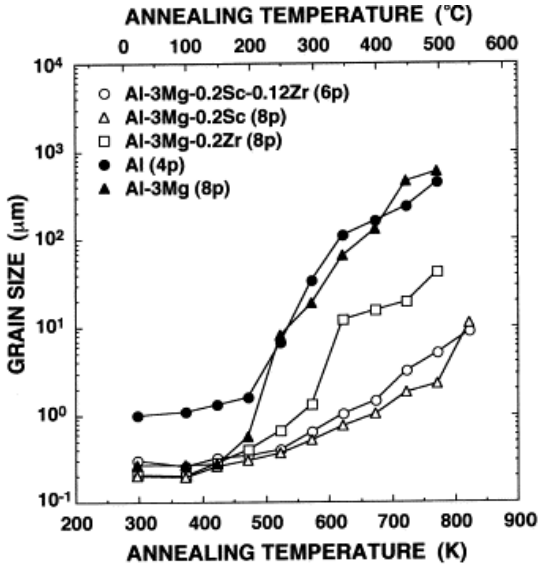

Figure 4.17: Thermal stability of different kind of aluminum solid solutions processed by ECAP. (p=number or passes)[32]

4.5. Crystallographic texture

The crystallographic texture was evaluated by Electron Backscatter Diffraction (EBSD) as well by X-Ray Diffraction (XRD) method. The degree of orientation of the crystallographic basal planes with respect to the macroscopic disk axis was estimated by the Lotgering method[33].

Figure 4.18 shows the X-ray diffraction patterns of pure bismuth telluride raw powders, HP samples and HPT samples, respectively. In the case of the bulk samples, the diffraction patterns correspond to the planes perpendicular to the pressing direction.

All diffraction patterns show strong 00l peaks, indicating that the crystallographic basal planes are preferentially oriented. In case of the raw powders, one would expect a random distribution of orientations because the particles should be indiscriminately distributed on the sample holder. However, Bi_2Te_3 tends to break along the basal plane due to the weak bonding between Te-Te layers. Therefore, Bi_2Te_3 particles processed by conventional powder metallurgy usually have a flake shape (see figure 4.1) parallel to the basal plane. Thus, big particles have the tendency to accommodate in a preferred orientation and consequently the 00l peaks have unusual strong intensities. The high *c*-axis alignment of the HP samples can be also attributed to this geometrical effect. We believe that the big particles tend to stack aligned with the *c* axis parallel to the HP loading direction. This hypothesis supports the observation that the orientation factor increases with increasing particle size but do not depend on the sintering temperature[34]. The work of D.H. Kim et al.[35] also validate our point. The authors studied the influence of powder morphology on the thermoelectric anisotropy of SPS-ed *p*-type Bi_2Te_3 based thermoelectric materials. For that propose, they prepared three types of raw powders with three different morphologies by a chemical reaction method (clusters of spherical particles about 50 nm in size), a conventional pulverization method (flake-like shape) and a gas atomizing method (spherical shape). The study concluded that the bulk samples whose starting powders were flake-like shaped, have

anisotropic thermoelectric properties because the grains exhibit a preferred orientation, whereas the sintered bodies, whose powder were composed of spherical particles, show isotropic thermoelectric properties.

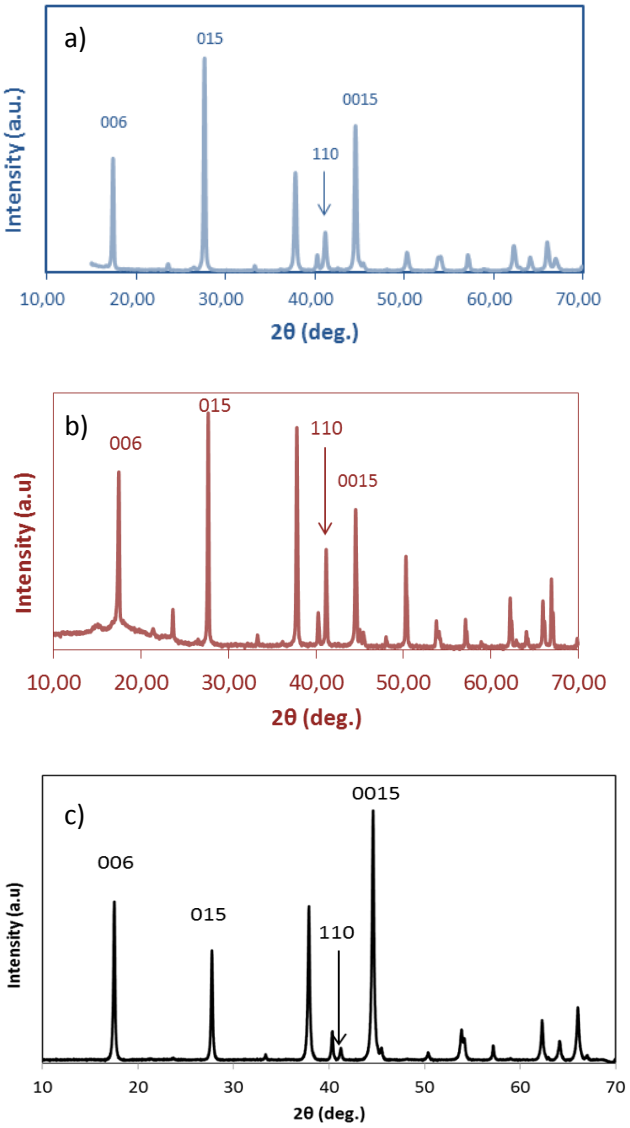

Figure 4.18: XRD patters of pure Bi_2Te_3. a) Raw powders b) HP sample c) HPT sample. In the case of bulk samples, the incident X-ray beam is perpendicular to the pressing direction.

Therefore, as it has been reported elsewhere [26,36–38], big particles fabricated by conventional pulverization method can be easily preferably aligned through HP or SPS methods. In contrast, when the powders are crushed into fine-particles by high energetic milling processes such as ball-milling; the flake-like shape is lost and consequently is very difficult to reach highly textured nanostructured TE materials through conventional consolidation processes. Conversely, HPT samples despite of having a submicrometer grain size (see figure 4.15), exhibit a very strong 001 texture (basal plane normal coincident with the normal to the disk plane) as shown figure 4.18 c. Such texture is to be expected from the easy glide on the 00l planes. Since the lamellar crystal structure and the weak van der Waals bonding between Te-Te layers, when the grains are deformed by shearing, they easily slip along the basal planes and the *c*-axis tends to be aligned parallel to the pressing direction.

The crystallographic texture of the Bi_2Te_3-based solid solutions after been processed by HPT does not significantly differ from the pure one. Figure 4.19 shows the X-ray diffraction patterns of $Sb_{1.6}Bi_{0.4}Te_3$ raw powders, HP samples, and HPT samples, respectively. It seems that the alloying has not a significant effect on the texture development and as in the case of pure Bi_2Te_3 alloys, ultrafine grained and highly textured $Sb_{2-x}Bi_xTe_3$ thermoelectric materials were processed by SPD.

Table 4.IV collects the orientation factor (*OF*) of HP and HPT samples. As discussed above, since the flake-like shape of the raw powders, they tend to accommodate in the sample holder in a preferred position; consequently, the P_0 value, i.e. the ratio of preferentially oriented basal planes for a sample without any texture, has been estimated using the data available in the ICDD PDF cards (see appendix I). For HPT samples the orientation factors of all Bi_2Te_3 based solid solutions are in the range of 0.5-0.6, which is in a good agreement with the OF of the 00l planes estimated by M. Ashida et al.[39] for HPT-ed $Bi_{0.5}Sb_{1.5}Te_{3.0}$ deformed up to von Mises tensile equivalent true strain of about 110 at 473 K under a hydrostatic pressure of 6.0 GPa

(*OF*=0.525). The differences in *OF* for HP samples can be attributed to differences in the morphology of the starting powders.

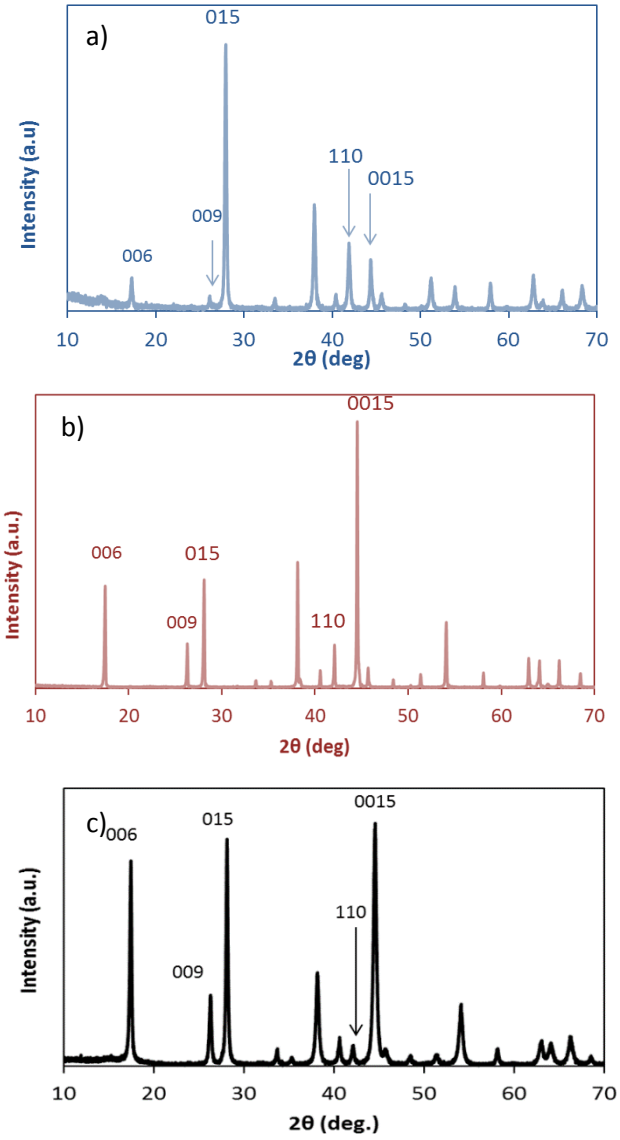

Figure 4.19: XRD patters of $Sb_{1.6}Bi_{0.4}Te_3$. a) Raw powders b) HP sample c) HPT sample. In the case of bulk samples, the incident X-ray beam is perpendicular to the pressing direction.

The broadening of the diffraction peaks observed in the diffraction patterns corresponding to HPT samples puts in evidence the nano-sized grain of such samples. Due to the peak width (FWHM) is inversely proportional to the crystallite size (L), the Scherrer equation enables to estimate the crystallite size[40] of the HPT samples, which is 40 ± 2 nm and 28 ± 4 nm for pure Bi_2Te_3 and alloyed $Sb_{1.6}Bi_{0.4}Te_3$ respectively. The bigger crystallite size of HPT-ed Bi_2Te_3 sample comparing with $Sb_{1.6}Bi_{0.4}Te_3$ is in a good accordance with TEM observations (figure 4.15); however the estimated crystallite size is significantly smaller. It should be pointed that the Scherrer formula provides a lower bound on the grain size because, besides instrumental effects, other factors including sub-boundaries, dislocations, stacking faults, twins or micro-stresses can contribute to the diffraction peak broadening[40].

Table 4.IV: orientation factors (OF) of HP and HPT samples evaluated by the Lotgering method.

Solid solution	HP	HPT
Bi_2Te_3	0.20	0.57
$Sb_{1.5}Bi_{0.5}Te_3$	0.39	0.56
$Sb_{1.6}Bi_{0.4}Te_3$	0.392	0.51
$Sb_{1.8}Bi_{0.2}Te_3$	0.21	0.59
Sb_2Te_3	0.66	0.76

EBSD measurements also confirm the preferred alignment of the 00l planes (figure 4.20). All samples have a very strong (000l) fiber texture, (i.e. the crystallographic *c* axis and the disk axis are parallel). Such texture is not surprising, for instance, it has been observed, after HPT of hexagonal close packaged (HCP) metals like Zn were glide on basal plane is preferred to prismatic or pyramidal glide systems[41,42].

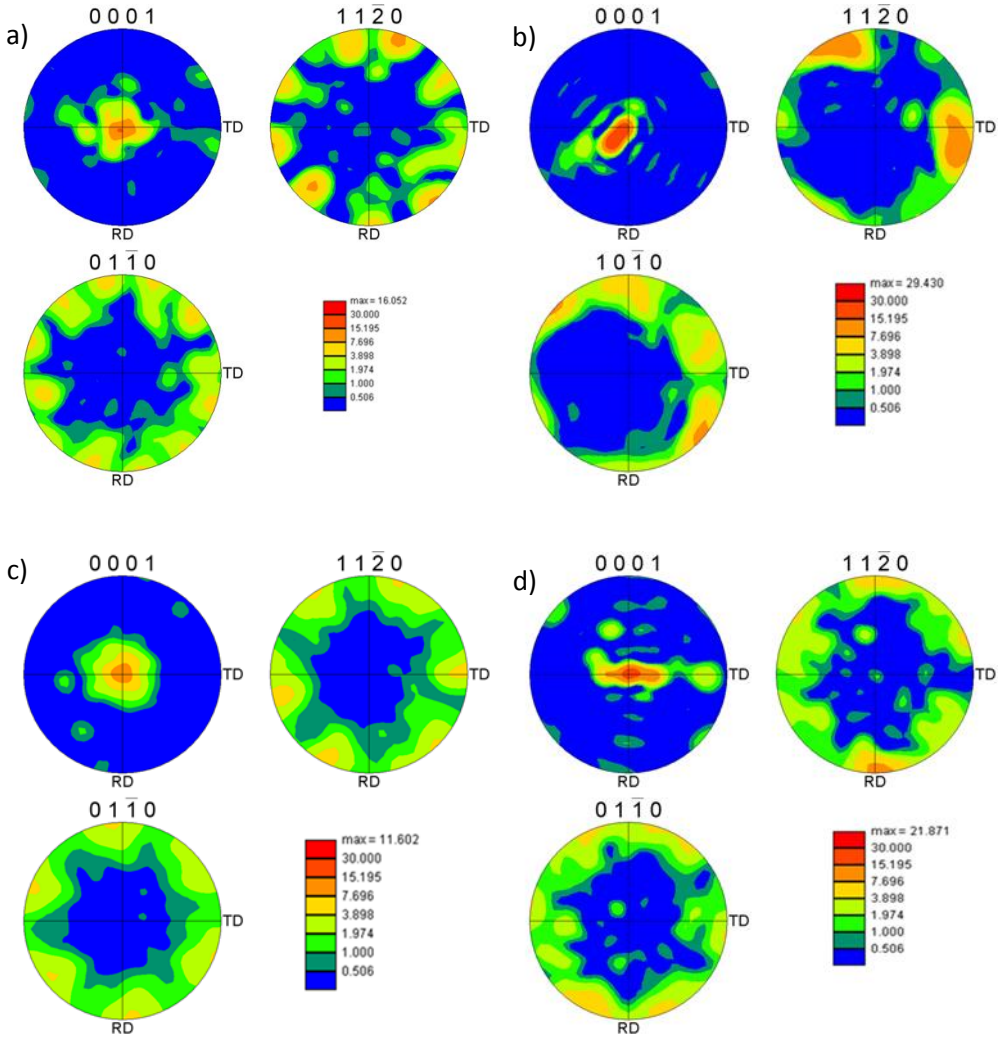

Figure 4.20: 0001, $11\bar{2}0$, and $01\bar{1}0$ pole figures. The pole figure is projected on the disk plane of the sample. a) HP Bi_2Te_3 b) HPT Bi_2Te_3, c) HP $Sb_{1.6}Bi_{0.4}Te_3$, d) HPT $Sb_{1.6}Bi_{0.4}Te_3$. A very strong 0001 fiber texture is observed in all the cases. ND is parallel to the macroscopic disk axis wile RD is parallel to the shear direction.

4.6. References

1. Kavei, G. & Karami, M. A. Formation of anti-site defects and bismuth overstoichiometry in p-type Sb 2 − x Bi x Te 3 thermoelectric crystals. Eur. Phys. J. Appl. Phys. 73, 67–73 (2008).

2. Custódio, M. C. C. & Hernandes, A. C. Tellurium-rich phase in n-type bismuth telluride crystals grown by the Bridgman technique. J. Cryst. Growth 205, 523–530 (1999).

3. Luo, Y. et al. Melting and solidification of bismuth antimony telluride under a high magnetic field: A new route to high thermoelectric performance. Nano Energy 15, 709–718 (2015).

4. Faleev, S. V. & Léonard, F. Theory of enhancement of thermoelectric properties of materials with nanoinclusions. Phys. Rev. B 77, 214304 (2008).

5. D.M. Rowe. CRC Handbook of Thermoelectrics. (1995).

6. Pippan, R. et al. Saturation of Fragmentation During Severe Plastic Deformation. Annu. Rev. Mater. Res. 40, 319–343 (2010).

7. Satterthwaite, C. B. & Ure, R. W. Electrical and Thermal Properties of Bi2Te3. Phys. Rev. 108, 1164–1170 (1957).

8. Yamashita, O., Ochi, T. & Odahara, H. Effect of the cooling rate on the thermoelectric properties of p-type (Bi0.25Sb0.75)2Te3 and n-type Bi2(Te0.94Se0.06)3 after melting in the bismuth–telluride system. Mater. Res. Bull. 44, 1352–1359 (2009).

9. Pavlova, L. M., Shtern, Y. I. & Mironov, R. E. Thermal expansion of bismuth telluride. High Temp. 49, 369–379 (2011).

10. Bachmaier, A., Hafok, M. & Pippan, R. u. Mater. Trans. 51, 8–13 (2010).

11. Estrin, Y. & Vinogradov, A. Extreme grain refinement by severe plastic deformation: A wealth of challenging science. Acta Mater. 61, 782–817 (2013).

12. Hansen, N., Mehl, R. F. & Medalist, A. New discoveries in deformed metals. Metall. Mater. Trans. A 32, 2917–2935 (2001).

13. Hebesberger, T., Stüwe, H. P., Vorhauer, a., Wetscher, F. & Pippan, R. Structure of Cu deformed by high pressure torsion. Acta Mater. 53, 393–402 (2005).

14. Jiang, H., Zhu, Y. T., Butt, D. P., Alexandrov, I. V & Lowe, T. C. Microstructural evolution, microhardness and thermal stability of HPT-processed Cu. Mater. Sci. Eng. A 290, 128–138 (2000).

15. Humphreys, F. J. & Hatherly, M. Recrystallization and related annealing phenomena. Acta Metall. Mater. (2004). doi:10.1016/B978-008044164-1/50005-0

16. Tomashik, V. & Perrot, P. Bismuth–Antimony–Tellurium. (Springer).

17. Bachmaier, A., Hafok, M. & Pippan, R. Rate Independent and Rate Dependent Structural Evolution during Severe Plastic Deformation. Mater. Trans. 51, 8–13 (2010).

18. Zhilyaev, a & Langdon, T. Using high-pressure torsion for metal processing: Fundamentals and applications. Prog. Mater. Sci. 53, 893–979 (2008).

19. An, X. H. et al. The influence of stacking fault energy on the mechanical properties of nanostructured Cu and Cu–Al alloys processed by high-pressure torsion. Scr. Mater. 64, 954–957 (2011).

20. Balogh, L. et al. Influence of stacking-fault energy on microstructural characteristics of ultrafine-grain copper and copper–zinc alloys. Acta Mater. 56, 809–820 (2008).

21. Qu, S. et al. Microstructural evolution and mechanical properties of Cu–Al alloys subjected to equal channel angular pressing. Acta Mater. 57, 1586–1601 (2009).

22. Doherty, R. D. et al. Current issues in recrystallization: a review. Mater. Sci. Eng. A 238, 219–274 (1997).

23. Nes, E., Ryum, N. & Hunderi, O. On the Zener drag. Acta Metall. 33, 11–22 (1985).

24. Bachmaier, A., Hohenwarter, A. & Pippan, R. New procedure to generate stable nanocrystallites by severe plastic deformation. Scr. Mater. 61, 1016–1019 (2009).

25. Liu, D.-W., Li, J.-F., Chen, C. & Zhang, B.-P. Effects of SiC Nanodispersion on the Thermoelectric Properties of p-Type and n-Type Bi2Te3-Based Alloys. J. Electron. Mater. 40, 992–998 (2010).

26. Zhao, L.-D. et al. Thermoelectric and mechanical properties of nano-SiC-dispersed Bi2Te3 fabricated by mechanical alloying and spark plasma sintering. J. Alloys Compd. 455, 259–264 (2008).

27. Keshavarz, M. K., Vasilevskiy, D., Masut, R. A. & Turenne, S. Synthesis and characterization of bismuth telluride-based thermoelectric nanocomposites containing MoS2 nano-inclusions. Mater. Charact. 95, 44–49 (2014).

28. Keshavarz, M., Vasilevskiy, D., Masut, R. & Turenne, S. Effect of Suppression of Grain Growth of Hot Extruded (Bi0.2Sb0.8)2Te3 Thermoelectric Alloys by MoS2 Nanoparticles. J. Electron. Mater. 43, 2239–2246 (2014).

29. Satyala, N. et al. Reduction of thermal conductivity of bulk nanostructured bismuth telluride composites embedded with silicon nano-inclusions. J. Appl. Phys. 115, - (2014).

30. Bachmaier, A. & Pippan, R. Effect of oxide particles on the stabilization and final microstructure in aluminium. Mater. Sci. Eng. A 528, 7589–7595 (2011).

31. Valiev, R. Z., Islamgaliev, R. K. & Alexandrov, I. V. Bulk nanostructured materials from severe plastic deformation. Prog. Mater. Sci. 45, 103–189 (2000).

32. Lee, S. et al. Influence of scandium and zirconium on grain stability and superplastic ductilities in ultrafine-grained Al–Mg alloys. Acta Mater. 50, 553–564 (2002).

33. Lotgering, F. K. Topotactical reactions with ferrimagnetic oxides having hexagonal crystal structures—I. J. Inorg. Nucl. Chem. 9, 113–123 (1959).

34. Chen, L., Jiang, J. & Shi, X. Thermoelectric performance of textured Bi2Te 3-based sintered materials prepared by spark plasma sintering. MRS Proc. 793, S9.3 (2003).

35. Kim, D. H., Kim, C., Heo, S. H. & Kim, H. Influence of powder morphology on thermoelectric anisotropy of spark-plasma-sintered Bi–Te-based thermoelectric materials. Acta Mater. 59, 405–411 (2011).

36. Poudel, B. et al. High-thermoelectric performance of nanostructured bismuth antimony telluride bulk alloys. Science 320, 634–8 (2008).

37. Kim, D. H., Kim, C., Je, K.-C., Ha, G. H. & Kim, H. Fabrication and thermoelectric properties of c-axis-aligned Bi0.5Sb1.5Te3 with a high magnetic field. Acta Mater. 59, 4957–4963 (2011).

38. Zhang, Z., Sharma, P. a., Lavernia, E. J. & Yang, N. Thermoelectric and transport properties of nanostructured Bi2Te3 by spark plasma sintering. J. Mater. Res. 26, 475–484 (2011).

39. Ashida, M. et al. Texture of bismuth telluride-based thermoelectric semiconductors processed by high-pressure torsion. J. Phys. Chem. Solids 70, 1089–1092 (2009).

40. Cullity, B. D. & Stock, S. R. Elements of X-ray diffraction, 3rd edition. Prentice Hall Chapter 1 (2001).

41. Zühlke, T. thermomechanical and microstructural properties of ZnCuTi under different deformation conditions.PhD thesis, University of Navarra (2014).

42. Srinivasarao, B., Zhilyaev, a. P., Langdon, T. G. & Pérez-Prado, M. T. On the relation between the microstructure and the mechanical behavior of pure Zn processed by high pressure torsion. Mater. Sci. Eng. A 562, 196–202 (2013).

43. Predel, B. in B-Ba – C-Zr SE - 592 Landolt-Börnstein - Gr. IV Phys. Chem. Vol. 5b, (Madelung, O.) 5b, 1–7 (Springer Berlin Heidelberg, 1992).

Chapter 5: Thermoelectric characterization

5.1. Introduction

In the previous chapter, it has been shown that high-pressure torsion (HPT) is an outstanding technique to produce ultrafine grained and highly textured thermoelectric (TE) materials by means of severe plastic deformation (SPD). It is expected that the grain refinement resulting from HPT processing will significantly decrease the thermal conductivity, without affecting the mobility of the free charge carriers. Besides, due to the layered rhombohedral structure of the Bi_2Te_3 based alloys, the TE properties of such compounds are very anisotropic. The Seebeck coefficient (*S*) is almost isotropic while the electrical and thermal conductivities along the basal plane are respectively about four and two times larger than those along the *c*-axis[1]. The developed strong fiber texture during HPT deformation should enhance the so-called power factor (P*F*). Therefore, the simultaneous grain refinement and the strong fiber texture of Bi_2Te_3 based alloys after HPT processing should significantly improve its dimensionless figure of merit (*zT*). However, due to its layered crystallographic structure and van der Waals bonding between Te(1)–Te(1) layers, Bi_2Te_3 is easily cleaved along the *c*-plane, consequently, it is an extremely brittle material. This fact strongly difficulties the HPT processing and in order to deform Bi_2Te_3 based solid solutions without cracking (cracks reduce drastically the electrical conductivity and degrade the mechanical properties) several parameters

such anvil geometry, processing temperature, and strain rate should be optimized.

This chapter summarizes the thermoelectric properties of HPT-ed Bi_2Te_3 based TE materials. Besides, the TE properties of severely deformed samples are compared with those processed by conventional powder metallurgy methods (hot pressing method).

Firstly, the viability of the HPT method to process thermodynamically highly efficient TE materials was explored. For that purpose, the thermoelectric properties of severely deformed pure Bi_2Te_3 and Sb_2Te_3 were studied. After that, with the aim of optimizing the stoichiometry that maximizes *zT*, we adjusted the chemical composition of Bi_2Te_3 solid solutions. Finally, we tried to get the optimum free carrier concentration after HPT processing by tuning the doping level and/or by performing low-temperature annealing treatments (200° C).

5.2. Exploring the viability of the HPT by studying the thermoelectric properties of SPD-ed pure Bi_2Te_3 and Sb_2Te_3

5.2.1. Pure Bi_2Te_3

Pure Bi_2Te_3 was selected as the first candidate to explore the viability of the HPT processing to produce thermodynamically highly efficient thermoelectric materials by severe plastic deformation. Bismuth telluride is a well-known thermoelectric material with optimum thermoelectric performance close to room temperature[1]. Among others, this feature makes Bi_2Te_3 a very suitable candidate to being processed by HPT because the submicron grained structures obtained after HPT are expected to be preserved during the TE device operation.

The first report that bismuth telluride is an effective thermoelectric material appeared in 1954[2]. A thermocouple made of a *p*-type sample of the Bi_2Te_3 compound connected to a negative thermoelement made of pure bismuth was found to yield a cooling effect of 26 K below ambient temperature by

means of the Peltier effect. The compound in the first experiments was produced by the zone melting of a mixture of the elements in the correct proportions. R.W. Douglas and H.J. Goldsmid did not make any attempt to optimize the doping level. However, the carrier concentration of the zone melted Bi_2Te_3 ingots was close to the optimum one, exhibiting a Seebeck coefficient of about 220 μV/K. The original sample was aligned with current flow perpendicular to the *c*-direction and the electrical and thermal conductivities were found to be $4 \cdot 10^4\ \Omega^{-1}m^{-1}$ and 2.1 W/m K, respectively[3]. Nowadays is well-known that melt-grown bismuth telluride does not have the stoichiometric formula Bi_2Te_3. Instead, there is an excess of Bi atoms, with corresponding vacancies on some of the Te sites. The excess Bi atoms appear to act as acceptor impurities leading to *p*-type conduction[3].

In the case of bismuth telluride based solid solutions, the concentration of point defects such Frenkel defects, (interstitial sites occupied by atoms, together with an equal concentration of vacancies at the proper sites), Schottky-Wanger defects (vacancies of both, anion and cation atoms giving electrical neutrality) and antisite defects (anions on cations sites or conversely cations on anion sites) depends strongly on the composition. The smaller the differences in electronegativity (χ) between the elements that constitute the thermoelectric material, the easier is the formation of antisite defects[4]. On the other hand, by increasing the size difference between the cation and anion atoms, anion vacancies form more readily[5]. Table 5.I shows the electronegativity, covalent radius and, the relative atomic mass of the basic elements that compose the $Sb_{2-x}Bi_xTe_3$ solid solutions. It is well-known that the hole concentration in bismuth telluride based alloys is closely related to the concentration of antisite defect[4]. Since the electronegativity difference between Bi and Te atoms is rather big, this kind of defects are not easily promoted, and undoped Bi_2Te_3 alloys are weak *p*-type semiconductors. However, the carrier concentration of Bi_2Te_3-based alloys is also sensitive to the lattice defects generated during mechanical deformation. Consequently, the new point defects introduced into the lattice

due to the plastic deformation can change the transport behavior of pure Bi_2Te_3 from *p*-type to *n*-type, as reported elsewhere [6–10].

Table 5.I: Electronegativity, covalent radius, and relative atomic mass of the basic elements[11].

Element	Bi	Sb	Te
Electronegativity	2.02	2.05	2.1
Covalent radius [Å]	1.46	1.40	1.36
Relative atomic mass	208.98	121.75	127.6

Figure 5.1 shows the Seebeck coefficient as a function of measuring temperature for the HP samples before and after HPT processing. The Seebeck coefficient of HP samples is negative indicating that it is an *n*-type material. As I aforementioned, this change in transport behavior from *p*-type to *n*-type is due to the hot-deformation process that takes place during the HP consolidation, which introduces a large concentration of point defects into the lattice. Schultz et al.[6] pointed that plastic deformation produces at least 3 Te to 2 Bi vacancy-interstitial pairs. In Bi_2Te_3-based alloys Te vacancies ($V_{Te}^{\circ\circ}$) are easily produced on Te(1)–Te(1) bonding planes because dislocations are preferably created at such planes during plastic deformation. The point defects arise primarily as a result of dislocation intersections; thus, the generation of tellurium vacancies is promoted at those planes. When abundant Te vacancies are created, Bi atoms tend to enter into Te vacancies due to the small electronegativity difference between both elements (see table 5.I). Based on this idea, Navratil and co-workers[12] proposed an equation that describes the interaction between Te and Bi vacancies and antisite defects as follows:

$$2V_{Bi}^{'''} + 3V_{Te}^{\circ\circ} + Bi_{Te}^{'} = V_{Bi}^{'''} + Bi_{Bi}^{X} + 4V_{Te}^{\circ\circ} + 6e^{'} \quad (5.1)$$

where $V_{Bi}^{'''}$ and $V_{Te}^{\circ\circ}$ are the Bi and Te vacancies generated from the deformation process, $Bi_{Te}^{'}$ is the antisite defect and e' is the produced excess electron. Which means that additional negative carriers can be introduced into the lattice during HP sintering process, that are responsible for the *n*-type conduction behavior of the HP samples. This effect is usually named as the deformation-induced donor-like effect.

The Seebeck coefficient value of the HP samples (in absolute value) is slightly lower than that the reported for spark plasma sintered pure Bi_2Te_3 (~ 120-130 μV/K at 325 K)[9,10]. Nevertheless, it should be pointed that at that works, the powders were ground into fine powders by ball milling, so that the deformation-induced donor-like effect would be promoted as proposed by Ionescu et al.[13]. For HP samples, the magnitude of Seebeck coefficient ([*S*]) reaches the maximum value close to 343 K and after that, ([*S*]) is reduced by increasing the temperature. This reduction can be attributed to the bipolar effects (i.e. simultaneous charge/heat transport by holes and electrons). Bismuth telluride is a narrow-band semiconductor (the forbidden energy gap was found to be 0.16 eV at 300 K)[1]. Having a small forbidden gap is generally positive for thermoelectric performance because leads to a higher carrier mobility, however, if the gap is too small electron-hole pairs are produced at the conduction band by thermal excitation of the minority carriers across the forbidden energy gap, and *S* is significantly suppressed because electrons and holes have opposite charges[3]. By this way, the "$10k_BT$ rule" states that good thermoelectric materials should have energy gaps that are $10k_BT_{op}$, where k_B is the Boltzmann constant ($8.617 \cdot 10^{-5}$ eV/K) and T_{op} is the operating temperature of the device respectively[14].

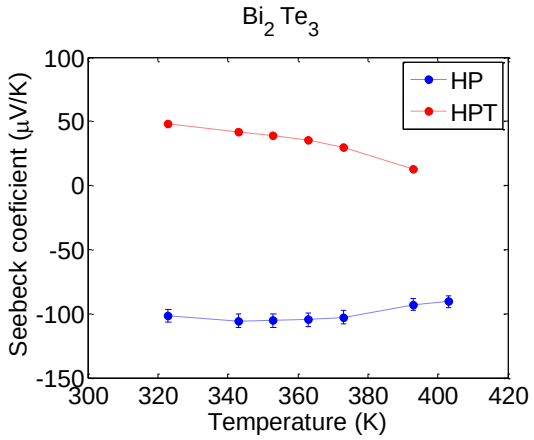

Figure 5.1: Temperature dependence of Seebeck coefficient of pure Bi_2Te_3 HP and HPT samples. HP samples are *n*-type materials whereas HPT samples are *p*-type.

In contrast, as figure 5.1 shows, HPT samples are *p*-type TE materials. For pure Bi_2Te_3, it has been reported that grain boundaries might play the role of acceptors[8]; therefore, the negative carriers introduced to the lattice by the deformation-induced donor-like effect can be compensated with the acceptor role of the boundaries. Note that HPT samples have a very high density of grain boundaries because of their ultrafine-grained microstructure.

The low Seebeck coefficient of the HPT samples indicates that the carrier concentration is far away from the optimum value. Similarly, the abrupt drop of *S* by increasing the temperature shows that HPT-ed pure bismuth telluride is a weak *p*-type semiconductor and hence, mixed conduction is the dominant mechanism to transport charge and heat.

Figure 5.2 shows the temperature dependence of the thermal conductivity (along the axial direction of the disks) of HP and HPT samples. As expected, the grain refinement reduces significantly the thermal conductivity (κ) since phonons are strongly scattered at grain boundaries. Comparing to the coarse-grained polycrystalline samples (HP samples), close to room temperature, κ is reduced up to 45 % obtaining a good experimental reproducibility. Observing κ as a function of the measuring

temperature is evident that in the case of HPT samples, the bipolar thermal conductivity is a significant component of the total thermal conductivity.

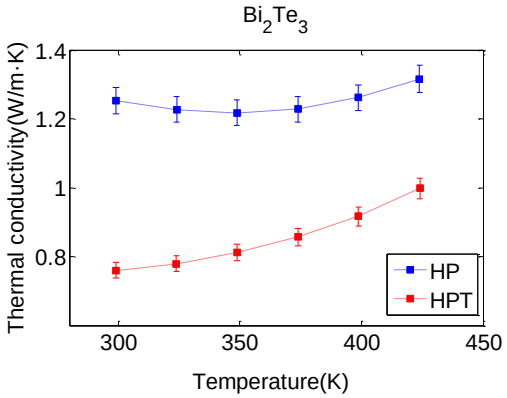

Figure 5.2: Temperature dependence of the thermal conductivity of pure Bi_2Te_3 HP and HPT samples.

The thermal conductivity of insulators and semiconductors in mainly due to the lattice contribution (κ_L), however in the case of heavily doped or near degenerate semiconductors, the electronic (κ_e) and bipolar (κ_b) components, the last one at elevated temperatures, may become significant. Thus, the total thermal conductivity can be expressed as:

$$\kappa_{total} = \kappa_L + \kappa_e + \kappa_b \qquad (5.2)$$

As was discussed in chapter 2, At elevated temperatures ($T >> \theta_D$, where θ_D is the Debye temperature, which is 164.9 K for Bi_2Te_3)[15] κ_L is inversely proportional to temperature (equation 1.19). It is well known that the lattice thermal conductivity is closely related to both, the heat capacity per unit volume (C) and to the mean free path of phonons between collisions (l)[16], (see equation 1.17); at high temperatures, C reaches a constant value which is known as the Dulong and Petit value, whereas l is proportional to $1/T$. At elevated temperatures the number of excited phonons is proportional to T, so the collision frequency between phonons must be proportional to the number of them, and hence $l \propto 1/T$. Thus, κ_L should be $\propto 1/T$ [16].

Similarly assuming a metallic conduction behavior, which is the case of the Bi_2Te_3 based TE materials, the electronic thermal conductivity is also inversely proportional to the temperature as predicted the Wiedemann-Franz law[16]. Thus, the increase of the total thermal conductivity that is shown in figure 5.2 can be attributed to the bipolar effects. In the case of the HP samples, κ is proportional to $1/T$ until ~350 K, coinciding with the temperature in which mixed conduction takes place (figure 5.1). In contrast, the thermal conductivity of the HPT-ed samples increases monotonously as T increases because the mixed conduction is present in all measured temperature range.

Analyzing those results we can conclude that HPT processing is a very suitable method to reduce the thermal conductivity of pure Bi_2Te_3, however, since this compound is a weak *p*-type semiconductor; the plastic deformation has a great effect on its carrier concentration and pure Bi_2Te is not a suitable candidate to explore if HPT improves its thermoelectric properties.

5.2.2. Pure Sb_2Te_3

Since Ioffe proposed that the formation of solid solutions between two semiconductors that have the same crystal structure leads to a lower thermal conductivity, pure Bi_2Te_3 has been repeatedly alloyed with Sb_2Te_3 to produce *p*-type $Sb_{2-x}Bi_xTe_3$ solid solutions. As described in chapter 2, sections 2.4 and 2.7, optimum alloying of Bi_2Te_3 with Sb_2Te_3 besides reducing the thermal conductivity improves the so-called weighted mobility and optimizes the carrier concentration[3], which enhances the dimensionless thermoelectric figure of merit (zT).

Undoped Sb_2Te_3, owing to the large difference in electronegativity and atomic size between Sb and Te atoms[4] exhibits very strong *p*-type characteristics. Therefore, its carrier behavior is not expected to change from *p*-type to *n*-type as a result of the induced lattice defects due to severe plastic deformation.

Thus, pure Sb_2Te_3 was processed by HPT to study the effect of SPD on its thermoelectric properties. Figure 5.3 shows the transport properties as a function of temperature for HP-ed and HPT-ed pure Sb_2Te_3 samples. Both samples have positive Seebeck coefficients indicating that they are *p*-type semiconductors. However, *S* is significantly higher after severe plastic deformation. The Seebeck coefficient (*S*) and electrical resistivity *(ρ*) in terms of the carrier concentration (*n*) can be expressed as follows[1]:

$$S = \pm \frac{k_B}{e}\left((r+2) + \ln \frac{2(2\pi m^* k_B T)^{3/2}}{h^3 n} \right) \quad (5.3)$$

$$\rho = \frac{1}{ne\mu} \quad (5.4)$$

Here, k_B is the Boltzmann's constant, *e* is the electron charge, *r* is the scattering factor, m^* is effective mass, *h* is the Planck constant, and μ is the carrier mobility. Therefore, as equations 5.3 and 5.4 shows, *S* and ρ can be increased by reducing the carrier concentration. Thus, the simultaneous increase of *S* and ρ after severe plastic deformation process can be attributed to the reduction of the hole concentration owing to the deformation-induced donor-like effect that introduces a excess of negative carriers in the lattice. Similarly, the high density of defects as such grain boundaries and dislocations can affect negatively the mobility of the free carriers decreasing the electrical conductivity (σ) of the severely deformed samples.

From an almost linearly variation of the Seebeck coefficient with respect to temperature *S*(*T*) one can extract the charge carrier density, *n*, employing Mott's formula[17]:

$$S = \frac{\pi^2 k_b^2 T}{3e} \frac{d \log[\sigma(E)]}{dE}\bigg|_{E=E_F} \quad (5.5)$$

Assuming, an isotropic parabolic band and acoustic-mode lattice scattering ($r = -1/2$), Mott's formula can be rewritten as[18]:

$$S = \frac{8\pi^2 k_b^2}{3eh^2} m^* T \left(\frac{4\pi}{3n}\right)^{2/3} \quad (5.6)$$

Due to the anisotropy of the ellipsoidal hole pockets, the effective mass of the upper and lower valence bands in Sb_2Te_3 varies from $m^*=0.34m_e$ to $1.24m_e$ [19]. Assuming that Sb_2Te_3 has six valleys, and the effective masses along the axes of symmetry (m_1,m_2,m_3) within each valley reported by Yavorsky et al.[20], m^* is equal to $0.203m_e$ ($m^* = N_V^{2/3}(m_1 m_2 m_3)^{1/3}$), where N_V is the number of valleys. The estimated carrier concentration for HP and HPT samples is $3.46 \cdot 10^{20}$ cm^{-3} and $2.38 \cdot 10^{20}$ cm^{-3}, respectively (table 5.II). The estimated value for n for HP samples is close to the reported one ($n \sim 3.1 \cdot 10^{20}$ cm^{-3} at 300 K) for melt-spun and spark-plasma-sintered pure Sb_2Te_3 [21].

Table 5.II: estimated charge carrier density employing Mott's formula ($m^*=0.203m_e$) for pure Sb_2Te_3 HP and HPT samples

Sample	n(cm^{-3})
HP	$3.46 \cdot 10^{20}$
HPT	$2.38 \cdot 10^{20}$

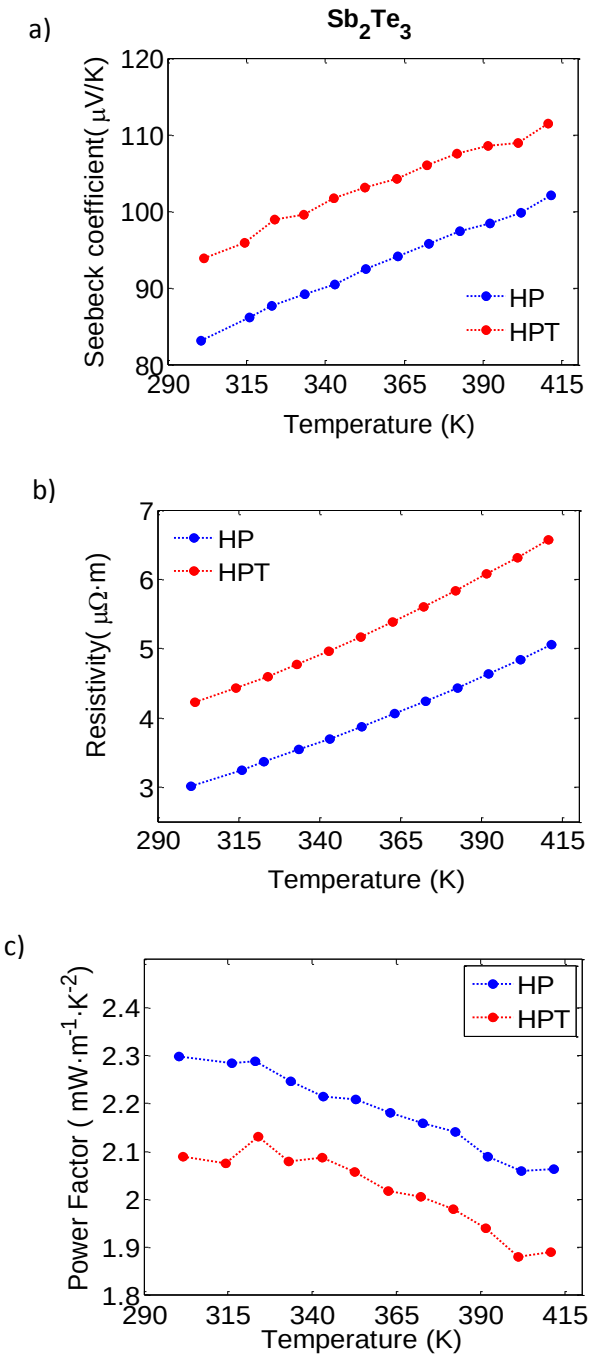

Figure 5.3: Transport properties of HP-ed and HPT-ed pure Sb_2Te_3 samples. a) Seebeck coefficient, b) Resistivity c) Power factor.

Although the *PF* after HPT is about a 10 % lower, the axial thermal conductivity is notoriously reduced (figure 5.4) due to the phonon grain boundary scattering (as in the case of pure Bi_2Te_3) and this leads to a significant improvement of the dimensionless figure of merit (figure 5.5). However, it should be noted that the restrictions in sample dimension do not allow the in-plane thermal conductivity measurement of the HPT samples. Both HP and HPT samples are highly textured having the *c*-axis preferably aligned parallel to the macroscopic disk axis (see section 4.5); consequently the in-plane thermal conductivity should be substantively higher than the out-of-plane one. For single crystalline Sb_2Te_3 the thermal conductivity in the basal plane is 3.5 times higher than along the c axis; i.e. $\kappa_{11} / \kappa_{33} = 3.5$ [22]

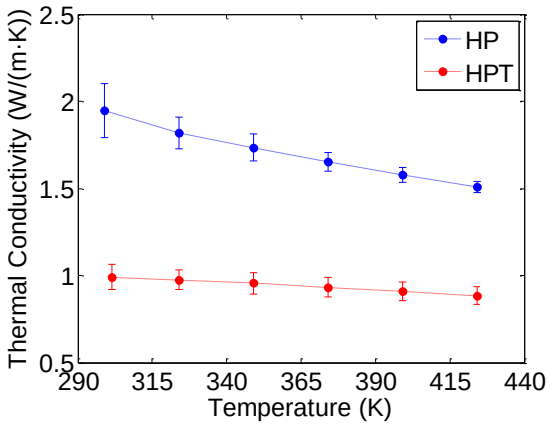

Figure 5.4: Temperature dependence of the axial thermal conductivity of pure Sb_2Te_3 HP and HPT samples.

Summarizing, the enhancement of the dimensionless thermoelectric figure of merit in high pressure torsioned Sb_2Te_3 samples is mainly due to the ultrafine-grained microstructure; low to middle-frequency phonons are scattered at the high density of lattice defects such as grain boundaries, point defects and dislocations decreasing the thermal conductivity without affecting greatly the power factor. Pure Sb_2Te_3 displays near-metallic properties with a low Seebeck coefficient and a high thermal conductivity, thus its thermoelectric properties are not excellent. However, this problem

can be solved by producing $Sb_{2-x}Bi_xTe_3$ solid solutions, which in an optimum stoichiometry, simultaneously reduce the thermal conductivity and improve the weighted mobility.

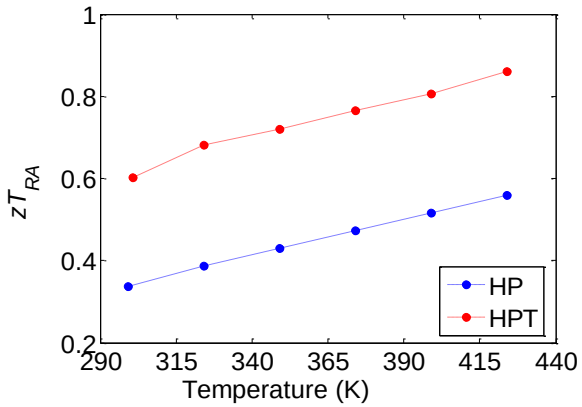

Figure 5.5: Dimensionless figure of merit zT_{RA} *(PF* was determined in the disk plane whereas the thermal conductivity was measured along the disk axis) of pure Sb_2Te_3 samples.

The figure of merit (zT_{RR}) with both electrical and thermal properties measured along in-plane direction will be estimated by taking into account the crystallographic texture of the polycrystalline samples and the thermal anisotropy ratio of the single crystalline samples. This issue will be discussed in section 5.5.

5.3. Adjusting the chemical composition of $Sb_{2-x}Bi_xTe_3$ alloys to improve the thermoelectric efficiency.

In the present section the thermoelectric properties of severely deformed $Sb_{2-x}Bi_xTe_3$ solid solutions will be studied. It is well known that $Sb_{1.5}Bi_{0.5}Te_3$ compounds have the optimal hole concentration and the maximum *zT* value[23] for unidirectionally solidified ingots. However, as I mentioned above, plastic deformation produces non-basal slip in Bi_2Te_3-based alloys, which can generate excess negative carriers (called deformation-induced donor-like effect), changing the optimum carrier concentration. Consequently, for HPT processing the optimum stoichiometry which will lead to the best *zT* is not known yet. For instance, Hu et al.[11] showed that for polycrystalline samples produced by hot pressing and subsequent hot deformation process the optimum composition is shifted to a higher Sb content due to the deformation induced donor-like effect.

In this work, $Sb_{1.5}Bi_{0.5}Te_3$ and $Sb_{1.6}Bi_{0.4}Te_3$ solid solutions were fabricated by melting and solidification of raw Bi_2Te_3 and Sb_2Te_3 powders.

Figure 5.6 shows the transport properties as a function of temperature for HP-ed and HPT-ed $Sb_{1.5}Bi_{0.5}Te_3$ samples. Since HPT processing simultaneously reduces the Seebeck coefficient and the resistivity, it seems that the hole concentration of the severely deformed samples is higher. Similar results have been reported for equal channel angular pressed $Sb_{1.52}Bi_{0.48}Te_3$ (with 4.0% excess Te, and 1.8 % Se as dopant)[24] or for nanocrystalline *p*-type BiSbTe alloys made by hot- pressing the ball-milled nanopowders from crystalline ingots[25,26]. We believe that this effect can be closely related to the high grain boundary density of HPT samples. Poudel et al.[25] suggested that antisite defects are more likely to occur at interfaces being responsible for charge buildup at grain boundaries. Therefore, antisite defects increase the hole density in the interfaces which leads to rising the net hole concentration.

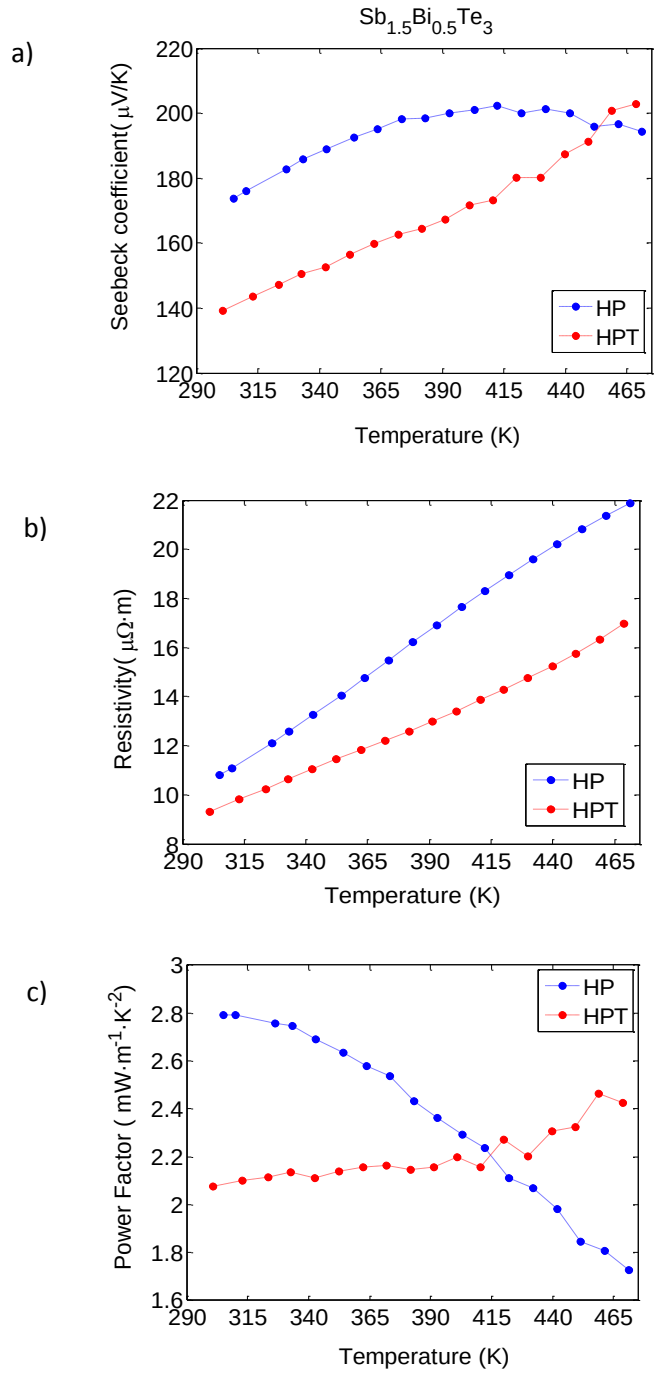

Figure 5.6: Transport properties of $Sb_{1.5}$ $Bi_{0.5}Te_3$ HP-ed and HPT-ed samples. a) Seebeck coefficient, b) Resistivity c) Power factor.

High-resolution transmission electron microscopy (HRTEM) images support this idea, Lan, Y. et al.[27] showed that about 50 % of the grains in the nanograined bulk material prepared by a ball-milling and hot-pressing method are surrounded by a nanometric thick interface region which is about 4 nm thick and slightly bismuth-rich (figure 5.7). The authors attributed the Bi excess to the formation of bismuth antisite defects (i.e. Bi atoms replacing Te atoms) which creates a hole carrier[28]. Similarly, Bi antisite defects induce Bi vacancies inside the grain which donates three holes more. In this way, an excess of holes is introduced into the lattice decreasing both, the electrical resistivity, and the Seebeck coefficient.

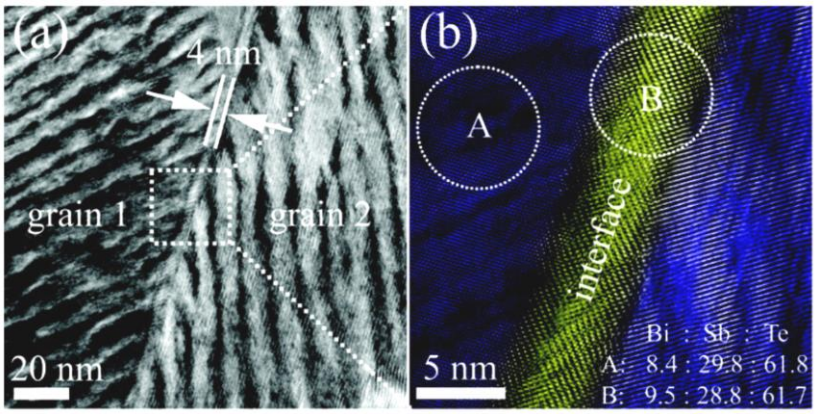

Figure 5.7: a) TEM and b) HRTEM images of the bismuth-rich interface region between two grains in the nanograined bulk material prepared by a ball-milling and hot-pressing method. The dotted circles indicate the region in which energy dispersive X-ray (EDS) analyses were performed (chemical composition for each region is given in atomic %). [27]

As figure 5.6 shows, for HP samples the Seebeck coefficient reaches the maximum value at 400 K, after that point the bipolar conduction is very pronounced, consequently *S* is degraded while at the same time the thermal conductivity increases (figure 5.8) because of the bipolar contribution to the electronic thermal conductivity. However, it is evident that HPT processing reduces significantly the bipolar conduction. Since at the interfaces, due to the Bi antisite defects, the hole concentration is higher than inside the grain;

an electrostatic potential is generated at grain boundaries. As a result, grain boundaries preferentially scatter electrons, the bipolar conduction is reduced and this leads to an higher power factor at elevated temperatures[27].

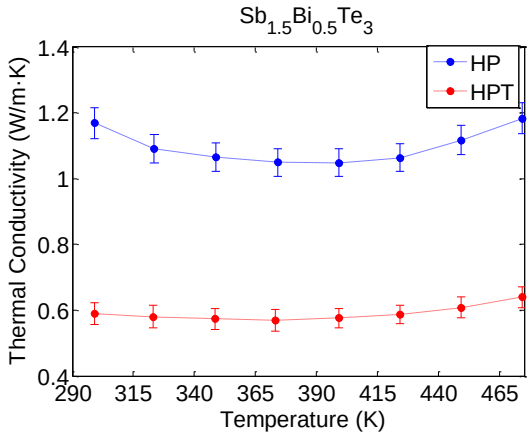

Figure 5.8: Temperature dependence of the thermal conductivity of $Sb_{1.5}$ $Bi_{0.5}Te_3$ HP and HPT samples.

Thus, HPT processing results in a high density of crystal lattice defects, in particular, vacancies, dislocations and grain boundaries, that act as phonon scattering centers largely reducing the thermal conductivity (close to a 50%). Additionally, since the grain boundaries preferentially scatter electrons, which results in a reduction of the bipolar conduction, the *PF* is enhanced at elevated temperatures. Consequently, HPT processing largely enhances zT_{RA} (figure 5.9). However, after HPT the hole concentration drastically increases shifting from the optimum value; consequently, to improve even more the dimensionless thermoelectric figure of merit, donor doping is necessary. Reducing the lattice defects by annealing treatments could be another option to control and optimize the carrier concentration. Those aspects will be discussed in the next section.

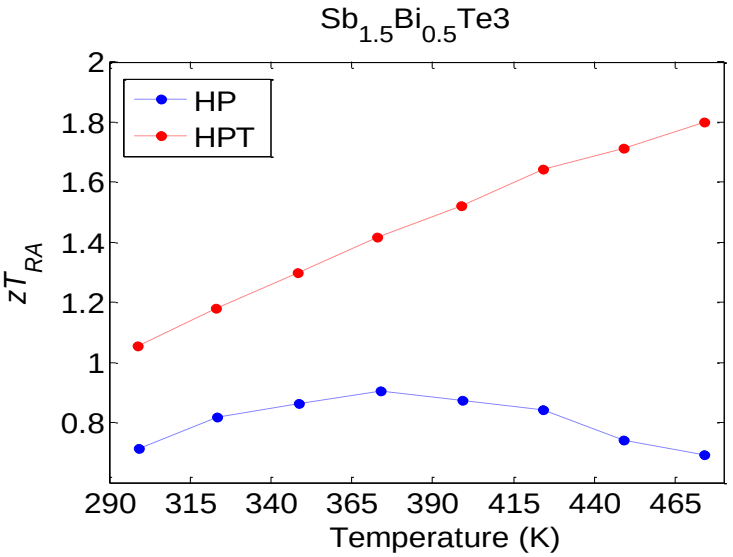

Figure 5.9: Dimensionless figure of merit zT_{RA} (*PF* was determined in the disk plane whereas the thermal conductivity was measured along the disk axis) of $Sb_{1.5}$ $Bi_{0.5}Te_3$ samples.

Similar results were obtained for $Sb_{1.6}Bi_{0.4}Te_3$ compounds. As expected, the hole concentration increases by increasing the Sb amount. Thus, this compound displays a lower Seebeck coefficient and a higher electrical conductivity, however, the power factor is higher than for $Sb_{1.5}Bi_{0.5}Te_3$ (figure 5.10).

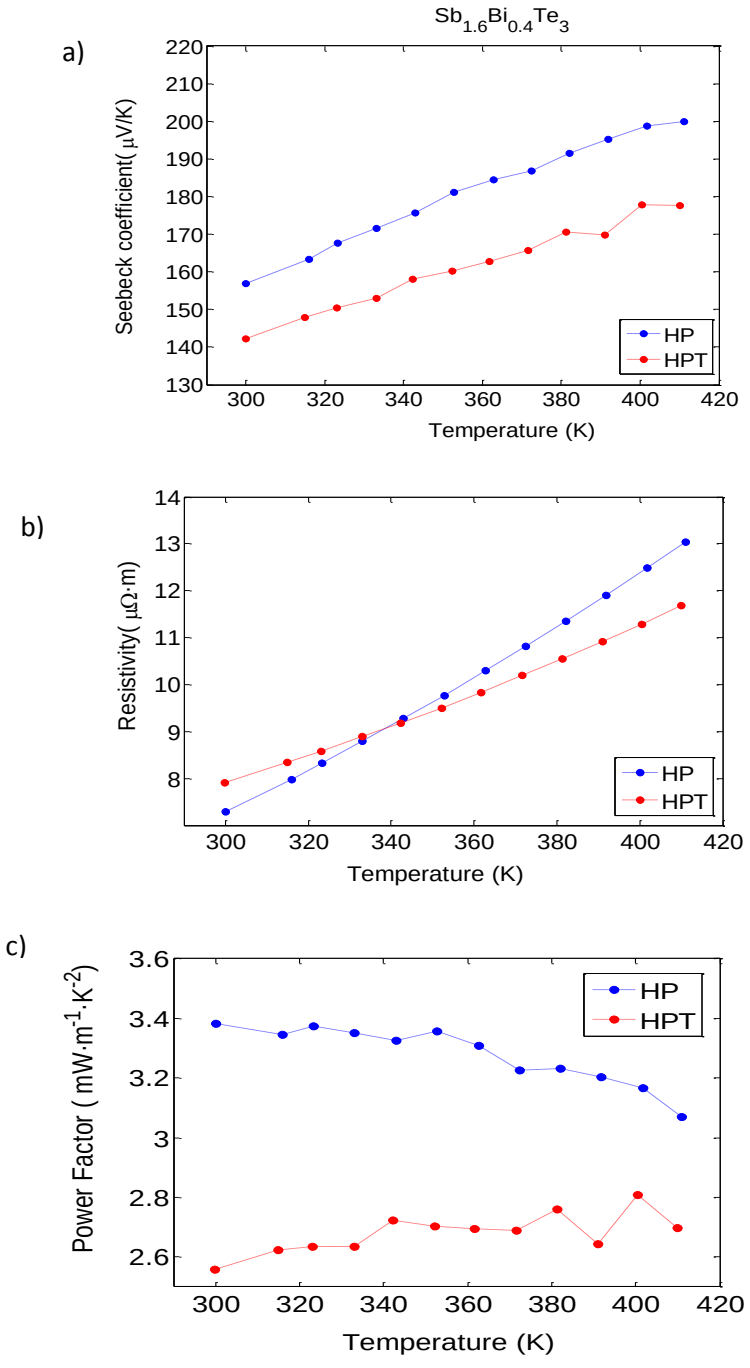

Figure 5.10: Transport properties of $Sb_{1.6}$ $Bi_{0.4}Te_3$ HP-ed and HPT-ed samples. a) Seebeck coefficient, b) Resistivity c) Power factor.

The thermoelectric properties of the studied HPT samples are summarized in figure 5.11. The $Sb_{1.6}Bi_{0.4}Te_3$ compound exhibits the best thermoelectric performance. As expected the thermal conductivities of the samples increase by increasing the Sb amount. It is well known that the minimum lattice conductivity is found to be when the concentration of Sb_2Te_3 is about 75% and rises rapidly as increasing the Sb amount[3,29] (see figure 2.20). Similarly, the electric conductivity is enhanced by adding more Sb_2Te_3, which increases the electronic thermal conductivity. Thus, since the $Sb_{1.6}Bi_{0.4}Te_3$ compound exhibits a suitable power factor and a low thermal conductivity, it has a very promising thermoelectric performance in a wide temperature range.

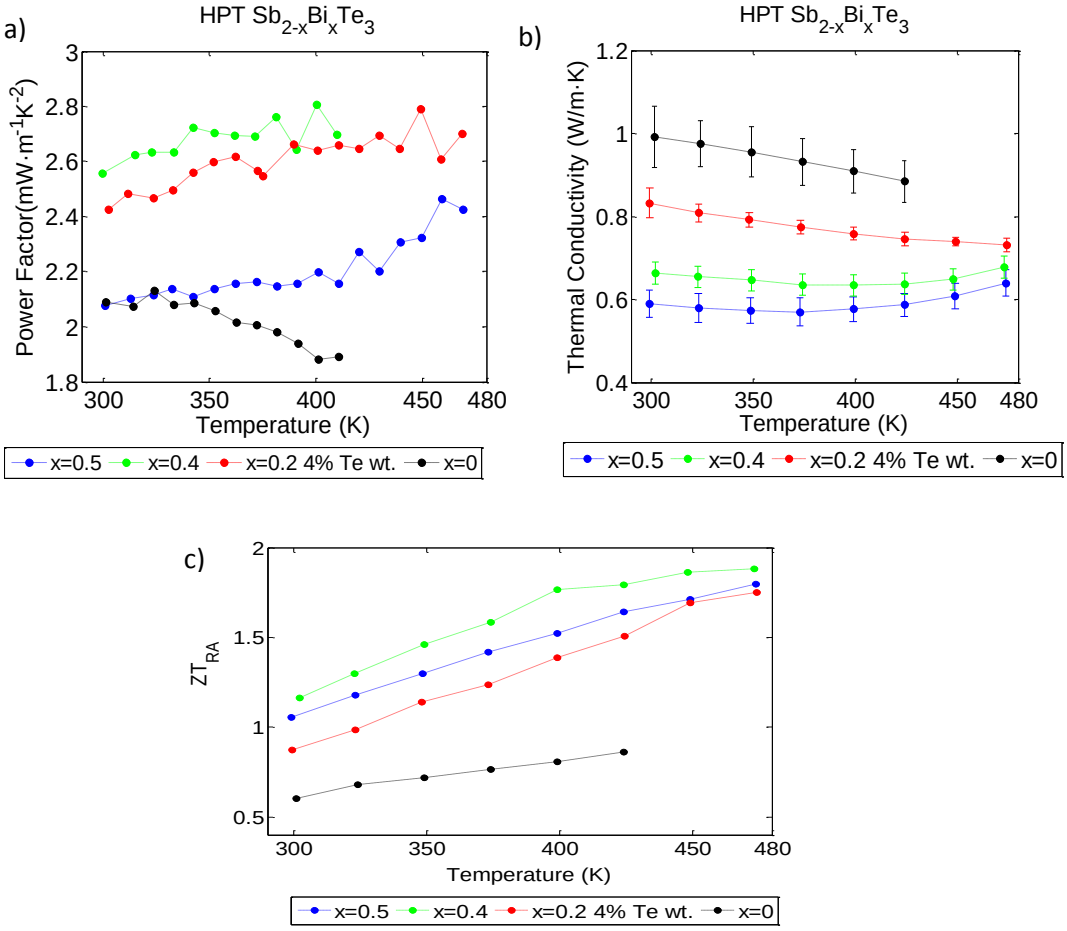

Figure 5.11: Thermoelectric properties of HPT-ed Sb_{2-x} Bi_xTe_3 alloys. a) Power factor b) thermal conductivity c) zT_{RA}

5.4. Controlling the carrier concentration by tellurium doping and thermal treatments.

In the previous section, it was shown that HPT processing is a suitable method to enhance the thermoelectric properties of Bi_2Te_3-based materials. However, as discussed, the plastic deformation induces many lattice defects such vacancies and grain boundaries that are 'electrically-active' and change the carrier concentration. In order to reduce those defects and optimize the carrier concentration, two strategies that can be also combined are proposed.

The first one consists in adding an excess of pure Te as a dopant; it is well-known that, in *p*-type Bi_2Te_3-based alloys, additional holes are created due to the occupation of Te sites with Bi or Sb atoms (i.e. Bi antisite defects). According to Poudel et al.[25] antisite defects are more likely to occur at interfaces; therefore, since HPT samples have a high density of grain boundaries we believe that antistructure defects are easily generated, which cause the increase of the hole concentration of the HPT samples. Thus, the addition of excess Te to the melt might inhibit the formation of anti-site defects; consequently, the carrier concentration of the HPT samples would be closer to the optimum one, which would improve even more the thermoelectric performance. The same strategy is generally used to reduce the hole concentration of unidirectionally grown ingots[23].

The second one consists of performing annealing treatments at relatively low temperatures to reduce the lattice defects while avoiding the grain growth. Annealing treatments promote the diffusion of Te atoms into their own lattice sites which prevent the formation of acceptor-like antisite defects[6]. For instance, Hyun et al.[30] showed that the Seebeck coefficient of mechanically deformed $(Bi_{0.25}Sb_{0.75})_2Te_3$ samples by cold-pressing improves as the annealing time increases and reaches a constant value of about 260 μV/K after being annealed at 623 K for 15 min. In our case, the annealing treatments were carried out at 473 K under helium atmosphere for

20 min. This way, two main effects are pursued: on the one hand, an improvement of the thermoelectric performance of the HPT samples and, on the other hand, a stabilization of the microstructure of the samples (the operating range temperature of Bi_2Te_3-based alloys is usually between RT and 450 K).

Figure 5.12 shows the effect of annealing on the electrical transport properties as a function of the measuring temperature for HP-ed and HPT-ed samples. The annealing treatments were carried out in the Seebeck coefficient/resistivity measuring system (LSR -3 Linseis). Firstly, the samples were heated at a heating rate of 3 K/min from room temperature (RT) up to 473 K and S and ρ were determined during the heating stage. Afterwards, the samples were held at 473 K during 20 min and cooled at the same cooling rate while S and ρ were measured. This cycle was named HP and HPTBan (before annealing) for hot pressed and high pressure torsioned samples, respectively. The same cycle was repeated for HPT samples named as HPTAan (after annealing).

The electrical transport properties of HP samples are not affected by the annealing treatment. It should be noted that the hot-pressing cycle was performed at 723 K; therefore the diffusion of Te atoms into their own lattice sites is promoted during hot-pressing and an additional heat treatment at 473 K will not compensate more acceptor-like antisite-defects.

In contrast, the Seebeck coefficient of HPT samples increases after annealing. At the first thermal treatment, the measured electrical transport properties are not the same at the heating and cooling cycles. However, this short annealing treatment stabilizes the microstructure, and in the second measurement cycle there are not significant differences between the heating and cooling cycles. Apparently, the heat treatment decreases the antistructure defects concentration, which reduces the hole concentration and hence increases strongly the Seebeck coefficient and very slightly the electrical resistivity. As a result, the thermal treatment substantially improves the power factor; specially up to 400 K. Similar results were

reported for SPS-ed $Sb_{1.6}Bi_{0.4}Te_3$, after performing an annealing treatment for 10 h in an Ar-sealed quartz tube in a furnace at 593 K, the hole concentration decreased from $10.3 \cdot 10^{18}$ cm^{-3} to $8.9 \cdot 10^{18}$ cm^{-3} [31].

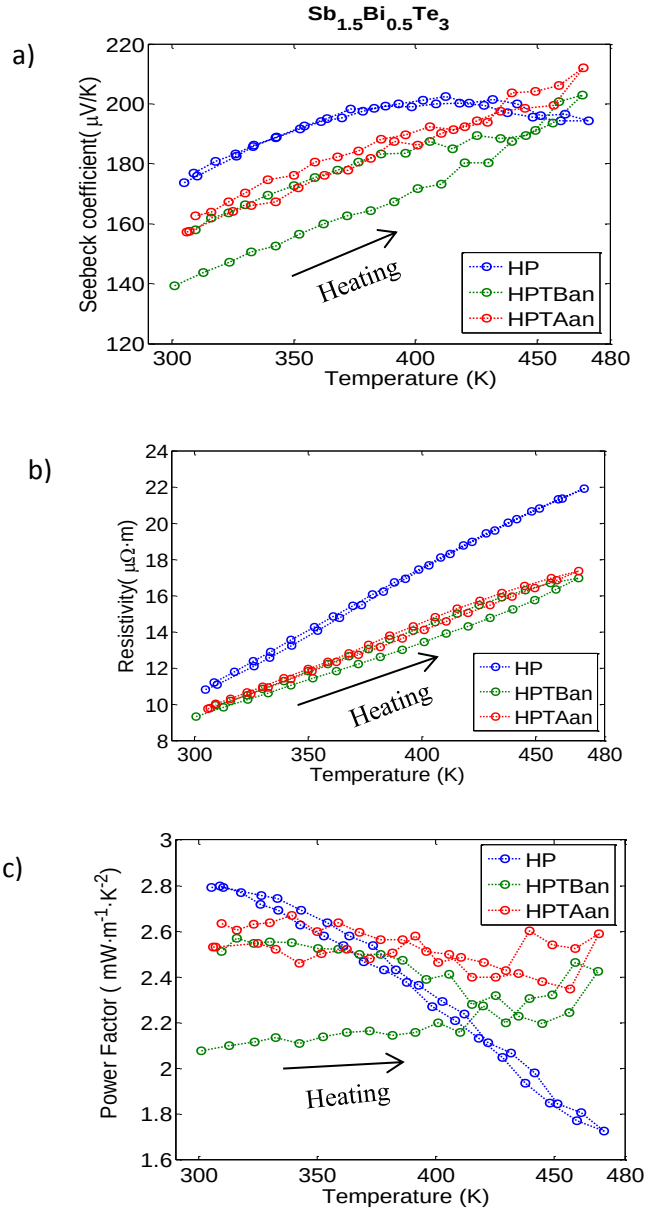

Figure 5.12: Electrical transport properties of HP-ed and HPT-ed $Sb_{1.5}$ $Bi_{0.5}Te_3$ alloys before (HPTBan) and after annealing (HPTAan). a) Seebeck coefficient b) electrical resistivity c) Power factor.

Similarly, an excess (4% wt.) of pure Te was added to the melt in order to compensate the Bi antisite defects and hence improve the thermoelectric efficiency. As expected, Te doping increases the Seebeck coefficient of both HP and HPT samples because it reduces the hole concentration. Nevertheless, the reduction of the hole concentration affects negatively the electrical resistivity and can also reduce the mobility of the free carriers as is reported for other dopants like Se or TeI [32,33]. Thus, the excess of tellurium enhances *S* about a 33% and 27% but reduces the electrical conductivity about a 38% and 46% for HP and HPT respectively (close to RT). This leads to a slight improvement of the power factor close to room temperature (figure 5.13). However, as temperature increases, the electrical transport properties rapidly become degraded. As *p*-type Bi_2Te_3 based materials are narrow gap semiconductors, electrons are easily produced at the conduction band by thermal excitation across the forbidden energy gap. After Te doping, $Sb_{1.5}Bi_{0.5}Te_3$ exhibits lower *p*-type characteristics, therefore the electron-holes ratio at elevated temperatures should be smaller than the undoped one leading to accentuate the bipolar effects.

After adding excess tellurium, the electrical transport properties are barely affected by the annealing treatment; we believe that the excess of tellurium compensates the Te vacancies, which inhibit the formation of antistructure defects during severe plastic deformation.

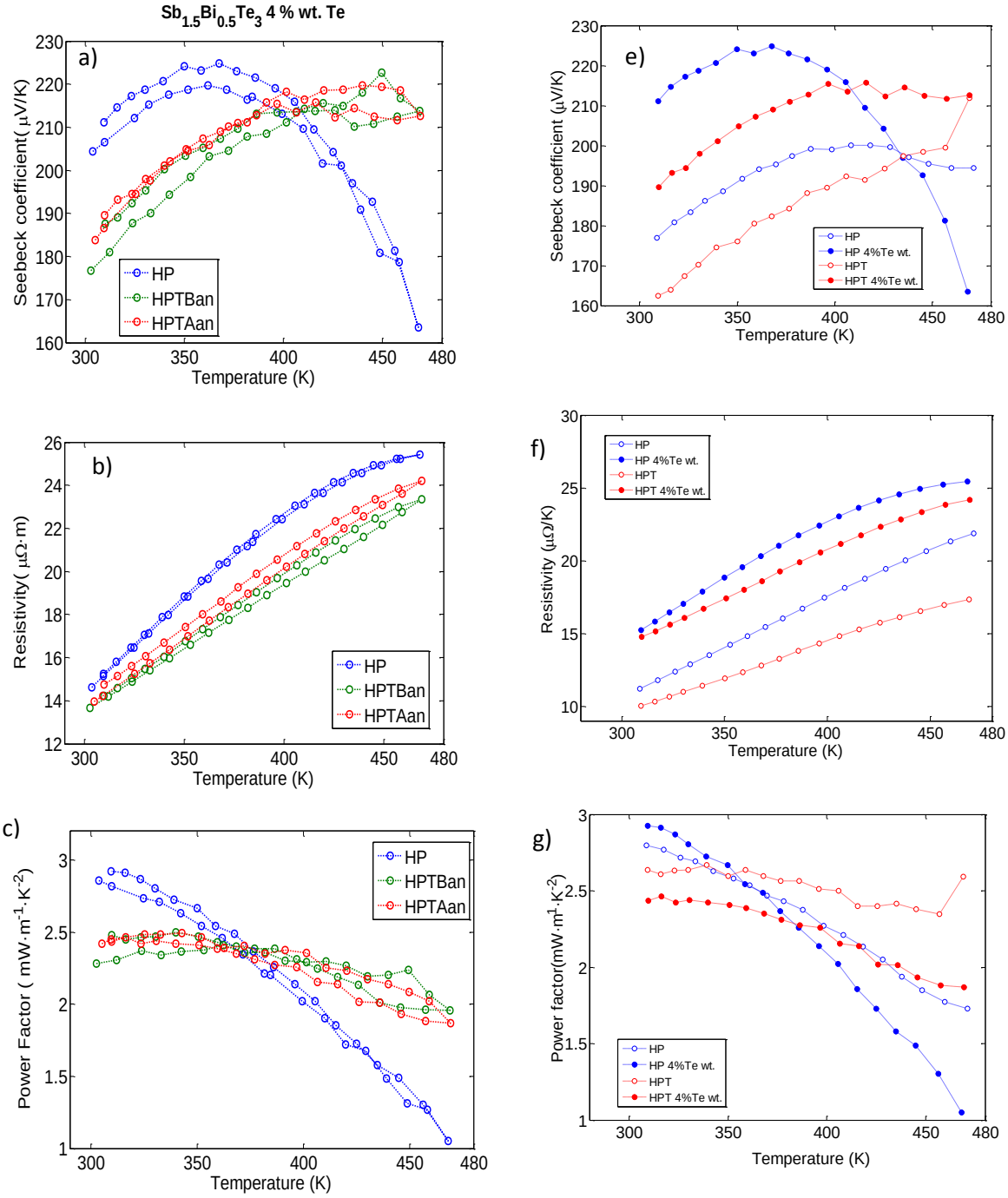

Figure 5.13: Electrical transport properties of HP-ed and HPT-ed $Sb_{1.5}$ $Bi_{0.5}Te_3$ samples before (HPTBan) and after (HPTAan) annealing. a) Seebeck coefficient b) electrical resistivity c) Power factor. e).f) g) Te dopping effect on the Te properties of $Sb_{1.5}$ $Bi_{0.5}Te_3$ samples after annealing.

Thermal treatments are satisfactory to enhance the electrical transport properties of HPT samples by reducing the antisite defect. Now, the important question that must be answered is whether or not the thermal conductivity is affected by the annealing treatments. The thermal conductivities of doped and undoped HPT-ed $Sb_{1.5}$ $Bi_{0.5}Te_3$ compounds are shown in figure 5.14. As it can be seen, the subsequent heating and cooling cycles do not alter the measurement, which means that the reached saturated grain size is stable up to 473 K. The thermal stability of SPD microstructures was discussed in section 4.4.2. It should be pointed that $Sb_{1.5}$ $Bi_{0.5}Te_3$ alloys are heavily doped, having inherently a high density of point defects that effectively scatter long to middle-frequency phonons. So, reducing antisite defects generated by SPD should not significantly decrease the thermal conductivity (the density of points defects will not be greatly reduced by the annealing). On the other hand, the annealing treatment decreases the electronic thermal conductivity due to the increase in resistivity; these facts may explain why the thermal conductivity is barely altered after the annealing treatment.

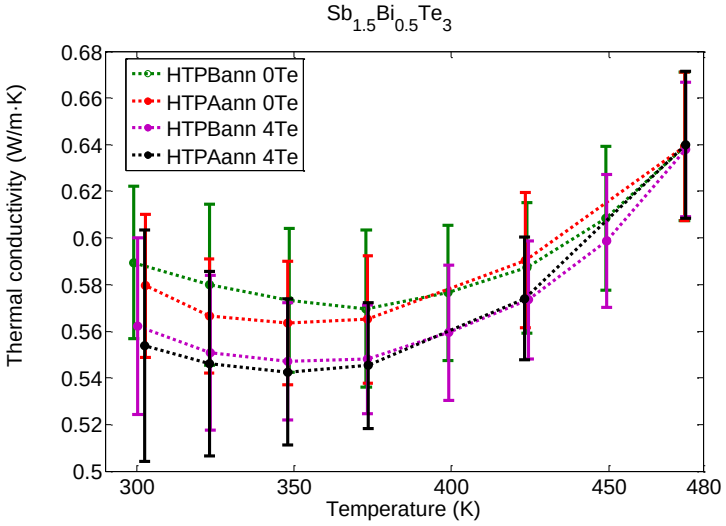

Figure 5.14: Thermal conductivities of the doped and undoped $Sb_{1.5}$ $Bi_{0.5}Te_3$ alloys during the subsequent heating and cooling cycles. As seen, the thermal conductivity is unaffected by the cycles.

Adding Te as a dopant reduces slightly the thermal conductivity; a similar behavior has been reported for unidirectionally grown ingots[34] and SPS-ed samples[35].

Similar results have been observed for $Sb_{1.6}Bi_{0.4}Te_3$ compounds. As figure 5.15 shows, performing an annealing treatment at a relatively low temperature (473 K) after SPD processing drastically improves its electrical transport properties. Reducing the excess of antisite defects leads to a considerable improvement of the Seebeck coefficient without decreasing excessively the electrical conductivity. Thus, after the heat treatment the HPT-ed compounds exhibit a satisfactory power factor value of about 3.6 $mW \cdot m^{-1} \cdot K^{-2}$ close to RT.

As in the case of $Sb_{1.5}Bi_{0.5}Te_3$, doping with tellurium also degrades the transport properties of $Sb_{1.6}Bi_{0.4}Te_3$. After doping the electrical resistivity significantly increases, decreasing the power factor (figure 5.16). In this compound, the annealing treatment enhances the electrical transport properties, but the improvement is significantly lower than the reached one for its undoped counterpart. Thus, as for $Sb_{1.5}Bi_{0.5}Te_3$, adding pure Te inhibits the formation of antisite defects during SPD, however, it seems that tellurium doping affects negatively the carrier mobility; hence, the simultaneous reduction of hole concentration and its mobility cause a substantial increment of its resistivity.
Conversely, when the undoped samples are annealed, the antisite defects are reduced by diffusion of Te atoms into their own lattice sites, decreasing the excess of hole concentration without affecting its mobility. Therefore, it can be concluded that performing annealing treatments after HPT processing is a better strategy to reduce the excess of holes.

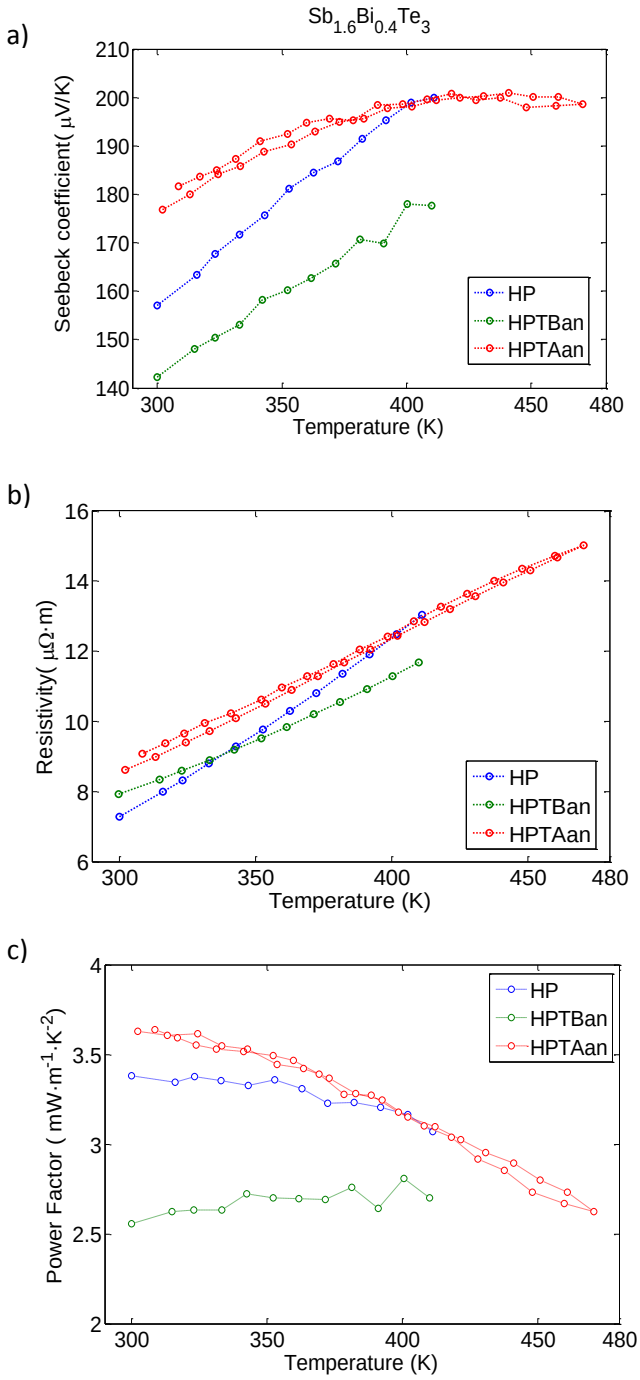

Figure 5.15: Electrical transport properties of HP-ed and HPT-ed $Sb_{1.6}$ $Bi_{0.4}Te_3$ samples before (HPTBan) and after (HPTAan) annealing. a) Seebeck coefficient b) electrical resistivity c) Power factor.

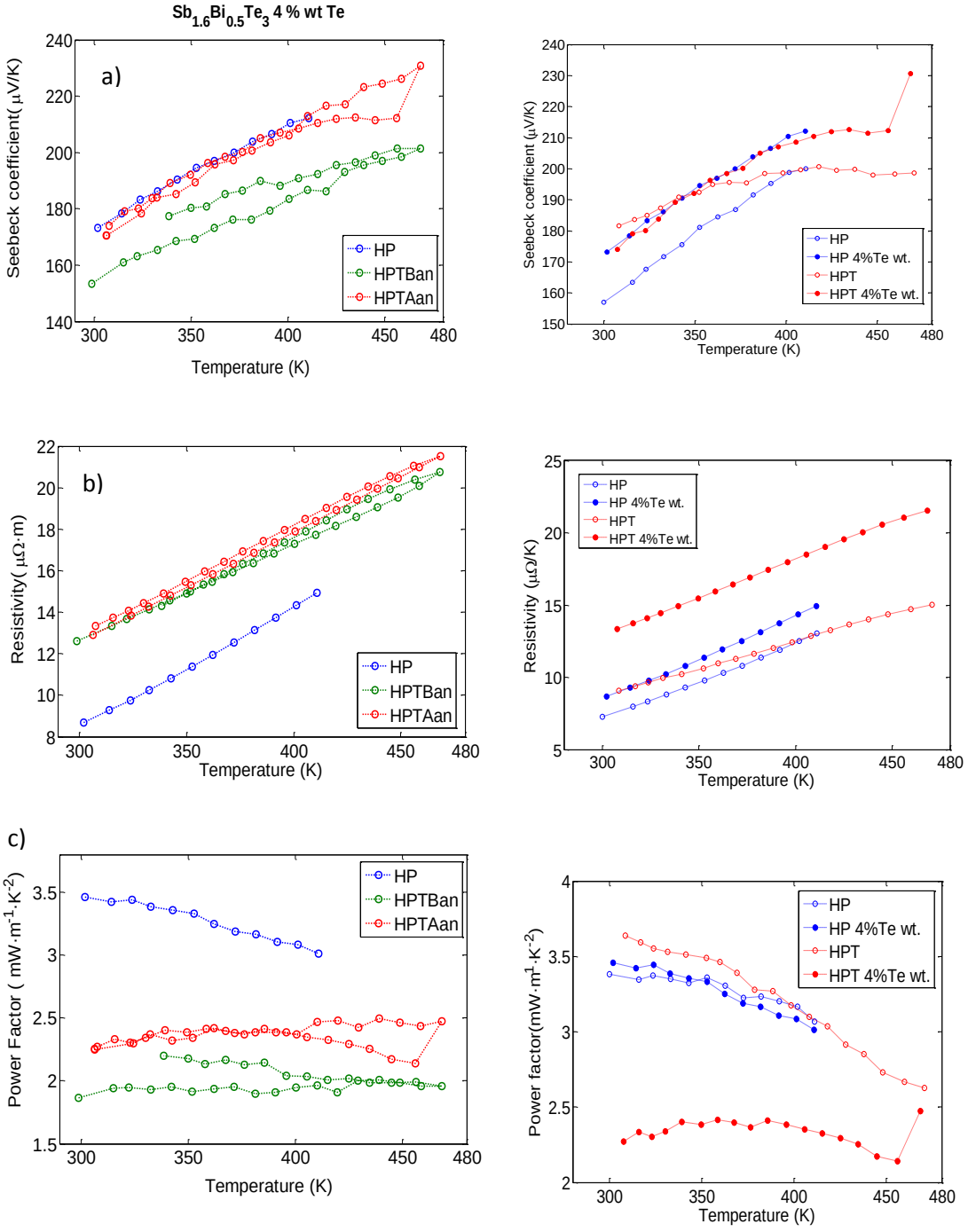

Figure 5.16: Electrical transport properties of HP-ed and HPT-ed Te doped (4 %wt.) $Sb_{1.6}$ $Bi_{0.4}Te_3$ samples before (HPTBan) and after (HPTAan) annealing. a) Seebeck coefficient b) electrical resistivity c) Power factor. e).f) g) Te dopping effect on the Te properties of $Sb_{1.6}$ $Bi_{0.4}Te_3$ samples after annealing.

Finally, the thermoelectric properties of $Sb_{1.8}Bi_{0.2}Te_3$ with 4.0% Te excess in wt. % as a dopant were investigated. Because of the high content of Sb, it was expected that the compound would display near-metallic properties. Adding pure telluride reduces the hole concentration enhancing the Seebeck coefficient[34,36] Thus, a decrease in the hole concentration and an improvement of the thermoelectric performance was expected. The transport properties of hot-pressed and high pressure torsioned samples are shown in figure 5.17.

Despite adding pure Te, the compound shows a near-metallic behavior; nevertheless, the electrical transport properties are quite satisfactory.

The $Sb_{1.8}Bi_{0.2}Te_3$ compound with 4% wt. of Te excess displays good TE properties at high temperatures because the forbidden energy gap (E_g) becomes bigger as increasing the Sb concentration, (E_g is equal to 0.16, 0.19 and 0.3 eV for Bi_2Te_3, $Sb_{1.5}Bi_{0.5}Te_3$, and Sb_2Te_3, respectively)[1] which hinders the mixed conduction. Also, the hole concentration increases as increases the Sb amount; consequently, at the usual operation temperature, it is not easy the excitation of sufficient minority electrons across the forbidden energy gap that degrade the thermoelectric performance. Thus, it seems that this compound is quite interesting to be used as thermoelectric generator close to 250° C.

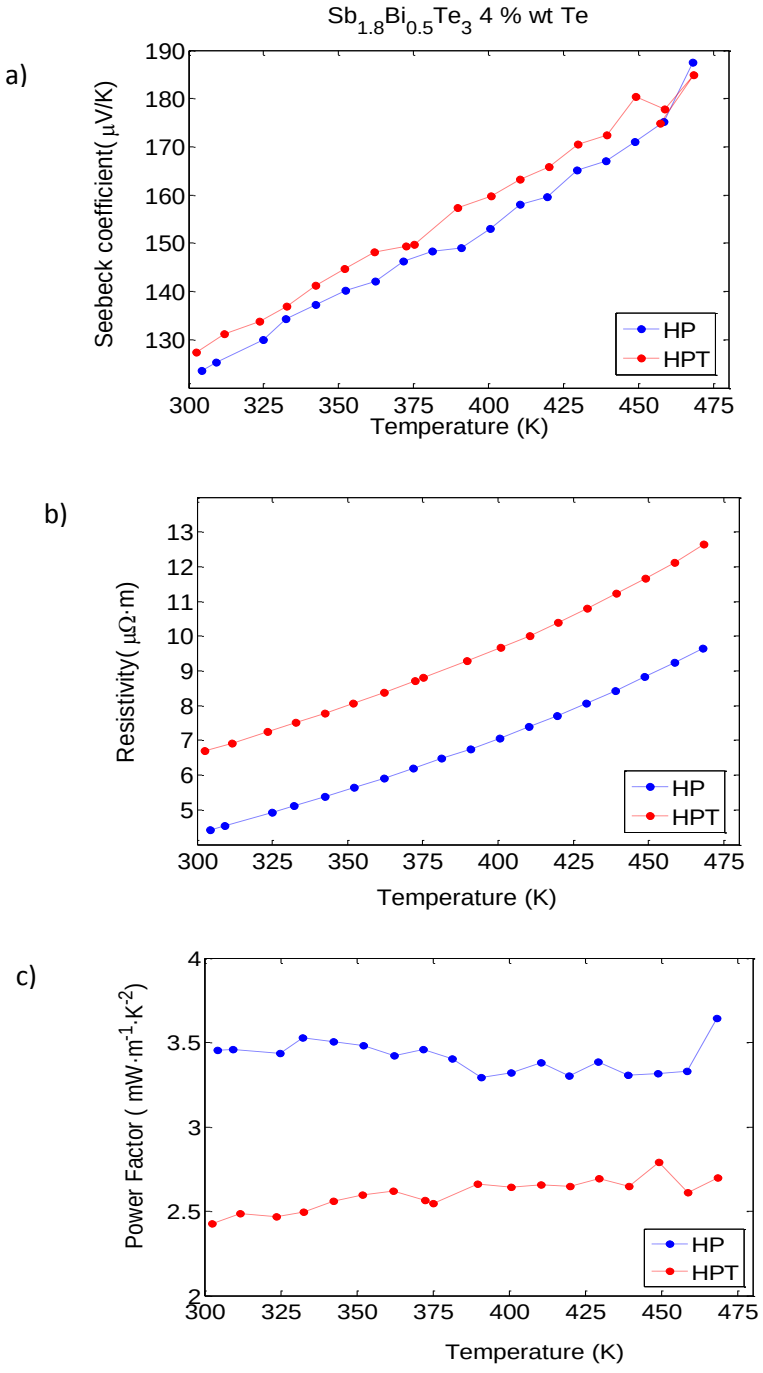

Figure 5.17: Transport properties of $Sb_{1.8}$ $Bi_{0.2}Te_3$ (Te doped 4 % wt.). HP-ed and HPT-ed samples. a) Seebeck coefficient, b) Resistivity c) Power factor.

The thermoelectric properties of the studied HPT samples after annealing treatments are summarized in figure 5.18. The best thermoelectric performance is achieved for the undoped $Sb_{1.6}Bi_{0.4}Te_3$ compound, which exhibits a satisfactory performance in all the measured temperature range, having the maximum ZT_{RA} value at 425 K.

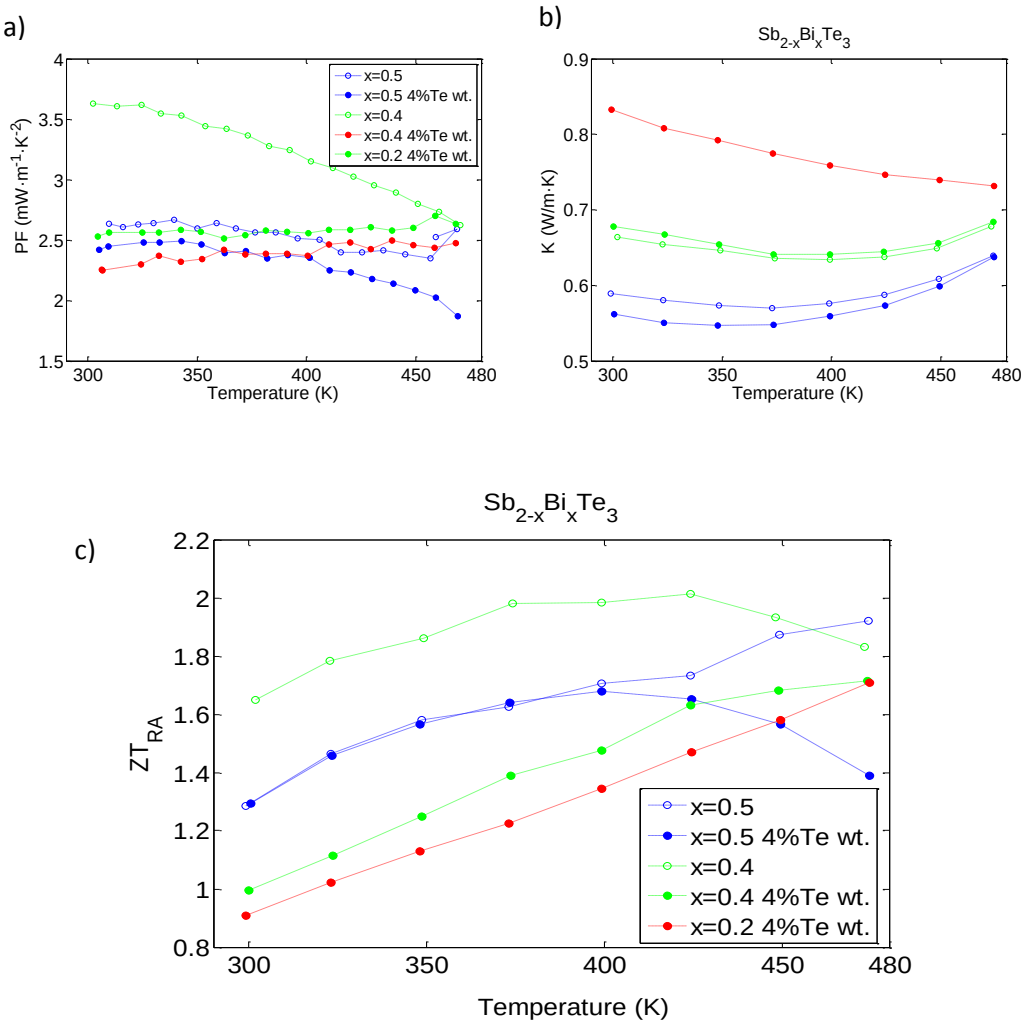

Figure 5.18: Thermoelectric properties of Sb_{2-x} Bi_xTe_3 alloys after annealing treatment a) Power factor b) Thermal conductivity c) ZT_{RA}

5.5. Estimating the in-plane thermal conductivity

Due to the lack of sufficiently thick samples it was not possible for us to obtain the in-plane thermal conductivity of HPT samples. HPT samples are highly textured having the *c*-axis preferably aligned parallel to the macroscopic disk axis. Since the thermal conductivity in the basal plane is higher than along the *c*-axis, the in-plane thermal conductivity of HPT samples should be substantially higher than the out-of-plane one. This issue leads to an overestimated dimensionless thermoelectric figure of merit when the *PF* is determined in the disk plane and the thermal conductivity is measured along the disk axis (i.e. the zT_{RA} is higher than the zT_{RR}).

The anisotropy ratio $(\kappa_{11}/\kappa_{33})$ of the Bi_2Te_3-based compounds depends on stoichiometry. For single crystalline (SC) pure Bi_2Te_3, the thermal conductivity in the basal plane is 2 times higher than along the *c* axis[37]. However, this anisotropy ratio is lower for alloyed *n*- and *p*-type compounds. The reported $(\kappa_{11}/\kappa_{33})$ values at room temperature are respectively 1.52 and 1.30 for *n*-type $(Bi_2Te_3)_{90}(Sb_2Te_3)_5(Sb_2Se_3)_5$ and compensated *p*-type $(Sb_2Te_3)_{72}(Bi_2Te3)_{25}(Sb_2Se_3)_3$ semiconductor alloys[38].

Polycrystalline and textured samples also exhibit anisotropic thermal properties. For instance, *p*-type $Bi_{0.4}Sb_{1.6}Te_3$ compounds processed by equal channel angular extrusion exhibit a preferential orientation. After plastic deformation, the (110) plane is preferentially oriented along the perpendicular direction to extrusion whereas the basal planes (001) is oriented along the extrusion direction. The orientation factor (*OF*) of the basal planes with respect to the extrusion direction is about 0.36. Due to the preferential crystal orientation, the thermal conductivity (κ) in the extrusion direction (//) is higher than the measured one along the perpendicular direction to the extrusion axis ($\perp$). The thermal anisotropy $(\kappa_{//}/\kappa_{\perp})$ of those samples is respectively about 1.08 and 1.10 at room temperature and 200° C, and adding a 4% wt. Te does not change significantly this ratio[39].

p -type $Bi_{0.5}Sb_{1.5}Te_3$ compounds sintered by SPS under a high magnetic of 6 T also have a strong *c* axis alignment. Due to the flake-like shape of the

coarse particles, they tend to stack aligned with the *c* axis parallel to the loading direction, similarly the magnetic field helps to align the fine particles. Thus, in compounds processed this way, the crystallographic *c* axis is strongly aligned parallel to the pressing direction and consequently the thermal conductivity along the pressing direction is about 1.25 times lower than the measured one along its normal direction. Table 5.III summarizes the thermal anisotropy ratios that are found in literature for *n*- and *p*-type SC or textured polycrystalline samples. .

Table 5.III: literature review of the thermal anisotropy at room temperature of SC or textured Bi2Te3-based compounds

Compound	$\kappa_{axial}/\kappa_{radial}$ **or** κ_{11}/κ_{33}	**Fabrication method**	**Reference**
SC Bi_2Te_3	2.0	Bridgman type solidification	[37]
SC *n*-type $(Bi_2Te_3)_{90}(Sb_2Te_3)_5(Sb_2Se_3)_5$	1.50	Horizontal Bridgman-grown	[38]
***SC p*-type $(Sb_2Te_3)_{72}(Bi_2Te3)_{25}(Sb_2Se_3)_3$**	1.30	horizontal Bridgman-grown	[38]
$Bi_{0.4}Sb_{1.6}Te_3$	~1.08	equal channel angular extrusion	[39]
$Bi_{0.5}Sb_{1.5}Te_3$	~1.26	SPS+ high magnetic field	[40]
$Bi_{0.5}Sb_{1.5}Te_3$	~1.10	Solidification under a 6 T magnetic field	[41]
$Bi_{0.5}Sb_{1.5}Te_3$	1.09	Cold pressing + sintering	[42]
$Bi_{0.4}Sb_{1.6}Te_3$	1.02	Cold pressing + sintering	[42]
$Bi_{0.3}Sb_{1.7}Te_3$	1.06	Cold pressing + sintering	[42]
$Bi_2Se_{0.3}Te_{2.7}$	1.48	HP+ hot forging	[43]

In the present section, it is shown a simple and novel three step model that allows the estimation of the in-plane thermal conductivity of HPT samples. The model has the following steps:

- First, in-plane (κ_R) and out of plane (κ_A) conductivities are measured on a large reference sample. In our case HP-ed samples with a strong (000l) fiber texture were used as a reference.
- Second, the thermal conductivities in the basal plane (κ_{11}) and along the *c* axis (κ_{33}) of a single crystal are estimated from κ_R and κ_A considering the actual crystallographic texture as determined by EBSD.
- Finally, we estimate κ_R of the HPT samples from κ_A and the crystal texture calculated by EBSD.

To measure κ_R and κ_A of the HP samples, bars of about ~10×14× 20 mm^3 were made by HP as described in section 3.1.2-1. After that, the thermal conductivity along the normal direction (N_D) (i.e axial thermal conductivity) and, transverse (T_D) and reference (R_D) directions (i.e. radial conductivities) were determined by the laser flash method (see figure 5.19). Finally, crystallographic texture measurements were performed by means of the EBSD technique.

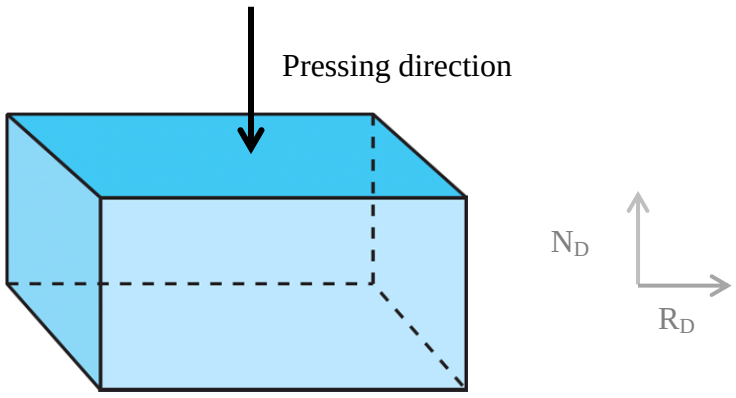

Figure 5.19: Scheme of the HP bar and the reference coordinate.

Figure 5.20 shows the crystallographic texture of the HP bar. The texture of the bar is very similar to that measured on the disk-shaped HP samples (section 4.5). The bar has a strong (000l) fiber texture; the basal planes are oriented close to the pressing direction and near randomly rotated along the perpendicular direction to the pressing direction.

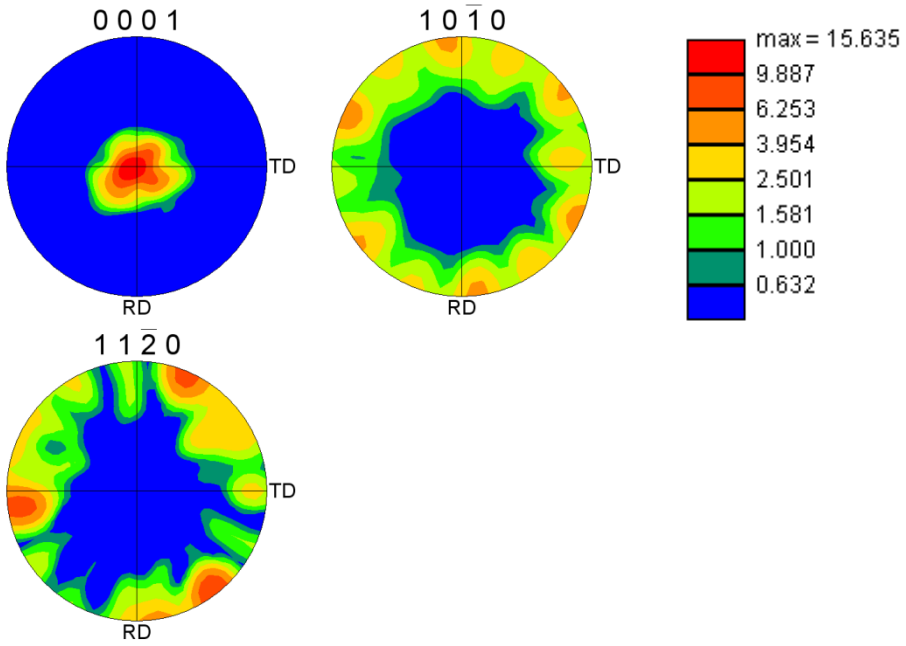

Figure 5.20: $0001, 10\bar{1}0$ and $11\bar{2}0$ pole figures of p-type $Bi_{0.5}Sb_{1.5}Te_3$ HP bar. The basal planes are oriented close to the pressing direction and randomly rotated along the perpendicular direction to the pressing direction

Bi_2Te_3-based alloys have trigonal symmetry which means that the thermal conductivity along the basal plane is isotropic (i.e. $\kappa_{11} = \kappa_{22} \neq \kappa_{33}$)[44]. Since both the HP and HPT samples have textures which are very close to the perfect (000l) fiber texture, the in-plane thermal conductivity should be near-isotropic.

Figure 5.21 shows the thermal conductivities measured along N_D, T_D, and R_D directions. As expected, in the plane perpendicular to the pressing direction the thermal conductivity is almost isotropic and it is significantly

higher than the measured one in the axial direction (N_D direction).

The radial thermal conductivity of HP samples is very similar to the reported value for coarse grained (initial particle size ~180-380 μm) and highly textured *p*-type 20 mol% Bi_2Te_3–80 mol% Sb_2Te_3 Te doped samples[31].

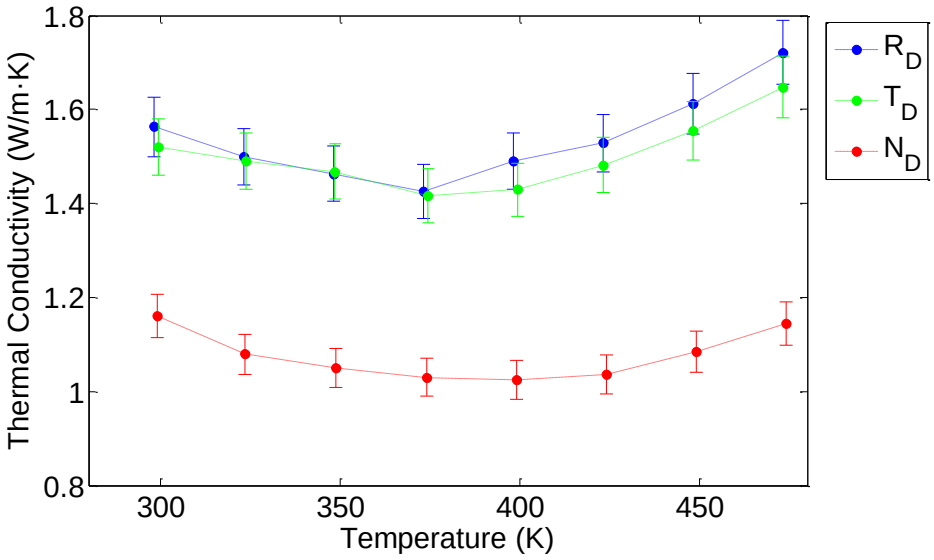

Figure 5.21: Thermal conductivities of HP-ed $Bi_{0.5}Sb_{1.5}Te_3$ samples along R_D, N_D and N_D directions.

It can be easily shown that, for tetragonal, hexagonal or trigonal systems, the thermal conductivity of a SC measured along a general direction oriented at an angle θ to the *c*-axis (figure 5.22) is given by[44]:

$$\begin{aligned}\kappa(\theta) &= \kappa_{11}\sin^2\theta + \kappa_{33}\cos^2\theta \\ &= \kappa_{11} + (\kappa_{33} - \kappa_{11})\cos^2\theta\end{aligned} \qquad (5.7)$$

were κ_{11} and κ_{33} are the thermal conductivities in the basal plane and along the *c* axis of the single crystal.

EBSD measurements allow to determine the crystallographic orientations of a scanned area (for HP samples a 1000×1000 μm^2 with a step of 2 μm was considered) by indexing the Kikuchi lines (see section 3.2.6). The orientation relationship between the macroscopic sample coordinate system

(N_D, T_D, R_D) and the crystal coordinate (*a*,*b*,*c*) system can be defined by a rotation matrix R (crystal → sample) that transforms directions (expressed in sample coordinates) into equivalent directions expressed in crystal coordinates. Thus, the sample N_D vector in the crystal coordinate system is describes as follows:

$$\begin{pmatrix} u \\ v \\ w \end{pmatrix}_{Crystal,N_D} = R^T \begin{pmatrix} 0 \\ 0 \\ 1 \end{pmatrix}_{Sample,N_D} \quad (5.8)$$

where, R^T is the transposed matrix of *R*. The *w* component in equation (5.8) corresponds to the direction cosine of the c-axis, i.e., $w_{ND} = \cos\theta$ in equation (5.7) (see figure 5.22). Thus, if we average $\left\langle w_{ND}^2 \right\rangle_{EBSD} = \left\langle \cos^2 \theta_{ND} \right\rangle_{EBSD}$ over all the points in the EBSD scan and introduce it to the equation (5.7) we get:

$$\kappa_{ND} = \kappa_A = \kappa_{11} + (\kappa_{33} - \kappa_{11}) \left\langle \cos^2 \theta_{ND} \right\rangle_{EBSD} \quad (5.9)$$

Similarly, an arbitrary sample radial vector in the crystal coordinate system can be calculated as follows:

$$\begin{pmatrix} u_\alpha \\ v_\alpha \\ w_\alpha \end{pmatrix}_{Crystal,RD} = R^T \begin{pmatrix} \sin\alpha \\ \cos\alpha \\ 0 \end{pmatrix}_{Sample,RD} ; \text{with } \alpha \in [0, 2\pi] \quad (5.10)$$

Since the thermal conductivity of an arbitrary crystal grain in the sample along the radial direction is not isotropic unless it is perfectly oriented (N_D // *c* axis), a mean radial value of $\left\langle w_\alpha^2 \right\rangle_{RD} = \left(\overline{\cos^2 \theta} \right)_{RD}$ must be calculated before making the average of it over all the points in the EBSD scan, i.e.:

$$\kappa_{RD} = \kappa_R = \kappa_{11} + (\kappa_{33} - \kappa_{11}) \left\langle \left(\overline{\cos^2 \theta} \right)_{RD} \right\rangle_{EBSD} \quad (5.11)$$

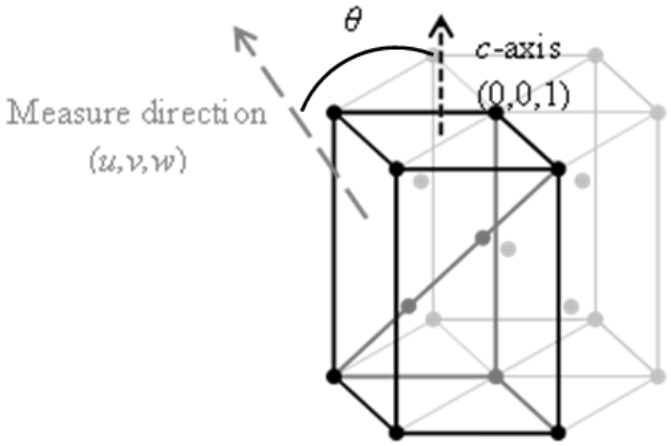

Figure 5.22: Rhombohedral lattice and the components of the thermal conductivity measuring direction in the crystal system.

Thus, by combining equations 5.9 and 5.11 κ_{11} and κ_{33} values can be derived (Table 5.IV) from the κ_A and κ_R obtained from the large HP reference sample. The estimated anisotropy ratio κ_{11}/κ_{33} and κ_{11} are in accordance with literature values[38,45,46].

Table 5.IV: Estimated κ_{11} and κ_{33} values for single crystalline $Bi_{0.5}Sb_{1.5}Te_3$ samples, as a function of temperature.

Temperature (K)	κ_{11} **(W/m·K)**	κ_{33} **(W/m·K)**	κ_{11}/κ_{33}
298	1.58	1.08	1.47
323	1.55	0.99	1.56
348	1.52	0.96	1.58
373	1.46	0.96	1.53
398	1.51	0.94	1.61
423	1.55	0.94	1.65
448	1.63	0.97	1.69
473	1.74	1.02	1.70

Finally, the radial thermal conductivity of HPT samples has been estimated according to the anisotropy ratio evaluated above, their axial thermal conductivity and their crystallographic texture. The results are plotted in figure 5.23

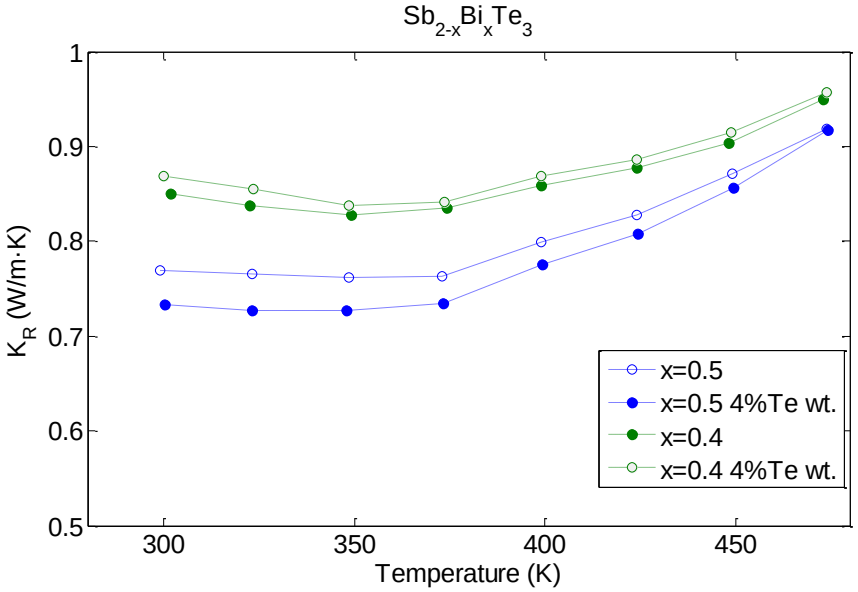

Figure 5.23: Estimated radial thermal conductivities for HPT samples using the proposed model.

Due to the nanosized grain size of the HPT samples their thermal conductivity is comparable or lower than the reported values using more conventional fabrication methods. Table 5.V summarizes the fabrication method and the thermal conductivity values at room temperature that are found in the literature.

Table 5.V: Comparison of the thermal conductivity of $Bi_xSb_{2-x}Te_3$ samples fabricated by different methods.

Compound	Fabrication method	κ (W/m·K)	Reference
***P*-type $(sb,Bi)_2Te_3$**	Ball milling + HP	1.05	[26]
***P*-type $(sb,Bi)_2Te_3$**	Commercial ingot	1.39	[26]
50% mol Sb_2Te_3/ 50% mol Bi_2Te_3 nanocomposite	Hydrothermal systhesis + HP	1.10	[47]
$Bi_{0.52}Sb_{1.48}Te_3$	melt spinning + SPS	0.65	[48]
0.4% SiC doped BiSbTe nanocomposite	Ball milling + SPS	0.82	[49]
$(Bi_{0.24}Sb_{0.76)2}Te_3$ with 4.0% excess Te, and 1.8 % Se	Rotary-die equal channel angular pressing	0.79	[50]
Hot forged BiSbTe nanostructured alloys	Two-step hot forging process	0.99	[51]

5.6. Dimensionless thermoelectric figure of merit (zT_{RR})

Once estimated the radial thermal conductivity of the HPT samples as proposed in the previous section, it is possible to assess the in-plane dimensionless thermoelectric figure of merit of HPT samples (zT_{RR}). Figure 5.24 summarizes the thermoelectric performance of the studied HPT samples. By optimizing the Sb content and controlling the excess of antisite defects through an annealing treatment, the nanostructured and highly textured *p*-type $Bi_{0.4}Sb_{1.6}Te_3$ compound shows an excellent thermoelectric performance. The highest dimensionless figure of merit $zT_{RR,max}$ reaches 1.51 at 374 K. Besides, since electrons are more effectively scattered than holes at the grain boundaries, the bipolar conduction is drastically suppressed in HPT samples; consequently, there is a significant improvement of the average $zT_{RR,av}$ throughout the studied temperature range (RT-473 k), which is 1.41 for the undoped and annealed $Bi_{0.4}Sb_{1.6}Te_3$ sample (Figure 5.24 e).

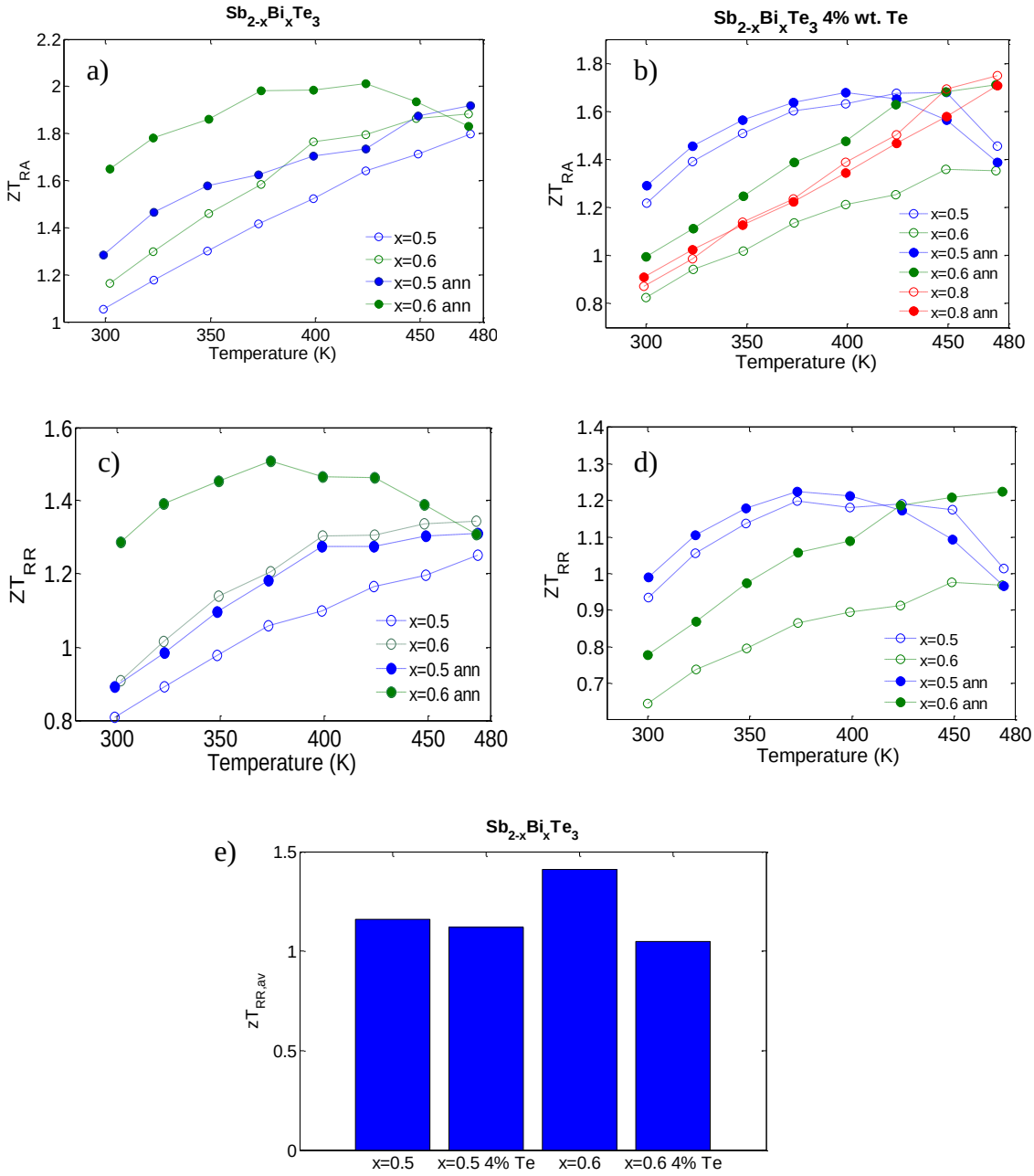

Figure 5.24: Temperature dependence of the dimensionless thermoelectric figure of merit of the HPT-ed $Sb_{2-x}Bi_xTe_3$ compounds before and after the annealing treatment (ann). a) zT_{RA} of undoped samples. b) zT_{RA} of the Te doped samples. c) zT_{RR} of undoped samples. d) zT_{RR} of the Te doped samples. e) $zT_{RR,av}$ of the annealed HPT $Sb_{2-x}Bi_xTe_3$ compounds.

Table 5.VI lists the maximum *zT* values of bismuth telluride based bulk thermoelectric materials prepared by the most successful methods to date for comparison. It can be seen that the maximum *zT* value of HPT-ed $Bi_{0.4}Sb_{1.6}Te_3$ compound is comparable or even higher to the reached ones by those methods. It is also worth pointing out that the thermoelectric performance of the HPT samples is quite stable throughout the studied temperature range. The dimensionless figure of merit of the thermocouple is close to the mean value of each thermo-element, $(ZT = ((zT_p) + (zT_n))/2)$. However the maximum *zT* of Bi_2Te_3-based *n*- and *p*-type elements take place at quite different temperatures[11,49,52]. Thus, to improve the efficiency of the thermoelectric modules, the thermo-elements must have an excellent performance in a wide range of temperatures.

The results allow concluding that the HPT method is a very effective method to fabricate high-performance materials for thermoelectric modules.

Table 5.VI: Comparison of thermoelectric properties of $Bi_xSb_{2-x}Te_3$ bulk samples processed by different promising methods.

Compound	Fabrication method	*zT*	Reference
$Bi_{0.5}Sb_{1.5}Te_3$	Traditional melting	1.02	[1]
$Bi_{0.3}Sb_{1.7}Te_3$ with 0.4 vol% SiC	Ball milling + SPS	1.33	[53]
$Bi_{0.5}Sb_{1.5}Te_3$	Two-step hot forging process	1.56	[51]
$Bi_{0.48}Sb_{1.52}Te_3$	Melt spinning+SPS	1.56	[48]
50% mol Sb_2Te_3/ 50% mol Bi_2Te_3 nanocomposite	Hydrothermal systhesis + HP	1.47	[47]
$Bi_{0.5}Sb_{1.5}Te_3$	High magnetic solidification	1.71	[41]
$Bi_{0.4}Sb_{1.6}Te_3$	HPT	1.51	Present work

5.7. References

1. D.M. Rowe. CRC Handbook of Thermoelectrics. (1995).

2. R.W. Douglas H.J. Goldsmid. The use of semiconductors in thermoelectric refrigeration. Br. J. Appl. Phys. 5, 386 (1954).

3. H.Julian Goldsmith. Introduction to Thermoelectricity. (2010). doi:10.1007/978-3-642-00716-3

4. Starý, Z., Horák, J., Stordeur, M. & Stölzer, M. Antisite defects in Sb2−xBixTe3 mixed crystals. J. Phys. Chem. Solids 49, 29–34 (1988).

5. Horák, J., Stary, Z., Lošťák, P. & Pancíř, J. Anti-site defects in n-Bi2Se3 crystals. J. Phys. Chem. Solids 51, 1353–1360 (1990).

6. Schultz, J. M., McHugh, J. P. & Tiller, W. a. Effects of Heavy Deformation and Annealing on the Electrical Properties of Bi2Te3. J. Appl. Phys. 33, 2443 (1962).

7. Zhang, Z., Sharma, P. a., Lavernia, E. J. & Yang, N. Thermoelectric and transport properties of nanostructured Bi2Te3 by spark plasma sintering. J. Mater. Res. 26, 475–484 (2011).

8. Kim, D.-H. & Mitani, T. Thermoelectric properties of fine-grained Bi2Te3 alloys. J. Alloys Compd. 399, 14–19 (2005).

9. Zhao, L. D., Zhang, B.-P., Liu, W. S., Zhang, H. L. & Li, J.-F. Effects of annealing on electrical properties of n-type Bi2Te3 fabricated by mechanical alloying and spark plasma sintering. J. Alloys Compd. 467, 91–97 (2009).

10. Zhao, L. D., Zhang, B.-P., Li, J.-F., Zhang, H. L. & Liu, W. S. Enhanced thermoelectric and mechanical properties in textured n-type Bi2Te3 prepared by spark plasma sintering. Solid State Sci. 10, 651–658 (2008).

11. Hu, L., Zhu, T., Liu, X. & Zhao, X. Point defect engineering of high-performance bismuth-telluride-based thermoelectric materials. Adv. Funct. Mater. 24, 5211–5218 (2014).

12. Navrátil, J., Starý, Z. & Plecháček, T. Thermoelectric properties of p-type antimony bismuth telluride alloys prepared by cold pressing. Mater. Res. Bull. 31, 1559–1566 (1996).

13. Ionescu, R., Jaklovszky, J., Nistor, N. & Chiculita, A. Grain size effects on thermoelectrical properties of sintered solid solutions based on Bi2Te3. Phys. status solidi 27, 27–34 (1975).

14. Tritt, T. M. Recent Trends in Thermoelectric Materials Research I. (2001).

15. in Non-Tetrahedrally Bonded Elements and Binary Compounds I 1–4 (Springer-Verlag). doi:10.1007/10681727_966

16. Kittel, C. Introduction to Solid State Physics. (Wiley, 2004). at <

17. Cutler, M. & Mott, N. F. Observation of anderson localization in an electron gas. Phys. Rev. 181, 1336–1340 (1969).

18. Chen, X., Parker, D. & Singh, D. J. Importance of non-parabolic band effects in the thermoelectric properties of semiconductors. Sci. Rep. 3, 3168 (2013).

19. Zuev, Y. M., Lee, J. S., Galloy, C., Park, H. & Kim, P. Diameter Dependence of the Transport Properties of Antimony Telluride Nanowires. Nano Lett. 10, 3037–3040 (2010).

20. Yavorsky, B. Y., Hinsche, N. F., Mertig, I. & Zahn, P. Electronic structure and transport anisotropy of Bi2Te3 and Sb2Te3. Phys. Rev. B 84, 165208 (2011).

21. Xie, W. et al. High performance Bi2Te3 nanocomposites prepared by single-element-melt-spinning spark-plasma sintering. J. Mater. Sci. 48, 2745–2760 (2012).

22. Rowe, D. M. Thermoelectrics handbook: macro to nano. (CRC press, 2005).

23. Yim, W. M. & Rosi, F. D. Compound tellurides and their alloys for peltier cooling—A review. Solid. State. Electron. 15, 1121–1140 (1972).

24. Sun, Z. M. et al. Effect of rotary-die equal channel angular pressing on the thermoelectric properties of a (Bi,Sb)2Te3 alloy. J. Mater. Res. 20, 895–903 (2011).

25. Poudel, B. et al. High-thermoelectric performance of nanostructured bismuth antimony telluride bulk alloys. Science 320, 634–8 (2008).

26. Ma, Y. et al. Enhanced thermoelectric figure-of-merit in p-type nanostructured bismuth antimony tellurium alloys made from elemental chunks. Nano Lett. 8, 2580–2584 (2008).

27. Lan, Y. et al. Structure study of bulk nanograined thermoelectric bismuth antimony telluride. Nano Lett. 9, 1419–22 (2009).

28. Pecheur, P. & Toussaint, G. Tight-binding studies of crystal stability and defects in Bi2Te3. J. Phys. Chem. Solids 55, 327–338 (1994).

29. Birkholz, U. Untersuchung der intermetallischen Verbindung Bi2Te3 sowie der festen Lösungen Bi2-xSbxTe3 und Bi2Te3-xSex hinsichtlich ihrer Eignung als Material für Halbleiter-Thermoelemente. Zeitschrift für Naturforsch. A 13, 780–792 (1958).

30. Hyun, D.-B., Hwang, J.-S., Shim, J.-D. & Oh, T. Thermoelectric properties of (Bi0.25Sb0.75)2Te3 alloys fabricated by hot-pressing method. J. Mater. Sci. 36, 1285–1291 (2001).

31. Jiang, J., Chen, L., Bai, S. & Yao, Q. Thermoelectric performance of p-type Bi–Sb–Te materials prepared by spark plasma sintering. J. Alloys Compd. 390, 208–211 (2005).

32. Kim, H. C., Oh, T. S. & Hyun, D.-B. Thermoelectric properties of the p-type Bi2Te3–Sb2Te3–Sb2Se3 alloys fabricated by mechanical alloying and hot pressing. J. Phys. Chem. Solids 61, 743–749 (2000).

33. Jiang, J., Chen, L., Yao, Q., Bai, S. & Wang, Q. Effect of TeI4 content on the thermoelectric properties of n-type Bi–Te–Se crystals prepared by zone melting. Mater. Chem. Phys. 92, 39–42 (2005).

34. Hwang, C.-W., Hyun, D.-B., Ha, H.-P. & Oh, T. S. Effects of excess Te on the thermoelectric properties of p-type 25% Bi2Te3-75% Sb2Te3 single crystal and hot-pressed sinter. J. Mater. Sci. 36, 3291–3297 (2001).

35. Fan, X. et al. Thermoelectric properties of p-type Te-doped (Bi,Sb)2Te3 alloys by mechanical alloying and plasma activated sintering. J. Alloys Compd. 448, 308–312 (2008).

36. Heon Phil Ha, Young Whan Cho, Ji Young Byun & Jae Dong Shim. The effect of excess tellurium on the thermo electric properties of Bi2Te3-Sb2Te3 solid solutions. J. Phys. Chem. Solids 55, 1233–1238 (1994).

37. Fleurial, J. P., Gailliard, L., Triboulet, R., Scherrer, H. & Scherrer, S. Thermal properties of high quality single crystals of bismuth telluride—Part I: Experimental characterization. J. Phys. Chem. Solids 49, 1237–1247 (1988).

38. Taylor, P. J., Maddux, J. R., Jesser, W. a. & Rosi, F. D. Room-temperature anisotropic, thermoelectric, and electrical properties of n-type (Bi[sub 2]Te[sub 3])[sub 90](Sb[sub 2]Te[sub 3])[sub 5](Sb[sub 2]Se[sub 3])[sub 5] and compensated p-type (Sb[sub 2]Te[sub 3])[sub 72](Bi[sub 2]Te[sub 3])[sub 25](Sb[sub. J. Appl. Phys. 85, 7807 (1999).

39. Fan, X. A. et al. Preferential orientation and thermoelectric properties of p-type Bi0.4Sb1.6Te3 system alloys by mechanical alloying and equal channel angular extrusion. J. Alloys Compd. 461, 9–13 (2008).

40. Kim, D. H., Kim, C., Je, K.-C., Ha, G. H. & Kim, H. Fabrication and thermoelectric properties of c-axis-aligned Bi0.5Sb1.5Te3 with a high magnetic field. Acta Mater. 59, 4957–4963 (2011).

41. Luo, Y. et al. Melting and solidification of bismuth antimony telluride under a high magnetic field: A new route to high thermoelectric performance. Nano Energy 15, 709–718 (2015).

42. Euvananont, C., Jantaping, N. & Thanachayanont, C. Effects of composition and preferred orientation on microstructure and thermoelectric properties of p-type (BixSb(1−x))2Te3 alloys. Curr. Appl. Phys. 11, S246–S250 (2011).

43. Yan, X. et al. Experimental studies on anisotropic thermoelectric properties and structures of n-type Bi2Te2.7Se0.3. Nano Lett. 10, 3373–8 (2010).

44. Nye, J. F. Physical properties of crystals: their representation by tensors and matrices. (Oxford university press, 1985).

45. Jiang, J., Chen, L., Bai, S., Yao, Q. & Wang, Q. Thermoelectric properties of p-type (Bi2Te3)x(Sb2Te3)1−x crystals prepared via zone melting. J. Cryst. Growth 277, 258–263 (2005).

46. Yamashita, O. & Sugihara, S. High-performance bismuth-telluride compounds with highly stable thermoelectric figure of merit. J. Mater. Sci. 40, 6439–6444 (2005).

47. Cao, Y. Q., Zhao, X. B., Zhu, T. J., Zhang, X. B. & Tu, J. P. Syntheses and thermoelectric properties of Bi2 Te3 Sb2 Te3 bulk nanocomposites with laminated nanostructure. Appl. Phys. Lett. 92, (2008).

48. Xie, W., Tang, X., Yan, Y., Zhang, Q. & Tritt, T. M. Unique nanostructures and enhanced thermoelectric performance of melt-spun BiSbTe alloys. Appl. Phys. Lett. 94, 102111 (2009).

49. Liu, D.-W., Li, J.-F., Chen, C. & Zhang, B.-P. Effects of SiC Nanodispersion on the Thermoelectric Properties of p-Type and n-Type Bi2Te3-Based Alloys. J. Electron. Mater. 40, 992–998 (2010).

50. Sb, D. Effect of rotary-die equal channel angular pressing on the thermoelectric properties of a (Bi , Sb) 2 Te 3 alloy. 895–903 (2005). doi:10.1557/JMR.2005.0120

51. Jiang, Q. et al. Large ZT enhancement in hot forged nanostructured p-type Bi0.5Sb1.5Te3 bulk alloys. J. Mater. Chem. A 2, 5785 (2014).

52. Pan, Y., Wei, T.-R., Cao, Q. & Li, J.-F. Mechanically enhanced p- and n-type Bi2Te3-based thermoelectric materials reprocessed from commercial ingots by ball milling and spark plasma sintering. Mater. Sci. Eng. B 197, 75–81 (2015).

53. Li, J. et al. BiSbTe-Based Nanocomposites with High ZT : The Effect of SiC Nanodispersion on Thermoelectric Properties. Adv. Funct. Mater. 23, 4317–4323 (2013).

Chapter 6: Mechanical Properties

6.1. Introduction

In the former chapter, it is shown that high pressure torsion is an outstanding method to process thermodynamically efficient (i.e. with enhanced dimensionless figure of merit (*zT*)) thermoelectric (TE) materials. Improving the *zT* is essential for everyday use of the TE devices in a broad range of applications; however, it is equally important to improve their mechanical properties. During their operation life, TE modules are subjected to thermo-mechanical stresses that may incite the formation of micro or macro-cracks causing the premature death of the thermoelements.
The most promising TE materials such as skutterudites, PbTe-based alloys or Bi_2Te_3 alloys are usually very brittle materials[1–8]. Thus, enhancing their mechanical properties is a critical issue for long term reliability.

In the case of Bi_2Te_3 alloys, the compounds have a rhombohedral structure with R3m space group; the crystal is composed of atomic layers in the order of Te(1)-Bi-Te(2)-Bi-Te(1) along the *c* axis. Bi-Te(2) and Bi-Te(1) bonds are ionic-covalent type, while bonding between Te(1)-Te(1) layers is due to the van der Waals interaction. As a result of the weak van der Waals bonding, Bi_2Te_3 is easily cleaved along the *c*-plane, and consequently, it is an extremely brittle material[9]. As grain refining has a toughening effect in brittle polycrystals, nanostructuring Bi_2Te_3-based TE materials is expected to have a mechanical benefit besides its benefit on the *zT*. Similarly, the weak bonding across the Te(1)–Te(1) layers makes the *c*-slip very easy; nanostructuring is expected to strengthen the plastic resistance of Bi_2Te_3 through the Hall–Petch effect too.

In this chapter, the mechanical properties of Bi_2Te_3-based alloys are investigated by means of multi-scalar mechanical tests such as Vickers hardness, nanoindentation, micro-compression and the ball on three balls (B3B) test. Special emphasis has been placed on studying the effect of texture on the mechanical properties.

6.2. Vickers microhardness tests

Vickers hardness test were carried out (load 1.96 N) on the tangential cross-section of the HPT samples. The imposed equivalent strain at the samples is linearly dependent on the distance from the HPT torsion axis (see equation 1.23), which means that the microstructures obtained by HPT are not homogeneous (figure.6.1). Thus, the hardness should have a radial dependence. To account the strain-dependence hardness, the indents were performed along the tangential cross-section of the disk.

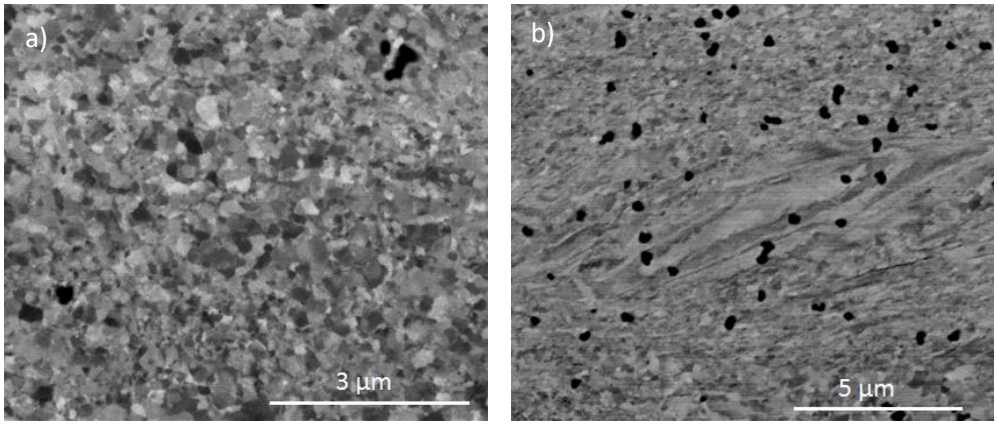

Figure 6.1: The microstructure of Bi_2Te_3 HPTed samples at the disk rim (i.e. maximum imposed shear strain) (a) and close to the disk center (null shear strain) (b). Since the imposed equivalent strain at the samples is dependent on the distance from the HPT torsion axis, close to the disk center the grain size is not saturated and coarse grains can be observed.

The Vickers hardness increases from about 300 MPa for the HP samples to 1300 MPa for the severely deformed ones (HPT). Remember that the equivalent flow stress is approximately HV/3 The hardness saturates after reaching a Von Mises equivalent deformation of the order of ε=20. There are not significant differences between the pure and alloyed compounds (figure 6.2 and figure 6.3). Note that, although the imposed shear strain is null in the center of the HPT sample, the sample was subjected to compression, and therefore, strain hardening is also expected in the center of the disk. The results show the strengthening effect of ultrafine grain refining. The grain boundaries, especially the high angle ones, act as pinning points inhibiting dislocation motion and preventing their movement in a continuous slip plane. This hinders the onset of plasticity increasing the hardness and yield strength of the material according to the Hall–Petch relationship. The high density of dislocations that are typical of SPD samples can also increase the hardness.

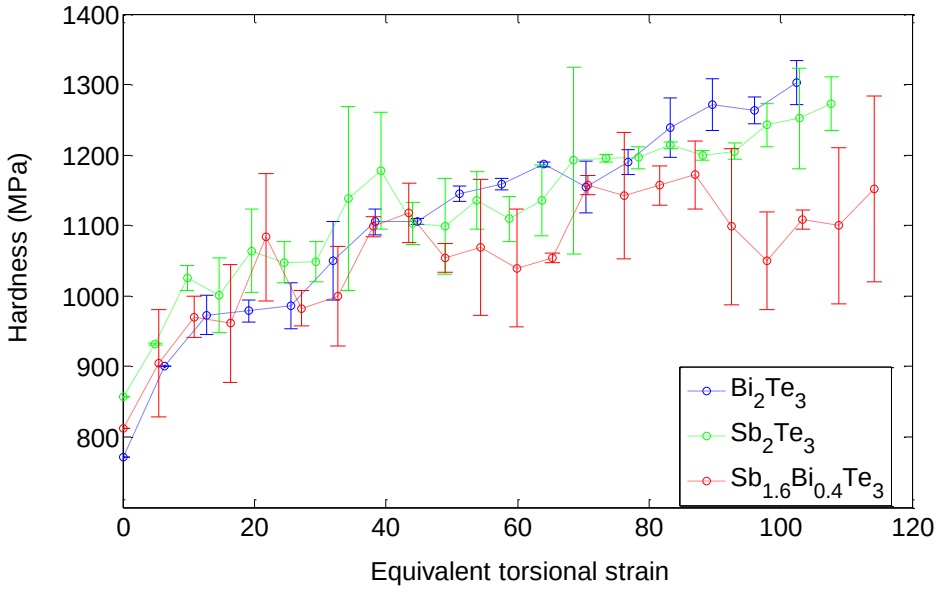

Figure 6.2: Vickers hardness (1.96 N) vs. imposed von Mises equivalent strain (calculated for the torsional strain) for HPTed samples.

The hardness values of HP samples are in accordance with those published for single-crystalline or polycrystalline Bi_2Te_3-based alloys (200-570 MPa)[7,10] and are higher than the measured ones for fine-grained compounds prepared by high-energy milling and spark plasma sintering (SPS)[7,11,12]

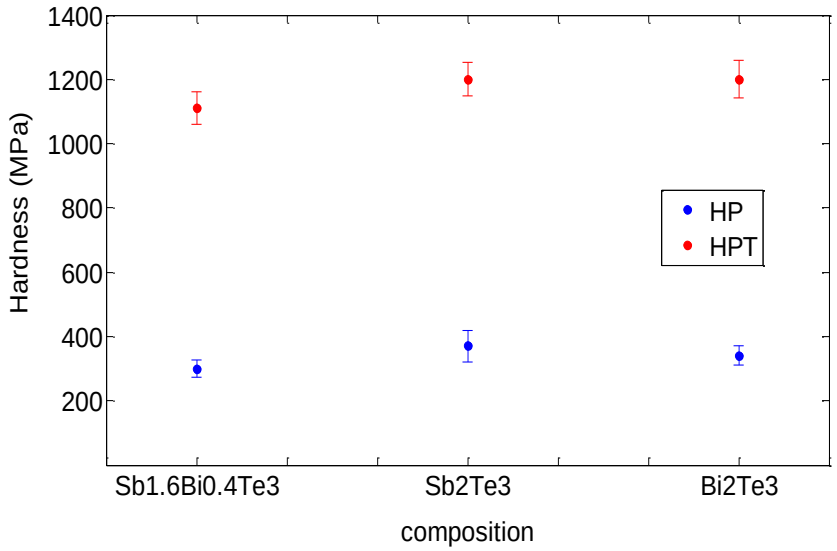

Figure 6.3: Vickers hardness of HP and HPT samples. In the case of HPT samples the, value corresponds to the mean value in the saturated region.

6. 3 Nanoindentation test

High-pressure torsioned (HPT) Bi_2Te_3-based compounds were characterized by nanoindentation too. Instrumented indentation, particularly nanoindentation, is a high-resolution tool for characterizing the mechanical properties in very small specimens or in localized volumes. The method developed by Oliver and Pharr[13] offers a standard procedure to measure both hardness and Young's modulus of materials by means of this technique.

The aim to perform such test was to assess the hardness and Young's modulus. Besides, the indentation size effect (ISE) and the strain rate sensitivity (SRS) at room temperature were studied.
For HPT-ed Bi_2Te_3-based alloys, anisotropic elastic and plastic properties were expected because during the SPD process a very strong (0001) fiber texture is developed. Consequently, the nanoindentation tests were carried out on the disk surface (S) and on its tangential cross section (CS). In both cases, the measurements were performed at the disk rim (i.e. at maximum imposed shear strain).

6.3.1 Elastic modulus

The procedure proposed by Oliver and Pharr[13] to assess the reduced modulus (E_r) is based on on Sneddon's[14] work, which assumes a purely isotropic elastic contact. The method works well for materials that exhibit very isotropic elastic properties such as aluminum or tungsten, but it is not suitable for highly anisotropic materials. Even if the triaxiality of the stress field around an indentation is quite high, the measurement of the indentation modulus through Sneddon's equation is still anisotropic for anisotropic materials. This problem was studied by J.J. Vlassak et al.[15]. The authors computed the contact of an indenter of arbitrary shape on an elastically anisotropic half space., They proposed an analytical procedure to calculate the indentation modulus for a general axisymmetric problem by considering an elliptic contact area and assuming that the solution for the contact problem is the one that maximizes the load on the indenter for a given indentation depth.

Figure 6.4 shows the contour plot in the stereographic projection corresponding to the indentation modulus (left) calculated using the same procedure as Vlassak et al.[15] and the Young's modulus at 300 K (right) constructed from the elastic constants of single-crystalline Bi_2Te_3 measured by Jenkins and Rayn[16] . Because of the high triaxiality involved during the

indentation process, the elastic anisotropy estimated by the procedure described by Vlassak et al. is significantly lower. However, the plots make evident the strong elastic anisotropy of Bi_2Te_3. The Young's modulus ranges from 31.5 GPa [along (0001)] to 86.3 GPa. To estimate the Young modulus of HPT samples, a perfect fiber texture was considered with grains of (000l) planes perfectly parallel to the disk plane and randomly rotated around their common [0001] direction. The calculated surface values (S) and cross-sectional (CS) values were 31.5 and 43.2 GPa respectively (Reuss average). Similarly, the estimated indentation modulus was 46.6 and 54.8 GPa for S and CS respectively.

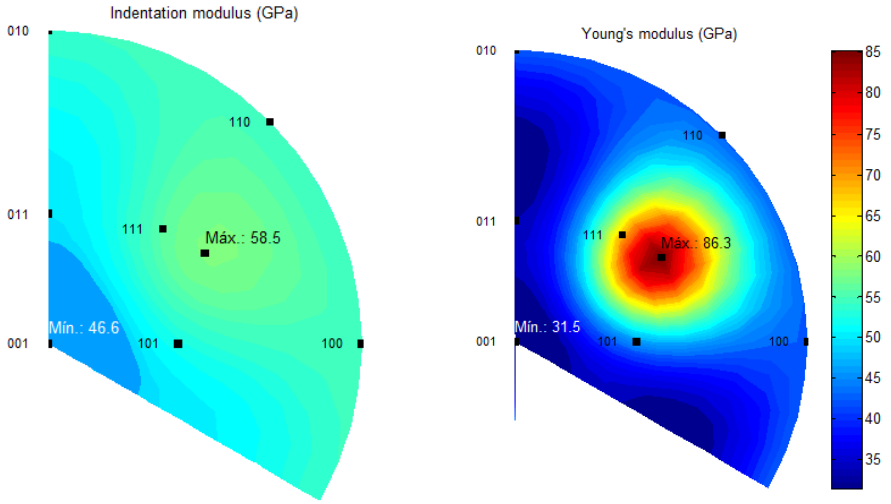

Figure 6.4.: Stereographic projection of indentation modulus of Bi_2Te_3 (left) calculated using the procedure proposed by Vlassak et al.[15] and the Young's modulus (right) at 300 K calculated based on the elastic constants measured by Jenkins and Rayne[16].

The experimental values determined by nanoindentation using the Oliver and Pharr method are close to the values estimated by using the procedure proposed by Vlassak et al. (see Table 6.I).

It seems that alloying with Sb_2Te_3 increases the stiffness of Bi_2Te_3 alloys. This is not surprising because the indentation modulus of Sb_2Te_3 is higher than Bi_2Te_3 one.[17]

Table 6.I.: Estimated indentation modulus using the approach proposed by Vlassak et al.[15] and the experimentally obtained one calculated using the Oliver and Pharr method[13]

Sample	Orientation	Indentation modulus Vlassak (GPa)*	Measured Indentation modulus (GPa)
Bi_2Te_3	S	46.6	42.8 ± 0.1
Bi_2Te_3	CS	54.8	48.1 ± 0.1
$Sb_{1.5}Bi_{0.5}Te_3$	S	–	44.0 ± 0.2
$Sb_{1.5}Bi_{0.5}Te_3$	CS	–	53.3 ± 0.2

* Calculated with the S.C. elastic constants given by Jenkins and Rayn[16] and assuming a perfect axial [0001] texture.

6.3.2 Hardness, indentation size effect (ISE) and strain-rate sensitivity (SRS)

Nanoindentation can be also used to assess the strain-rate sensitivity exponent (m) of the flow stress in an easy and rapid way. Traditionally, indentation creep has been the most extended indentation-based method to determine the strain-rate sensitivity (SRS). Nevertheless, determining SRS by means of continuous indentation creep has two important drawbacks that they accentuate at the nano-scale. Firstly, the resolution of the indentation creep is limited by the thermal drift and secondly, the indentation-size effect[18] (it will be discussed later) leads to an uncertainty in the SRS values. Due to the creep, the materials suffer softening which decreases the hardness and hence increases the imprint size. However, the hardness is closely related to the imprint size (the well-known indentation size effect), and it is not easy to determine which amount of the reduction of hardness is associated to creep and which one to ISE.

To avoid those problems, a nanoindentation strain-rate jump technique has been recently developed for determining the local strain-rate sensitivity (SRS)[19,20] The method consists in applying sudden changes in the logarithmic load rate χ during the loading step. In this way, the produced abrupt changes in χ, allows the measurement of SRS at different depth and different strain rates by measuring only the changes in hardness (for further details see reference 19):

$$m = \frac{d \ln H}{d \ln(\dot{h}/h)} = \frac{d \ln H}{d \ln \chi} \approx \frac{\ln(H_f / H_i)}{\ln(\chi_f / \chi_i)} \qquad (6.1)$$

Where, H is hardness, h is the indentation depth and $\dot{h}$ is the penetration rate. The subscripts i and f denote the values of H and χ before and after the rate-jump, respectively.

In the present work, nanoindentation strain-rate jump technique has been used to determine the strain-rate sensitivity of ultrafine grained Bi_2Te_3 based alloys. Nanoindentation experiments were conducted using a Nanoindenter G200 (Agilent Technologies, Chandler, AZ, USA now Keysight Technologies) equipped with a continuous stiffness measurement (CSM) unit[13,21] (details of the CSM method can be found at reference 13, appendix I or reference 21) and a three-sided diamond Berkovich pyramidal tip. The indentation strain rate was kept constant (0.05 s^{-1}) up to an indentation depth of 500 nm; afterward, reversible strain rate jumps were applied every 500 nm changing χ from 0.05 to 0.005 and 0.001.

Figure 6.5 shows the measured hardness from the performed strain-rate jump test. It is found that the hardness of ultrafine grained Bi_2Te_3-based alloys depends on the indentation strain rate. The hardness is smaller at lower strain rates. However, the tests prove that at room temperature the alloys are weakly dependent on strain rate, m<0.2 (Table 6.II).

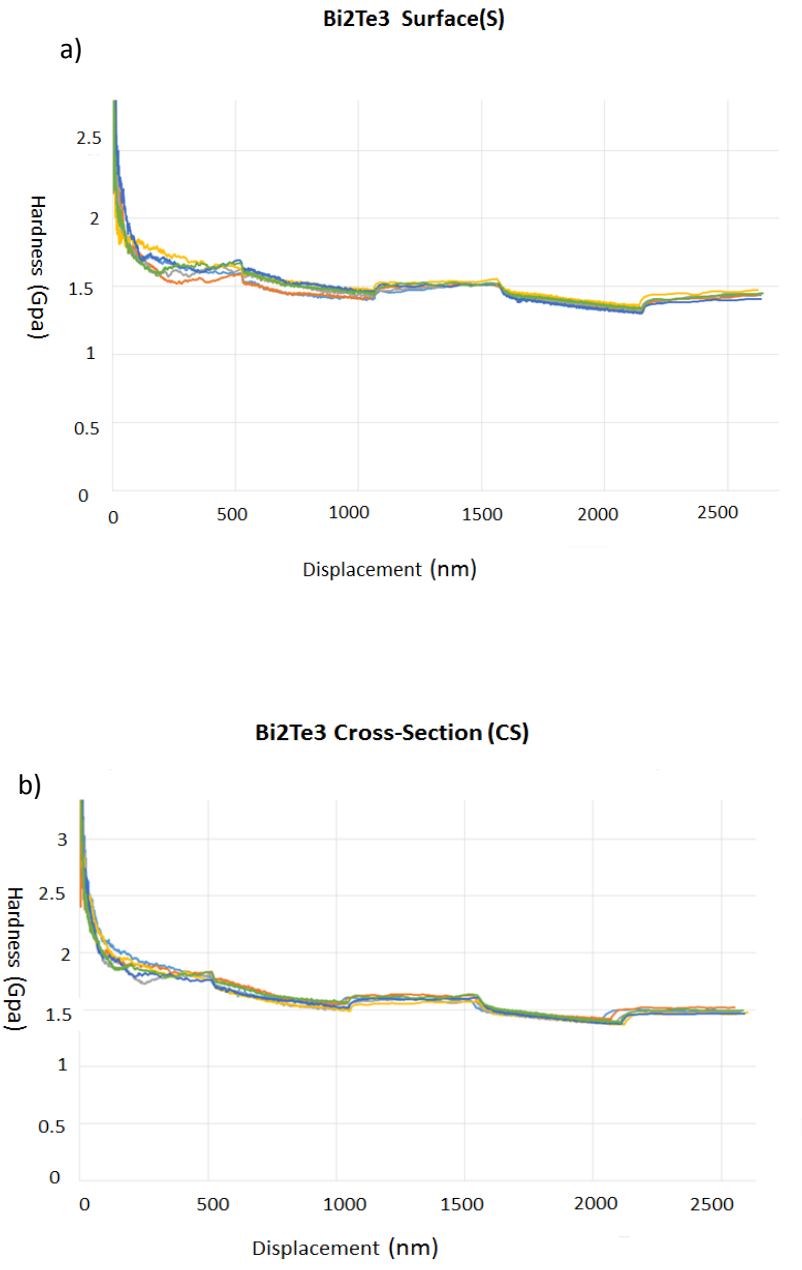

Figure 6.5.: The hardness of ultrafine-grained Bi_2Te_3-based alloys determined by a nanoindentation strain-rate jump experiment with reversible strain-rate jumps ($0.05s^{-1}$-$0.001s^{-1}$. Six indentations were performed for each orientation. a) S orientation b) CS orientation.

The hardness of the *CS* orientation is slightly higher than the measured one for *S* orientation. Thus, it confirms that as well as elastic properties, the plastic properties are very anisotropic. To assess the plastic anisotropy of ultrafine-grained Bi_2Te_3-based alloys, microcompression test were performed, the results will be discussed in the next section.

Figure 6.5 evidences the strong indentation size effect of the compounds. The increase in hardness for small indentation depths has been repeatedly observed in many different crystalline materials[22–24] and it has been attributed to the additional contribution of geometrically necessary dislocations (GND) to the plastic strength[18]. Based on a cinematically admissible model and on the classical strengthening relationship, Nix and Gao[18] proposed the following relation between indentation hardness (*H*) and indentation depth (*h*):

$$H = H_0\sqrt{1+\frac{\hat{h}}{h}} \qquad (6.2)$$

Where H_0 is the hardness in the limit on infinite depth (which is free of GNDs), and $\hat{h}$ is a characteristic length that depends on the shape of the indenter, the Burgers vector, and the statistically stored dislocation density.
Bi_2Te_3-based alloys follow pretty well the Nix and Gao relation. Figure 6.6 shows the linear fitting according to Nix-Gao relationship between the square of the indentation hardness (*H*), and the inverse of the indentation depth (*h*). The extrapolated hardness to infinite size (H_0) for HPT Bi_2Te_3 measured on the *CS* orientation with a Berkovich indenter was 1.83 GPa with $\hat{h}$=24 nm. H_0 value agrees well with the Vickers hardness, $HV_{0.2}$=1.11 $\pm$ 0.05 GPa. It should be pointed that Vickers hardness is determined by measuring the contact area whereas, in nanoindentation test the hardness is measured by estimating the projected area, this entails a factor of 0.94.

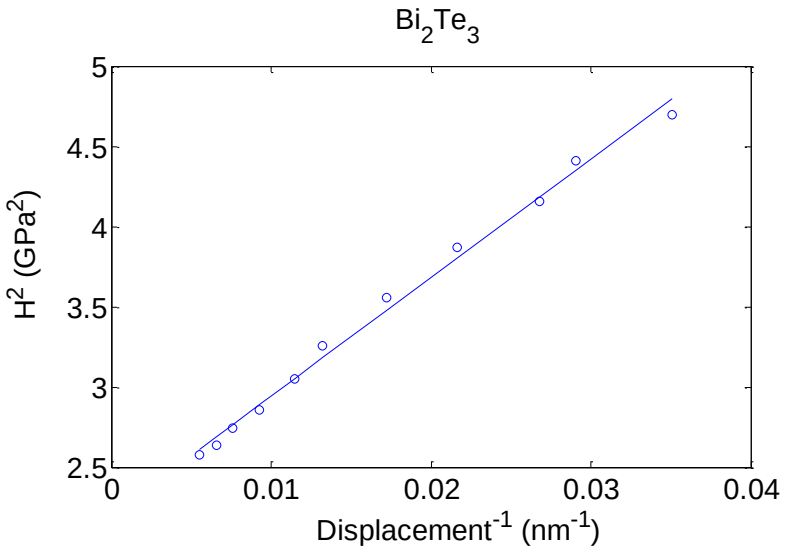

Figure 6.6.: Derivation of Nix-Gao relationship for HPT-ed Bi_2Te_3. The hardness was measured on *CS* orientation with Berkovich indenter.

Similar results were obtained for alloyed $Sb_{1.6}Bi_{0.4}Te_3$. The hardness of alloyed samples is slightly higher than the measured one for pure Bi_2Te_3 (Table 6.II, figure 6.7). This is in good agreement with the hardness values reported by Jing-Fung Li et al. for fine-grained Bi_2Te_3 and *p*-type $Sb_{1.5}Bi_{0.5}Te_3$ prepared by high-energy milling and SPS, 0.62 GPa [11] and 0.81 GPa [12] respectively. Similarly, G Li et al[25] studied the mechanical properties of submicron-grained $Sb_{2-x}Bi_xTe_3$ samples (fabricated by hot-pressing nanopowders produced through ball-milling crystalline ingots) performing nanoindentation test and FEM simulations. They showed that, as in our case, the hardness stayed constant after reaching an indentation depth of about 200 nm. However, due to the smaller grain size (Hall–Petch strengthening effect) of SPD-ed samples, the hardness of alloyed HPT samples is significantly higher than the reported one by G Li et al.. The average grain size of submicron-grained $Sb_{2-x}Bi_xTe_3$ samples is about 500 nm and have a hardness of 0.95 GPa at an indentation depth of 200 nm, whereas the grain size of alloyed HPT samples is about 100 nm (figure

4.11) having a hardness of 2.09 GPa (*CS* orientation) at the same indentation depth. The extrapolated values for alloyed HPT samples are H_0=2.04 GPa and $\hat{h}$ =11 nm.

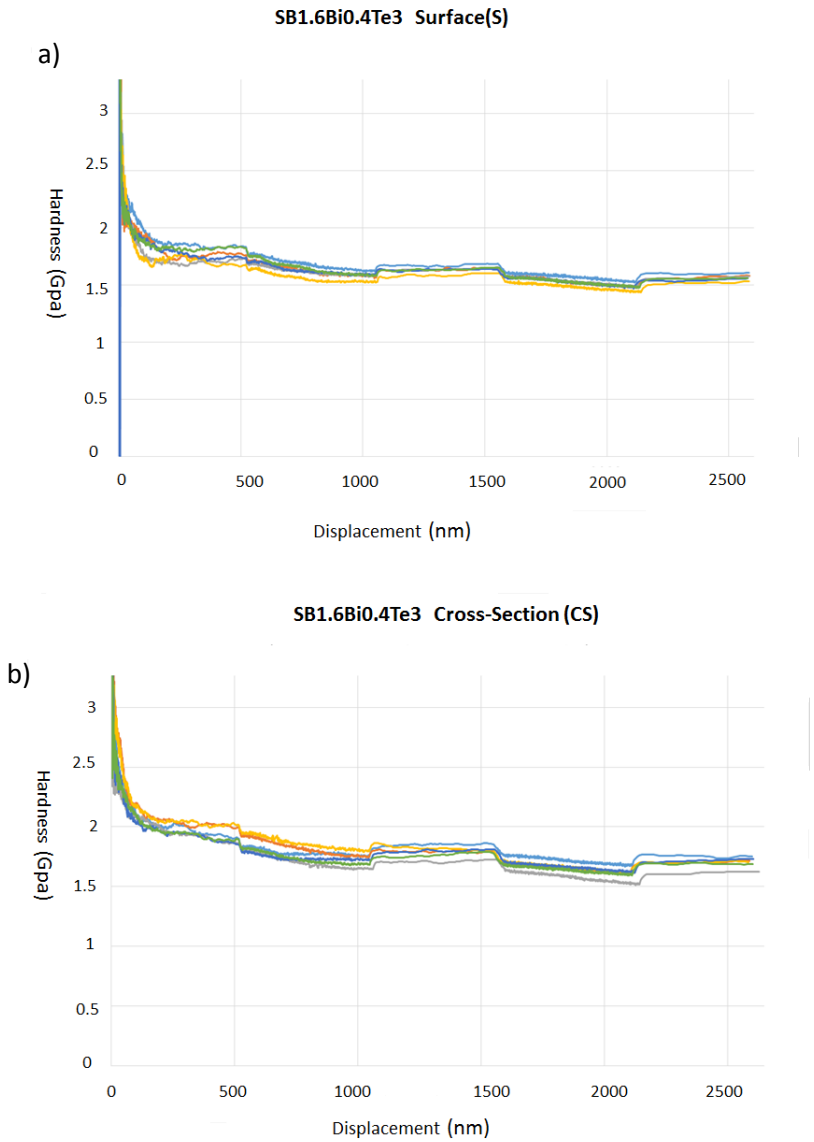

Figure 6.7.: The hardness of ultrafine-grained $Sb_{1.6}Bi_{0.4}Te_3$ alloy determined by a nanoindentation strain-rate jump experiment with reversible strain-rate jumps. Six indentations were performed for each orientation. a) S orientation b) CS orientation.

Table 6.II: Hardness and strain-rate sensitivity exponent (*m*) of HPT samples.

Sample	Orientation	Hardness* (GPa)	m
Bi_2Te_3	S	1.63 ± 0.01	0.018 ± 0.003
Bi_2Te_3	CS	1.72 ± 0.01	0.018 ± 0.002
$Sb_{1.6}Bi_{0.4}Te_3$	S	1.74 ± 0.01	0.013 ± 0.002
$Sb_{1.6}Bi_{0.4}Te_3$	CS	1.92 ± 0.02	0.016 ± 0.003

* The nanoindentation hardness value corresponds to the average value of indentation depths between 500 and 2400 nm.

6. 4. Microcompression tests

Because of the high triaxiality involved during the indentation process there is not direct relationship with other material parameters such as yield stress. In fact, it has been repeatedly shown that there is not a one-to-one correspondence between instrumented sharp indentation and elastic-plastic properties[26–28]. This point is one of the biggest drawbacks for fully exploiting nanoindentation to evaluate the mechanical properties of materials. For this reason, alternative/complementary micro-scale testing techniques have been developed during the last years such as micro-tensile[29], microcompression[30,31] and micro-cantilever fracture tests[32,33]. To obtain suitable samples for micro-compression experiments Focused Ion Beam (FIB) [34,35] or electrodeposition techniques are employed [36]. Because of its simplicity and ease of operation probably the first one is the most used method.

The strain-stress curve of the micro/nano-pillars cannot be derived as easy as in macroscopic tests which are performed employing a perfectly cylindrical sample. Artefacts like machining inaccuracies, the misalignment between the pillar and the indenter tip, the friction between them, and the fact that the machined microsamples do not usually stand frictionless on a flat rigid substrate affect the mechanical response. Therefore, it is most convenient to combine micro-compression experiments with numerical

simulations to assess more accurately the mechanical response of the samples during the test.

In this thesis work, *ex-situ* micropillar microcompression testing was used to study the plastic anisotropy of Bi_2Te_3. Since the samples processed by HP have a rather coarse grain size, single-crystalline (SC) pillars with three different orientations have been fabricated by focused ion beam (FIB) from the surface of HP samples (for further details see section 3.4.4-1 Sample fabrication). Their crystallographic orientation is described by their three Euler angles (Bunge convention, Table 6.III). The selected orientations were expected to show large differences in mechanical behavior. The (0001) plane of grain R is nearly parallel to the disk plane, whereas the [0001] direction of grain G is not far from normal to the disk axis, and that of grain B is tilted about 45° from the disk axis (see figure 6.8).

Table 6.III: Crystallographic orientations of the SC micropillars. Euler angles, Bunge convention.

Pillar	φ_1	Φ	φ_2
R	78.0	176.3	15.4
G	66.7	135.6	58.2
B	6.8	78.5	15.8

In the case of the HPT samples, which develop a strong fiber texture, axially oriented pillars have been fabricated on the subsurface and tangentially oriented ones on the cross-sectional surface of HPT samples.

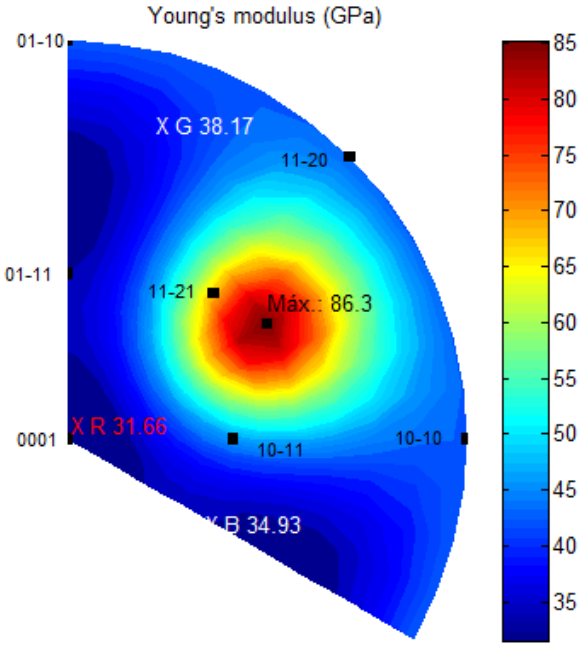

Figure 6.8: Contour plot (stereographic projection) of the Young's modulus of Bi_2Te_3 at 300 K computed by the elastic constants measured by Jenkins[16].

As figure 6.9 shows, all the machined pillars were about 2 μm in diameter and 4.5 μm in height having a taper angle of approximately 5.5°. The pillars of HPT samples are rougher because the ion sputtering rates are function of the chemistry, crystal orientation, and surface topology[37]

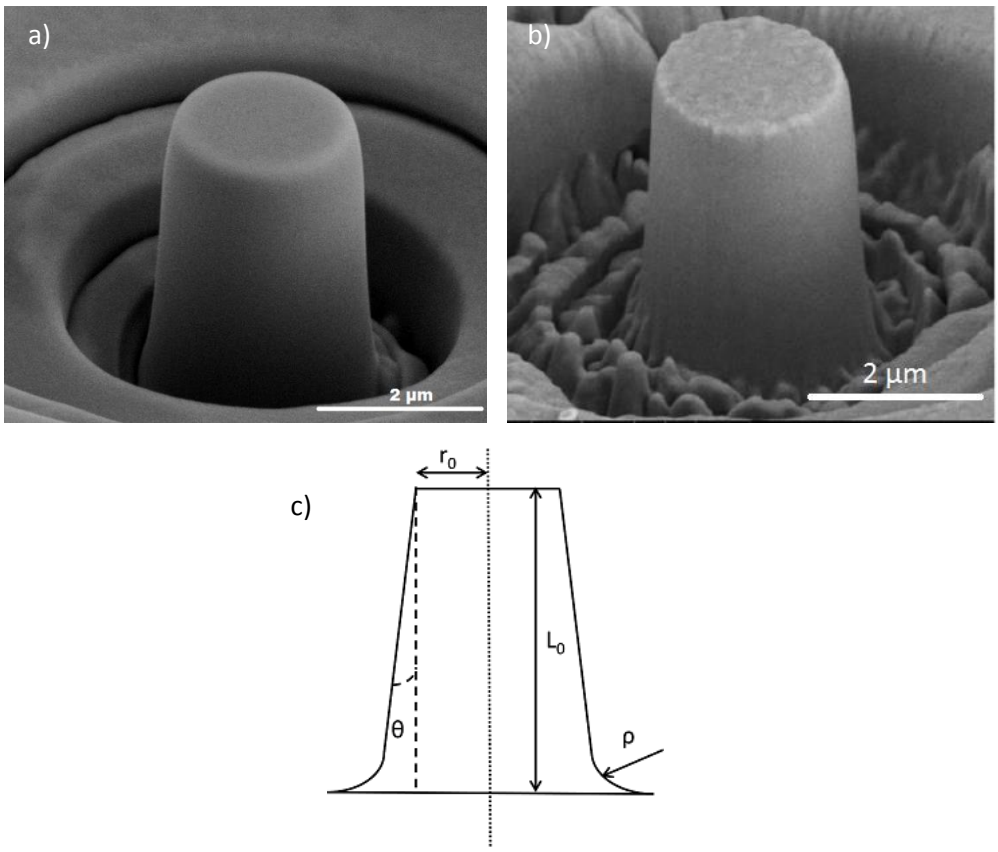

Figure 6.9: a) A 2 µm diameter microcompression sample machined into a Bi_2Te_3 single-crystal. b) A 2 µm diameter microcompression sample machined into a Bi_2Te_3 HPT sample. c) Scheme of the approximate geometry for FIB-milled microcompression

It is well-known that the mechanical properties of the micropillars could be affected by the Ga^+ ion bombardment. The milling was performed at high-incident angles, which reduces the thickness of the damaged layer[38]. However, many reports show that for different soft metals, such as copper or magnesium, the affected layer is less than ~20 nm when the milling is performed at high incident angles using an accelerating voltage of 30 kV[38,39]. Rubanov and Munroe[40] reported that the side walls of FIB-milled silicon trenches at 30 kV revealed very uniform amorphous layers, which were about 30 nm in thickness. The damaged layer can contain point defects, dislocations, and Ga-based precipitates, which may increase the flow stress [39,41]. The ion damage should not be very significant for HPTed

samples since samples processed via SPD have inherently a high density of crystal lattice defects[42]. Thus, for specimens of micrometer size, the ion damage contributes only in a minor way, since the affected layer is small compared with the pillar volume; however, for submicrometer samples (especially for SC ones), this artifact can become significant[43].

Similarly, many studies demonstrated that material strength increases as the critical sample dimension is decreased (i.e. many materials exhibit strong size effects at the submicron scale) [18,41,44,45]. Currently, many theories have been proposed to explain this effect. One predominant theory for micro-compression pillars developed by Greer and Nix referred to as 'dislocation starvation' assumes that mobile dislocations escape from the crystal at the nearest free surface before multiplying via cross-slip or dislocation interaction. Such processes lead to a dislocation-starved state, requiring high stresses to nucleate new dislocations in order to continue with plastic deformation[46].

The few studies that exist up to date on the application of the micropillar compression test to multilayered materials suggest that when the behavior is dominated by a characteristic length scale (the layer thickness) smaller than the sample dimensions, then the results are independent of the pillar diameter [47–50]. Since the grain size of HPT samples is close to 200 nm, no plastic size effect is expected for polycrystalline samples. In contrast, single-crystal micrometer-sized pillars may present an important size effect; the measured compressive strengths; therefore, should be considered as an upper bound of the actual strengths of single-crystalline Bi_2Te_3.

6.4.1. *Ex-situ* microcompresion and data analysis

All micropillars were tested *ex-situ* using a flat diamond tip (more details at section 3.4.4. Micro-mechanical tests). For each orientation, at least four pillars were tested until a nominal compressive strain of 5 % or until failure under a constant displacement rate of 10 nm/s (i.e., at a nominal equivalent strain rate of 2.2 10^{-3} s^{-1}). The stress–strain curves were either estimated by using an analytical approximation described by Greer et al.[51] or by comparison with FEM calculations using the real geometry of the pillar and trying to reproduce the elastic slopes and the plastic strength level with a set of tentative material parameters taken from a matrix of flow stresses and several angles of inclination between the top sample surface and the flat tip of the indenter, as will be explained in the next section.

6.4.2. FEM simulations

The microcompression results have been analyzed with the help of finite element (FEM) elasto–plastic simulations (ABAQUS/standard 6.13-3) accounting for their real geometry. The aim of performing FEM simulations was to study the effect of the geometrical inaccuracies on the mechanical response, determine the influence of contact misalignment between the pillar top surface and the indenter tip, and subtract the base compliance to compute the real pillar stiffness and hence the elastic modulus.

The real pillar geometry was approximated by assuming a taper angle of 5.5° and a fillet radius of 0.5 μm (see figure 6.9.), on account of measurements taken on the real pillars milled by FIB. In the model, anisotropic elastic behavior and rate-independent elastic–plastic behavior have been assumed. The six independent elastic constants, C_{11}, C_{66}, C_{33}, C_{44}, C_{13}, and C_{14}, that define the anisotropy of a trigonal crystal system, were taken from the literature[16].

To understand the influence of experimental uncertainties, pillar–indenter tip misalignment was systematically varied from 0° up to 3°. The size of the substrate was large enough to neglect edge effects on the calculated results.

Figure 6.10 shows the 3D scheme. The indenter tip was modeled as a rigid surface. Coulombian friction, with a friction coefficient of 0.12, was assumed to model the contact between the pillar top surface and the flat indenter tip; the friction coefficient between diamond and a well-polished metallic surface is typically between 0.1 and 0.15.[52] The geometrical parameters used in the simulations are summarized in Table 6.IV. The misalignment degree (α) has been quantified as the angle between the pillar axis and the normal axis of the rigid surface. For model discretization, eight-node linear hexahedron elements (C3D8R) with reduced integration were used.

Table 6.IV: Range of parameters explored in FEM simulations.

Radius of pillar top (r_0)	1 µm
Height (L_0)	4.5 µm
Fillet radius of pillar base (ρ)	{0,0.5} µm
Taper angle (θ)	{0,5.5} °
Misalignment angle (α)	{0, 1, 2, 3} °
Friction coefficient	0.12

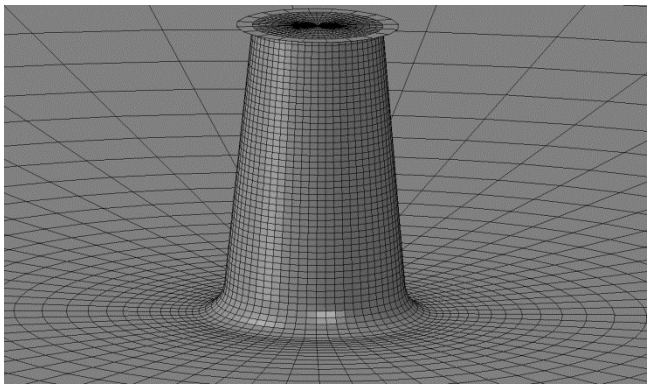

Figure 6.10: a) Scheme and FEM discretization used in FEM simulations.

6.4.3. Microcompression of single-crystalline pillars

In figure 6.11, the engineering stress–strain curves of the three different crystallographic orientations are shown, together with images of pillars after the tests. At least four individual samples have been tested per orientation. Substrate compliance must be properly accounted to assess analytically the Young's modulus. The substrate compliance can be estimated using an analytical approach proposed by Sneddon[14] to compute the depth of penetration of a rigid circular flat punch indenting an isotropic elastic half-space. On the basis of the equation proposed by Sneddon and taking into account the actual geometry of each tested pillar (figure 6.9); we have used the following equation:

$$C_{Sneddon} = \frac{1-\nu^2}{2E\left[a_c + L_0 \tan(\theta)\right]} \quad (6.1)$$

Where, ν is the Poisson ratio, E is the elastic modulus, L_0 is the initial length of the pillar, and a_c is the contact radius, [$a_c=\eta(r_0+\rho)$]; η is constant proposed by H. Zhang et al[53] which takes into account the actual geometry of the pillar-substrate connection. By comparison with FEM simulations, setting η=1.53 delivers the best results. Prior to testing, the top radius (r_0) of each pillar was measured by SEM. The top surface was placed normal to the electron gun to determine r_0 by averaging the measured two diameters. After that, we tilted the sample until we observed the base of the pillar; at this point, we were able to measure accurately the initial length of the pillar (L_0). Finally, two pillars were cross-sectioned to measure the fillet radius (ρ) and base radius (r_b) as suggested by Lilleodden[31].The pillar stiffness is calculated by subtracting Sneddon compliance from the compliance measured in the elastic zone of the load-displacement curve:

$$S_{pillar} = \frac{1}{C_{measure} - C_{Sneddon}} \quad (6.2)$$

Therefore, the Young modulus of a pillar with a taper angle of θ can be estimated as follows:

$$E = \frac{S_{pillar} L_0}{\pi r_0 \left[r_0 + L_0 \tan(\theta) \right]} \quad (6.3)$$

As it is evident from figures. 6.11 a), 6.11e) and 6.13, the initial elastic loading slopes differ significantly from the unloading slopes. The reason for this difference is the effect of the initial misalignment between the pillar and the indenter tip. FEM calculations show that this effect is very strong on the initial, elastic, loading slope. The results show that a misalignment angle of 2° better fits the experimental results obtained. This misalignment, however, is not critical for the unloading case, since plastic deformation of the pillar in the neighborhood of the contact zone promotes a correct surface alignment, as it will be shown below.

The apparent elastic moduli obtained from the loading slopes of the microcompression tests by applying Eq. (6.3), i.e., considering Sneddon's correction and actual geometry of the pillars are 14 ± 3, 11 ± 2, and 13 ± 3 GPa for R, B, and G orientations. The values are in good accordance with the apparent elastic modulus calculated by FEM with 2° of misalignment angle, but they are well below the expected Young's modulus (see Fig. 6 and Table 6.V). This confirms the strong effect of small misalignments on the experimental elastic loading slopes. However, the elastic moduli calculated from the unloading slopes fits perfectly with the expected values according to Table 6.V (orientations R and G). Unfortunately, in the case of single-crystal pillars with B orientation, premature catastrophic fracture did not permit a correct measurement of the unloading curve.

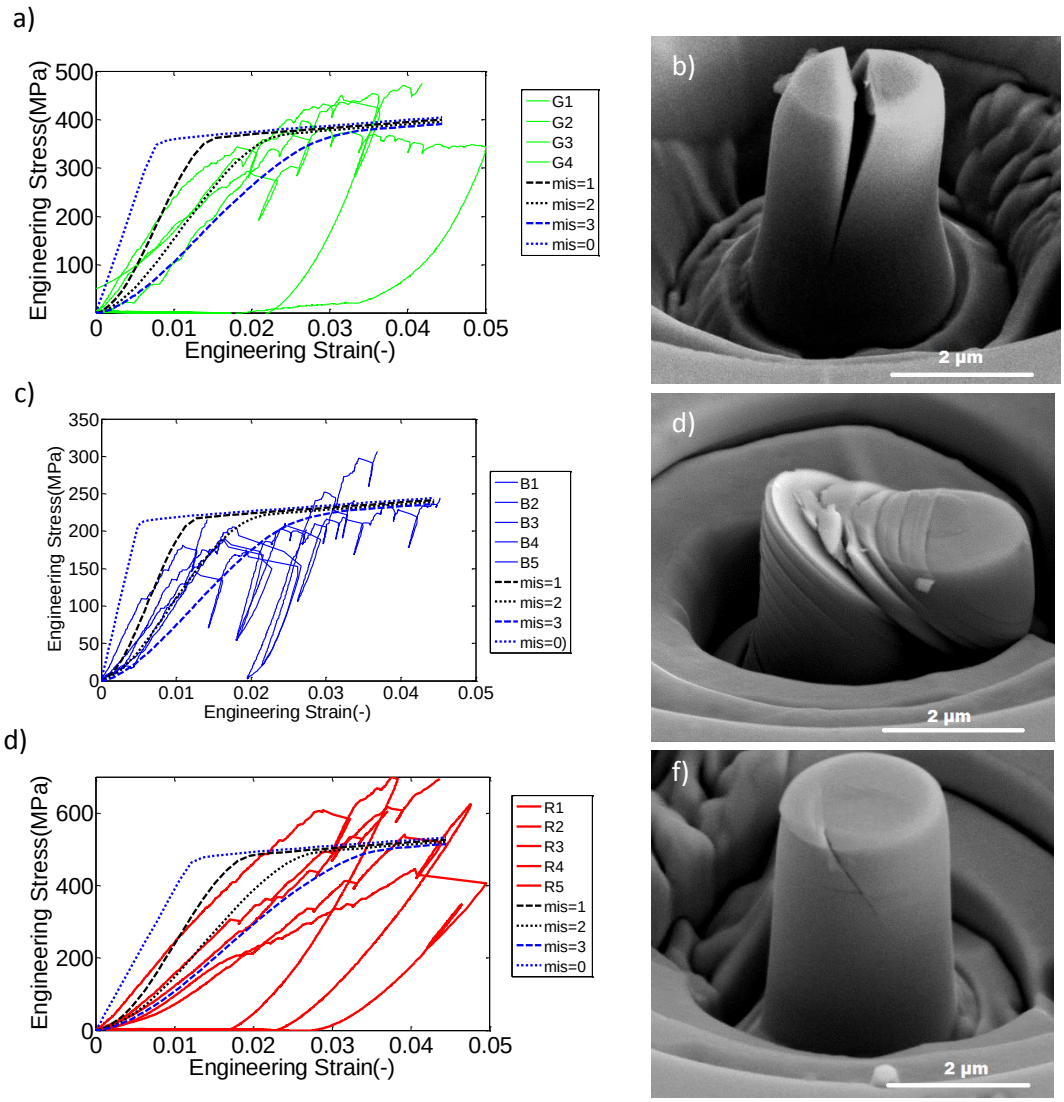

Figure 6.11: a) Engineering stress-strain curves and SEM images of deformed SC micropillars for the studied 3 orientations. (a,b) G orientation, (c,d) B orientation, and (e,f) R orientation.

Table 6.V: Analytically expected Young's modulus of simulated pillars using the Sneddon's correction without and with a misalignment degree of 2 ° ($E_{mis0°}$ and $E_{mis2°}$). Experimentally obtained modulus calculated using the loading (E_{load}) and unloading (E_{unload}) slope. Apparent yield stress measured using the 0.2 % offset method ($\sigma_{y0.2\%}$.)

Sample	**Orientation**	**Analytically expected uniaxial modulus (GPa)**	**FEM Calculated uniaxial modulus, $E_{mis0°}$ (GPa)**	**FEM Calculated loading modulus, $E_{mis2°}$ (GPa)**
HP	R	31.7	32.6	19.4
HP	G	37.9	39.0	16.4
HP	B	34.9	35.7	10.7
HPT	S	31.5*	-	-
HPT	CS	43.2*	-	-
Sample	**Orientation**	**Measured E_{load} (GPa)**	**Measured E_{unload} (GPa)**	**$\sigma_{y0.2\%}$.(MPa)**
HP	R	14±3	28±5	380±40
HP	G	13±3	39±2	310±20
HP	B	11±3	-	180±10
HPT	S	18±1	32±2	590±30
HPT	CS	22±2	43±2	340±20

** Reuss average*

In figure 6.12, the measured stress–plastic strain flow curves for the three orientations are shown (the apparent elastic strain has been subtracted from the total strain). The superposed dashed lines correspond to simulations assuming the actual geometry and an ideal plastic behavior (the apparent plastic strain hardening is a consequence of the taper angle). Two facts stand out: the big plastic anisotropy of Bi_2Te_3 and the different behaviors of orientation, R, with respect to orientations G and B. As for the anisotropy, the yield strength of the three crystals scales inversely with the angle between their [0001] direction and the compression axis, a confirmation that the basal plane is an easy glide plane. FEM analyses suggest yield stresses of about 320, 270, and 150 MPa, respectively for R, G, and B orientations. After an initial short period of strain hardening, the flow stresses of the three crystals reach a rather constant value of their flow stresses amounting to about 550, 350, and 200 MPa, respectively, for the R, G, and B orientations.

Crystal B suffers a plastic collapse after several episodes of localized (0001) basal slip as shown in figure 6.11d); in the stress–strain response, figure 6.11 c), the repeated relaxations should correspond to the successive slip avalanches. In crystal G, slip on the (0001) plane is very difficult as the normal to this easy glide plane and the compression axis form an angle of 80°; the G micropillars undergo a rather uniform plastic deformation at nearly constant stress, figure 6.11 a), until basal cleavage occurs, figure 6.11 b); no external signs of the active plastic mechanisms are evident in the surface of the broken micropillar. Nonbasal slip or twinning is most probably taking place in crystal G. Finally, in crystal R, the basal (0001) plane normal is nearly parallel to the compression axis, i.e., again basal slip is not favored, and other plastic mechanisms must be activated; each relaxation by a plastic event of this crystal (partial unloading) is followed by a strong hardening increment, in contrast with the behavior of the two other crystal orientations; nonbasal slip or rhombohedral twinning could be happening here too. In figure 6.11 f), a nonbasal slip band or crack compatible with the angle between the $(0\bar{1}12)$ plane and the basal one (57.6°) is crossed by a short cleavage propagation on the basal plane. It is to be noted that a very small deviation from the ideal [0001] orientation (here such deviation is approx. 4°) allows for basal slip to occur in Mg,[54] i.e., such basal cleavage could have been triggered by a burst of basal slip associated to the passage of the non-basal slip band or crack.

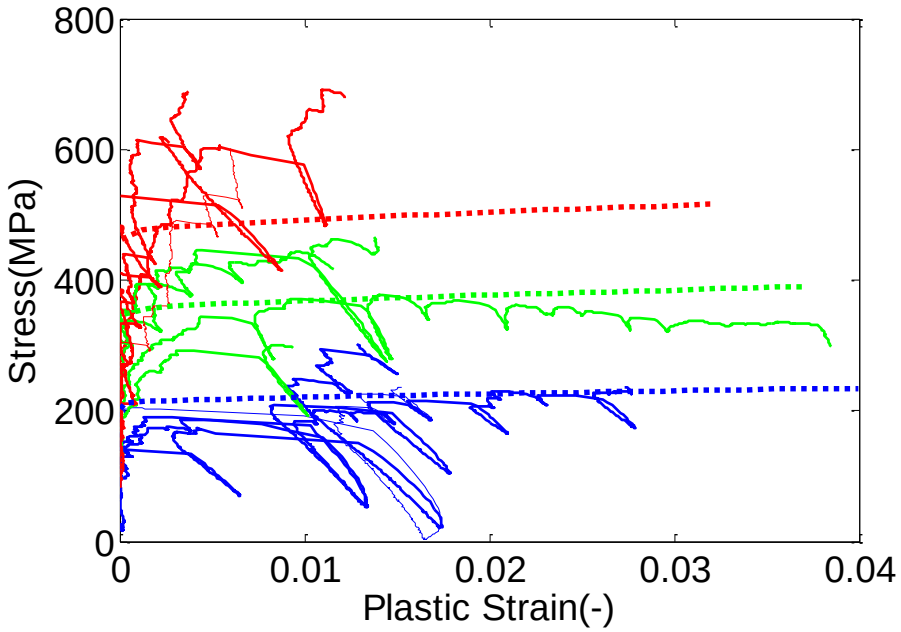

Figure 6.12: Plastic stress-strain curves of the three orientations. Red color corresponds to R orientation, green color to G and blue color to B. The dashed lines correspond to FEM simulations assuming an ideal plastic behavior.

6.4.4. Microcompression of ultrafine grained (UFG) pillars (HPTed material)

HPT samples exhibits a very strong (000l) fiber texture; thus, since the layered crystal structure of Bi_2Te_3, anisotropic mechanical properties are foreseen. Consequently, UFG polycrystalline micropillars were machined on the disk surface (S) and on its cross section (CS) of the disk-shaped samples in the tangential direction. The obtained stress–strain curves are plotted in figures 6.13 and 6.14. As expected, because of the strong basal texture the mechanical properties are very different.

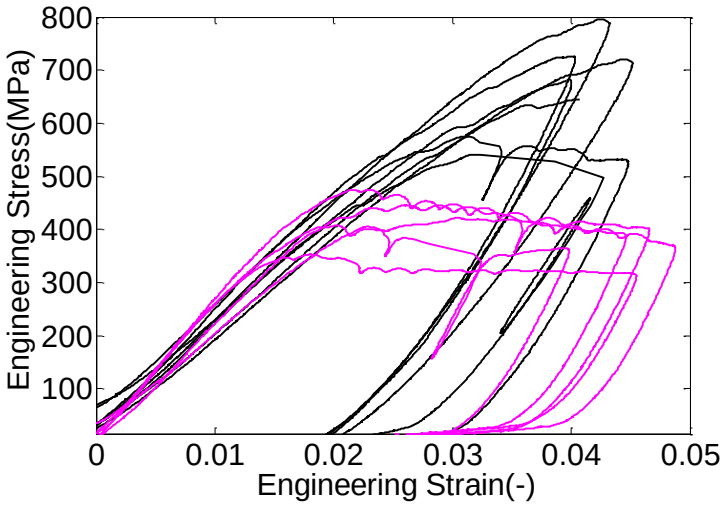

Figure 6.13: Engineering stress-strain curves of the ultrafine-grained pillars. Black color corresponds to S orientation, and magenta color to CS.

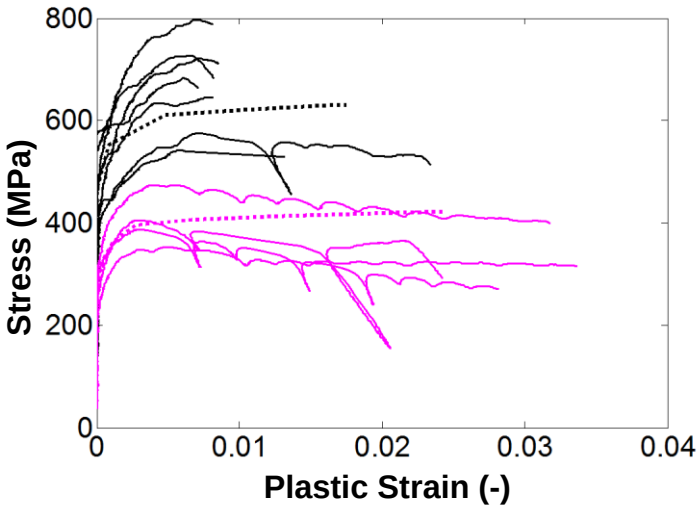

Figure 6.14: Plastic stress-strain curves of the ultrafine-grained pillars. Black color corresponds to S orientation, and magenta color to CS. The dashed lines correspond to FEM simulations assuming an ideal plastic behavior. In the case of S orientation a strong strain hardening is observed while in CS orientation a softening behavior is observed.

In the case of the HPTed samples, to estimate the Young's modulus based on the elastic constants measured by Jenkins, a perfect fiber texture was considered with grains of (0001) planes perfectly parallel to the disk plane and randomly rotated around their common [0001] direction. The calculated surface values (S) and cross-sectional values (CS) were 31.5 and 43.2 GPa, respectively; (Reuss average). The estimations based on the experimental stress–strain curves agree very well with the values expected from the measured texture. The elastic moduli, after the Sneddon correction of the experimental stress–strain slope and accounting for the actual geometry, are 32 ± 2 and 43 ± 2 GPa for, the S and CS samples, respectively.

The apparent yield stresses (0.2% offset method) for S and CS orientations are 590 ± 30 MPa and 390 ± 20 MPa, respectively. The actual corresponding yield stresses according to FEM analysis assuming perfect plastic behavior beyond the yield stress (no plastic strain hardening) would be 500 ± 30 and 340 ± 20 MPa (Table 6.V). The orientation S, with most of its grains with the *c* axis axially oriented, shows much work hardening after yield, as it occurred with its single-crystal counterpart, R, of <0001> axial orientation.

A comparison with the strengths of the single-crystalline micropillars suggests significant Hall–Petch strengthening effect obtained from grain refinement. Single-crystalline pillars with B orientation provide with a measure of the critical resolved shear stress (CRSS) for the basal slip system: as the assumed slip plane is tilted 45° from the pillar axis, a lower bound (because of our ignorance on the orientation of the slip direction), although very close to the actual value of such CRSS (on account of the symmetry of the basal plane), is half of the measured compressive yield or flow stress (i.e., 75 MPa at yield and 100 MPa at saturation, respectively. Similarly, the results of pillars with G or R orientation furnish an estimation for the CRSS of the hard, nonbasal slip, or twinning systems; assuming again an orientation factor of 2 (it will provide us now with an upper bound), the CRSS of the hard systems is estimated to be 160 MPa at yield and 275 MPa at saturation. If there was any effect of grain size, one would

expect for the yield stress of polycrystalline pillars to be between 150 MPa (basal slip, softest orientation) and 480 MPa (hard slip or twinning systems, random orientation with a factor of 3). The actually measured values range from 390 to 590 MPa. As the measurements of the yield or flow stresses of the single crystals or polycrystals have been obtained from micropillars of the same size, such strengthening is only attributable to a Hall–Petch type effect and not to some micropillar size effect. The same conclusions are derived if the saturation stresses of both materials are compared.

After the compression tests, figure 6.15, the polycrystalline micropillars show microcracks below the contact zone, oriented parallel to the axis in the *CS* specimen and tilted a small angle with it in sample *S*, in both cases as expected from the preferred orientation of the cleavage planes in their grains. Comparing figures 6.11 b) and 6.15 b), the toughening effect of the nanostructuration of Bi_2Te_3 by HPT is evident; the microcracks in sample *CS* have not propagated catastrophically as in single crystalline sample G, figure 6.11 b).

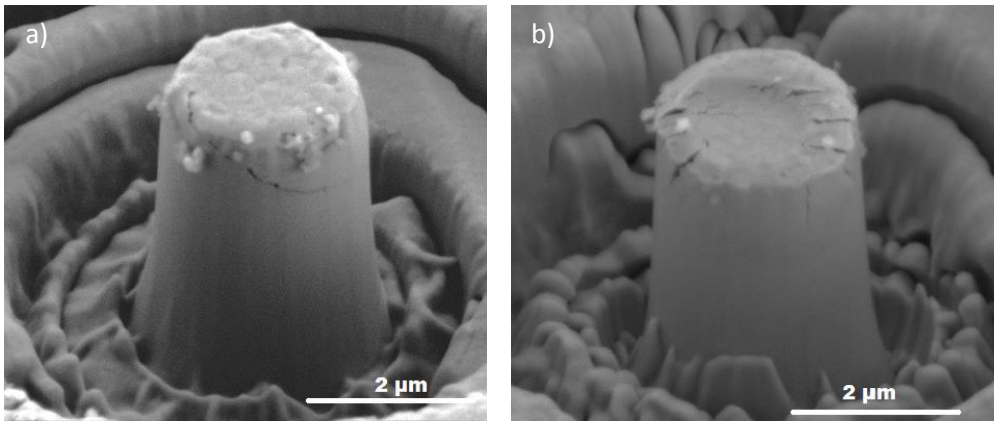

Figure 6.15: FEG-SEM images of the ultrafine-grained pillars after performing the micro-compression test: a) S orientation b) CS orientation.

6. 5. The ball on three balls (B3B) test results

Finally, The biaxial flexural strength (σ_{bf}) was measured using the ball on three balls (B3B) test[55,56] (details of the tests are given in section 3.4.2. The ball on three balls (B3B) test). B3B testing is very suitable to determine the strength of HPT samples because it has been recognized to be very tolerant for some out of flatness of the disk or some misalignment.[56]

The biaxial flexural strength is 77 ± 2 MPa and 35 ± 4 MPa for alloyed ($Sb_{1.6}Bi_{0.4}Te_3$) HP and HPT samples respectively. The lower σ_{bf} of HPT samples can be ascribed to the strong preferred orientation of HPT samples. It is well-known that the bending strength of brittle materials is closely related to the critical stress for crack propagation[57]; because the layered structure and weak van der Waals bonding between Te(1)-Te(1) layers, Bi_2Te_3-based alloys are easily cleaved along the *c*-plane. As figure 6.15 a) and 6.17 b) shows, since the grains are highly oriented, the cracks propagate along the grain boundaries with low resistance and the samples then fracture at relatively small loads. Thus, although HP samples have a small residual porosity and larger grain size (figure 6.17 a), they exhibit a higher biaxial flexural strength because their weaker texture compared to HPT samples.

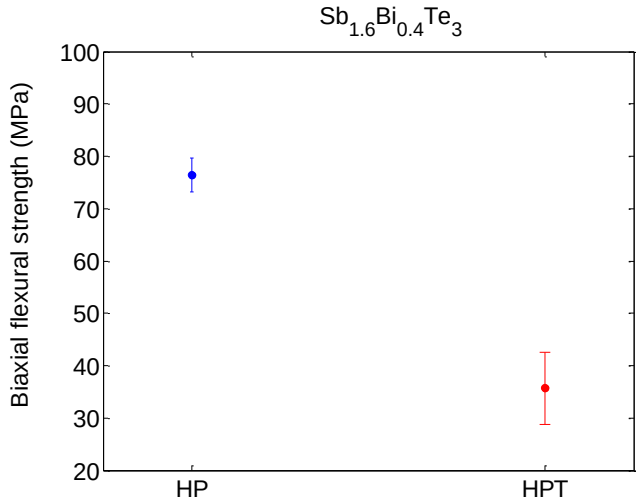

Figure 6.16: Biaxial flexural strength of HP and HPT samples

Nevertheless, the flexural strength of HPT samples despite being lower than the measured ones for HP samples is higher than that of the materials prepared by unidirectional crystal growing method such Bridgman method (19.2 MPa)[58], zone-melting (10 MPa)[59] or single-crystalline commercial ingots (16.97 MPa)[7]. However, σ_{bf} is smaller than the reported one for polycrystalline materials consolidated by spark plasma sintering (SPS), hot pressing (HP), or hot-forging methods. For instance literature reports the following flexural strength values: zone-melt-ing/grinding + SPS (80 MPa, average grain size ~100 μm)[59], mechanical alloying + SPS (65.8 MPa)[12], ball-milling+ SPS (58.72 MPa)[7], melting/grinding +hot-pressing (50 MPa, average grain size 38 μm)[58], ingot hot-extruding method (61.2 MPa, the grain size ~4 μm)[60] or ball-milling + SPS + hot forging (120 MPa)[6].

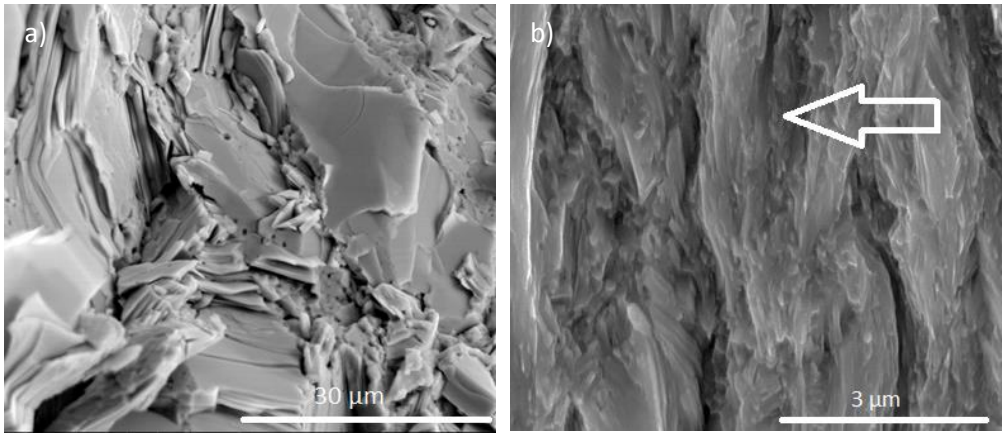

Figure 6.17: FEG-SEM fractographs of $Sb_{1.6}Bi_{0.4}Te_3$ samples. a) HP sample b) HPT sample. The c axis is preferred oriented in the direction parallel to the arrow.

Adding a small fraction of SiC nanoparticles could be a promising approach to improve the strength of the highly textured samples processed by HPT. HPT method is a very effective tool to disperse effectively second-phase particles[61]. As described by Li et al.[11,12,62] the nanodispersion of SiC particles enhances the fracture toughness (K_{IC}) of Bi_2Te_3-based alloys which leads to improving the flexural strength. It is expected that the homogeneous nanodispersion of SiC particles into BiSbTe matrix will hinder the crack propagation along the grain boundaries in HPT samples improving σ_{bf}. Besides improving the mechanical properties, adding an optimum fraction of SiC nanoparticles is beneficial for enhancing the thermoelectric performance due to the following advantageous aspects:

- Introducing second-phase nanoparticles is a well-known approach to reducing the thermal conductivity because they act as scattering centers dispersing the low-to-mid frequency phonons.[11,63]
- It is well-known that second-phase particles prevent the recovery and recrystallization processes during the SPD because they act as growth inhibitors by Zener pinning which leads to obtaining a finer saturated grain size. By this way, since the average grain size is smaller, the SiC nanoparticles promote the phonon-grain boundary scattering further reducing the lattice thermal conductivity[64].
- SiC nanoparticles can filter out many low-energy carriers by the scattering effect, enhancing the Seebeck coefficient of *p*-type Bi_2Te_3 alloys[12,62].
- Second-phase particles improve the thermal stability of pure or alloyed metals processed by SPD methods[65,66] .

These ideas will, of course, require further work beyond this thesis.

6.6. References

1. Salvador, J. R. *et al.* Transport and mechanical properties of Yb-filled skutterudites. *Philos. Mag.* **89,** 1517–1534 (2009).

2. Zhang, L. *et al.* Mechanical properties of filled antimonide skutterudites. *Mater. Sci. Eng. B Solid-State Mater. Adv. Technol.* **170,** 26–31 (2010).

3. Eilertsen, J., Subramanian, M. A. & Kruzic, J. J. Fracture toughness of Co4Sb12 and In0.1Co4Sb12 thermoelectric skutterudites evaluated by three methods. *J. Alloys Compd.* **552,** 492–498 (2013).

4. Gelbstein, Y., Gotesman, G., Lishzinker, Y., Dashevsky, Z. & Dariel, M. P. Mechanical properties of PbTe-based thermoelectric semiconductors. *Scr. Mater.* **58,** 251–254 (2008).

5. Ni, J. E. *et al.* Room temperature Young's modulus, shear modulus, Poisson's ratio and hardness of PbTe–PbS thermoelectric materials. *Mater. Sci. Eng. B* **170,** 58–66 (2010).

6. Zhao, L. D., Zhang, B.-P., Li, J.-F., Zhang, H. L. & Liu, W. S. Enhanced thermoelectric and mechanical properties in textured n-type Bi2Te3 prepared by spark plasma sintering. *Solid State Sci.* **10,** 651–658 (2008).

7. Pan, Y., Wei, T.-R., Cao, Q. & Li, J.-F. Mechanically enhanced p- and n-type Bi2Te3-based thermoelectric materials reprocessed from commercial ingots by ball milling and spark plasma sintering. *Mater. Sci. Eng. B* **197,** 75–81 (2015).

8. Santamaría, J. A., Alkorta, J. & Gil Sevillano, J. Microcompression tests of single-crystalline and ultrafine grain Bi2Te3 thermoelectric material. *J. Mater. Res.* **30,** 2593–2604 (2015).

9. H.Julian Goldsmith. *Introduction to Thermoelectricity*. (2010). doi:10.1007/978-3-642-00716-3

10. Kim, H. & Hong, S. Microstructure and Thermoelectric Properties of N-type 95%Bi2Te3-5%Bi2Se3 Compound Prepared by High Energy Milling and Hot Extrusion. *Curr. Nanosci.* **10,** 118–122 (2014).

11. Zhao, L.-D. *et al.* Thermoelectric and mechanical properties of nano-SiC-dispersed Bi2Te3 fabricated by mechanical alloying and spark plasma sintering. *J. Alloys Compd.* **455,** 259–264 (2008).

12. Liu, D.-W., Li, J.-F., Chen, C. & Zhang, B.-P. Effects of SiC Nanodispersion on the Thermoelectric Properties of p-Type and n-Type Bi2Te3-Based Alloys. *J. Electron. Mater.* **40,** 992–998 (2010).

13. Oliver, W. C. & Pharr, G. M. An improved technique for determining hardness and elastic modulus using load and displacement sensing indentation experiments. *J. Mater. Res.* **7,** 1565–1583 (1992).

14. Sneddon I.N. the relation betwenn load and penetration in the axisymmetric boussinesq problem for a punch of arbitrary profile. *Int. J. Eng. Sci.* **3,** 47–57 (1965).

15. Vlassak, J. J., Ciavarella, M., Barber, J. R. & Wang, X. The indentation modulus of elastically anisotropic materials for indenters of arbitrary shape. *J. Mech. Phys. Solids* **51,** 1701–1721 (2003).

16. Jenkins, J. O. & Rayne, J. A. Elastic moduli of Bi2Te3 from 4.2 to 300 K. *Phys. Lett. A* **30,** 349 (1969).

17. Han, S. W. *et al.* Multi-physics analysis for the design and development of micro-thermoelectric coolers. *ICCAS (June), KINTEX, Gyeonggi-Do, Korea* (2005).

18. Nix, W. D. & Gao, H. Indentation size effects in crystalline materials: A law for strain gradient plasticity. *J. Mech. Phys. Solids* **46,** 411–425 (1998).

19. Alkorta, J., Martínez-Esnaola, J. M. & Gil Sevillano, J. Critical examination of strain-rate sensitivity measurement by nanoindentation methods: Application to severely deformed niobium. *Acta Mater.* **56,** 884–893 (2008).

20. Maier, V. *et al.* Nanoindentation strain-rate jump tests for determining the local strain-rate sensitivity in nanocrystalline Ni and ultrafine-grained Al. *J. Mater. Res.* **26,** 1421–1430 (2011).

21. Li, X. & Bhushan, B. A review of nanoindentation continuous stiffness measurement technique and its applications. *Mater. Charact.* **48,** 11–36 (2002).

22. Ma, Q. & Clarke, D. R. Size dependent hardness of silver single crystals. *J. Mater. Res.* **10,** 853–863 (1995).

23. McElhaney, K. W., Vlassak, J. J. & Nix, W. D. Determination of indenter tip geometry and indentation contact area for depth-sensing indentation experiments. *J. Mater. Res.* **13,** 1300–1306 (1998).

24. Alkorta, J., Martínez-Esnaola, J. & Gil Sevillano, J. Detailed assessment of indentation size-effect in recrystallized and highly deformed niobium. *Acta Mater.* **54,** 3445–3452 (2006).

25. Li, G. *et al.* Mechanical properties of Bi x Sb 2− x Te 3 nanostructured thermoelectric material. *Nanotechnology* **23,** 065703 (2012).

26. Tho, K. K., Swaddiwudhipong, S., Liu, Z. S., Zeng, K. & Hua, J. Uniqueness of reverse analysis from conical indentation tests. *J. Mater. Res.* **19,** 2498–2502 (2011).

27. Chen, X., Ogasawara, N., Zhao, M. & Chiba, N. On the uniqueness of measuring elastoplastic properties from indentation: The indistinguishable mystical materials. *J. Mech. Phys. Solids* **55,** 1618–1660 (2007).

28. Alkorta, J., Martínez-Esnaola, J. M. & Sevillano, J. G. Absence of one-to-one correspondence between elastoplastic properties and sharp-indentation load–penetration data. *J. Mater. Res.* **20,** 432–437 (2011).

29. Jennings, A. T. & Greer, J. R. Tensile deformation of electroplated copper nanopillars. *Philos. Mag.* **91,** 1108–1120 (2011).

30. Byer, C. M., Li, B., Cao, B. & Ramesh, K. T. Microcompression of single-crystal magnesium. *Scr. Mater.* **62,** 536–539 (2010).

31. Lilleodden, E. Microcompression study of Mg (0 0 0 1) single crystal. *Scr. Mater.* **62,** 532–535 (2010).

32. Iqbal, F., Ast, J., Göken, M. & Durst, K. In situ micro-cantilever tests to study fracture properties of NiAl single crystals. *Acta Mater.* **60,** 1193–1200 (2012).

33. Matoy, K. *et al.* A comparative micro-cantilever study of the mechanical behavior of silicon based passivation films. *Thin Solid Films* **518,** 247–256 (2009).

34. Volkert, C. a. & Lilleodden, E. T. Size effects in the deformation of sub-micron Au columns. *Philos. Mag.* **86,** 5567–5579 (2006).

35. Uchic, M. D. & Dimiduk, D. M. A methodology to investigate size scale effects in crystalline plasticity using uniaxial compression testing. *Mater. Sci. Eng. A* **400-401,** 268–278 (2005).

36. Bei, H. *et al.* Compressive strengths of molybdenum alloy micro-pillars prepared using a new technique. *Scr. Mater.* **57,** 397–400 (2007).

37. Orloff, J., Utlaut, M., Swanson, L. & Wagner, A. *High Resolution Focused Ion Beams: FIB and Its Applications*. *Kluwer Academic/Plenum* **57,** (2003).

38. Mikmeková, Š. *et al.* FIB Induced Damage Examined with the Low Energy SEM. *Materials Transactions* **52,** 292–296 (2011).

39. Kiener, D., Motz, C., Rester, M., Jenko, M. & Dehm, G. FIB damage of Cu and possible consequences for miniaturized mechanical tests. *Mater. Sci. Eng. A* **459,** 262–272 (2007).

40. S. Rubanov P. R. Munroe. FIB-induced damage in silicon. *J. Microsc.* **214,** 213–221 (2004).

41. Soler, R. *et al.* Micropillar compression of LiF [111] single crystals: Effect of size, ion irradiation and misorientation. *Int. J. Plast.* **36,** 50–63 (2012).

42. Zhilyaev, a & Langdon, T. Using high-pressure torsion for metal processing: Fundamentals and applications. *Prog. Mater. Sci.* **53,** 893–979 (2008).

43. Kiener, D., Motz, C. & Dehm, G. Micro-compression testing: A critical discussion of experimental constraints. *Mater. Sci. Eng. A* **505,** 79–87 (2009).

44. Huang, Y. *et al.* A model of size effects in nano-indentation. *J. Mech. Phys. Solids* **54,** 1668–1686 (2006).

45. Frick, C. P., Clark, B. G., Orso, S., Schneider, A. S. & Arzt, E. Size effect on strength and strain hardening of small-scale [111] nickel compression pillars. *Mater. Sci. Eng. A* **489,** 319–329 (2008).

46. Greer, J. R. & Nix, W. D. Nanoscale gold pillars strengthened through dislocation starvation. *Phys. Rev. B* **73,** 245410 (2006).

47. Li, N., Mara, N. A., Wang, Y. Q., Nastasi, M. & Misra, A. Compressive flow behavior of Cu thin films and Cu/Nb multilayers containing nanometer-scale helium bubbles. *Scr. Mater.* **64,** 974–977 (2011).

48. Lotfian, S., Molina-Aldareguia, J. M., Yazzie, K. E., Llorca, J. & Chawla, N. High-temperature nanoindentation behavior of Al/SiC multilayers. *Philosophical Magazine Letters* **92,** 362–367 (2012).

49. Uchic, M. D., Shade, P. A. & Dimiduk, D. M. Plasticity of Micrometer-Scale Single Crystals in Compression. *Annual Review of Materials Research* **39,** 361–386 (2009).

50. Greer, J. R. & De Hosson, J. T. M. Plasticity in small-sized metallic systems: Intrinsic versus extrinsic size effect. in *Progress in Materials Science* **56,** 654–724 (2011).

51. Greer, J. R., Oliver, W. C. & Nix, W. D. Size dependence of mechanical properties of gold at the micron scale in the absence of strain gradients. *Acta Mater.* **53,** 1821–1830 (2005).

52. Spear, K. E. Diamond-Ceramic Coating of the Future. *J. Am. Ceram. Soc.* **72,** 171–191 (1989).

53. Zhang, H., Schuster, B. E., Wei, Q. & Ramesh, K. T. The design of accurate micro-compression experiments. *Scr. Mater.* **54,** 181–186 (2006).

54. Hosford, E. W. K. and W. F. Plane-Strain Compression of Magnesium and Magnesium Alloy Crystals. *Trans. Metall. Soc. AIME* **242,** 5 (1968).

55. Börger, A., Supancic, P. & Danzer, R. The ball on three balls test for strength testing of brittle discs: stress distribution in the disc. *J. Eur. Ceram. Soc.* **22,** 1425–1436 (2002).

56. Börger, A., Supancic, P. & Danzer, R. The ball on three balls test for strength testing of brittle discs: Part II: Analysis of possible errors in the strength determination. *J. Eur. Ceram. Soc.* **24,** 2917–2928 (2004).

57. Klingbeil, N. W. & Beuth, J. L. Interfacial fracture testing of deposited metal layers under four-point bending. *Eng. Fract. Mech.* **56,** 113–126 (1997).

58. Shin, H. S., Ha, H. P., Hyun, D. Bin, Shim, J. D. & Lee, D. H. Thermoelectric properties of 25% Bi 2 Te 3-75% Sb 2 Te 3 solid solution prepared by hot-pressing method. *J. Phys. Chem. Solids* **58,** 671–678 (1997).

59. Jiang, J., Chen, L., Bai, S., Yao, Q. & Wang, Q. Thermoelectric properties of textured p-type (Bi,Sb)2Te3 fabricated by spark plasma sintering. *Scr. Mater.* **52,** 347–351 (2005).

60. Park, K., Seo, J. H., Cho, D. C., Choi, B. H. & Lee, C. H. Thermoelectric properties of p-type Te doped Bi0.5Sb1.5 Te3 fabricated by powder extrusion. **88,** 103–106 (2002).

61. Tamayo-Ariztondo, J. Analysis and Optimization of the Cu-C Interface in Copper Matrix Composites Reinforced with Carbon Nanotubes and Nanofibres. (Universidad de Navarra, 2015).

62. Li, J. *et al.* BiSbTe-Based Nanocomposites with High ZT : The Effect of SiC Nanodispersion on Thermoelectric Properties. *Adv. Funct. Mater.* **23,** 4317–4323 (2013).

63. He, J., Kanatzidis, M. G. & Dravid, V. P. High performance bulk thermoelectrics via a panoscopic approach. *Mater. Today* **16,** 166–176 (2013).

64. Humphreys, F. J. & Hatherly, M. *Recrystallization and related annealing phenomena*. *Acta Metallurgica et Materialia* (2004). doi:10.1016/B978-008044164-1/50005-0

65. Lee, S. *et al.* Influence of scandium and zirconium on grain stability and superplastic ductilities in ultrafine-grained Al–Mg alloys. *Acta Mater.* **50,** 553–564 (2002).

66. Bachmaier, A. & Pippan, R. Effect of oxide particles on the stabilization and final microstructure in aluminium. *Mater. Sci. Eng. A* **528,** 7589–7595 (2011).

Chapter 7: Lead telluride based alloys as thermoelectric materials

7.1. Introduction

High pressure torsion has been applied also to nanostructure or consolidate other thermoelectric families such as Ag_2Se, SnSe, and PbTe. In this chapter, I will focus in PbTe. Lead telluride based alloys are typically used for mid-temperature power generation (500-900 K)[1,2]. The first radioisotope thermoelectric generator (RTG) contained simple alloys of PbTe for both the *n*- and *p*- type elements and was used by NASA for its first RTG powered spacecraft[3], the Transit 4A. With the arrival of the Voyager missions, NASA switched to Si-Ge alloys which are well-known high-temperature (> 900 K) thermoelectric (TE) materials with a superior long-term reliability at elevated temperatures.[4] However, NASA returned to PbTe based alloys to provide power to the most sophisticated Mars Science Lab rover Curiosity to date[5]. Similarly, mid-temperature thermoelectric materials, like skutterudites or PbTe-based alloys have attracted the attention of the automotive industry to be used as long-life thermoelectric generators[6,7].

For everyday use of the TE devices in a broad range of applications, especially as TEG in the automotive industry, it is essential to improve their thermodynamic performance, the target goal of $zT>2$ is usually set[8]. In the recent years record-high zT values in the range 1.5–1.8 at 750–900 K have been reported by means of the successful strategy of nanostructuring to

reduce the lattice thermal conductivity.[9 10 11], nevertheless, the *zT* value is still lower than the desired threshold *zT* value of 2. Nanostructures in bulk thermoelectric materials allow effective phonon scattering of phonons with a wide range of frequencies, but phonons with long mean free paths remain largely unaffected.
Fortunately, recently huge *zT* values (between~1.8-2.2) have been reached via the band engineering or the hierarchical length-scale approaches [4,8,12].

As is the case of Bi_2Te_3 alloys, alloying PbTe with Se (i.e. forming solid solutions with isoelectronic atoms) is a well-established approach to reducing the lattice thermal conductivity due to the scattering of phonons with point defects[13–15] . Besides reducing the thermal conductivity, tuning the Se amount leads to tailoring the electronic band of bulk PbTe-based alloys, giving rise to a further improvement of its thermoelectric performance[16,17]. The electronic performance of a thermoelectric semiconductor depends primarily on its weighted mobility (*U*) defined as $U = \mu(m^*/m_e)^{3/2}$, where m^* and m_e are the density of states effective mass and the free electron mass respectively, and μ the mobility of carriers [2,14]. *m** can be expressed as a function of the effective masses along the axes of symmetry (m_1,m_2,m_3) within each single valley, and valley degeneracy (N_v) as: $m^* = N_V^{2/3}(m_1 m_2 m_3)^{1/3}$ [14]. Thus, there are two ways to improve *m**: (1) increase the effective masses of each single valley or (2) reach high valley degeneracy. The first approach should be deleterious to the thermoelectric performance due to free charge carriers tend to be predominantly scattered by the acoustic phonons, which reduces its mobility[18 19], $\mu \propto m^{*-5/2} T^{-3/2}$ [20]. In contrast, the convergence of many charge carrying valleys does not affect negatively the carrier mobility in a significant way. Consequently, it is well known that high valley degeneracy in the electronic band conducts to a high *zT* [19].
Convergence of many valleys can occur in high-symmetry crystal structures (such as PbTe and Bi_2Te_3 alloys) if the Fermi surface forms isolated pockets

at low symmetry points[16]. For instance, the widely *p*-type Bi_2Te_3 alloys studied in this thesis have a significant valley degeneracy, with $N_v=6$ in both the conduction and valence bands[14]. In the case of PbTe, the valence band extremum occurs at the *L* point in the Brillouin zone, here N_v is 4. However, in PbTe there is a second valence band along Σ line, which its energy is about 0.2 eV below the *L* band and has a valley degeneracy of 12[16] (figure 7.1).

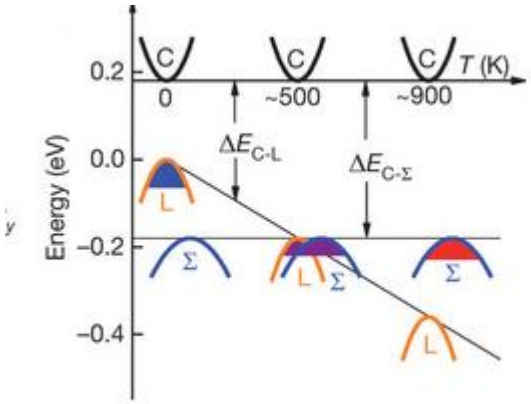

Figure 7.1: Relative energy of the valence bands in $PbTe_{0.85}Se_{0.15}$ [16]

Pei et at. [16] pointed that alloying PbTe with Se increases the convergence temperature of the *L* and Σ bands. In this way, they were able to reduce the energy difference between the two bands to less than approximately $2k_bT$ (here k_b is the Boltzmann constant 8.6173324×10^{-5} $eV\cdot K^{-1}$), making the bands effectively converged even at high temperatures.

In summary, the work of Pei et al.[16] demonstrated that alloying PbTe with Se benefits the thermoelectric performance of PbTe-based alloys as follows:

1. Reduces the lattice thermal conductivity due to the formation of isoelectronic solid solutions.
2. Enhances the electronic performance by effectively converging the *L* and Σ bands at high temperature.
3. Increases the bandgap leading to a reduction of the bipolar conduction.

Thanks to these advantageous aspects, a high zT value of 1.8 ± 0.1 at 850 K has been reported for Na-doped (2 at.%) $Pb_{0.98}Na_{0.02}Te_{0.85}Se_{0.15}$ alloy[16] (figure 7.2).

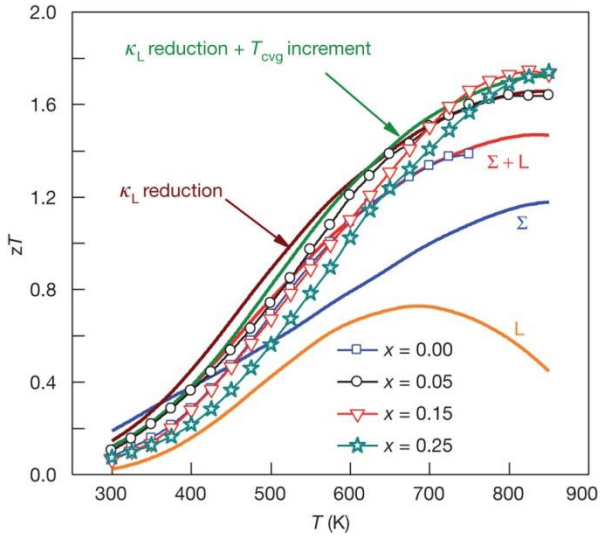

Figure 7.2.: Temperature dependence of zT of p- type $PbTe_{1-x}Se_x$ materials doped with 2 % at. Na. As is shown, the convergence between the L and Σ bands leads to a high thermoelectric performance [16]

Despite the satisfactory zT values obtained by the band engineering approach,[16,17] it is reasonable to think that the synergy between the band engineering and the hierarchical length-scale approach[8] should conduct to a further increment of the dimensionless figure of merit.

The hierarchical length-scale approach is based on introducing phonon scattering centers (such point defects, second-phase nanoparticles, and grain boundaries) at different length scales to reduce the lattice thermal conductivity (κ_L). By this approach, a broader spectrum of phonons is strongly dispersed at those scattering centers, which leads to a drastic reduction of κ_L. Due to the drastic thermal conductivity reduction reached by means of the all-scale hierarchical approach, a record zT value of ~2.2 has been achieved at 915 K for spark-plasma-sintered (SPS) samples of PbTe–SrTe (4mol %) doped with 2 mol % Na[8].

Alike in the case of heavily doping of PbTe with (>~0.5 at. %) Na, when PbTe is doped with ATe compounds, where A= Mg, Ca, Sr, Ba or Cd, ATe nanoprecipitates are formed, with a size of 1-10 nm, embedded in the PbTe matrix; this happens because ATe compounds have a very low but finite solubility limit[4]. Due to the similar crystallographic structure, alignment and mass density between Na-rich precipitates and the PbTe matrix, the Na-rich precipitates do not effectively scatter phonons and thus, do not contribute in a significant way to reduce the lattice thermal conductivity of PbTe alloys[4]. However, this is not the case for ATe doping. It has been reported that ATe precipitates (very promising results have been reported for SrTe[8,21] and MgTe[22]) are very effective for scattering short to medium wavelength phonons, while they have only a small effect on the electrical transport properties of the system.

Nanoprecipitates and the generated point defects due to the solubility of ATe in PbTe disperse phonons with short and medium mean free paths (~3-100 nm) but they are not able to scatter phonons with longer mean free paths (~0.1-1 μm). Grain-boundary scattering is an effective way to reduce the thermal conductivity (κ)[23–25]: low-frequency phonons, although they are scarce, their free path length is large and they make a remarkable contribution to the lattice conductivity [26]. It is well-known that due to their long free path, low-frequency phonons are particularly sensitive to boundary scattering. Therefore, the generation of submicron grained (SMG) structures further reduce the κ and hence improve *zT*.

Summarizing, via introducing all scale phonon scattering centers, as proposed by Biswas, K. et al.[8], a great improvement of *zT* is achieved in PbTe-based alloys (figure 7.3).

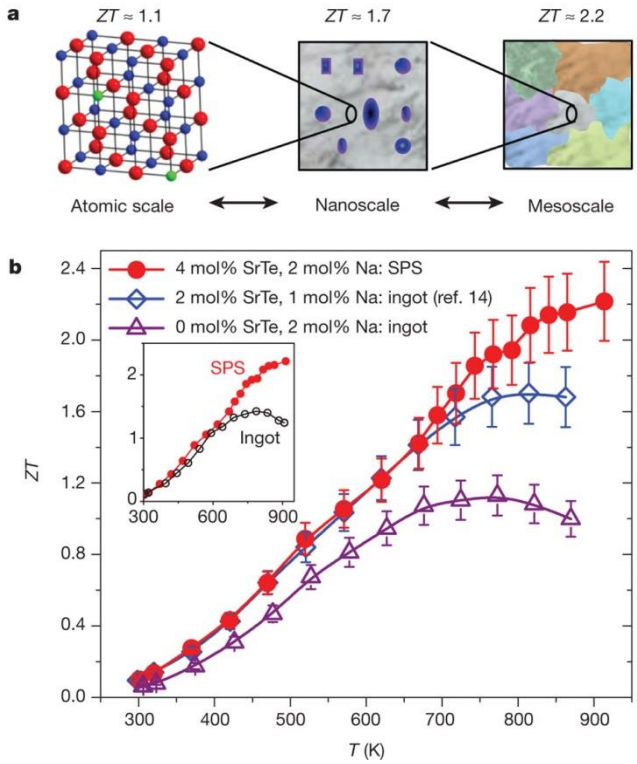

Figure 7.3.: a) Maximum achieved *zT* values for PbTe-based alloys via introducing defects at different length-scales. b) *zT* as a function of temperature for an ingot of PbTe doped with 2 mol% Na (only point defects scattering), PbTe–SrTe (2 mol %) doped with 1 mol% Na (point defects scattering plus scattering of middle frequency phonons with nanoprecipitates) and spark-plasma-sintered PbTe–SrTe (4 mol %) doped with 2% Na (point defects scattering plus nanoprecipitate scattering plus grain boundary scattering)[8].

As figure 7.3 shows, creating submicron grained (SMG) structures (the average size of the spark-plasma-sintered PbTe–SrTe (4 mol %) doped with 2% Na is about 0.8 μm[8]) improves *zT* from ~1.7 at 800 K to ~2.2 at 915 K. This enhancement of the dimensionless figure of merit is attributed mainly to the simultaneous reduction of the thermal conductivity and bipolar conduction due to the effect of the high density of grain boundaries. As in the case of *p*-type Bi_2Te_3 alloys, the grain boundaries of PbTe based alloys cause the build-up of charge, which produces an electrostatic potential. This electrostatic potential scatters electrons and holes differentially which leads

to deteriorating the bipolar conduction [8,23,27]

The results show that the grain boundaries play a significant role in enhancing the thermoelectric performance, especially at elevated temperatures. Besides reducing both, the thermal conductivity, and the bipolar conduction, grain boundaries can also act as energy barrier filtering enhancing the Seebeck coefficient[28–30]

HPT processing should be a promising alternative to SPS in order to generate SMG structures in PbTe-ATe compounds. We believe that PbTe-MgTe system can be the most interesting one. Mg alloying in PbTe makes the energy offset between the L and Σ bands decrease with respect to the alloying fraction. On the other hand, due to the low solubility of MgTe in PbTe, nanoprecipitates of a size between 1-10 nm are formed in this system[31].
Thus, HPT processing of PbTe-MgTe alloys can lead to achieving a record *zT* values via converging the band engineering and the hierarchical all-length scale approaches. We expect that HPT processing of this system should be more beneficial than the SPS due to the following aspects: (1) we expect that the final saturated mean grain size of PbTe-MgTe alloys will be significantly finer than the reached one by SPS. The second phase particles (MgTe precipitates) ought to be grain growth inhibitors by Zener pinning, (i.e. they should pin dislocations and grain boundaries), they should prevent recovery and recrystallization during the deformation process. Consequently, an extremely fine microstructure should be obtained after HPT processing of this system at a low or relatively moderate temperature[32,33]. The case of Zn is a good example which proves the importance of the Zener pinning in achieving a SMG microstructure. HPT processing of pure Zn leads to a relatively coarse recrystallized grain size, however after adding very small amount of Ti (0.8 wt.% Ti), an ultrafine-grained structure is reached by HPT due to the pinning effect of the intermetallic $TiZn_{16}$ phase[34]. Having a higher grain boundary density should

decrease even more the lattice thermal conductivity because it is promoted the phonon grain boundary scattering. (2) The presence of stable precipitates should prevent grain growth; therefore we anticipate that the obtained nanostructures will be thermally stable[35]. (3) Due to the huge imposed strains, supersaturated solid solutions can be processed by SPD[36]. Mg content alters the band energy for $Mg_x Pb_{1-x}Te$ alloys as[31]:

$$\begin{aligned} E_{C-L}\,(\text{eV}) &= 0.18 + 4T\,/10000\ \text{K} + 2.4x, \\ E_{C-\Sigma}\,(\text{eV}) &= 0.36 + 1.4\,x \text{ and} \\ E_{L-\Sigma}\,(\text{eV}) &= 0.18 - 4T\,/10000\ \text{K} - x, \end{aligned} \qquad (7.1)$$

Thus, increasing the solubility of MgTe in PbTe (the solubility limit is ~0.06 for T>525 K)[31] can be very interesting to converge the *L* and *Σ* band in a wide range of temperatures and increase the bandgap.

As described, in the last years several attempts have been done to improve the thermoelectric performance of PbTe-based alloys, however, little efforts have been done to improve their mechanical properties. PbTe based alloys are very brittle materials [37,38]; this is a critical issue that has limited the use of TE materials in many commercial applications; particularly to be used as TEG in the automotive industry. As grain refining has a toughening effect in brittle polycrystals, nanostructuring PbTe-based alloys is expected to have a mechanical benefit besides its benefit in the thermoelectric figure of merit.

In the present thesis, a preliminary work has been performed to study the viability of HPT processing to produce ultrafine-grained pure PbTe TE materials with superior thermoelectric and mechanical properties. The main goals of this work are the following two:

(1) Prove that the thermal conductivity of pure PbTe can be significantly reduced by the phonon grain boundary scattering.
(2) Improve the mechanical properties of pure PbTe by grain refining.

If the results are satisfactory, the next step will be to process PbTe-MgTe

alloys by HPT (future work).

7.2. Materials and Experimental method

High-purity PbTe powders (99.99%, <325 mesh, Fox chemicals gmbH, Germany) were used as raw material. Disks of 2.5 mm thickness and a 13 mm diameter were compacted by hot-pressing (HP) at 823 K under an axial compressive stress of 60 MPa in an Ar atmosphere (HP system Sintris 10STV). Holding time under load was 3 min. The graphite punches in contact with the sample were covered with a boron nitride layer in order to avoid any reaction with the material.

After that, The HP specimens, embedded in polytetrafluoroethylene (PTFE) rings with 13 mm/15 mm inner/outer diameter and the same thickness, were then processed at 423 K by HTP under a hydrostatic pressure of 3GPa. The disks were deformed by applying 5 revolutions to the mobile anvil with a rotational speed of 0.29 rpm.
The bulk density of each sample was determined by water immersion technique (Archimedes' method). Near-theoretical densities have been achieved (97 % and 99 %HP, for HP and HPT samples respectively).

The microstructure was characterized by scanning electron microscopy (FEG-SEM, FEI Quanta 3D) and transmission electron microscopy (TEM, JEOL JEM-2100F). The thin lamellas for TEM observations were made by the FIB "lift-out" technique.[39] Grain size and crystal orientation were determined by electron backscatter diffraction (EBSD- Oxford HKL Channel 5 equipped with a Nordlys II detector). For grain size determination, only high-angle boundaries were considered ($\theta > 12º$).

Thermal diffusivity coefficient (D) of square samples of ~$10 \times 10 \times 1.5$ mm^3, cut from the disk samples, was measured as a function of temperature by means of the laser flash technique (Nertzsch LFA 427). Density (d) was measured at room temperature by water immersion technique (Archimedes' method). The specific heat (Cp) was estimated according to literature[40 41],

and it was in good accordance with the indirectly derived values using a Pyroceram 9606 standard. The density in all the temperature range between room temperature and 700 K was estimated using the linear thermal expansion coefficient of pure PbTe ($\alpha_L = 20.4 \cdot 10^{-6} °C^{-1}$)[42]. The thermal conductivity (κ) was then calculated as $\kappa = DC_p d$.

In order to assess the mechanical properties of PbTe, micro- and nano-indentation tests, and biaxial flexure test (The ball on three balls (B3B) test) were carried out at constant displacement (0.05 mm/min) at a commercial tensile compression testing machine (Instron Mini 44). Vickers hardness (HV) was determined by performing at least 25 Vickers indentations on the sub-surface of the HP or HPT disks (at half thickness). The applied load was 1.96 N. The hardness and the Young modulus were also measured by instrumented nanoindentation (Berkovich indenter, at maximum loads of 1 mN and 6 mN). The Oliver and Pharr method was used for deriving the elastic modulus[43].

7.3. Structure and crystallographic texture

HPT is an effective tool to reach SMG-ed PbTe. The hot-pressed samples show a polycrystalline structure with 22 ± 3 μm mean linear intercept grain size (95% c.l.). The distribution of sizes is heterogeneous (figure 7.4 a). After HPT, the grains appear equiaxed on the shear plane and their size distribution is narrow (figure 7.4 b). The mean grain size has been extraordinarily reduced (270±60 nm, mean linear intercept, 95% c.l.)

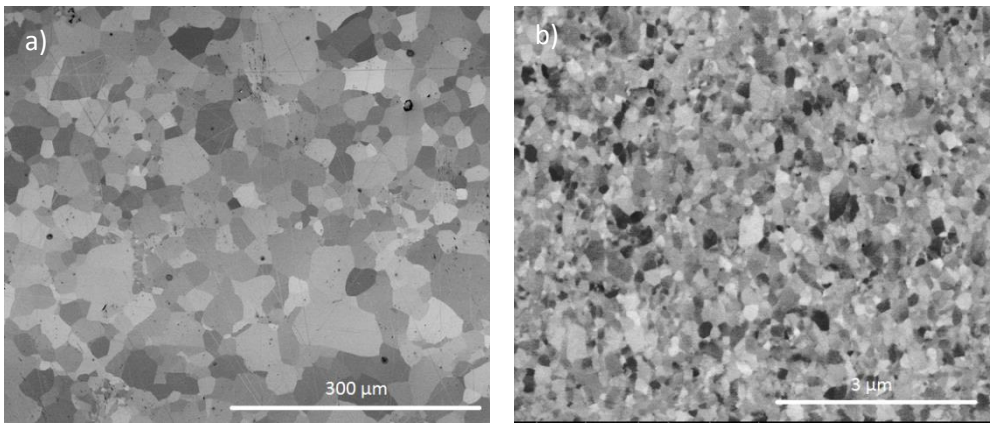

Figure 7.4: FEG-SEM images of disk subsurfaces: a) HP sample and b) HPT sample, disk rim after 5 revolutions at 423 K.

In the tangential cross-section the grains appear elongated (its shape factor is approximately 3) and oriented in a direction close to the macroscopic shear direction (figure 7.5). The final structure consists of well recovered grains with few dislocations inside (figure 7.5).

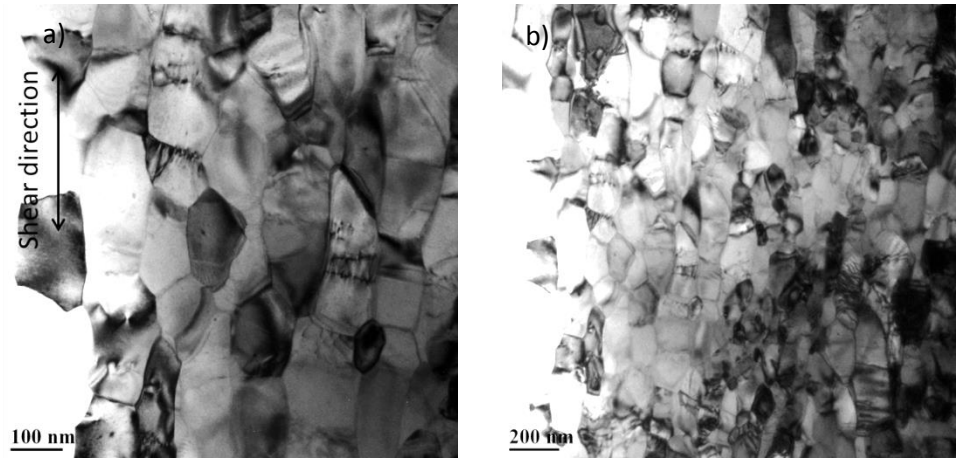

Figure 7.5: a) TEM high-magnification image of pure PbTe taken on the tangential cross-section near the disk rim. The elongated grains are aligned in a direction close to the macroscopic shear direction. b) TEM low magnification image, the saturated grain size is close to 300 nm.

Thus, the microstructure of pure PbTe after being processed by HPT is composed by ultrafine grains with a high density of high-angle grain boundaries (HAGBs) (figure7.6). These kinds of microstructures are typical for SPD-ed metals strained at relatively low homologous temperature[44].

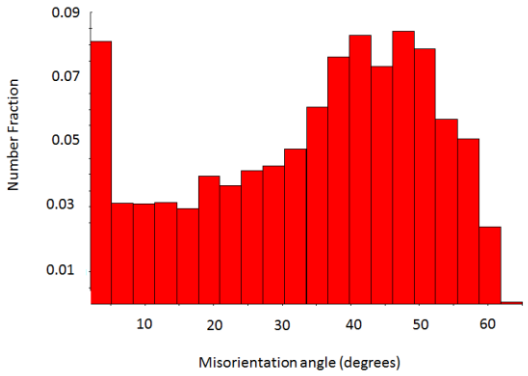

Figure 7.6: Misorientation angle between two adjacent grains for HPT-ed pure PbTe samples determined by EBSD.

HP samples do not show any preferential crystal orientation (figure 7.7a). On the other hand, the crystallographic texture of HPT samples is weak (figure 7.7 b). The orientations are mainly loosely clustered near the {111}<011> orientation (respectively, shear plane and shear direction). This texture component is found in the simple shear textures of other materials with ClNa structure, for instance, in moderately deformed ClNa rock salt at 473 K [45] and in (Mg0.5Fe0.5)O magnesiowüstite deformed at 1273-1473 K[46]. The shear texture of ClNa type materials is always very weak, although it is not clear if such weakness is intrinsic to the multi-slip mediated deformation involving several different slip systems with very different critical resolved shear stresses or to some kind of dynamic recrystallization.

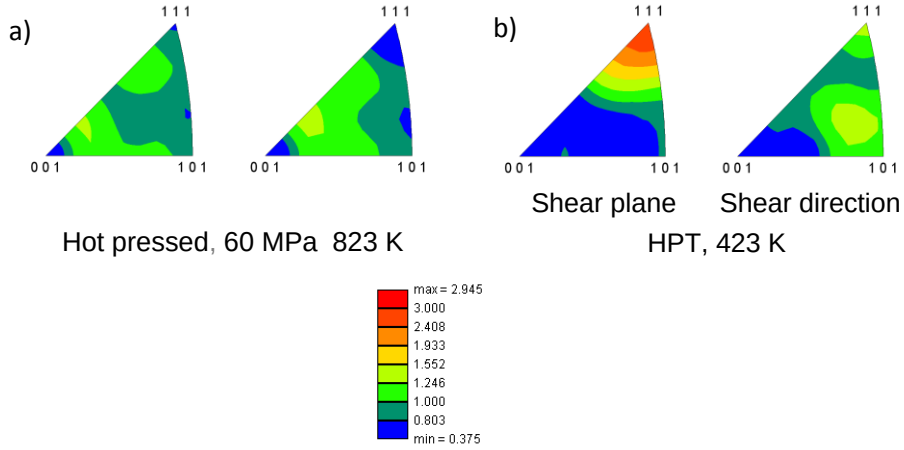

Figure 7.7: Inverse pole figures of pure PbTe samples. a) HP sample b) HPT sample near the disk rim. The shear plane normal (left) the shear direction (right).

7.4. Influence of HPT on the thermal conductivity of pure PbTe.

As expected, the grain refinement reduces significantly the thermal conductivity, (figure 7.8). Comparing to the coarse grained polycrystalline samples (HP), after HPT, the thermal conductivity is reduced up to about 20% and 30% at room temperature (RT) and 700 K (near the optimum operating temperature) respectively.

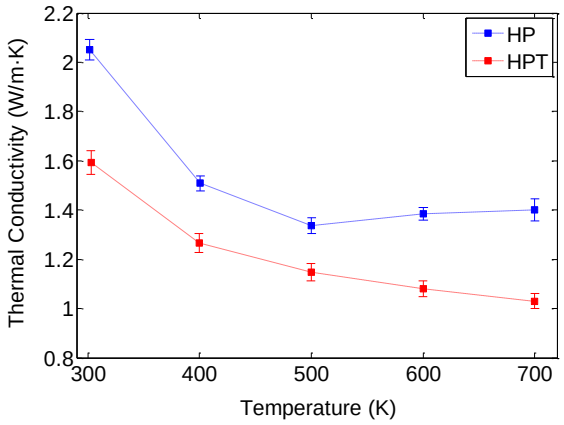

Figure 7.8: temperature dependence of thermal conductivity for HP and HPT samples.

B. Qiu et al. performed molecular dynamics (MD) simulations to predict the lattice thermal conductivity of PbTe bulk samples in the temperature range of 300–800 K[47]. According to the simulations, around ~25% of the lattice thermal conductivity in PbTe is contributed by acoustic phonon modes with mean free paths of less than 5 nm, about 55% is given by phonon modes with mean free paths between 5 and 100 nm, and the remaining ~20 % is contributed by phonon modes with mean free paths of 100-1000 nm (figure 7.9). As aforementioned, phonons with short, medium and long mean free paths can be effectively scattered by,respectively, atomic-scale point defects, nano-precipitates or second phase nanoparticles, and submicron grain boundaries. In the present work, ultrafine-grained pure PbTe has been processed by means of HPT; therefore, the main mechanism to reduce the lattice thermal conductivity is the phonon grain boundary scattering (few phonons with short mean free paths can be also scattered by dislocations). Thus, since the thermal conductivity of pure PbTe after HPT has been reduced close to 20% at RT (i.e. the same percentage corresponding to phonon modes with mean free paths of 100-1000 nm), we have proven that HPT is an outstanding tool to reduce the lattice thermal conductivity via phonon grain boundary scattering.

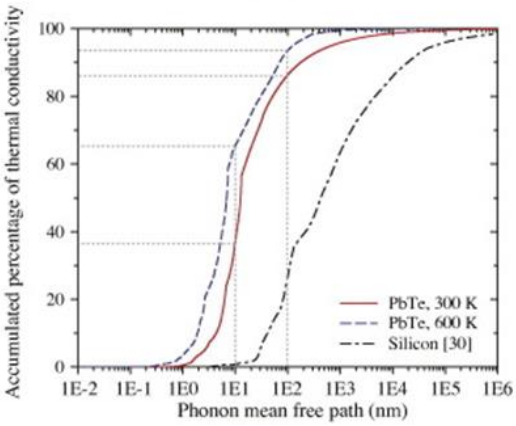

Figure 7.9: Accumulated percentage of thermal conductivity with respect to phonon mean free path in pure PbTe bulk at 300 and 600 K [47].

Close to the optimum operation temperature of PbTe-based modules the reduction of the thermal conductivity is even higher (~30 %). Since PbTe is a narrow-gaped semiconductor (E_g=0.32 eV[48]), electron-hole pairs are easily produced at the conduction band by thermal excitation of the minority carriers across the forbidden energy gap. The mixed conduction (bipolar conduction) leads to an increment of the thermal conductivity because the electronic thermal conductivity is enhanced. However, in the HPT-ed samples the bipolar contribution is negligible due to the existence of a high density of grain boundary interfaces that scatters more effectively electrons than holes[23,27].

7.5. Mechanical properties

7.5.1. Micro- and nano- hardness

Vickers hardness was measured on the disk plane along the radial direction to account the radius-dependent hardness from the axis to the rim of the disk (figure 7.10). The imposed equivalent strain at the samples is dependent on the distance from the HPT torsion axis (see equation 1.23), which means that the hardness should have a radial dependence. Nanostructuring by HPT enhances the Vickers hardness of polycrystalline PbTe from 374±3 MPa (HP samples) to 810±15 MPa (mean value in the saturated region) (95% c.l.). The values of HP samples are in accordance with those published for single-phase single-crystalline or polycrystalline PbTe compounds (300 to 800 MPa)[37,49,50]. A hardness value comparable to the measured one in the present work for pure PbTe after HPT processing has only been reported for fine-grained materials of the two-phase PbTe-PbS system[38].

The measured hardness after HPT corresponds to an equivalent uniaxial strength of about $\bar{\sigma}$ =300 MPa according to the usual conversion, $\bar{\sigma} \cong$HV/3. The compressive strengths of PbTe compounds with grain size in the 25-30 μm range are, depending on the composition, between 80 to 150 MPa[37].

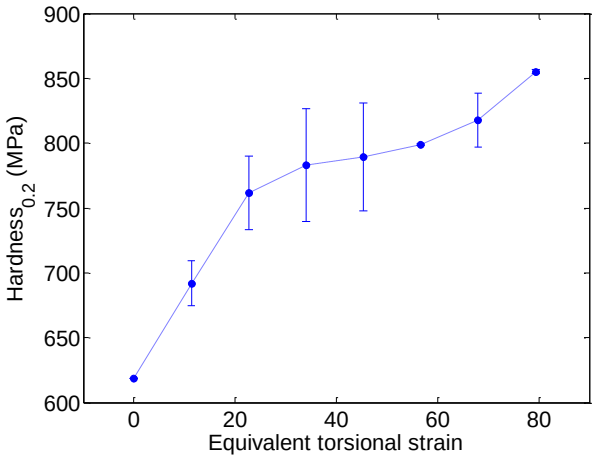

Figure 7.10: Vickers hardness against imposed equivalent torsional strain for HPTed pure PbTe samples.

The strain dependent hardness is better evidenced from the detailed measurements performed through nanoindentation, with high spatial resolution, (figure 7.11).

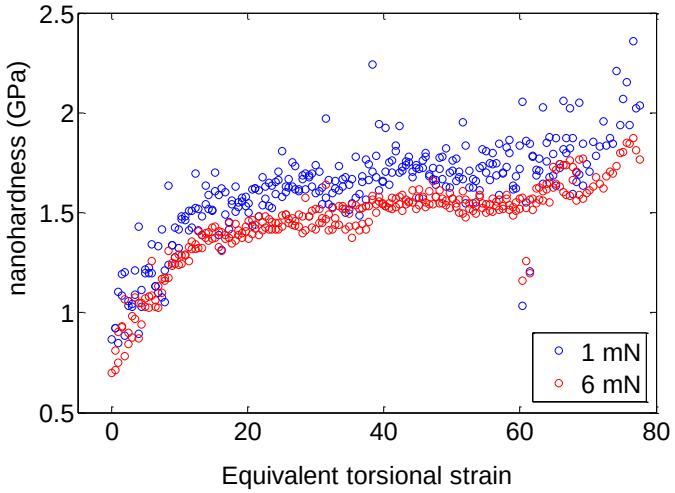

Figure 7.11: Nano-hardness against imposed equivalent torsional strain for HPTed pure PbTe samples.

PbTe shows a very high strain hardening ability. The hardness does not saturate until reaching a Von Mises equivalent torsional strain of $\varepsilon \sim 20$. Nanoindenation tests also suggest that there is a size effect. The nanohardness of HPT samples in the saturated region measured at maximum loads of 1 mN and 6 mN are 1.73±0.02 GPa and 1.56±0.01 GPa, respectively, and both are much higher than the corresponding Vickers micro-hardness, 0.81±0.02 GPa. The increase in hardness for small indentation depths has been repeatedly observed in many different crystalline materials[51–53] and it has been attributed to the additional contribution of geometrically necessary dislocations (GND) to the plastic strength[54].

7.5.2. Elastic modulus

The Young's modulus of PbTe has also been extracted from the nanoindentation tests. Mean values of 66±3 GPa and 65.±1 GPa have been obtained for respectively the HP and HPT samples. The values are of the order of the isotropic modulus derived from the single-crystal elastic constants calculated by Houston et al.[42] using the ultrasonic pulse echo technique (58.05 GPa at 303.2 K), undoped PbTe polycrystalline ingots grown by the Bridgman method measured by resonant ultrasound spectroscopy (RUS) technique (57.5±0.3 GPa at 300 K)[55] or of the values measured for extruded polycrystalline PbTe compounds (58.05 GPa at RT)[56].

7.5.3 Biaxial flexural strength

As expected, the biaxial flexural (σ_{bf}) of HPT samples is slightly higher than the measured one for HP samples; 39 ± 4 MPa and 34 ± 3 MPa respectively. It seems that grain refining has a toughening effect in polycrystalline PbTe compounds. The increase of the flexural strength by decreasing the grain size has been observed in other PbTe-based alloys; for instance, as-solidified ingots with large grain sizes (between 500-700 µm) have σ_{bf} values of 12.9 ± 2.4 MPa and 25.7 ± 6.3 MPa for $Ag_{0.43}Pb_{18}Sb_{1.2}Te_{20}$ and $Ag_{0.86}Pb_{19}Sb_{1.0}Te_{20}$ compositions respectively, whereas the σ_{bf} of their counterpart fine-grained hot pressed specimens was as high as 22-42 MPa and ~50 MPa[57].

The results show that the mechanical properties of PbTe- based alloys are very sensitive to the chemical composition. Y. Gelbstein et al. also lead to the same conclusion[37]. Unfortunately, no biaxial flexure or uniaxial flexure strength data are available in the literature for pure PbTe.

Figure 7.12 shows the SEM micrograph of the fracture surface of HP and HPT samples; in both cases intergranular fractures are observed. The fractography also confirms the extreme grain refinement induces by HPT.

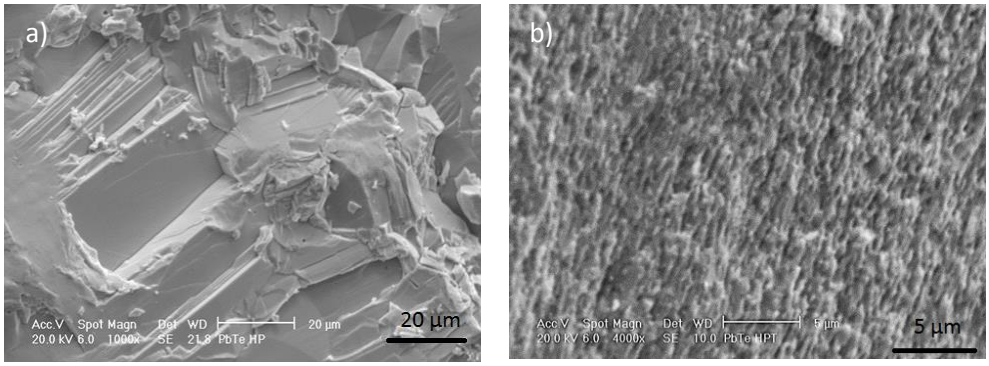

Figure 7.12: SEM micrograph of the fracture surface of a) HP and b) HPT samples.

7.6. References

1. Delaire, O. et al. Giant anharmonic phonon scattering in PbTe. Nat Mater 10, 614–619 (2011).

2. D.M. Rowe. CRC Handbook of Thermoelectrics. (1995).

3. US dept of Energy. Atomic power in space,a history. at <http://www.fas.org/nuke/space/index.htnl.>

4. He, J., Kanatzidis, M. G. & Dravid, V. P. High performance bulk thermoelectrics via a panoscopic approach. Mater. Today 16, 166–176 (2013).

5. Rowe, D. M. Thermoelectrics handbook: macro to nano. (CRC press, 2005).

6. Yang, J. & Stabler, F. R. Automotive applications of thermoelectric materials. in Journal of Electronic Materials 38, 1245–1251 (2009).

7. Yang, J. & Caillat, T. Thermoelectric Materials for Space and Automotive Power Generation. MRS Bull. 31, 224–229 (2006).

8. Biswas, K. et al. High-performance bulk thermoelectrics with all-scale hierarchical architectures. Nature 489, 414–8 (2012).

9. Snyder, G. J. & Toberer, E. S. Complex thermoelectric materials. Nat. Mater. 7, 105–114 (2008).

10. Chen, G., Dresselhaus, M. S., Dresselhaus, G., Fleurial, J.-P. & Caillat, T. Recent developments in thermoelectric materials. Int. Mater. Rev. 48, 45–66 (2003).

11. Kanatzidis, M. G. Nanostructured Thermoelectrics: The New Paradigm? Chem. Mater. 22, 648–659 (2009).

12. Zhao, L.-D., Dravid, V. P. & Kanatzidis, M. G. The panoscopic approach to high performance thermoelectrics. Energy Environ. Sci. 7, 251–268 (2014).

13. Ioffe A. Semiconductor Thermoelements and Thermoelectric Cooling. (1957).

14. H.Julian Goldsmith. Introduction to Thermoelectricity. (2010). doi:10.1007/978-3-642-00716-3

15. Basu, R. et al. Dramatic thermal conductivity reduction in PbSe[sub 0.5]Te[sub 0.5]. 1002, 1002–1003 (2013).

16. Pei, Y. et al. Convergence of electronic bands for high performance bulk thermoelectrics. Nature 473, 66–9 (2011).

17. Pei, Y., Wang, H. & Snyder, G. J. Band engineering of thermoelectric materials. Adv. Mater. 24, 6125–6135 (2012).

18. Goldsmid, H. J. Thermoelectric Refrigeration. Plenum (1964). doi:10.1007/978-1-4899-5723-8

19. Tritt, T. M. Recent Trends in Thermoelectric Materials Research I. (2001).

20. Ravich, Y. I., Efimova, B. A. & Smirnov, I. A. in Semiconducting Lead Chalcogenides SE - 7 (ed. Stil'bans, L. S.) 5, 263–322 (Springer US, 1970).

21. Biswas, K. et al. Strained endotaxial nanostructures with high thermoelectric figure of merit. Nat Chem 3, 160–166 (2011).

22. Ohta, M. et al. Enhancement of Thermoelectric Figure of Merit by the Insertion of MgTe Nanostructures in p-type PbTe Doped with Na2Te. Adv. Energy Mater. 2, 1117–1123 (2012).

23. Poudel, B. et al. High-thermoelectric performance of nanostructured bismuth antimony telluride bulk alloys. Science 320, 634–8 (2008).

24. Minnich, A. J., Dresselhaus, M. S., Ren, Z. F. & Chen, G. Bulk nanostructured thermoelectric materials : current research and future prospects. Energy Environ. Sci. 2, 466–479 (2009).

25. Xie, W., Tang, X., Yan, Y., Zhang, Q. & Tritt, T. M. Unique nanostructures and enhanced thermoelectric performance of melt-spun BiSbTe alloys. Appl. Phys. Lett. 94, 102111 (2009).

26. Tritt, T. M. Thermal Conductivity Theory, Properties, and Applications. (2004).

27. Lan, Y. et al. Structure study of bulk nanograined thermoelectric bismuth antimony telluride. Nano Lett. 9, 1419–22 (2009).

28. Kishimoto, K. & Koyanagi, T. Preparation of sintered degenerate n-type PbTe with a small grain size and its thermoelectric properties. J. Appl. Phys. 92, 2544 (2002).

29. Martin, J., Wang, L., Chen, L. & Nolas, G. S. Enhanced Seebeck coefficient through energy-barrier scattering in PbTe nanocomposites. Phys. Rev. B 79, 115311 (2009).

30. Kuo, C.-H. et al. Thermoelectric Properties of Fine-Grained PbTe Bulk Materials Fabricated by Cryomilling and Spark Plasma Sintering. Mater. Trans. 52, 795–801 (2011).

31. Pei, Y. et al. Stabilizing the optimal carrier concentration for high thermoelectric efficiency. Adv. Mater. 23, 5674–8 (2011).

32. Humphreys, F. J. & Hatherly, M. Recrystallization and related annealing phenomena. Acta Metallurgica et Materialia (2004). doi:10.1016/B978-008044164-1/50005-0

33. Nes, E., Ryum, N. & Hunderi, O. On the Zener drag. Acta Metall. 33, 11–22 (1985).

34. Zühlke, T. thermomechanical and microstructural properties of ZnCuTi under different deformation conditions. (tecnun Universidad de Navarra, 2014).

35. Lee, S. et al. Influence of scandium and zirconium on grain stability and superplastic ductilities in ultrafine-grained Al–Mg alloys. Acta Mater. 50, 553–564 (2002).

36. Valiev, R. Z., Islamgaliev, R. K. & Alexandrov, I. V. Bulk nanostructured materials from severe plastic deformation. Prog. Mater. Sci. 45, 103–189 (2000).

37. Gelbstein, Y., Gotesman, G., Lishzinker, Y., Dashevsky, Z. & Dariel, M. P. Mechanical properties of PbTe-based thermoelectric semiconductors. Scr. Mater. 58, 251–254 (2008).

38. Ni, J. E. et al. Room temperature Young's modulus, shear modulus, Poisson's ratio and hardness of PbTe–PbS thermoelectric materials. Mater. Sci. Eng. B 170, 58–66 (2010).

39. Giannuzzi, L. a. & Stevie, F. a. A review of focused ion beam milling techniques for TEM specimen preparation. Micron 30, 197–204 (1999).

40. Pashinkin, A. S., Mikhailova, M. S., Malkova, A. S. & Fedorov, V. A. Heat capacity and thermodynamic properties of lead selenide and lead telluride. Inorg. Mater. 45, 1226–1229 (2009).

41. Pei, Y.-L. & Liu, Y. Electrical and thermal transport properties of Pb-based chalcogenides: PbTe, PbSe, and PbS. J. Alloys Compd. 514, 40–44 (2012).

42. Houston, B. Elastic Constants, Thermal Expansion, and Debye Temperature of Lead Telluride. J. Appl. Phys. 39, 3913 (1968).

43. Oliver, W. C. & Pharr, G. M. An improved technique for determining hardness and elastic modulus using load and displacement sensing indentation experiments. J. Mater. Res. 7, 1565–1583 (1992).

44. Pippan, R. et al. Saturation of Fragmentation During Severe Plastic Deformation. Annual Review of Materials Research 40, 319–343 (2010).

45. Wenk, H.-R., Armann, M., Burlini, L., Kunze, K. & Bortolotti, M. Large strain shearing of halite: Experimental and theoretical evidence for dynamic texture changes. Earth Planet. Sci. Lett. 280, 205–210 (2009).

46. Long, M. D., Xiao, X., Jiang, Z., Evans, B. & Karato, S. Lattice preferred orientation in deformed polycrystalline (Mg,Fe)O and implications for seismic anisotropy in D″. Phys. Earth Planet. Inter. 156, 75–88 (2006).

47. Qiu, B., Bao, H., Zhang, G., Wu, Y. & Ruan, X. Molecular dynamics simulations of lattice thermal conductivity and spectral phonon mean free path of PbTe: Bulk and nanostructures. Comput. Mater. Sci. 53, 278–285 (2012).

48. Dughaish, Z. H. Lead telluride as a thermoelectric material for thermoelectric power generation. Phys. B Condens. Matter 322, 205–223 (2002).

49. Crocker, A. J. & Wilson, M. Microhardness in PbTe and related alloys. J. Mater. Sci. 13, 833–842 (1978).

50. Schmitz, A., Stiewe, C. & Müller, E. Variations of Thermoelectric and Mechanical Properties of Large Lead Telluride Samples Produced by a Short-Term Sintering Method. J. Electron. Mater. 40, 543–546 (2011).

51. Ma, Q. & Clarke, D. R. Size dependent hardness of silver single crystals. J. Mater. Res. 10, 853–863 (1995).

52. McElhaney, K. W., Vlassak, J. J. & Nix, W. D. Determination of indenter tip geometry and indentation contact area for depth-sensing indentation experiments. J. Mater. Res. 13, 1300–1306 (1998).

53. Alkorta, J., Martínez-Esnaola, J. & Gil Sevillano, J. Detailed assessment of indentation size-effect in recrystallized and highly deformed niobium. Acta Mater. 54, 3445–3452 (2006).

54. Nix, W. D. & Gao, H. Indentation size effects in crystalline materials: A law for strain gradient plasticity. J. Mech. Phys. Solids 46, 411–425 (1998).

55. Ren, F. et al. The high-temperature elastic moduli of polycrystalline PbTe measured by resonant ultrasound spectroscopy. Acta Mater. 56, 5954–5963 (2008).

56. Vasilevskiy, D., Masut, R. a. & Turenne, S. Thermoelectric and Mechanical Properties of Novel Hot-Extruded PbTe n-Type Material. J. Electron. Mater. 41, 1057–1061 (2012).

57. Ren, F. et al. Mechanical Characterization of PbTe-based Thermoelectric Materials. in MRS Proceedings 1044, 1044–U04–04 (2007).

Chapter 8: Conclusions

- Nanostructured and highly textured Bi_2Te_3-based alloys have been obtained by means of severe plastic deformation (SPD). Grain sizes of about 100 nm were obtained after 5 turns under 3 GPa at 150ºC.

- After HPT, the thermal conductivity of $Sb_{2-x}Bi_xTe_3$ alloys has been drastically reduced (up to ~50%) without affecting significantly the electronic conduction. This leads to promising zT values, zT_{RA} (i.e. PF measured in-plane and κ out of plane) of ~2 at 425 K for $Sb_{1.6}Bi_{0.4}Te_3$, zT_{RR} (estimated) ~1.5 at 375 K

- The high density of lattice defects generated by SPD (especially the grain boundaries and antisite defects) has a great effect on the carrier concentration of the $Sb_{2-x}Bi_xTe_3$ alloys. To optimize the thermoelectric performance of HPT processed alloys, the carrier concentration has to be finely tuned. Tellurium doping is a well-established strategy to reduce the antisite defects and hence to control the carrier concentration; however, Te heavy doping (% 4 wt.) has a negative effect on the mobility of the free carriers.

- Annealing treatments after SPD is also a suitable strategy to reduce the antisite defects. The annealing treatments do not affect negatively the carrier mobility but, grain growth may take place if the annealing temperature is too high. Bi_2Te_3-based nanostructures and properties have shown to be thermally stable up to 473 K.

- The suppression of mixed conduction due to the high density of grain boundaries leads to a widening of the temperature range with optimum thermoelectric performance.

- The performed macro-, micro- and nano-mechanical tests make evident that the elastic and plastic anisotropic properties of Bi_2Te_3-based alloys. The plastic resistance is mainly dictated by the inclination of the basal plane with respect to the compression axis.

- HPT processing enhances the hardness and compressive strength of $Sb_{2-x}Bi_xTe_3$ alloys. However, cracks propagate easily along the grain boundaries due to the strong preferred orientation of HPT samples. Consequently, although the flexure strength of HPT samples is higher than those of materials prepared by unidirectional crystal growing method, it is not as high as the reported ones for fine-grained samples processed by conventional powder metallurgy methods. Further work is needed for improving the toughness of HPT-processed alloys.

- HPT has also been successfully applied to pure PbTe. After HPT, thermal conductivity has been largely reduced due to the phonon grain boundary scattering. Thus, HPT is a promising tool to process high-performance PbTe-based bulk thermoelectric materials with all-scale hierarchical architectures with enhanced mechanical properties.

Chapter 9: Future work

In this thesis, it has been shown that HPT is a suitable method to improve the thermoelectric efficiency of Bi_2Te_3-based thermoelectric (TE) materials via grain refinement and texture enhancement. However, SPD methods, especially HPT, are not conventional methods to process bulk nanostructured TE materials. Therefore, still higher thermoelectric performances can be obtained by optimizing some processing factor and combining SPD methods with recent approaches.
Some guidelines are proposed to improve the thermoelectric and mechanical properties of the studied TE families:

- The effect of the HPT processing temperature and the subsequent annealing treatments on the carrier concentration should be deeply studied. By adjusting such parameters and the dopants an optimum carrier concentration can be reached which will lead to an optimized thermoelectric performance.

- Dispersing second-phase nanoparticles into the matrix is an effective strategy to reduce the lattice thermal conductivity. On the one hand, low-to medium-wavelength phonons are effectively scattered with nanoparticles. On the other hand, the second-phase nanoparticles act as grain growth inhibitors preventing recovery and recrystallization during the deformation; consequently adding second-phase particles decreases the final saturated grain size, which increases the phonon grain boundary scattering. HPT enables a homogeneous dispersion of the second-phase particles; therefore, record *zT* values could be achieved by dispersing nanoparticles produced by scalable and cost-effective methods, for instance by wet chemical approaches, through HPT.

- Recently record *zT* values have been reported in nanostructured bulk Na-doped PbTe-SrTe and PbTe-MgTe systems with all-scale hierarchical architectures. In these systems, a broad spectrum of phonons is scattered by atomic-scale point defects, nanoscale precipitates and grain boundaries. In the present work, ultrafine-grained pure PbTe has been processed by HPT. The grain refinement, besides reducing the thermal conductivity due to the phonon grain boundary sacattering, enhances its mechanical properties. Thus, the next step should be to process by HPT the PbTe-SrTe or the PbTe-MgTe system. Due to the high density of nanoprecipitates that reduce the grain boundary mobility through Zener pinning, we expect that the saturated grain size after HPT processing will be even finer and thermally stable. The superior grain refinement ability of HPT demonstrated in this work with respect to spark plasma sintering makes it an excellent candidate to improve the state-of-the-art thermoelectric efficiency of PbTe-based materials.

APPENDIX I: X-ray Patterns Cards

Bi_2Te_3:

00-015-0863 Nov 22, 2015 8:46 PM (admate)

PDF Card Report

Status: Primary QM: Star (S) Pressure/Temperature: Ambient Chemical Formula: Bi2 Te3
Empirical Formula: Bi2 Te3 Weight %: Bi52.20 Te47.80 Atomic %: Bi40.00 Te60.00
Compound Name: Bismuth Telluride Mineral Name: Tellurobismuthite, syn

Experimental

Author's Reported Data

Radiation: CuKá1 : 1.5406Å d-Spacing: Diff. Intensity: Diffractometer I/Ic: 6.3
Reference: Natl. Bur. Stand. (U.S.) Monogr. 25 3, 16 (1964).

Physical

SYS: Rhombohedral SPGR: R-3m (166)

Author's Cell

AuthCell a: 4.3852Å	AuthCell c: 30.483Å	AuthCell Vol: 507.65Å³
AuthCell Z: 3.00	AuthCell MolVol: 169.22	

Reference: Ibid. Dcalc: 7.858g/cm³ Dmeas: 7.815g/cm³ SS/FOM: F(30) = 36.4(0.0147, 56)

Crystal

ICDD Calculated Parameters

Space Group: R-3m (166) Molecular Weight: 800.76

Crystal Data

XtlCell a: 4.385Å	XtlCell b: 4.385Å	XtlCell c: 30.483Å
XtlCell : 90.00°	XtlCell : 90.00°	XtlCell : 120.00°
XtlCell Vol: 507.65Å³	XtlCell Z: 3.00	

Crystal Data Axial Ratio

a/b: 0.0000	c/b: 6.9513

Reduced Cell

RedCell a: 4.385Å	RedCell b: 4.385Å	RedCell c: 10.472Å
RedCell : 77.91°	RedCell : 77.91°	RedCell : 60.00°
RedCell Vol: 169.22Å³		

Structure

Crystal (Symmetry Allowed): Centrosymmetric

Miscellaneous

Pearson: hR5.00 Prototype Structure: Bi2 Te3 Prototype Structure (Alpha Order): Bi2 Te3

Mineral Classification: Tetradymite (Supergroup), 5R (Group)

Subfile(s): Inorganic, Metals & Alloys, Mineral Related (Mineral ,Synthetic), NBS Pattern, Primary Pattern

Last Modification Date: 01/24/2009

Cross-Ref PDF #'s: 00-002-0524 (Alternate), 00-008-0021 (Deleted), 01-072-2036 (Primary), 01-082-0358 (Alternate), 01-085-0439 (Alternate), 04-002-0233, 04-002-0234, 04-002-0580, 04-002-5479, 04-003-2510, 04-003-5939, 04-004-5233, 04-004-5238, 04-004-5529, 04-004-5960, 04-004-7432, 04-004-7571, 04-004-7783, 04-004-7785, 04-004-8858, 04-005-5906, 04-005-6292, 04-006-8100, 04-006-8147, 04-007-1004

Comments

Database Comments: Analysis: Spectroscopic analysis (wt.%): 0.0001 to 0.001 each of Mg and Si. Color: Gray. Opaque Optical Data: Opaque mineral optical data on specimen from Oya mine, Japan: R1Ro=61.3, RR2Re=58.7, Disp.=16, Color values 1 .315, .320, 61.6, 2 .312, .317, 59.0, Ref.: IMA Commission on Ore Microscopy QDF. Sample Source or Locality: Sample was obtained from Semitronics Inc., Winchester, Massachusetts, USA. Temperature of Data Collection: Pattern taken at 298 K. Unit Cell: Rhombohedral cell: a=10.472, á=24.17°. Unit Cell Data Source: Powder Diffraction.

00-015-0863 (Variable Slit Intensity) - Cu K1 1.54056Å

2	d(Å)	I	h	k	l	*	2	d(Å)	I	h	k	l	*
8.6961	10.160000	2	0	0	3		80.7905	1.188600	<3	2	0	20	
17.4497	5.078000	6	0	0	6		83.1287	1.161000	<3	1	0	25	
23.5982	3.767000	4	1	0	1		84.4293	1.146400	<3	2	1	16	
26.2041	3.398000	<1	1	0	4		86.9045	1.120000	<3	0	1	26	
27.6632	3.222000	100	0	1	5		89.2748	1.096300	<3	2	2	0	
33.2918	2.689000	3	0	1	8		90.2684	1.086800	<3	2	0	23	
37.8333	2.376000	34	1	0	10		91.6051	1.074400	<3	3	0	15	
40.2637	2.238000	6	0	1	11		94.8045	1.046400	<4	1	0	28	
41.1466	2.192000	37	1	1	0		95.8301	1.037900	<4	3	1	5	
42.1522	2.142000	4	1	1	3		97.2997	1.026100	<4	0	2	25	
44.5759	2.031000	10	0	0	15		98.5636	1.016300	<4	0	0	30	
44.9962	2.013000	7	1	1	6		101.0640	0.997800	<4	2	0	26	
45.4247	1.995000	4	1	0	13		101.3720	0.995600	7	1	3	10	
48.1027	1.890000	<2	0	1	14		104.5590	0.973800	<4	1	2	23	
50.3139	1.812000	15	2	0	5		105.9360	0.964900	<4	2	2	15	
53.8178	1.702000	4	1	0	16		107.6900	0.954000	<4	3	0	21	
54.1272	1.693000	<2	0	0	18		108.0530	0.951800	<4	1	0	31	
57.1277	1.611000	12	0	2	10		109.2990	0.944400	<4	0	2	28	
58.9694	1.565000	<3	2	0	11		110.3740	0.938200	<4	0	4	5	
62.2536	1.490100	18	1	1	15		111.9500	0.929400	<4	2	1	25	
62.9343	1.475600	5	0	2	13		112.9860	0.923800	<4	0	0	33	
64.1123	1.451300	<3	0	0	21		116.0600	0.908000	<4	1	2	26	
66.0156	1.414000	10	0	1	20		116.3850	0.906400	<4	4	0	10	
66.9238	1.397000	14	1	2	5		123.3620	0.875000	<4	2	2	21	
69.8831	1.344900	5	0	2	16		125.2800	0.867300	8	2	1	28	
70.1524	1.340400	<3	1	1	18		125.4590	0.866600	<4	3	1	20	
72.7633	1.298600	10	2	1	10		126.4990	0.862600	<4	2	3	5	
74.9532	1.266000	6	3	0	0		129.6290	0.851200	<4	1	1	33	
75.9817	1.251400	<3	0	1	23		130.3220	0.848800	<4	0	1	35	
77.9841	1.224200	<3	2	1	13		133.7110	0.837700	<4	3	2	10	
79.0533	1.210300	<3	1	1	21		136.7500	0.828600	<4	4	1	0	

$Bi_{0.5}Sb_{1.5}Te_3$:

00-049-1713 Nov 22, 2015 9:03 PM (admate)

PDF Card Report

Status: Primary QM: Low-Precision (O) Pressure/Temperature: Ambient
Chemical Formula: Bi0.5 Sb1.5 Te3 Empirical Formula: Bi0.5 Sb1.5 Te3
Weight %: Bi15.60 Sb27.26 Te57.14 Atomic %: Bi10.00 Sb30.00 Te60.00
Compound Name: Bismuth Antimony Telluride

Experimental

Author's Reported Data

Radiation: CuKá1 : 1.5406Å d-Spacing: Diff. Intensity: Diffractometer
Reference: Ritter, J., National Inst. of Standards and Technology, Gaithersburg, MD, USA. Private Communication (1997).

Physical

SYS: Rhombohedral SPGR: R-3m (166)

Author's Cell

AuthCell a: 4.28424Å	AuthCell c: 30.52389Å	AuthCell Vol: 485.20Å³
AuthCell Z: 3.00	AuthCell MolVol: 161.73	

Reference: Ritter, J., Maruthamuthu, P. Inorg. Chem. 36, 260 (1997). Dcalc: 6.878g/cm³
SS/FOM: F(23) = 8.2(0.069, 41)

Crystal

ICDD Calculated Parameters

Space Group: R-3m (166) Molecular Weight: 669.92

Crystal Data

XtlCell a: 4.284Å	XtlCell b: 4.284Å	XtlCell c: 30.524Å
XtlCell : 90.00°	XtlCell : 90.00°	XtlCell : 120.00°
XtlCell Vol: 485.20Å³	XtlCell Z: 3.00	

Crystal Data Axial Ratio

a/b: 0.0000 c/b: 7.1247

Reduced Cell

RedCell a: 4.284Å	RedCell b: 4.284Å	RedCell c: 10.471Å
RedCell : 78.20°	RedCell : 78.20°	RedCell : 60.00°
RedCell Vol: 161.73Å³		

Structure

Crystal (Symmetry Allowed): Centrosymmetric

Miscellaneous

Pearson: hR5.00 Prototype Structure: Bi2 Te3 Prototype Structure (Alpha Order): Bi2 Te3
Subfile(s): Inorganic, Metals & Alloys, Primary Pattern Entry Date: 02/02/1998
Last Modification Date: 01/24/2009 Cross-Ref PDF #'s: 04-002-0106, 04-002-0492

Comments

Database Comments: Analysis: Chemical analysis (wt.%): "Bi" 16.33, "Sb" 23.20, "Te" 57.53. General Comments: May contain unknown second phase, accounting for some observed reflections. Sample Preparation: "Te" and "Bi2 O3" were dissolved in "H N O3", then "Sb2 O3" was dissolved at 90 C. A char was produced after heating at 350 C. The pulverized char was heated under "H2" at 300 C for 6 hours and at 400 C for 6 hours.

00-049-1713 (Variable Slit Intensity) - Cu K1 1.54056Å

2	d(Å)	I	h	k	l	*	2	d(Å)	I	h	k	l	*	2	d(Å)	I	h	k	l	*
8.6468	10.217800	1	0	0	3		40.4380	2.228760	12	0	1	11		57.1552	1.610290	4	0	1	17	
14.3716	6.157930	2					42.1989	2.139740	46	1	1	0		58.2423	1.582790	19	0	2	10	
17.4035	5.091370	5	0	0	6		44.5357	2.032740	33	0	0	15		59.9944	1.540690	5	2	0	11	
19.3625	4.580450	5					45.8277	1.978390	12	1	1	6		63.0082	1.474050	35	1	0	19	
23.0294	3.858750	2					47.0217	1.930900	7					64.0951	1.451650	7	0	0	21	
26.2403	3.393400	3	0	0	9		48.4525	1.877170	6	0	1	14		66.1600	1.411260	16	0	1	20	
28.1143	3.171320	100	0	1	5		49.6036	1.836270	6	2	0	2		67.8239	1.380630	5	2	1	4	
33.6681	2.659800	5	0	1	8		50.4766	1.806540	9	0	2	4		68.7549	1.364190	26	1	2	5	
36.5060	2.459280	6					51.4975	1.773100	26	2	0	5								
38.1580	2.356520	75	1	0	10		54.0664	1.694760	15	0	0	18								

$Bi_{0.4}Sb_{1.6}Te_3$:

03-065-3674 Nov 22, 2015 9:01 PM (admate)

PDF Card Report

Status: Primary QM: Indexed (I) Pressure/Temperature: Ambient
Chemical Formula: Bi1.20 Sb4.80 Te9 Empirical Formula: Bi1.2 Sb4.8 Te9
Weight %: Bi12.64 Sb29.46 Te57.90 Atomic %: Bi8.00 Sb32.00 Te60.00
Compound Name: Bismuth Antimony Telluride

Experimental

Author's Reported Data

Radiation: CuKá1 : 1.5406Å d-Spacing: Calculated Intensity: Calculated I/Ic: 16.39

Reference: M.M.Stasova & N.Kh.Abrikosov Izv. Akad. Nauk SSSR, Neorg. Mater. 6, 1090 (1970). Calculated from NIST using POWD-12++.

Physical

SYS: Rhombohedral SPGR: R-3m (166)

Author's Cell

AuthCell a: 4.3000(40)Å	AuthCell c: 30.28(3)Å	AuthCell Vol: 484.87Å³
AuthCell Z: 1.00	AuthCell MolVol: 484.87	

Reference: Ibid. Dcalc: 6.793g/cm³ SS/FOM: F(30) = 379.6(0.0025, 31)

Crystal

ICDD Calculated Parameters

Space Group: R-3m (166) Molecular Weight: 1983.58

Crystal Data

XtlCell a: 4.300Å	XtlCell b: 4.300Å	XtlCell c: 30.280Å
XtlCell : 90.00°	XtlCell : 90.00°	XtlCell : 120.00°
XtlCell Vol: 484.87Å³	XtlCell Z: 1.00	

Crystal Data Axial Ratio

a/b: 0.0000 c/b: 7.0419

Reduced Cell

RedCell a: 4.300Å	RedCell b: 4.300Å	RedCell c: 10.394Å
RedCell : 78.06°	RedCell : 78.06°	RedCell : 60.00°
RedCell Vol: 161.62Å³		

Structure

Crystal (Symmetry Allowed): Centrosymmetric

Miscellaneous

Pearson: hR5.00 Prototype Structure (Alpha Order): Bi2 Te3
Subfile(s): Inorganic, Metals & Alloys, NIST Pattern, Primary Pattern Entry Date: 02/11/2005
Last Modification Date: 02/02/2009

Comments

Database Comments: NIST M&A collection code: N AL6493 2110. Temperature Factor: IB=Te,Bi,Sb. Minor Warning: No Rfactor reported/abstracted.

03-065-3674 (Variable Slit Intensity) - Cu K1 1.54056Å

2	d(Å)	I	h	k	l	*	2	d(Å)	I	h	k	l	*
8.7537	10.093300	19	0	0	3		93.5170	1.057390	86	0	3	15	
17.5589	5.046670	29	0	0	6		93.7972	1.054970	50	2	1	19	
24.0579	3.696060	9	1	0	1		94.2126	1.051410	11	2	2	6	
24.5979	3.616130	6	0	1	2		95.7544	1.038520	45	1	0	28	
26.4702	3.364440	13	0	0	9		96.7015	1.030850	57m	1	2	20	
26.6554	3.341480	10	1	0	4		96.7015	1.030850	m	3	1	2	
28.1066	3.172170	1000	0	1	5		97.5673	1.024000	8m	2	2	9	
31.6782	2.822190	13	1	0	7		97.5673	1.024000	m	1	3	4	
33.7368	2.654540	43	0	1	8		98.3241	1.018130	117	3	1	5	
35.5480	2.523330	7	0	0	12		98.6960	1.015290	73	0	2	25	
38.2789	2.349360	465	1	0	10		99.4872	1.009330	8	0	0	30	
40.7272	2.213600	48	0	1	11		100.1280	1.004590	8m	0	1	29	
41.9880	2.150000	469	1	1	0		100.1280	1.004590	m	1	3	7	
42.9762	2.102820	12	1	1	3		100.9230	0.998816	40	0	3	18	
44.8629	2.018670	86	0	0	15		101.2600	0.996397	27	3	1	8	
45.9168	1.974760	71m	1	0	13		101.5500	0.994337	8	1	1	27	
45.9168	1.974760	m	1	1	6		102.3110	0.988991	8	2	2	12	
48.6423	1.870290	15	0	1	14		102.5440	0.987379	15	2	0	26	
48.9727	1.858440	7	0	2	1		103.9960	0.977526	95	1	3	10	
49.2669	1.848030	7	2	0	2		105.6060	0.967002	15	3	1	11	
50.3234	1.811680	17	1	1	9		106.4780	0.961479	54	1	2	23	
50.4309	1.808070	12	0	2	4		108.5460	0.948846	72	2	2	15	
51.2914	1.779740	278	2	0	5		109.3390	0.944168	25m	1	0	31	
53.5375	1.710250	7	0	2	7		109.3390	0.944168	m	1	3	13	
54.3310	1.687130	42	1	0	16		109.9320	0.940730	25	0	3	21	
54.5027	1.682220	46	0	0	18		110.9140	0.935143	39	0	2	28	
54.9086	1.670740	18	2	0	8		111.9820	0.929222	8	0	4	2	
56.1571	1.636520	11	1	1	12		112.9450	0.924016	8	4	0	4	
57.2896	1.606830	7	0	1	17		113.6720	0.920168	53	0	4	5	
58.1100	1.586080	176	0	2	10		114.0730	0.918074	57m	2	1	25	
59.9268	1.542270	21	2	0	11		114.0730	0.918074	m	0	0	33	
63.1228	1.471650	213	1	1	15		114.9310	0.913661	19	1	1	30	
63.9604	1.454380	31	0	2	13		116.3440	0.906602	22	1	3	16	
64.5809	1.441900	16	0	0	21		116.5000	0.905838	36	2	2	18	
66.1692	1.411090	9	2	0	14		116.8700	0.904033	22	0	4	8	
66.6258	1.402520	68m	0	1	20		118.2880	0.897281	26	1	2	26	
66.6258	1.402520	m	1	2	2		119.1090	0.893483	9	3	1	17	
67.6480	1.383790	7	2	1	4		119.9050	0.889868	48	4	0	10	
68.3682	1.370960	263	1	2	5		121.0390	0.884846	9	0	3	24	
70.2704	1.338440	7	2	1	7		121.7190	0.881906	9	0	4	11	
70.9499	1.327270	29	0	2	16		125.4260	0.866729	9m	1	3	19	
71.0983	1.324870	81	1	1	18		125.4260	0.866729	m	1	0	34	
71.4478	1.319240	22	1	2	8		125.8770	0.864978	16	0	2	31	
73.5202	1.287090	7	2	0	17		126.0060	0.864482	16	4	0	13	
74.2422	1.276350	181	2	1	10		126.6990	0.861841	27	2	2	21	
75.2546	1.261670	7	0	0	24		127.8570	0.857539	68	2	1	28	
75.8539	1.253190	23	1	2	11		128.5220	0.855124	38	0	4	14	
76.7116	1.241300	150m	3	0	0		129.0590	0.853204	49m	3	1	20	
76.7116	1.241300	m	0	1	23		129.0590	0.853204	m	2	3	2	
77.3963	1.232020	8	0	3	3		130.2830	0.848934	9	3	2	4	
79.0183	1.210750	8	0	2	19		131.1640	0.845947	102	2	3	5	
79.4973	1.204650	34m	3	0	6		131.7700	0.843932	125m	2	0	32	
79.4973	1.204650	m	2	1	13		131.7700	0.843932	m	1	1	33	
80.0651	1.197530	39	1	1	21		132.1460	0.842700	16	0	1	35	
81.5279	1.179700	10	1	2	14		133.4290	0.838585	9	1	2	29	
81.9507	1.174680	40	2	0	20		133.5730	0.838134	9	3	2	7	
82.8176	1.164570	8	0	3	9		134.4650	0.835371	13	4	0	16	
83.9423	1.151810	24	1	0	25		135.1280	0.833359	13	2	3	8	
86.0044	1.129400	27	2	1	16		135.5320	0.832153	9	0	3	27	
86.7613	1.121480	8	0	0	27		138.0030	0.825073	9	0	4	17	
87.5073	1.113830	8	0	3	12		139.0500	0.822224	86	3	2	10	
87.7347	1.111530	19	0	1	26		140.5640	0.818258	9	2	2	24	
88.4549	1.104330	8	1	2	17		141.4870	0.815931	17	2	3	11	
90.1257	1.088150	8	1	1	24		142.8450	0.812624	153m	4	1	0	
91.5392	1.075000	102m	2	2	0		142.8450	0.812624	m	3	1	23	
91.5392	1.075000	m	2	0	23		146.7580	0.803867	9	4	0	19	
92.2072	1.068950	8	2	2	3		147.4330	0.802469	33m	2	1	31	

2	d(Å)	I	h	k	l	*	2	d(Å)	I	h	k	l	*
147.4330	0.802469	m	3	2	13		149.0250	0.799304	9	1	0	37	

Sb_2Te_3:

01-071-0393 Nov 22, 2015 9:05 PM (admate)

PDF Card Report

Status: Primary QM: Star (S) Pressure/Temperature: Ambient Chemical Formula: Sb2 Te3
Empirical Formula: Sb2 Te3 Weight %: Sb38.88 Te61.12 Atomic %: Sb40.00 Te60.00 ANX: A2X3
Compound Name: Antimony Telluride Mineral Name: Tellurantimony, syn

Experimental

Author's Reported Data

Radiation: CuKá1 : 1.5406Å d-Spacing: Calculated Intensity: Calculated I/Ic: 15.23

Reference: "Refinement of the Sb2 Te and Sb2 Te Se structures and their relationship to nonstoichiometric Sb2 Te3-y Sey compounds". Anderson, T.L., Krause, H.B. Acta Crystallogr., Sec. B: Struct. Crystallogr. Cryst. Chem. 30, 1307 (1974). Calculated from ICSD using POWD-12++. (2004).

Physical

SYS: Rhombohedral SPGR: R-3m (166)

Author's Cell

AuthCell a: 4.2640(10)Å	AuthCell c: 30.4580(70)Å	AuthCell Vol: 479.59Å³
AuthCell Z: 3.00	AuthCell MolVol: 159.86	

Reference: Ibid. Dcalc: 6.506g/cm³ Dstruc: 6.5g/cm³ SS/FOM: F(30) = 999.9(0.0001, 31)
R-factor: 0.036

Crystal

ICDD Calculated Parameters

Space Group: R-3m (166) Molecular Weight: 626.30

Crystal Data

XtlCell a: 4.264Å	XtlCell b: 4.264Å	XtlCell c: 30.458Å
XtlCell : 90.00°	XtlCell : 90.00°	XtlCell : 120.00°
XtlCell Vol: 479.59Å³	XtlCell Z: 3.00	

Crystal Data Axial Ratio

a/b: 0.0000 c/b: 7.1431

Reduced Cell

RedCell a: 4.264Å	RedCell b: 4.264Å	RedCell c: 10.447Å
RedCell : 78.22°	RedCell : 78.22°	RedCell : 60.00°
RedCell Vol: 159.86Å³		

Structure

Crystal (Symmetry Allowed): Centrosymmetric

Miscellaneous

Pearson: hR5.00 Prototype Structure: Bi2 Te3 Prototype Structure (Alpha Order): Bi2 Te3
Subfile(s): ICSD Pattern, Inorganic, Metals & Alloys, Mineral Related (Mineral ,Synthetic), Primary Pattern
Entry Date: 11/20/2008 Last Modification Date: 01/21/2009
Cross-Ref PDF #'s: 00-015-0874 (Primary), 01-072-1990 (Alternate), 03-065-3678 (Deleted)

Comments

Database Comments: ANX: A2X3. Analysis: Sb2 Te3. Formula from original source: Sb2 Te3. ICSD Collection Code: 2084. Calculated Pattern Original Remarks: New refinement based on previously measured intensities. Cell in 2nd reference: 4.262, 30.450 (synthetic) and 4.258, 30.516 (from Mattagami Lake mine, Quebec). Wyckoff Sequence: c2 a(R3-MH). Unit Cell Data Source: Single Crystal.

01-071-0393 (Variable Slit Intensity) - Cu K1 1.54056Å

2	d(Å)	I	h	k	l	*	2	d(Å)	I	h	k	l	*
8.7024	10.152700	17	0	0	3		87.2334	1.116620	19	0	1	26	
17.4555	5.076330	30	0	0	6		88.1324	1.107540	8	0	3	12	
24.2589	3.665890	6	1	0	1		88.7867	1.101060	8	1	2	17	
24.7886	3.588740	8	0	1	2		89.8770	1.090510	11	1	1	24	
26.3127	3.384220	24	0	0	9		91.4189	1.076100	34	2	0	23	
26.8095	3.322630	22	1	0	4		92.5373	1.066000	61	2	2	0	
28.2370	3.157820	1000	0	1	5		94.0716	1.052610	71	3	0	15	
31.7558	2.815470	14	1	0	7		95.1574	1.043450	41m	2	2	6	
33.7869	2.650720	42	0	1	8		95.1574	1.043450	m	1	0	28	
35.3333	2.538170	7	0	0	12		96.9399	1.028950	36	1	2	20	
38.2736	2.349670	435	1	0	10		97.8406	1.021870	8	3	1	2	
40.6943	2.215310	53	0	1	11		98.5046	1.016750	20m	0	2	25	
42.3595	2.132000	456	1	1	0		98.5046	1.016750	m	2	2	9	
43.3295	2.086490	9	1	1	3		98.7286	1.015040	14	1	3	4	
44.5868	2.030530	76	0	0	15		99.3973	1.010000	98m	0	1	29	
45.8292	1.978330	65	1	0	13		99.3973	1.010000	m	3	1	5	
46.1414	1.965670	27	1	1	6		101.1610	0.997100	14m	1	1	27	
48.5273	1.874450	30	0	1	14		101.1610	0.997100	m	1	3	7	
49.4109	1.842980	7	0	2	1		101.4000	0.995402	37	0	3	18	
49.6998	1.832940	7	2	0	2		102.2870	0.989165	18m	2	0	26	
50.5563	1.803880	38	1	1	9		102.2870	0.989165	m	3	1	8	
50.8432	1.794370	12	0	2	4		103.2070	0.982837	8m	2	1	22	
51.6890	1.766980	263	2	0	5		103.2070	0.982837	m	2	2	12	
53.8976	1.699670	11	0	2	7		105.0230	0.970767	73	1	3	10	
54.1608	1.692030	74m	0	0	18		106.6090	0.960664	57m	3	1	11	
54.1608	1.692030	m	1	0	16		106.6090	0.960664	m	1	2	23	
55.2468	1.661310	16	2	0	8		108.4390	0.949483	12	1	0	31	
56.3077	1.632500	11	1	1	12		109.3950	0.943840	48	2	2	15	
57.0913	1.611940	7	0	1	17		110.3330	0.938435	38m	0	3	21	
58.3993	1.578910	154	0	2	10		110.3330	0.938435	m	1	3	13	
60.1898	1.536160	23	2	0	11		110.5450	0.937225	35	0	2	28	
63.1841	1.470370	183m	1	0	19		112.4580	0.926634	15	3	1	14	
63.1841	1.470370	m	1	1	15		113.1410	0.922970	15m	0	0	33	
64.1678	1.450180	40m	0	2	13		113.1410	0.922970	m	4	0	1	
64.1678	1.450180	m	0	0	21		113.3830	0.921688	12m	0	1	32	
66.3399	1.407870	59m	0	1	20		113.3830	0.921688	m	0	4	2	
66.3399	1.407870	m	2	0	14		114.1190	0.917836	15	2	1	25	
67.3111	1.389900	7	1	2	2		114.3500	0.916639	12m	1	1	30	
68.2610	1.372850	12	2	1	4		114.3500	0.916639	m	4	0	4	
68.9692	1.360470	234	1	2	5		115.1090	0.912761	43m	2	0	29	
70.8428	1.329020	12	2	1	7		115.1090	0.912761	m	0	4	5	
71.0657	1.325400	100m	1	1	18		117.3050	0.901941	47m	1	3	16	
71.0657	1.325400	m	0	2	16		117.3050	0.901941	m	2	2	18	
72.0025	1.310440	15	1	2	8		118.2850	0.897293	26m	0	4	8	
72.9106	1.296340	7	1	0	22		118.2850	0.897293	m	1	2	26	
73.6062	1.285800	7	2	0	17		120.0640	0.889156	9	3	1	17	
74.7567	1.268840	154m	0	0	24		121.3510	0.883492	41m	3	0	24	
74.7567	1.268840	m	2	1	10		121.3510	0.883492	m	4	0	10	
76.3317	1.246530	68m	0	1	23		123.1710	0.875788	9	0	4	11	
76.3317	1.246530	m	1	2	11		124.4530	0.870573	9	1	0	34	
77.4788	1.230910	94	3	0	0		125.2650	0.867357	12	0	2	31	
78.1537	1.221960	8	0	3	3		126.3750	0.863071	16	1	3	19	
79.0395	1.210480	13	0	2	19		127.4720	0.858953	34m	2	2	21	
79.9311	1.199200	68m	1	1	21		127.4720	0.858953	m	4	0	13	
79.9311	1.199200	m	2	1	13		127.7360	0.857983	60	2	1	28	
80.1683	1.196250	42	3	0	6		130.0130	0.849866	31m	3	1	20	
81.9381	1.174830	42m	2	0	20		130.0130	0.849866	m	0	4	14	
81.9381	1.174830	m	1	2	14		130.8490	0.847006	64m	1	1	33	
83.4822	1.156980	24m	1	0	25		130.8490	0.847006	m	3	2	1	
83.4822	1.156980	m	0	3	9		131.1440	0.846015	16m	2	3	2	
86.1305	1.128070	8	0	0	27		131.1440	0.846015	m	2	0	32	
86.3665	1.125590	27	2	1	16		132.3680	0.841976	9	3	2	4	

2	d(Å)	I	h	k	l	*
133.2680	0.839095	80m	1	2	29	
133.2680	0.839095	m	2	3	5	
135.7340	0.831556	13m	0	3	27	
135.7340	0.831556	m	3	2	7	
136.0400	0.830657	13	4	0	16	
137.3320	0.826946	9	2	3	8	
138.6250	0.823369	9	1	3	22	
139.6440	0.820647	9	0	4	17	
141.3840	0.816187	67m	2	2	24	
141.3840	0.816187	m	3	2	10	
143.8980	0.810155	52m	3	1	23	
143.8980	0.810155	m	2	3	11	
145.8400	0.805820	83m	0	2	34	
145.8400	0.805820	m	4	1	0	
146.9490	0.803468	52m	2	1	31	
146.9490	0.803468	m	1	0	37	
148.6650	0.800005	13	4	0	19	

PUBLICATIONS

SCIENTIFIC PUBLICATIONS

- J.A. Santamaría, J. Alkorta, J. Gil Sevillano. Propiedades mecánicas del telururo de bismuto (Bi2Te3) procesado mediante torsión bajo alta presión (HPT), Boletín de la Sociedad Española de Cerámica y Vidrio 52(3),137-142,(2013)
- J.A. Santamaría, J. Alkorta, J. Gil Sevillano. Microcompression tests of single-crystalline and ultrafine grain Bi2Te3 thermoelectric material J. Mater. Res. 30, 2593–2604 (2015).

CONTRIBUTIONS TO CONFERENCES

- JA Santamaría, J. Alkorta, J. Gil Sevillano, Assessment of the fracture toughness of bismuth telluride compacted by high pressure torsion, XXIX encuentro del grupo español de fractura, Bilbao (Spain), 21-23.03.2012.

- JA Santamaría, J. Alkorta, J. Gil Sevillano, Mechanical properties of PbTe processed by HPT (high-pressure torsion), Materials Science & Technology 2013, Montreal (Canada), 27 – 31.10. 2013

- JA Santamaría, J. Alkorta, J. Gil Sevillano, Mechanical and thermoelectric properties of pure PbTe processed by HPT (high-pressure torsion), Progress in thermoelectric materials and systems & HITTEG workshop, Barcelona (Spain), 22.11.2013

- JA Santamaría, J. Alkorta, J. Gil Sevillano, Deformazio plastiko bortitzen bitartez prosezaturiko material termoelektrikoen karakterizazio mekaniko eta termoelektrikoa, Donostia-San Sebastián (Spain), 3-4 .07.2013

- J. Gil Sevillano, T. Zühlke, J.A. Santamaría, J. Alkorta, Enabling Zn for bioabsorbable implants by SPD nanostructuring. International Workshop "Modeling and Development of Nanostructured Materials for Biomedical Applications". Madrid (Spain), 6-7.02.2014

- JA Santamaría, J. Alkorta, J. Gil Sevillano, Mechanical Top-down approach for nanostructured Thermoelectric materials, "Ultra-versatile Nanoparticle Integration into Organized Nano-clusters", Industry Workshop – Barcelona, June 2015